DISSERTATION

INVESTIGATIONS INTO MAGNETIC RELAXATION FOR VANADIUM COMPLEXES

Submitted by

Cassidy Elizabeth Jackson

Department of Chemistry

In partial fulfillment of the requirements

For the Degree of Doctor of Philosophy

Colorado State University

Fort Collins, Colorado

Spring 2022

Doctoral Committee:

Advisor: Joseph M. Zadrozny

Matthew P. Shores
Eugene Y.-X. Chen
Katherine Ross

ABSTRACT

INVESTIGATIONS INTO MAGNETIC RELAXATION FOR VANADIUM COMPLEXES

Magnetic molecules represent an emerging class of complexes that can be used to understand quantum phenomena impactful for quantum computing, non-invasive magnetic resonance imaging, and information storage. These organometallic complexes have the electronic spin is centered on the metal ion. Magnetic molecules based on electronic spins are extremely sensitive to changes in their local environment, such as nuclear spins. Electronic spins on a metal ion were employed to understand how nuclear spins in the local environment modulate electron spin dynamics. In this work, vanadium(IV) was chosen to study with varying catechol ligands. Electron paramagnetic resonance (EPR) was used to study two properties of these metal complexes, spin-lattice relaxation (T_1) and phase memory relaxation (T_m or T_2). Investigation of these parameters and fitting of these parameters provided information of how the local environment played a role in shortening these lifetimes. The complexes developed in this work indicates that the local environment is an extremely important piece of relaxation due to drastic changes in relaxation times.

Chapter 1 introduces provides motivation for the work conducted in this dissertation and gives a thesis structure overview. Chapter 2 gives a broad summary of the field of molecular magnetism and provides metaphors for the synthetic chemist to learn about electron spin relaxation. Chapters 3 gives the first report of nuclear spin patterning on a ligand shell impacting spin relaxtion times Chapter 4 details high-field, high-frequency orientation dependence on spin relaxation times for the V(IV) ion. Chapter 5 explores proton nuclear spin dynamics as they relate to nuclear spin patterns on a ligand and ligand complexed to a diamagnetic metal ion. Chapter 6 explores counterion dynamics and how they impact spin relaxation times. Chapter 7 gives a summary and future directions.

ACKNOWLEDGEMENTS

My decision to pursue chemistry and go to graduate school is due to the guidance of Dr. Scott Lewis, who never stopped encouraging me to be the truest form of myself – no matter how loud. I am truly grateful for crossing paths with you, your confidence in my abilities to succeed changed the course of my life. I will always be thankful for your presence as a mentor and friend.

I would like to thank my committee – Prof. Joseph Zadrozny, Prof. Matt Shores, Prof. Eugene Chen, and Prof. Kate Ross – for their support and guidance during my Ph.D. work, defense, and dissertation.

I recognize that my work is performed on both the ancestral and currently occupied land of the Arapaho, Cheyenne, and Ute Nations and peoples. I acknowledge that my research is dependent on the occupation of these sovereign nations and encourage reparations when possible.

The work described in this dissertation would not have been possible without using instrumentation at the Analytical Resources Core (ARC), National High Magnetic Field Lab, and EPR Center at the University of Denver. Thank you to Dr. Hans van Tol, Dr. Sandra Eaton, and Dr. Gareth Eaton for sharing your immense EPR knowledge with an eager student. I am grateful for each of in shaping how I view science and think about magnetism.

I am grateful for my colleagues who were a part of the Zadrozny group at CSU. Each of you were impactful in my experience and taught me something about myself. Thank you to Dr. Chun-Yi Lin for shaping my hands as an air-free chemist. Thank you to Tyler Ozvat for your patience and friendship, I have learned the art of deliberate tranquility from you. Thank you to Anthony Campanella for your ability to lighten any conversation. Thank you to Ian Moseley for providing such a unique perspective on science, your big-picture thinking gives new views on science communication. Thank you, Roxanna Martinez, for being the comic relief at the most

unexpected moments. Finally, thank you to all the students and researchers in this group, I enjoyed interacting with each of you.

Thank you to Joe for your help, guidance, criticism, and support. This Ph.D. would not be the same without you. Your enthusiasm for magnetism encourages me to pursue a career of something I enjoy and am passionate about.

Thank you to Dr. Donna Amenta and Dr. John Gilje for showing me the joys of inorganic chemistry. I am grateful for these years as a learned how to do research in a supportive setting.

Obtaining this degree would never have been possible without a support system. Thank you to my friends who have reminded me I am capable. Thank you to my family who supported me for being a career student. There are so many people who deserve words of gratitude, and some, but not all, are detailed below.

During my Ph.D. I went to a jiu jitsu class thinking it would be a fun way to exercise. Instead, I found a place where I can grow, be challenged, learn, and be my loudest self only to be met with grace. Thank you to Z's gym for witnessing me grow as a better person, scientist, friend, and teammate, I will be grateful for the rest of my life that I kept coming back to get beat up. Thank you to Brian "Z" Zehler for encouraging me to keep pursuing my dreams. Your gym changed my outlook on life.

Thank you to my friend, Christina Charles, for finishing my sentences and my wine. Thank you for being a friend, colleague, and support system during my Ph.D.

I owe gratitude to Olivia Manahan who was always on my side ready to lift me up. Thank you for your weirdness, laughter, and friendship. I am a better person for meeting you and admire your unwavering spirit.

Finally, thank you to my partner, honey-muffin, and husband, Daniel Corbin. We started this journey together and we made it through an extremely long engagement, pandemic, wedding, and a Ph.D. for each of us. No one has supported me, cheered me on, challenged me, or encouraged me to pursue all my dreams in this life as you have. I admire your love for science

every day and I am excited to continue to cheer you on in supporting your dreams, no matter where they take us.

Acknowledgements of Co-author Contributions and Funding Agencies

Chapter 2: This dissertation chapter contains the manuscript of an article [Jackson, C. E.; Moseley, I. P.; Martinez, R.; Sung, S.; and Zadrozny, J. M. “A reaction-coordinate perspective of magnetic relaxation” *Chemical Society Reviews*, **2021**, *50*, 6684-6699.] All authors contriburted to the writing of the published manuscript. C. E. J. and J. M. Z. performed the editing. I. P. M. made the TOC graphic. C. E. J. made all other figures in this work. Thank you to C. D. Charles and D. A. Corbin for helpful feedback. The work described in this chapter was supported by the NSF (CHE-1836537), the NIH (R21EB027293), and Colorado State University (CSU) for financial support. CSU acknowledges, with respect, that the land the university is on today is the traditional and ancestral homelands of the Arapaho, Cheyenne, and Ute Nations and peoples. I. P. M. is supported by the National Science Foundation Graduate Research Fellowship Program under Grant No. (006784-0002).

Chapter 3: This dissertation chapter contains the manuscript of an article [Jackson, C. E.; Lin, C.-Y.; Johnson, S. H.; van Tol, J. Zadrozny, J. M. “Nuclear-spin-pattern control of electron-spin dynamics in a series of V(iv) complexes” *Chemical Science*, **2019**,*10*, 8447-8454.] C. E. J., S. H. J., and C.-Y. L. executed the syntheses and characterization. C.E.J., C.-Y. L., J. v. T. and J.M.Z. conducted spectroscopic analyses and data interpretation. All authors were involved in assembling the manuscript. This research detailed in this chapter was performed with the support of Colorado State University (CSU) and the National Science Foundation (CHE-1836537). X-band EPR and standard molecular characterization experiments were performed at the CSU Central Instrument Facility, which is supported by an NIH-SIG award (1S10OD021814-01) and the CSU-CORES Program. C. E. J. and J. M. Z. thank J. Joyce and Prof. Sandra Eaton for helpful insight. A portion of this work was performed at the National High Magnetic Field Laboratory, which is

supported by the National Science Foundation Cooperative Agreement No. DMR-1644779 and the State of Florida.

Chapter 4: This dissertation chapter contains the manuscript of an article [Jackson, C. E.; Lin, C.-Y.; van Tol, J. Zadrozny, J. M. “Orientation dependence of phase memory relaxation in the V(IV) ion at high frequencies” *Chemical Physics Letters*, **2020**, *739*, 137034-137039.] C. E. Jackson: Conceptualization, Investigation, Writing - original draft, Writing - review & editing. C.-Y. Lin: Conceptualization, Investigation, Writing - review & editing. J. van Tol: Investigation, Writing - review & editing. J. M. Zadrozny: Conceptualization, Writing - original draft, Writing - review & editing. The work described in this chapter was supported by Colorado State University and the National Science Foundation (CHE-1836537). A portion of this work was performed at the National High Magnetic Field Laboratory, which is supported by the National Science Foundation through NSF/DMR-1157490/1644779 and the State of Florida.

Chapter 5: This dissertation chapter contains the manuscript of an article [Johnson, S. H.; Jackson, C. E.; J. Zadrozny, J. M. *Inorganic Chemistry*, **2020**, *59*, 11, 7479–7486.] S.H.J. and C.E.J. executed the syntheses and characterization. S.H.J., C.E.J., and J.M.Z. conducted spectroscopic analyses and data interpretation. All authors were involved in assembling the manuscript. Thank you to Profs. Joseph DiVerdi and Richard Eykholt, and Mr. Buzz Walters and Matt Phelan for fruitful conversation and graphical assistance. This research was performed with the support of Colorado State University (CSU), the National Science Foundation (CHE-1836537). S. H. J was supported by the National Institutes of Health as an REU participant of the Northern Colorado Bridges to Baccalaureate Program (1R25GM115300-4) for part of this work and S. H. J. also acknowledges the CSU Energy Institute for summer funding. C. E. J. was supported by a CSU Program of Research and Scholarly Excellence fellowship through the Center of Advanced Magnetics. Nuclear magnetic resonance experiments and standard molecular characterization were performed at the CSU Central Instrument Facility, which is supported by an NIH-SIG award (1S10OD021814-01) and the CSU-CORES Program.

Chapter 6: This dissertation contains a submitted manuscript to the *Journal of Physical Chemistry C* titled as seen in chapter. Authors on this manuscript are as follows: Cassidy E. Jackson,[‡] Thacien Ngendahimana,[‡] Chun-Yi Lin Gareth R. Eaton, Sandra S. Eaton, and Joseph M. Zadrozny. This manuscript was written as a collaboration between CSU and the University of Denver with T. N. and C. E. J. both contributing equally as first authors. C. E. J. and T. N. executed synthesis, carried out characterization and conducted the experiments. All authors conducted spectroscopic analyses and data interpretation. All authors were involved in assembling the manuscript. We thank Ralph Weber, Bruker Biospin for experimental assistance and fruitful discussion. This work was performed with the support of Colorado State University, University of Denver, the Research Corporation for Scientific Advancement, and the National Science Foundation (CHE-1836537). A portion of this work was performed at the CSU Analytical Resources Core, which is supported by an NIH-SIG award (1S10OD021814-01) and the CSU-CORES Program.

DEDICATION

For Dr. Scott Lewis, who never stopped encouraging me to be the truest version of myself.

TABLE OF CONTENTS

CHAPTER 1 – INTRODUCTION

Motivations

Magnetic relaxation is the cornerstone to many next generation technologies ranging from quantum information processing (QIP)[1–3] and magnetic resonance imaging[4,5] to quantum sensing[6] and information storage[1]. These applications rely on an intimate understanding of what controls relaxation, so optimal relaxation times can be achieved. Commonly, extending relaxation times for as long as possible is desirable as electron spin relaxation times tend to be too short for ulitity.

Control over magnetic relaxation, if realized, could induce a paradigm shift in modern computation methods and directly accelerate security, non-invasive imaging, and information prcessing.[1,2,7,8] Magnetic relaxation, here T_2 or spin-spin relaxation, for electrons relies on a quantum superposition of two states. Electronic spins are promising candidates as their orientations can act as traditional binary states (e.g. “up” = 0, “down” = 1), and superpositions of these orientations are easily generated and manipulated via microwave frequencies.[9–11] A criterion for electrons used in any applications of magnetic relaxation is that they need to demonstrate a long coherence time, commonly referred to as spin-spin relaxation time (T_2) or phase memory time (T_m), which defines the lifetime of the generated superposition.[3] A major challenge in implementing any of these applications with electronic spins is that coherence times (T_2 or T_m) that are too short (< 10 μs).[9,12–14] For a qubit to be viable, the length of the superposition lifetime must be at least 100 μs.[10,15] Lengthening the lifetime of T_2 is thus a critical goal of many applications reliant on long magnetic relaxation times.

This thesis will leverage the tunability of magnetic molecules to understand how specific environments control T_2 (or T_m in this dissertation), specifically by studying coordination complexes of first-row transition metals. In any given system, the theoretical upper limit of T_2 is the spin-lattice relaxation time (T_1). T_2 is often much shorter than T_1 because of its extreme

sensitivity to molecular vibrations, other thermal effects, and nearby nuclear and electronic spins in its immediate vicinity (see Chapter 2). The origin of this shorter time length is an extreme sensitivity of spin-based qubits to the chaotic local magnetic environment imposed by the flipping or interaction of nearby magnetic species. This environment interacts with the electronic spin to cause collapse the spin superposition, a process known as decoherence.[7] An analogy to decoherence is like a spinning coin on a table where the spinning coin is the superposition and decoherence is the coin falling over into heads ("1") or tails ("0").

Understanding how to engineer long-lived superpositions (long T_2 times) in such environments is a major hurdle to using electron spin-based systems as qubits. This understanding can only be achieved by studying how specific manipulations in the local environment (ligand field) induce long-lived superpositions, which is the major motivation for the work presented in this thesis. Moreover, long-lived superpositions need to be accessible in the presence of magnetic noise because nearby electronic spins, nuclear spins, and stray fields from moving charges in devices will likely all be present in any foreseeable application (see Chapter 2 for more information).

Thesis Structure

The research described in this thesis is centered on understanding topics in inorganic chemistry, synthetic chemistry, and physical chemistry, but the focus of this research is centered on understanding how the local environment of an electron impacts electron spin relaxation times. This dissertation first details electron spin relaxation aimed at an undergraduate level, then describes the first report of nuclear spin patterning on a ligand shell over simply the presence or absence of nuclear spins, reports the first high-field orientation dependence of T_2 on a V(IV) ion, and describes nuclear spin dynamics on a diamagnetic complex. These studies relied on a deep

understanding of spin relaxation processes, which was only accomplished through collaborations with the National High Magnetic Field Laboratory and the EPR Center at the University of Denver.

This thesis follows journal style format based on published articles wherein each chapter is assembled after these publications. These chapters are focused on understanding how the local environment of an electron on a V(IV) ion is impacted by its local surroundings, and how these surroundings can impact magnetic relaxation. These chapters have the following titles:

1. A Reaction-Coordinate Perspective of Magnetic Relaxation (Chapter 2)[16]
2. Nuclear-Spin-Pattern Control of Electron-Spin Dynamics in a Series of V(IV) Complexes (Chapter 3)[17]
3. Orientation Dependence of Phase Memory Relaxation in the V(IV) Ion at High Frequencies (Chapter 4)[18]
4. Programmable Nuclear-Spin Dynamics in TI(IV) Coordination Complexes (Chapter 5)[19]
5. Impact of Counterion Methyl Groups on Spin Relaxation in $[V(C_6H_4O_2)_3]^{2-}$ (Chapter 6)

Chapter 2 gives a broad overview of electron spin magnetic relaxation. It details the mechanisms of relaxation, how these mechanisms are determined, instrumentation, experimental setup, and the current state-of-the-art for magnetic molecules. An in-depth explanation of what electron spin magnetic relaxation is, subsequent relaxation mechanisms, and how these mechanisms are determined is provided. An interested reader is directed to this chapter and references therein for further reading.

Chapter 3 details the first investigation into nuclear spin patterning. In this chapter, a series of complexes was compared to understand how different nuclear spins, or atoms, on a ligand shell impact phase memory time (T_m). Importantly, two complexes with the same molecular formula yet different ligand scaffolds show how small changes in nuclear spin patterning impacts electron spin relaxation times.

Chapter 4 reports the first high-field, high-frequency orientation dependence of phase memory time of the V(IV) ion. This chapter provides a thorough explanation of what orientation

dependence is and why measuring it is important for comparing relaxation times between complexes. The orientation dependence of the vanadium(IV) ion at high field is less pronounced than traditional X-band frequencies.

Chapter 5 is centered on understanding the interactions between nuclear spins on ligands. Here, a detailed nuclear magnetic resonance (NMR) reports provides a deeper dive into how nuclear spins interact and why these interactions play such an important role in electron spin relaxation times. Importantly, dipole-dipole interactions are the most important nuclear spin interactions for catecholate ligands on a metal ion.

Chapter 6 provides an in-depth investigation into counterion binding of tri-alkyl ammonium counter-cations. This chapter revisits a manuscript previously published in our group[20] to uncover the mechanisms of phase memory relaxation. This work also shows the importance of experimental set-up for electron spin relaxation studies. Finally, this work details the importance of the immediate surroundings for an unpaired electron spin.

Chapter 7 provides a summary of the main findings from Chapter 2-6 and gives future directions in the field of molecular magnetism as it pertains to molecular qubits.

References

1 Troiani, F.; Affronte, M. *Chem. Soc. Rev.* **2011**, *40* (6), 3119–3129.

2 Leuenberger, M. N.; Loss, D. *Nature* **2001**, *410* (6830), 789–793

3 DiVincenzo, D. P. *Fortschritte Phys.* **2000**, *48* (9–11), 771–783.

4 Klare, J. P. *Biomed. Spectrosc. Imaging* **2012**, *1* (2), 101–124.

5 Terreno, E.; Castelli, D. D.; Viale, A.; Aime, S. *Chem. Rev.* **2010**, *110* (5), 3019–3042.

6 Atzori, M.; Sessoli, R. *J. Am. Chem. Soc.* **2019**, *141* (29), 11339–11352.

7 Graham, M. J.; Zadrozny, J. M.; Fataftah, M. S.; Freedman, D. E. *Chem. Mater.* **2017**, *29* (5), 1885–1897.

8 Aromí, G.; Aguilà, D.; Gamez, P.; Luis, F.; Roubeau, O. *Chem. Soc. Rev.* **2012**, *41* (2), 537–546.

9 Zadrozny, J. M.; Niklas, J.; Poluektov, O. G.; Freedman, D. E. *J. Am. Chem. Soc.* **2014**, *136* (45), 15841–15844.

10 Zadrozny, J. M.; Niklas, J.; Poluektov, O. G.; Freedman, D. E. *ACS Cent. Sci.* **2015**, *1* (9), 488–492.

11 Yu, C.-J.; Graham, M. J.; Zadrozny, J. M.; Niklas, J.; Krzyaniak, M. D.; Wasielewski, M. R.; Poluektov, O. G.; Freedman, D. E. *J. Am. Chem. Soc.* **2016**, *138* (44), 14678–14685. https://doi.org/10.1021/jacs.6b08467.

12 Bader, K.; Winkler, M.; Slageren, J. van. *Chem. Commun.* **2016**, *52* (18), 3623–3626.

13 Atzori, M.; Tesi, L.; Morra, E.; Chiesa, M.; Sorace, L.; Sessoli, R. *J. Am. Chem. Soc.* **2016**, *138* (7), 2154–2157.

14 Atzori, M.; Sessoli, R. *J. Am. Chem. Soc.* **2019**, *141* (29), 11339–11352.

15 Bader, K.; Dengler, D.; Lenz, S.; Endeward, B.; Jiang, S.-D.; Neugebauer, P.; van Slageren, J. *Nat. Commun.* **2014**, *5*, 5304.

16 Jackson, C. E.; Moseley, I. P.; Martinez, R.; Sung, S.; Zadrozny, J. M. *Chem. Soc. Rev.* **2021**, *50* (12), 6684–6699.

17 Jackson, E.; Lin, C.-Y.; Johnson, S. H.; Tol, J. van; Zadrozny, J. *Chem. Sci.* **2019**, *10*, 8447-8454.

18 Jackson, C. E.; Lin, C.-Y.; van Tol, J.; Zadrozny, J. M. *Chem. Phys. Lett.* **2020**, *739*, 137034.

19 Johnson, S. H.; Jackson, C. E.; Zadrozny, J. M. *Inorg. Chem.* **2020**, *59* (11), 7479–7486.

20 Lin, C.-Y.; Ngendahimana, T.; Eaton, G. R.; Eaton, S. S.; Zadrozny, J. M. *Chem. Sci.* **2019**, *10*, 548-555.

CHAPTER 2 – A REACTION-COORDINATE PERSPECTIVE OF MAGNETIC RELAXATION

Overview

Understanding and utilizing the dynamic quantum properties of metal ions is the frontier of many next generation technologies. One property in particular, magnetic relaxation, is a complicated physical phenomenon that is scarcely treated in undergraduate coursework. Consequently, principles of magnetic relaxation are nearly impenetrable to starting synthetic chemists, who ultimately design the molecules that fuel new discoveries. In this Tutorial Review, we describe a new paradigm for thinking of magnetic relaxation in metal complexes in terms of a simple reaction-coordinate diagram to facilitate access to the field. We cover the main mechanisms of both spin-lattice (T_1) and spin-spin (T_2) relaxation times within this conceptual framework and how molecular and environmental design affects these times. Ultimately, we show that many of the scientific methods used by inorganic chemists to study and manipulate reactivity are also useful for understanding and controlling magnetic relaxation. We also describe the cutting edge of magnetic relaxation within this paradigm.

Key learning points

1. Magnetic relaxation is the process of a molecular magnetic moment flipping orientation while the spin system (either a single molecule or a bulk sample) returns to equilibrium.
2. Magnetic relaxation mechanisms are analogous to reaction pathways: they proceed from a high-energy “starting material” to a lower energy “product,” where the start and end points are different orientations.
3. The mechanisms of magnetic relaxation are controlled by varying chemical composition and structure.

4. The mechanisms of magnetic relaxation are also governed by extrinsic factors, such as applied magnetic field, temperature, and local environment.
5. The cutting edge of molecular magnetic relaxation research is designing species where relaxation processes are as slow as possible.

Introduction

Magnetic molecules are centerpiece components of numerous areas of research, ranging from quantum information processing[1–3] and classical data storage[1,4] to magnetic resonance imaging (Fig. 2.1) [5–7] and spin-controlled reactions.[8] Of these, open-shell transition metal complexes are particularly popular, with proposed applications as molecular qubits[2,3,9], spin-crossover sensors[10,11], single molecule magnets[12,13], and molecular spintronic materials.[14] Organic radicals are also studied for their biomedical imaging applications, polymer applications, and use in pharmaceuticals.[15,16] Molecular compounds such as these two classes are notably advantageous for these applications because they offer a blank slate to design magnetic properties by harnessing synthetic chemistry.

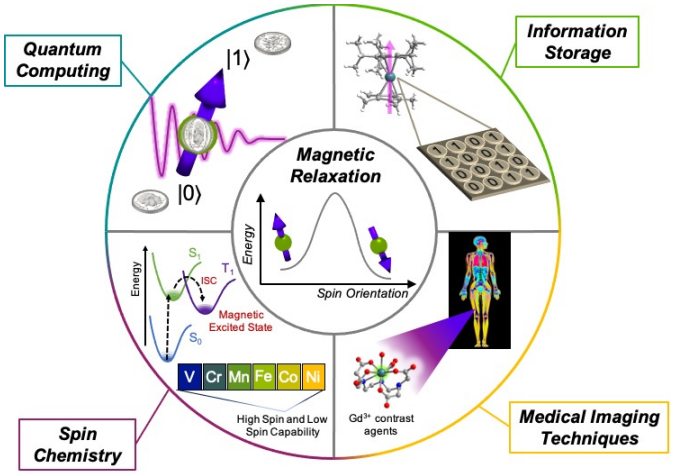

Figure 2.1. Overview of areas where understanding and designing magnetic relaxation in molecules is important to modern and future technological developments.

A specific magnetic property that is important in the foregoing applications is magnetic relaxation (sometimes called spin relaxation), or the response of the magnetic moment after misalignment from an applied magnetic field (from an MRI scanner or nuclear magnetic resonance spectrometer, for example). A slow relaxation rate permits many important and exciting possibilities, e.g. the storage of information (quantum or classical) in the orientation of the magnetic molecule (here a spin-up orientation could be “0” versus spin-down orientation of “1” in analogy to a simple bit). Slow relaxation rates will also enable certain magnetic resonance spectroscopic experiments (e.g. to noninvasively detect local chemistry) while fast relaxation can make these measurements more challenging. Therefore, there is a clear necessity to understand how to use synthetic design to control and slow down magnetic relaxation – an end goal that many groups are still in pursuit of.

Magnetic relaxation is driven by interaction of the relaxing species with local electronic and magnetic fields. These fields are influenced by intrinsic properties of the molecule. For example, metal-ion identity, spin state, oxidation state, ligand field, and geometry can all affect the relaxation rate of an open-shell metal ion. Extrinsic properties, such as counterion, concentration, temperature, and matrix (e.g. solvent or local chemical surroundings), are also important. Thus, there is considerable overlap between the molecular factors that control magnetic relaxation and those that dictate commonly approached properties by chemists, like reactivity.

Despite this conceptual overlap and the importance of dynamic magnetic properties in many cutting-edge fields, education in magnetic relaxation is typically absent from undergraduate chemical curricula.[17–19] As a consequence, concepts in magnetic relaxation can be intimidating for chemistry researchers to utilize in their research. Yet it is precisely these chemists that are needed to make the molecules that drive the observations of new processes, developments of new theories, and surmount the diabolical challenges to designing slow magnetic relaxation processes. This Tutorial Review aims to assist researchers unfamiliar with magnetic relaxation and provide them with an overview of the field in an accessible way. To do so, we draw a direct analogy between the complex quantum mechanical processes of spin relaxation and one of the most intuitive phenomena to the synthetic chemist: the reaction-coordinate diagram (Fig. 2.2). We focus primarily on metal complexes, though many of the concepts discussed here can be applied to organic radicals.

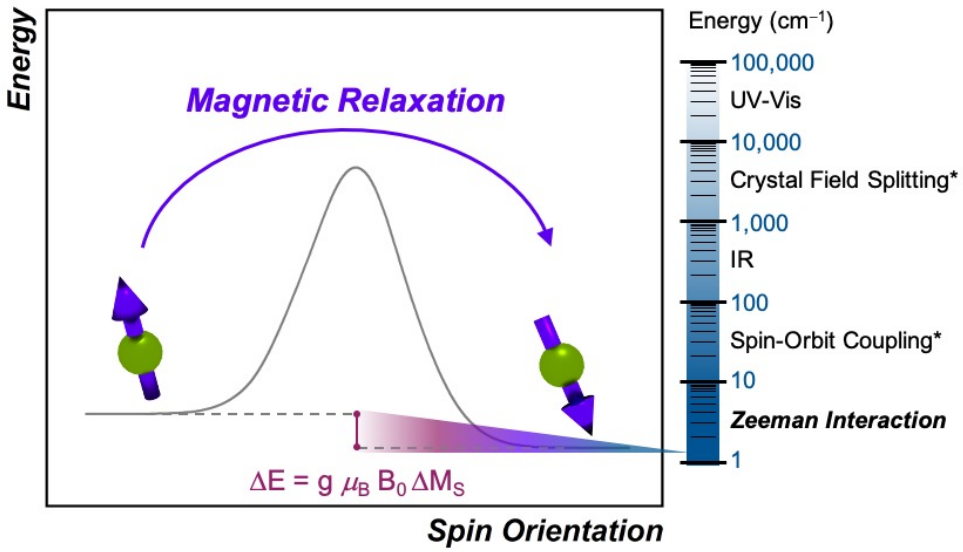

Figure 2.2. Magnetic relaxation in analogy to a standard reaction-coordinate diagram. Here, the reaction coordinate corresponds to spin orientation, with the products aligned parallel to the applied field and the starting materials aligned against it. The energy difference (ΔE) between the starting materials and products is the Zeeman energy, as defined in the plot. The energy scaling on the right compares the Zeeman interaction to other important energies. Scaling in the reaction coordinate diagram is arbitrary. Asterisks denote energy scaling for 3d transition metals.

A Reaction-Coordinate Picture of Relaxation

Magnetic relaxation is the process of a magnetic moment (or a spin) coming to alignment with an applied magnetic field from some other orientation. This misaligned orientation is an excited state while the ground state is when the spin is aligned with the field. For this reason, magnetic relaxation can be thought of analogous to an exergonic reaction that proceeds from relatively high energy reactants (the misaligned orientation) to lower-energy products (the aligned orientation). In the case of a single unpaired electron in an external magnetic field undergoing relaxation (Fig. 2.2), the starting materials could be "spin up", corresponding to the spin quantum number $m_S = +^1/_2$. Likewise, the products could be "spin down", bearing the $m_S = -^1/_2$ spin quantum number. The relaxation process is then the "reaction" that enables the spin to convert orientation. There are some important similarities between the relaxation process and a chemical reaction. Just like many reactions, the process of magnetic relaxation is thermodynamically favored.[15] There are also often many possible mechanisms by which the system can proceed with relaxation, similar to how many different reaction pathways can exist in a catalytic system. Though there are many of these pathways available to a molecule, again just like with a reaction system, it is the fastest relaxation process that typically proceeds under a given set of conditions. Several relaxation processes have an activation energy, directly analogous to a chemical reaction. However, other relaxation mechanisms can proceed by tunneling through the activation barrier, just like proton-tunneling reactions that can be interrogated through kinetic isotope studies.[20] Owing to all the foregoing similarities, it should be no surprise that elucidating the operative magnetic relaxation processes is just as rich and intellectually rewarding as mechanistic investigations of reactions.

There are also some critical differences between magnetic relaxation and a typical chemical reaction. First, the energy difference separating the starting materials and products is extremely small, typically on the order of a few wavenumbers or less so the relaxation process is

nearly thermoneutral. This small energy difference is because the energy separating the spin orientations in a typical applied magnetic field (from the "Zeeman" interaction, Fig. 2.2) is weak. This situation is in stark contrast to the multiple-kcal-energy magnitudes (1 kcal/mol = 350 cm^{-1}) separating starting materials and products in a general chemical reaction. Second, the transition states of molecules in the "relaxation reaction" can correspond to high-energy spin orientations, which are discrete and quantized energy levels with m_S (or M_S if $S > {}^1/_2$) values, or other quantum phenomena entirely. This point highlights a key contrast to a chemical reaction, where a transition state is a transient, high-energy, and distorted molecular geometry. Third, because these transition states are quantized, a given relaxation process does not proceed along a continuous potential-energy curve like molecular transformations, but instead by discrete jumps with emission/absorptions of energy.

We also note that, just like a chemical reaction, the rate of relaxation reflects the slowest step in the operative pathway. Indeed, there are often competing mechanisms, yet the slowest step in the fastest pathway is most important for the observed rate. In this light, the "rate-determining step" for magnetic relaxation is whether the environment can provide the energy to drive the process or accommodate the energy emitted during relaxation.[21] This process is in contrast to reactions where rate determining steps involve structural transformations or proton/electron transfers, and possibly isolable chemical intermediates.

The figure of merit for magnetic relaxation is the time constant of the process, the magnetic relaxation time, which is the inverse of the relaxation rate. The timescale of a magnetic relaxation time is highly variable, typically ranging from picosecond to minute timescales. There are two basic types of magnetic relaxation, spin-lattice relaxation, T_1, and spin-spin relaxation, T_2. Both of these parameters are vital for the applications in Fig. 2.1. In light of this importance, it is essential that we understand how to control the processes that govern these relaxation times and how they correlate to molecular structure. Below we describe the different relaxation mechanisms that

govern these two relaxation times, again in analogy to the basic chemical reaction-coordinate paradigm described above.

Basic Molecular Spin Properties Relevant to Relaxation

In evaluating the reactivity of a metal complex used in a reaction or as a catalyst, common considerations might be steric congestion or electron abundance/deficiency in the ligand scaffold. Similarly, for coarse-grain prediction of a magnetic relaxation property, there are several key magnetic parameters that are important to consider as a starting point. These parameters are the *g* factor, hyperfine coupling interactions, and zero-field splitting (Fig. 2.3). Comprehensive treatments of *all* the magnetic properties in metal complexes, which are diverse, can be found elsewhere.[15]

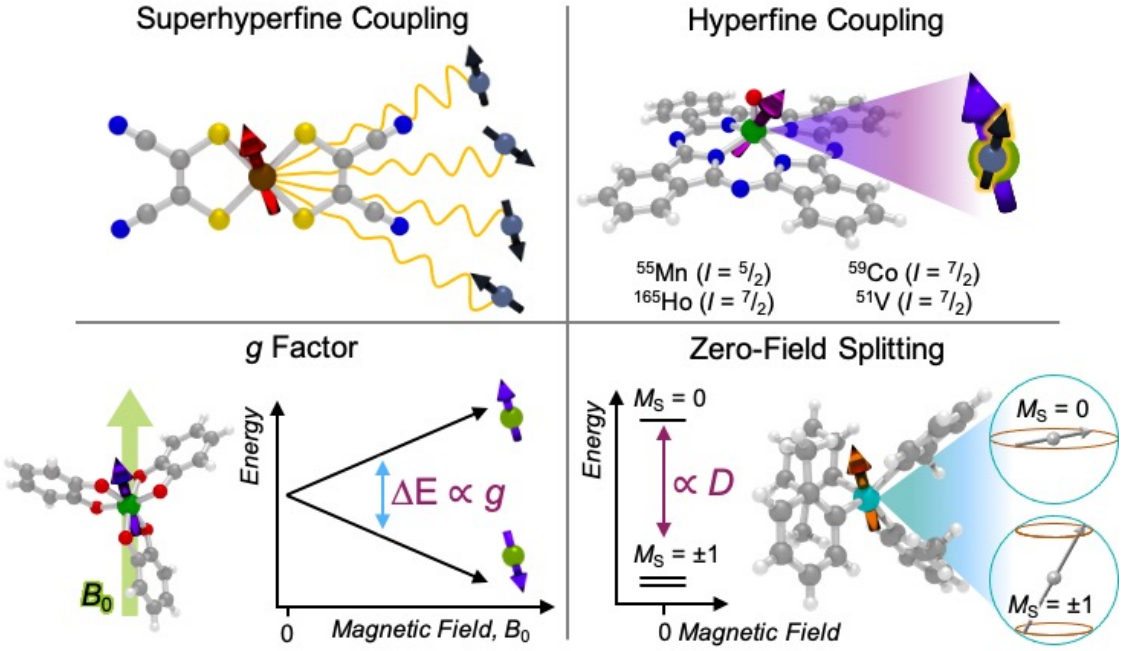

Figure 2.3. Graphical overview of chemical features that impact relaxation processes.

The first magnetic factor is the electron gyromagnetic ratio, or *g* factor. Electrons possess an intrinsic angular momentum that possesses a magnetic moment which interacts with an

applied magnetic field. The strength (or energy) of this interaction is proportional to the applied magnetic field (B_0), the Bohr magneton (m_B, a fundamental constant), the m_S value of the given spin orientation, and the *g* factor: $E = g m_b B_0 m_S$. The part relevant to relaxation is the *g* factor, a proportionality constant that describes the sensitivity of the magnetic moment to an external magnetic field. Simply stated – a larger *g* factor indicates a larger change in energy between different spin orientations in an applied magnetic field (Fig. 2.3).

The *g* factor often gives different values based on the orientation of a molecule in a magnetic field. The *g* value is often referred to as the *g* tensor for this point. For an organic radical, *g* will be close to 2.0023, which is the *g* factor for a free electron, and relatively independent of orientation. In contrast, metal complexes often have highly orientation dependent *g* values that can range from 0 to nearly 20 and are often anisotropic (i.e. g_x, g_y, and g_z are all different, x, y, and z here defined with respect to molecular axes). The largest and most anisotropic *g* factors tend to be found in rare-earth ions and low-coordinate transition metals.[22] Generally speaking, anisotropic *g* values tend to produce faster relaxation rates, though there are many exceptions.

The second important factor is the magnetic interaction between an unpaired electronic spin and a nuclear spin on the same atom. This interaction is known as the hyperfine coupling interaction and has a strength denoted by the hyperfine coupling constant (*A*) (Fig. 2.3). An example of this interaction occurs in Co(II) complexes, from the coupling of the magnetic nucleus of ^{59}Co ($I = {}^7/_2$) and the unpaired electrons. Hyperfine interactions are very similar to *J*-coupling in proton nuclear magnetic resonance (NMR) spectroscopy. Hyperfine couplings can also be anisotropic, just like the *g* factor.

Magnetic nuclei are abundant in complexes beyond the spin-bearing ion and are often located in the ligand shell, counterions, and the surrounding matrix (e.g. proton-rich organic solvents, $I = {}^1/_2$ ^{1}H). Magnetic interactions with these latter three classes of nuclei is commonly referred to as “superhyperfine” coupling. Typically, stronger superhyperfine interactions with

environmental magnetic species engender faster relaxation rates, though there is nuance to this statement that will be described later.

The final interaction that is noteworthy to highlight, known as the zero-field splitting, is a specific manifestation of spin-orbit coupling in metal ions with spin states *greater* than $^1/_2$ (as a result of bearing two or more unpaired electrons) (Fig. 2.3). For an electronic spin with $S > {}^1/_2$, there are $|2S + 1|$ accessible M_S levels. Each M_S level corresponds to a different alignment of the electronic spin relative to a molecular axis. A high $|M_S|$ value represents a spin precessing tightly around a molecular z axis, or closely aligned with that axis. A low $|M_S|$ value, in contrast, is a spin precessing far away from that same axis, commonly represented with perpendicular alignment to *z*. In the absence of zero-field splitting, or for a light atom (like an $S > {}^1/_2$ organic radical), the M_S levels are degenerate, or nearly so, at zero applied magnetic field. In the presence of zero-field splitting, which is common for heavy metal atoms (3d, 4d, 5d, 4f, and 5f elements) however, they are not, as shown in Fig. 2.3.

There are two parameters that describe the zero-field splitting. The first, the *axial* zero field splitting, or *D*, splits the energies of $|M_S|$ levels away from one another (e.g. it will separate a pair of $M_S = \pm 1$ levels from $M_S = 0$ levels as in Fig. 2.3). For first-row transition metal complexes, values of *D* can range from less than 1 cm^{-1} to hundreds of cm^{-1}.[22] The sign of *D* causes two limiting cases of M_S-level orderings. A positive *D* indicates a spin where the lowest energy level is $M_S = 0$ or $M_S = \pm {}^1/_2$, depending on whether *S* is integer (even number of electrons) or half-integer (odd number of electrons). A negative *D* indicates a spin where the M_S levels with largest $|M_S|$ are lowest in energy (e.g. $M_S = \pm 1$ for an $S = 1$ Cr^{4+} ion, as shown in Fig. 2.3). The second parameter, *E*, the *transverse* zero-field splitting or rhombic zero field splitting parameter, will cause an energy splitting of M_S levels in a pair (e.g., it will split $M_S = \pm 1$ levels from each other at zero field). The ratio $|E/D|$ is often referred to as the *rhombicity* parameter.[23]

The zero-field splitting is important for relaxation because individual M_S levels are the starting points, end points, and transition states of the magnetic relaxation process. Thus, the

zero-field splitting parameters directly modify the relaxation rates by dictating the relative energies of all involved steps in a relaxation pathway. The parameters *D* and *E* are also a direct result of the electronic structure of the metal complex, meaning that many intuitive molecular features, primarily symmetry and ligand field, can be modified to direct the sign and magnitude of *D* and *E*. This fact also means that general correlations between *D*, *E*, and relaxation times are challenging to make, and are best discussed on a case-by-case basis.

Spin-Lattice Relaxation (T_1)

Spin-lattice relaxation (also called longitudinal relaxation) refers to relaxation driven by interactions between the molecule and the environment, or "lattice," that exchange energy. Spin-lattice relaxation specifically describes the process for a spin to relax from a starting spin-up (destabilized) orientation to the spin-down (stabilized) product orientation (Fig. 2). There is an enormous mechanistic diversity in how this process occurs depending on how a magnetic molecule exchanges energy with the lattice.

The energy exchanged with the environment during spin-lattice relaxation is in discrete amounts. Here, energy is exchanged through phonons, which are collective, long-range vibrations in a solid, often spanning multiple molecules.[24] The availability of phonons in a system is dependent on the temperature of the system and the nature of the surrounding matrix (e.g. a crystalline v. frozen solvent glass environment).[27]

The rates of the different mechanisms of relaxation that we discuss below generally follow different temperature, magnetic field, or environmental dependencies. Furthermore, the rates of these processes may be impacted by the lattice just as much as the molecule itself. Thus, in any real system, unraveling the operative mechanisms requires measuring the dependence of the relaxation process on all of these parameters. This process, though applied to dynamic magnetic processes, is therefore comparable to how one might determine the full picture of potential reaction pathways in a catalytic system. Below we give an overview of each of the known

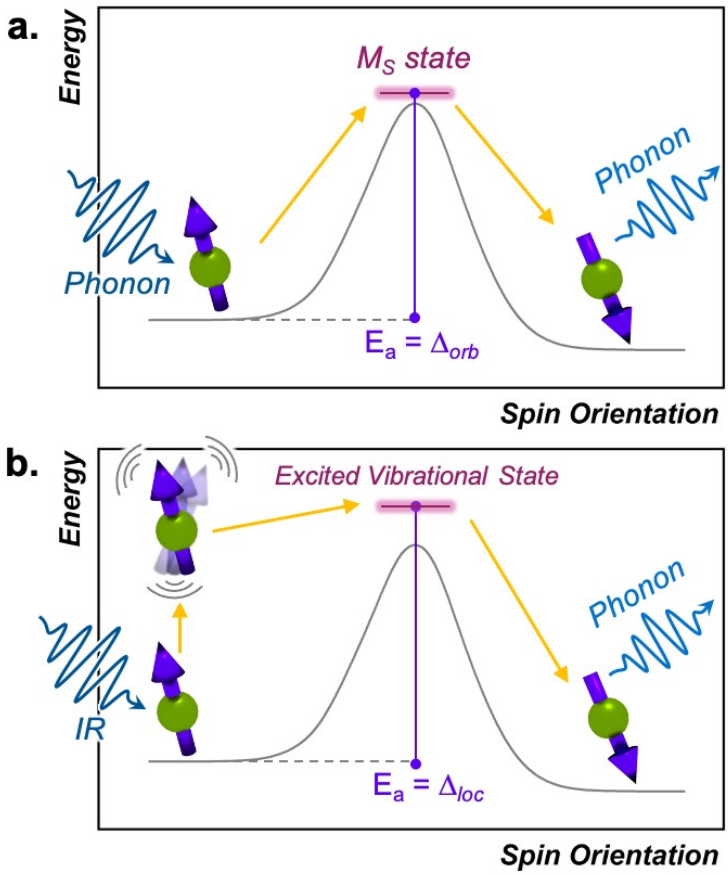

Figure 2.4. **(a)** Depiction of the Orbach process in analogy to a reaction-coordinate diagram. The transition state is an actual high-energy M_S level for the relaxing spin. **(b)** Energy profile of the local mode process. Here, discrete vibrations in a molecular species promote the spin to overcome the barrier and enable relaxation.

mechanisms of spin-lattice relaxation, their relation to the reaction analogy established earlier, and the dependence of the processes on the molecule and environment.

Measurement of T_1

Spin-lattice relaxation is measured primarily by two different instruments: a magnetometer such as a magnetic properties measurement system (MPMS), or a pulsed electron paramagnetic resonance (EPR) spectrometer. Magnetometers allow for the study of magnetic relaxation processes across a range of temperatures, time scales and magnetic field strengths with the technique of alternating current (ac) susceptibility. However, the limited frequency range for ac

susceptibility measurements (typically 0.01 Hz - 1500 Hz) means that quickly relaxing systems (T_1 < *ca.* 0.1 ms) are not able to be observed directly with this instrument. An alternative analysis is by pulsed EPR spectroscopy, which can measure T_1 through inversion or saturation recovery experiments. This technique can measure much faster relaxation times ($T_1 \sim 1$ ms lengths), but pulsed spectrometers are far less common than magnetometers. There are some slight differences in the time constant measured by the techniques, because ac susceptibility extracts T_1 from bulk magnetization while the EPR experiment is probing a specific transition.[25] However, at the microscopic level, the same process is occurring – a spin is flipping during the process of relaxation. We direct the interested reader to several key resources to learn about these techniques in deeper detail.[4,26]

Mechanisms of Spin-Lattice Relaxation

Below we discuss the collection of mechanisms that drive T_1 relaxation, starting from those that most closely resemble the reaction-coordinate analogy, then move on to processes that deviate from the analogy and demonstrate the complexity of relaxation phenomena in magnetic molecules.

Orbach Process

The Orbach process proceeds by excitation from the starting spin orientation to a higher energy spin orientation with energy provided by a phonon. This higher-energy M_S level is the effective transition state for the Orbach process. Relaxation then proceeds from this transition state to the lower energy spin orientation by releasing energy (in the form of a phonon) to the lattice (Fig. 4).[26,27] For this process to occur, there must be available phonons of the appropriate energy to excite to the transition state. The Orbach process is not limited to a single “transition

state" and can involve multiple steps to a higher energy M_S level before relaxation via phonon emission.

High-spin metal ions frequently relax via the Orbach process, as other M_S levels within the $|2S + 1|$ manifold often serve as transition states. In contrast, $S = {}^1/_2$ molecules do not show the Orbach process, as there are only two m_S levels for an $S = {}^1/_2$ system ($m_s = \pm{}^1/_2$) (and thus no transition state). The relaxation rate of the Orbach process is described by:

$$\frac{1}{T_1} = A_{orb} e^{(\Delta_{orb}/k_B T)} \qquad (1)$$

This equation mirrors the form of the Arrhenius law, where $1/T_1$ is the rate constant. A_{orb} is the attempt frequency for the Arrhenius description and a larger A_{orb} means there is higher probability the mechanism will contribute to relaxation. A_{orb} is determined by several factors: it decreases in magnitude with increasing phonon availability (or energy availability) and generally increases as the activation energy increases.[15] Hence, it is challenging to determine A_{orb} *a priori* on the basis of intuitive molecular considerations. Indeed, the basic theories for understanding relaxation (and the origins of A_{orb}) are developed for solid state defects, not molecular systems. As such, A_{orb} is frequently just extracted from experimental data, and is typically found with values of 10^{-2} to 10^{-10} s^{-1}.[4,15] The term D_{orb} is the activation energy (E_a) to the M_S-level transition state. Finally, note that A_{orb} is denoted as t_0 and D_{orb} as "U_{eff}" or "effective energy barrier" in the single-molecule magnet literature, which tends to focus on this parameter as the key figure of merit.[4] An example molecule that exhibits the Orbach process is presented in the state-of-the-art section.

Local Mode Processes

The local mode relaxation mechanism utilizes discrete vibrations ("local modes") on a molecule to facilitate relaxation.[28,29] Here, incoming energy excites the spin system from the starting configuration to a transition state that is a local vibration. From this transition state, the spin can then relax to the product spin orientation while releasing energy (Fig. 4).[30] The process

is in some ways like chemiluminescence, where the reaction product (the relaxed spin) is accompanied by an emission of energy, here in the form of a lattice vibration.

The temperature dependence of the relaxation rate of the local mode process is described by:

$$\frac{1}{T_1} = A_{loc} \frac{e^{\Delta_{loc}/k_bT}}{(e^{\Delta_{loc}/k_bT} - 1)^2} \qquad (2)$$

where A_{loc} is related to the amplitude of the active mode, local strain at the molecule, and is, ultimately, hard to empirically predict for a given molecule, just like A_{orb}. Therefore, also like A_{orb},

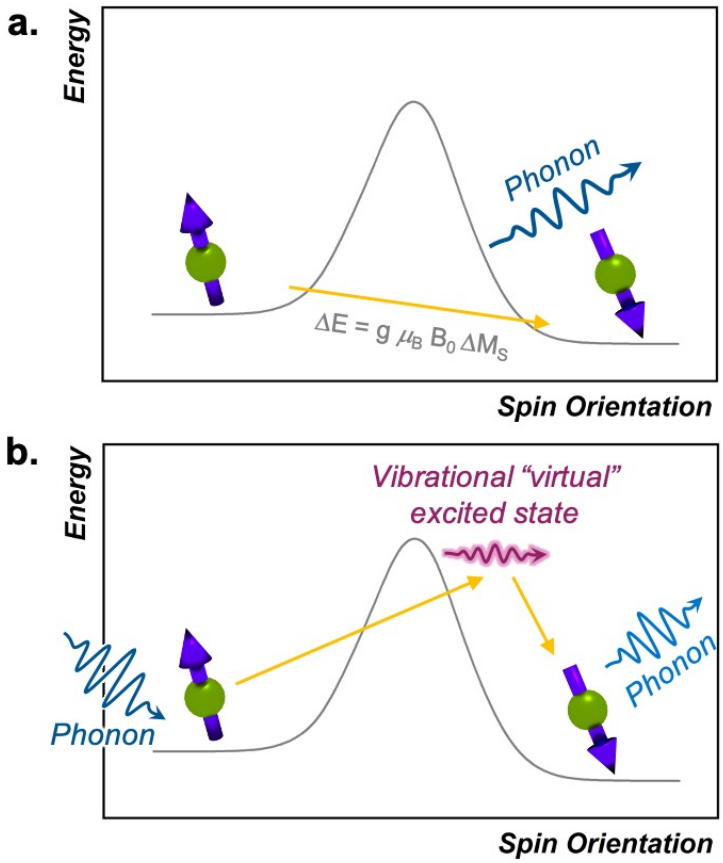

Figure 2.5. **(a)** Depiction of the direct process in analogy to a reaction coordinate diagram. The spin flip energy is the Zeeman energy and relaxation emits a single phonon of that energy to the lattice. **(b)** Depiction of the Raman process in analogy to a reaction coordinate diagram. The "virtual" transition state is a superposition of vibrational states in the solid and is not an actual defined energy level. Relaxation involves two phonons in a simultaneous excitation and deexcitation of the spins, ultimately transferring energy to the environment of an amount equal to the ΔE between the starting and product spin orientations.

A_{loc} is commonly extracted from experiment and considered as a "weight" for the contribution of this process to the overall relaxation rate. Δ_{loc} is the energy of the local mode. In some cases, the vibrations that enable the excitation can be assigned to molecular features using vibrational spectroscopy.[31,32] One example of a species that exhibits a local mode process is MoO(TTP)(OEt) (TTP = tetraphenylporphyrin) tentatively driven by a *ca.* 240 cm^{-1} local mode when measured near 100 K by pulsed EPR. This molecule is notable because the relaxation rate of the local mode process is approximately an order of magnitude greater than the V congener, a reflection of the high sensitivity of high-SOC spins to vibrations.[28]

Direct Process

The direct process is the first one we discuss that does not have an activation energy. In this process, a spin directly proceeds from the starting orientation to the final orientation because of an energy match between the energy separation of the two levels and a lattice phonon.[33,34] Importantly, the process effectively circumvents any possible transition states (Fig. 2.5). The direct process is analogous to the emission step of phosphorescence in photochemistry, where relaxation from an excited triplet to a ground singlet occurs without an activation energy, with a release of energy in the form of a phonon (a visible photon in the phosphorescence picture). However, unlike for phosphorescence emission, which involves a change in the number of unpaired electrons, the direct process is simply a change in spin orientation for the relaxing species.

The direct process has a distinctive magnetic field and temperature dependence that can enable diagnosis with relaxation studies. Indeed, the rate of relaxation for the direct process is described by the follow equation:

$$\frac{1}{T_1} = A_{dir} B^4 T \qquad (3)$$

A_{dir} is related to many features of a relaxing molecule's environment, specifically the number of phonons available that match the DE separation of the starting/end orientations and speed of sound of the matrix.[35,36] Like A_{loc} and A_{orb}, A_{dir} is generally treated as the weight of the contribution of this process to relaxation at a given field and temperature. B is the applied magnetic field, and T is the temperature. The linear dependence of relaxation rate on temperature and B^4 field dependence are characteristic of the direct process. Furthermore, the involved phonons must be

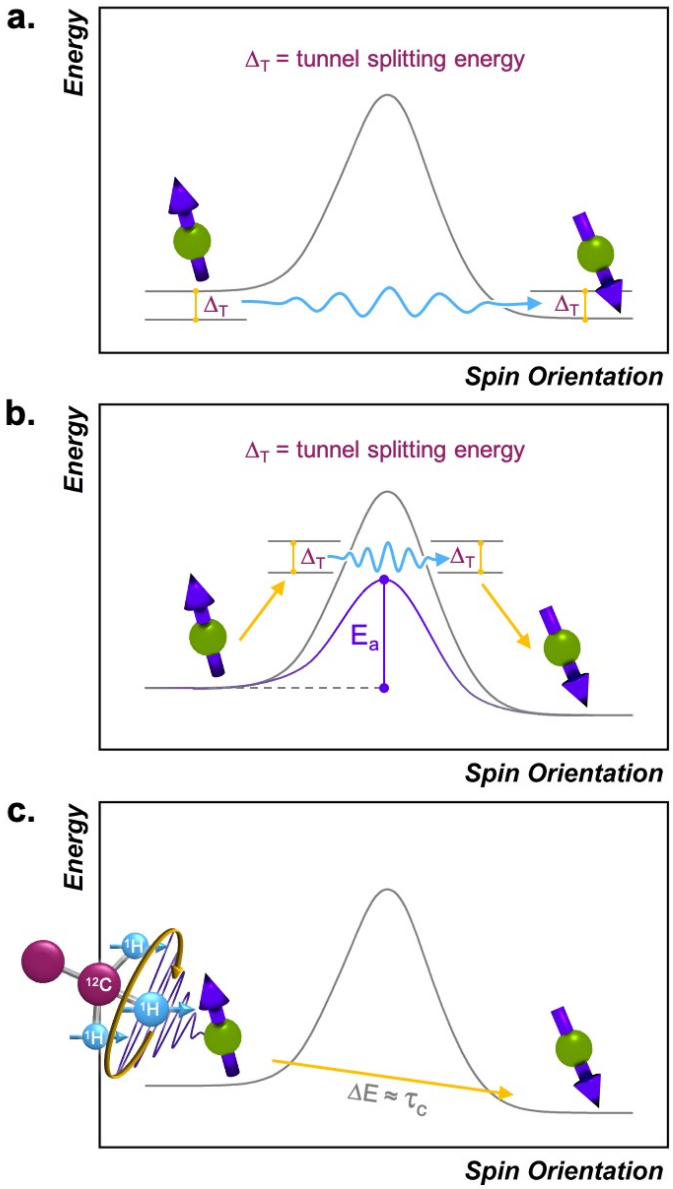

Figure 2.6. Reaction-coordinate depictions for (**a**) ground-state and (**b**) thermally assisted quantum tunneling of the magnetization processes and (**c**) thermally activated processes.

a direct energy match to the splitting of the starting materials and products of the spin system, which is small (usually 1-2 cm^{-1} or less) because the Zeeman energy is very small. As a result, this process is typically dominant only at low temperatures (< 10 K), when the only available phonons from the lattice are small in energy. Examples of the direct process are abundant in copper(II) square planar complexes which tend to exhibit relaxation through the direct process below 20 K.[37]

Raman Process

The Raman relaxation process is more common at higher temperatures than the direct process. The Raman relaxation process proceeds when a spin system simultaneously absorbs and emits phonons of differing energies. This action is fundamentally different than the direct process, which emits only one phonon, or the Orbach process, which involves successive absorption then emission. The difference in energies between the two phonons of the Raman process must match the difference in energy between the starting and final orientations. The fact that these phonons have defined energies suggests that there is absorption to and from a well-defined transition state. However, for the Raman process, that "state" is a superposition of lattice vibrations and does not actually exist, and is commonly referred to as a "virtual state"[15,33] (Fig. 2.5, b). This relaxation mechanism therefore does not have a clear connection to the classical reaction-coordinate picture developed earlier in this tutorial.[12] Nevertheless, the observation of the Raman process is incredibly common in relaxation studies. One example of a molecule exhibiting this process is the cobalt complex $[Co(acac)_2(H_2O)_2]$, which demonstrates the Raman process above 3 K when measured by ac susceptibility under *ca*. 1000 G magnetic fields.[38]

The rate of relaxation via the Raman process is described by the following equation:

$$\frac{1}{T_1} = A_{Ram}\left(\frac{T}{\theta_D}\right)^n J_8\left(\frac{\theta_D}{T}\right) \quad (2)$$

Where A_{Ram} is an experimentally determined factor like A_{loc}, A_{dir}, and A_{orb} (and controlled by many similar parameters).[35] Like those coefficients, it also describes the contribution from the Raman process to the overall relaxation rate. B is the applied magnetic field, T is the temperature, θ_D is the Debye temperature (which corresponds to the energy above which phonons do not exist in a solid, converted to an energy by 1 K $\approx$ 0.7 cm^{-1}), n is an exponent dependent on the relaxing system, and J_8 is the transport integral.[‡] The transport integral describes the energy distribution of phonons in the matrix. This integral and the characteristic temperature of the solid, or the Debye temperature (θ_D), depend on the physical composition of the solid.[39] Qualitatively, these two parameters signify that an environment with a larger distribution of accessible lattice vibrations will better facilitate the simultaneous absorption/emission process that drives the Raman process.

The Raman process produces a characteristic temperature dependence because of the exponent n. In theory, the rate of relaxation should scale with T^9 (n = 9) for species with a half-integer spin state and T^7 (n = 7) for integer spin state. In practice, however, multiple processes are often active and thus the apparent exponent extracted from fitting variable-temperature T_1 data is a non-integer value or ranges down to n = 2 to 3.[40] The Raman process commonly occurs at temperatures where the lattice does not have available phonons of sufficient energy to excite the spin system to an actual transition state for the relaxation process. For this reason, this process "undercuts" the barrier, just like the direct process.

Quantum Tunneling Processes

All previous mechanisms require energy input/release via interacting with the phonon system of the environment. However, there are two processes that circumvent this requirement by tunneling straight through the activation barrier for relaxation. It is for this reason that these processes are referred to as quantum tunneling of the magnetization (QTM) processes (Fig. 2.6).[23]

There are two QTM-based processes. One occurs directly between the starting and final spin orientations, without any input energy, and is referred to as “ground-state” QTM (Fig. 2.6). This type of tunneling mechanism is operative if there is a magnetic interaction between the wavefunctions of the starting and final spin orientations, which opens a tunnel-splitting energy gap in the barrier (D_T, Fig 6). Just like an electron tunnels because its spatial wavefunction can exist on both sides of an impenetrable barrier, the spin wavefunction of a system can exist on both sides of the activation barrier for reorientation. A stronger interaction between the starting and final orientations will generate a larger D_T and enable more efficient tunneling. Ground-state QTM is most facile near (or at) zero applied magnetic field, because interactions that drive QTM are strongest when the energy difference between the start and endpoint is smallest. Furthermore, the relaxation rate is generally temperature-independent because the tunneling mechanism does not require energy from phonons to ascend over a barrier. Tunneling is typically dominant only at the lowest temperatures, when the available phonons lack sufficient energy to enable any of the other processes. For example, the molecule $[Ph_4P]_2[Co(SPh)_4]$ displays tunneling below 2.5 K when measured by ac susceptibility under zero applied field.[41]

The second tunneling mechanism, thermally assisted QTM, requires exchange of energy with the lattice (Fig. 2.6). This mechanism involves an initial promotion (via phonon) of the starting spin orientation to a higher-energy M_S level. For the thermally assisted process, this level is below the highest-energy M_s level within a given manifold of an $S > {}^1/_2$ species (Fig. 2.6). Once promoted, the system then tunnels through the barrier to another M_s level, from which it can finally relax to the product. The thermally activated QTM mechanism behaves analogously to the Orbach process because of the promotion and phonon emission. However, this mechanism proceeds with an activation energy that is lower than the theoretical maximum defined by the zero-field splitting. An example of this phenomenon is illustrated with the $S = 2$ species $[(TPA^{tBu})Fe]^-$, which exhibits a D_{Orb} of 65 cm^{-1}, which is lower than the theoretical maximum of 192 cm^{-1} for this molecule.[42]

Thermally Activated Processes

Thermally activated processes are relaxation processes that are driven by thermal motion in the environment, e.g. methyl or amino group rotations, wherein magnetic nuclei are located on the moving structure (Fig. 2.6). This process is common at higher temperatures, when the surrounding matrix of a magnetic molecule softens to allow physical motion to occur, when they would otherwise be frozen at low temperature.[28,33,43] A given local motion will affect relaxation if the correlation time of that motion (t_c, or the inverse of the rate of the local motion) approaches the energy difference of the starting/ending orientation (w, in frequency).[43] The rates of thermally activated processes follow this equation:

$$\frac{1}{T_1} = A_{therm}\left(\frac{2\tau_c}{1+\omega^2{\tau_c}^2}\right) \qquad (4)$$

Here, A_{therm} correlates to the amplitude of the local magnetic field fluctuations from the thermally activated motion (but is generally treated as a weight for this process' contribution to T_1, like A_{orb}, A_{loc}, A_{Ram}, and A_{dir}), τ_c[§] is the correlation time of the thermally activated process, and *w* is the frequency of the energy gap between the starting/ending spin configurations.[43] t_c is temperature-dependent but depends on the activated motion and molecule, as t_c needs to approach 1/w. As such, there is no diagnostic temperature dependence for this process in the absence of other information about the molecular structure. One example of a molecule that displays this type of thermally activated process is in RbC_{60} fulleride, where a metal-to-insulator phase transition triggers fast relaxation (measured by pulsed EPR) at ca. 25 K and 3400 G.[43]

Intrinsic and Extrinsic Factors That Impact T_1

There are many chemical and physical factors that impact T_1 relaxation in 3d transition metal ions. First, we describe the important (and synthetically tunable) factors for T_1 that are intrinsic to molecules then move on to extrinsic parameters that impact T_1.

Strength and Symmetry of the Ligand Field

The effects of the ligand field on relaxation most commonly manifest through zero-field splitting in high-spin ions. This tendency is for two main reasons. First, the magnitudes of D and E, which are governed by the ligand field, can shift the energies of the M_S levels involved in relaxation. Thus, D and E will dictate the activation energies for both the Orbach and thermally assisted QTM mechanisms. Second, a nonzero value of E will induce ground-state QTM as an efficient relaxation pathway. Generally, the magnitudes of D and E are greater when the ligand field for a high-spin metal ion is weaker. However, the dependence of D (both in sign and magnitude) on the ligand field is extremely intricate, and so many exceptions to this rule exist. Furthermore, the magnitude of E is heavily dependent on symmetry. Coordination geometries that have one principal axis of rotation and adhere to nearly idealized uniaxial symmetry tend to have lower-magnitude E parameters and thus, suppressed ground-state tunneling. We refer the reader to excellent reviews of these parameters, which demonstrate the power of molecular design for tuning relaxation processes.[12,13,44,45]

Spin State

The effects of integer ("non-Kramers") versus half-integer spin ("Kramers") systems of unpaired electrons are evident most clearly in the QTM relaxation pathways. Here, a species with an integer spin is far more likely to exhibit relaxation by ground-state QTM than a half-integer-spin complex, because the term E is more effective at opening a tunneling gap for integer spin than half-integer-spin species.[4] A second place the spin state impacts relaxation is the difference in temperature dependence of the Raman process, as described earlier.

Isotopic Identity

Many metal ions possess isotopes that have non-zero nuclear spin, e.g. ^{59}Co (I = $^{7}/_{2}$, 100% natural abundance) or ^{165}Ho (I = $^{7}/_{2}$, also 100% natural abundance). The impact of a non-zero nuclear spin is primarily observed at zero field, low temperatures, and primarily affects quantum tunneling mechanisms.[46] The origin of this effect is the hyperfine coupling to the metal-ion nuclear spin, which can open a tunneling gap and increase the rate of QTM.

Spin-Orbit Coupling

Spin-orbit coupling (SOC) is an intrinsic property of a molecule. This fundamental electronic structure feature is broadly important in dictating relaxation, but has two different effects, generally depending on whether relaxation occurs at high temperature or low temperature. The high temperature impact is because the SOC interaction ties the energies of the M_S levels (e.g. potential activation energies for the Orbach process) directly to the spin-bearing orbital energies of the metal ion. Consequently, small changes in the structure of a molecule (e.g. from a vibration that modulates metal-ligand bond distances) impact the spin-bearing orbitals, when then modulate the M_S-level energies via the SOC to facilitate relaxation. The stronger the SOC for a given system, the more efficient this effect, and the shorter T_1 tends to become. For this reason, light-element species, e.g. organic radicals, tend to have T_1 values (often ms) that are longer at higher temperature than metal-ion systems. At lower temperature, the effect of a large SOC is different, particularly if the Orbach mechanism is active. In this case, a large SOC can push transition states to higher energies, enhancing the activation energy and ultimately slowing relaxation. The Dy-containing molecule in the state-of-the-art section later in the manuscript is a prime example of this point.

The importance of the SOC also means that the relaxation time can be dependent on precisely what orbital an electron resides in. Indeed, this effect is seen for the $[V(C_6H_4O_2)_3]^{2-}$ versus $[VO(C_6H_4O_2)_2]^{2-}$ molecules, which possess a single d electron in the d_{z2} versus d_{x2-y2}

orbital, respectively. T_1 is different by approximately an order of magnitude between these two molecules owing to this difference.[47–49]

Local Magnetic Species

The local magnetic species surrounding a molecule (the "spin bath") also exert important effects on relaxation. This factor is readily altered by the chemist, who can choose, for example, to co-crystallize a molecule of interest with other molecules or dilute by dissolution in different organic solvents.[4] These studies show that relaxation times generally increase when local magnetic content decreases, specifically the concentration of open-shell molecules. This general observation is because the presence of nearby magnetic units can hasten several of the above relaxation processes. For example, magnetic coupling to nearby electron spin systems will produce discrete spin levels that are relatively low-lying above the energies of the starting/ending spin orientations. Thus, the activation energy is lowered, and the relaxation rate accelerates via an Orbach process. Another common observed impact is through quantum tunneling, wherein proximate magnetic species enable the ground state QTM via a tunneling gap created by dipolar interactions.

Temperature

Temperature is one of the main extrinsic mechanisms of controlling relaxation. A given spin system will relax via the most efficient mechanism available. Thus, over a given temperature regime, one process is typically dominant, and cooling/heating the system can transition the system to relaxation via a different mechanism. The exact ordering of these domains with temperature is highly dependent on the studied system. Nevertheless, a general ordering scheme is still possible. Ground-state QTM and the direct process are often observed at the lowest temperatures, where high-energy phonons are unavailable. A system will then usually transition

to a regime where the Raman process is active upon warming. With further increasing temperature, where high-energy phonons become available in the solid, the Orbach process (or the analogous thermally assisted QTM) will typically take over. At even higher temperatures, local-mode and thermally activated mechanisms become active. A complete picture of magnetic relaxation for a molecule requires scanning an abundance of temperatures, just like understanding the kinetics of a chemical reaction.

Magnetic Field

The applied magnetic field is the second most-commonly varied extrinsic factor for studying relaxation. Most relaxation processes exhibit a field dependence, because the magnetic field will vary the energies of the starting and final spin orientations. The only relaxation process with a rate that has a field dependence explicitly written into the equation is the direct process, which displays a B^4 field dependence. However, in the case of processes that involve an M_S-level transition state, the applied field can also vary the energy of the transition state, thereby modifying the activation energies and rates, though this impact is relatively small. A changing applied field can also affect the efficiency of the thermally activated process, by modulating the difference between the ΔE for the starting/ending spin configurations and the correlation times of environmental motions. Applied fields are also enormously impactful in the quantum tunneling, as they split the M_S levels nominally involved in tunneling, effectively killing the process and inducing slower magnetic relaxation. The effect of a magnetic field is much stronger on the ground-state tunneling process than the thermally assisted one, as larger M_S levels have energies that are more sensitive to changes in the magnetic field. The foregoing discussion justifies the widespread nature of using variable fields for studying relaxation: it can enhance T_1 by orders of magnitude and is thus a powerful handle for optimization.

In summary, there are many dials available to the experimentalist to turn when controlling the operative T_1 processes. However, the foregoing points are not the only factors that affect T_1. Indeed, there are many other effects stemming from specifics of measurement. We direct the enthusiast to further reading for deeper information.[15]

The need for benchmarking

Frequently, a molecule will exhibit different relaxation processes depending on the aforementioned extrinsic factors. Because it is often too time-consuming to measure relaxation rates under every conceivable condition, the picture of magnetic relaxation in a molecule is often incomplete, and sometimes magnetic relaxation mechanisms are misassigned. Thus, numerical comparisons of the impacts of the foregoing extrinsic/molecular features can be quite challenging. We contend that a larger discussion about benchmarking relaxation parameters is desperately needed in this field to overcome this difficulty and pave the way to true understanding.

Spin-Spin Relaxation (T_2)

Spin-spin relaxation, or T_2, describes relaxation of a magnetic moment oriented in the plane perpendicular to the applied magnetic field (Fig. 2.7). The spin-spin relaxation time is one of the key figures of merit for quantum bits ("qubits) in quantum computing, quantum sensing, and other quantum-information based fields.[2,11] The given orientation-based description of T_2 is useful for instruction but note: the orientation of a spin is quantized and thus can only orient up or down in a magnetic field. The sideways depiction of the spin is in reality a unique quantum state known as a spin superposition, existing as both spin-up and spin-down orientations simultaneously. This quantum state is the cornerstone of the computational advantages for spin-based qubits.[2] A spinning-coin based analogy of the superposition is depicted in Fig. 2.7. Here, a spinning coin is

neither heads nor tails but both simultaneously. Similarly, the spin up or spin down orientations are heads or tails, while the superposition is both.

In general, the superposition is an extremely delicate state and will decay into its constituent states very quickly after it is generated. The lifetime of this decay is the spin-spin relaxation time, T_2. These values can range from very short (on the order of a few nanoseconds) to extremely long (on the order of milliseconds). For many applications of qubits, T_2 needs to be 100 ms, and pursuit of ever-larger T_2 values is a growing area of work.[1,2,50] This time constant is known by several other names in the literature: coherence time, transverse relaxation time, and phase memory relaxation time. We refer the interested reader to further references for the key differences between them.[15,33] In general, however, these terms are used interchangeably to describe the same relaxation process. In this review, we will use the term "spin-spin relaxation time" and T_2 to describe all forms of this type of relaxation.

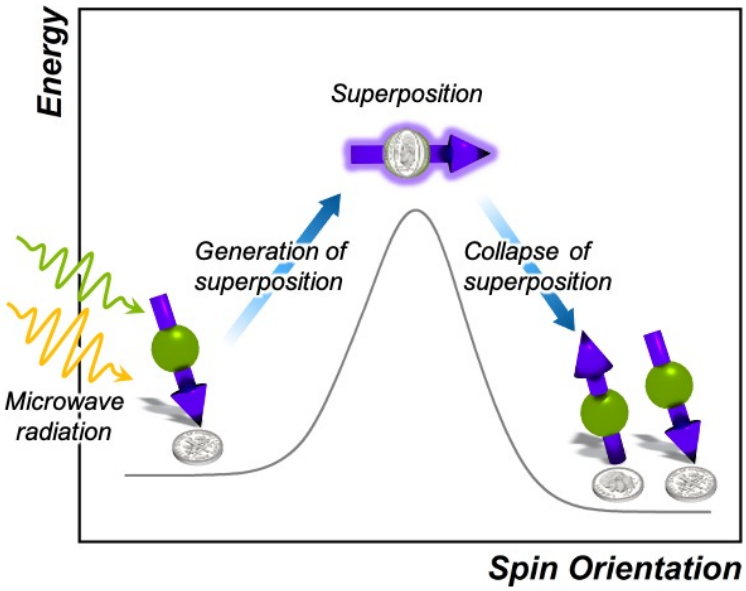

Figure 2.7. Reaction-coordinate depiction of spin-spin relaxation. Spin up and spin down are shown to illustrate that the superposition can collapse to either spin-up or spin-down states. Coins depict the commonly used analogy that a spinning coin is a superposition of both heads and tails, or spin-up and spin-down state, respectively.

The Spin-Spin Relaxation Process

The process of spin-spin relaxation is fundamentally different than spin-lattice relaxation because of the superposition state, which does not require thermal activation to relax. Instead, any interaction of the superposition with the environment that perturbs the energy of the spin will initiate relaxation. We refer the interested reader to deeper descriptions of the spin-spin relaxation process and superposition collapse,[33,51] as the ultimate goal here is to understand how local chemistry controls T_2. Importantly, because there are many ways that the environment can interact with the spin superposition, there are likewise many factors that affect T_2.

The immediate question, then, is how to apply the reaction-coordinate paradigm to understanding T_2. However, the typical reaction-coordinate diagram is insufficient to describing the process, because the superposition is, in some sense, the transition state itself. As such, the activation energy is the input from the experimentalist, often with pulses of microwaves and the technique of pulsed EPR, to generate the superposition in the first place (Fig. 2.7). This fact is why T_2 relaxation does not follow the typical temperature-dependent rules that T_1 does. As one final point, T_2 is often much faster than T_1. Whereas T_1 can approach second- and minute-long magnitudes for molecules, in most cases T_2 is at most hundreds of microseconds (rarely so), and more commonly tens of microseconds or less.[11]

Measurement of T_2

The most common way of measuring the T_2 of a magnetic molecule is through the use of a pulsed EPR spectrometer. This instrument can apply a brief pulse of microwaves (typically 10-to-100s of ns in length) to "tilt" the spin perpendicular in the applied magnetic field and generate the superposition. Then, after a delay, a second pulse of microwaves is applied, which triggers an emissive magnetic response, a *Hahn echo,* from the superpositions that have not decayed since the initial pulse. The time dependence of the echo intensity then provides a direct

measurement of the lifetime of the superposition, which is T_2. T_2 values typically have to be at least tens of nanoseconds in length to measure with commercial instrumentation. We direct the interested reader to several key volumes with more thorough descriptions of the techniques and instrumentation for analyzing T_2.[33]

Intrinsic and Extrinsic Factors That Impact T_2

There are many different ways that the local chemical environment will affect T_2 (Fig. 2.8). For metal complexes, it is important to note that the "local environment" does not exclude the molecule itself. Indeed, specific molecular features, as detailed below, can and do commonly control T_2 by imposing specific local environmental effects. First, as for the T_1 section, we describe specific molecular features that control T_2 that can be manipulated by the synthetic chemist. Then we cover a select number of important extrinsic tunable features in local environment that will affect T_2. The following description is not exhaustive of all of the features that can affect T_2, some of which can be induced by details of the measurement process itself. We refer the reader to other sources for descriptions of these effects.[15]

Electronic Structure

The main ways that the electronic structure of a metal ion affects T_2 is by enhancing or suppressing environmental interactions. High-spin states (and the oxidation states and ligand fields that enable such spin configurations) tend shorten T_2 because the larger magnetic moments of these spins display stronger dipolar interactions with environmental magnetism. This tendency is why molecular systems with the longest T_2 values tend to be $S = {}^1/_2$ ions, e.g. V(IV) and Cu(II).[48,52] In the final section of this review, we detail two additional cutting-edge methods of manipulating electronic structure to suppress environmental interactions.

The second way that electronic structure will affect T_2 is through manipulating spin-lattice relaxation. Spin-lattice relaxation is the upper limit of T_2 for a molecule, because relaxation in the plane perpendicular to the magnetic field will be rapid if the spin is also rapidly realigning with the applied magnetic field direction.[26] When T_1 is short enough, T_2 is effectively controlled by all of

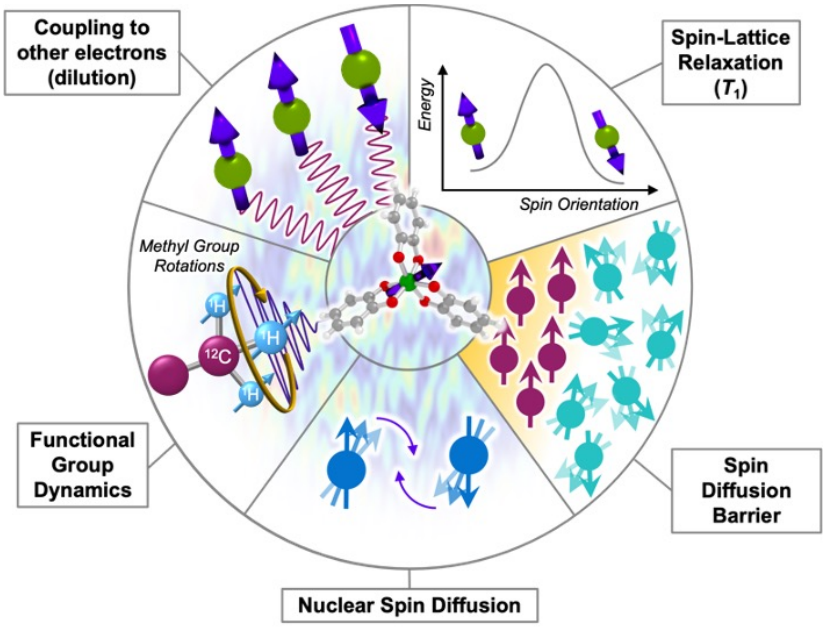

Figure 2.8. Graphical depiction of intrinsic and extrinsic processes that affect T_2. Processes that hasten T_2 relaxation via the creation of noise in the local magnetic field possess a "noisy" background.

the molecular factors described in the T_1 section. At the lowest temperatures, however, T_1 is usually orders of magnitude longer than T_2. In these situations, T_1 does not limit T_2, but with increasing temperatures, T_1 will frequently shorten, eventually becoming the dominant contributor to T_2 relaxation.[2,15]

Functional Groups, Counterions, and Their Dynamics

Functional groups are important for governing T_2, like for many other chemical properties of molecules. However, those functional groups have to exert a chaotic, noisy fluctuation in the local magnetic field to affect T_2. For example, the conventional "steric bulk" from a *tert*-butyl group will have an influence on a metal-ion T_2 not by impeding substitution-based reactivity, but because of a superhyperfine interaction with the nine magnetic protons (^{1}H, $I = {}^1/_2$, $\mu = 2.79\ \mu_N$ where μ is the nuclear magnetic moment in units of μ_N, the nuclear magneton) contained in the functional group.

There are two key points to make about the impacts of ligand and counterion-based magnetic nuclei. First, the motion of magnetic nuclei on functional groups in ligands and functional groups, such as rotation (e.g. in methyl groups), will generate potent changes in the local magnetic field that will shorten T_2. Molecular motion shows its greatest effect on T_2 when the rate of a given motion is on the timescale of the measurement of T_2 and the dynamic group is closer to the spin.[53] The impact of motion on T_2 does not have a specific temperature dependence like T_1, but instead will vary substantially at the temperatures where the timescale of a given motion approaches that of measurement. Second, the type, relative position, and number of magnetic nuclei on the ligand/counterion are all tunable handles to adjust T_2. For example, substitution of proton nuclei with lower-magnetic-moment nuclei (e.g. ^{2}H, $I = 1$, $m = 0.86\ \mu_N$) will result in longer T_2 values because those substitutions suppress the amplitude of fluctuations in the local magnetic field. Finally, modifying the relative interactions between magnetic nuclei and the magnetic ion by

varying the substitutional pattern on ligands (see Chapter 2), or changing the distance separating the metal ion and the magnetic nuclei, will also affect T_2. There is considerable power in manipulating T_2 via molecular design through these species, though there is much to learn in this area.

Librational Motion and Orientation Dependence

In many molecules, the relative orientation of the molecule to an applied magnetic field will affect the T_2 magnitude. This sensitivity stems from small molecular motions called librations (wagging/stretching of an entire molecule, not individual functional-group vibrations) that can occur at low temperatures. These librations will slightly change the orientation of the molecule in the applied magnetic field. If the *g* factor is anisotropic, as it is for many molecules, then the librations perturb the interactions with the applied magnetic field. This change in interaction drives T_2 relaxation. For many species, T_2 is greatest where a particular x, y, or z axis of the molecule is orientated parallel to the applied field, as slight changes at these orientations produce relatively small changes in the interaction with the applied field than “off-axis” orientations. There are two important practical outcomes of this effect. First, there is no single T_2 for a molecule, instead, a given molecule will often exhibit multiple different T_2 values depending on its orientation relative to in an applied external magnetic field. Second, because of the orientation dependence, orientation is a critical design concern for any proposed molecule-based quantum computing architecture, specifically surface-mounted ones.[54]

Local Magnetic Species

Fluctuations in local magnetism induced by other molecules in the environment also hasten T_2 relaxation. The strongest impacts come from proximate open-shell molecules, which exert their own local magnetic fields to hasten T_2. The impact of local magnetic species is also

more prominent when there are more of them, and T_2 can generally be observed to decrease with increasing concentration of open-shell species.[15,33] Conversely, dilution increases T_2 and thus most reported T_2 times for molecular complexes are measured in millimolar (or less) concentrations.[2,52,53,55,56]

A separate source local magnetic species is the collection of magnetic nuclei on surrounding molecules and matrix. The impacts of environmental nuclei can exert similar impacts on T_2 as nuclei in the ligand-shell. Hence, dynamic motion such as methyl rotations in the local matrix will shorten T_2 just as if it were part of the metal complex itself. A second mechanism through which nuclei can generate local magnetic noise and shorten T_2 is nuclear spin diffusion. Recall that the chemical shift of a magnetic nucleus is the energy required to flip that magnetic nucleus in a magnetic field. Spin diffusion occurs when two oppositely oriented nuclear spins (with identical chemical shifts) undergo a simultaneous flip, a “flip flop”, which produces changes to the local magnetic field (Fig. 8, bottom).

Nuclear spin diffusion is energy conserving, meaning that it cannot be frozen out by cooling to low temperatures, in contrast to other factors that affect T_2. Therefore, nuclear spin diffusion tends to become the main contributor to T_2 at the lowest temperatures. The impact of this process can be minimized somewhat if the environment is full of lower-moment magnetic nuclei, e.g. a frozen deuterated solvent matrix instead of a protiated one.[2,52,56]

Spin Diffusion Barrier

The requirement of matching chemical shifts between spin-diffusion-active nuclei generates a unique feature known as the spin diffusion barrier, which surrounds a relaxing open-shell molecule. Environmental magnetic nuclei interact with the magnetic molecule and that superhyperfine coupling strength grows as the magnetic nuclei approach the electronic spin. At a certain radius, even adjacent nuclei experience substantially different strengths of these superhyperfine interactions. As a consequence, the two nuclei now have significantly different

chemical shifts from each other and the other magnetic nuclei of the bath. Spin diffusion is thus deactivated for nuclei in close proximity to the electron, even if the two nuclei are right next to each other. Consequently (and counterintuitively) nuclei are the closest to an electronic spin will not generate substantial fluctuations in the local magnetic field to shorten T_2. The radius at which the T_2-shortening effect of magnetic nuclei is deactivated is the spin diffusion barrier.[58] Existing studies place the edge of the barrier at about 3-10 Å.[57,59] However, the actual radius is dependent on the system, and does not need to be spherical.[2,60] Finally, the barrier also precludes spin diffusion as a mechanism by which the hyperfine coupling to a metal-ion nuclear spin will impact T_2.[61]

State of the Art in Molecular Magnetic Relaxation

The length of the relaxation time for a system directly translates into potential utility. For example, realizing a long T_1 is a path toward storing and processing information in a system,[13] as well as controlling environmental ^{1}H dynamics for magnetic resonance imaging.[62] Producing long T_2 values enables quantum information processing[52] and enables the performance of advanced magnetic resonance detection protocols, as could be leveraged in, e.g. electron paramagnetic resonance imaging.[63] Below we highlight the forefront of this area of work, describing how the combined use of synthetic chemistry and electronic structure design strategies are producing new pathways to slowing magnetic relaxation.

Complexes with Slow Spin-Lattice Relaxation

One prominent class of molecular species with long spin-lattice relaxation times, single molecule magnets, features a single metal ion (transition-metal or lanthanide) with carefully crafted ligand shells to facilitate a long T_1. Many of these design strategies rely on controlling the activation energies of spin-lattice relaxation through the Orbach or thermally assisted QTM

process and suppressing the non-thermally activated processes. With a suitably high activation energy and the absence of these other processes, one may expect sufficiently long relaxation to enable information storage in a molecular magnetic moment. In pursuit of this goal, in 2017, Layfield, Chilton, Mills, and coworkers reported new Ln-based metallocene complexes that show a slow relaxation process up to and above liquid nitrogen temperatures (Fig. 2.9).[20,64] Analyses of the temperature dependence of T_1 in these species revealed that one molecule, $[(Cp^{iPr5})Dy(Cp^*)]^+$, exhibited an activation energy for relaxation of 1541(11) cm^{-1} for a thermally assisted QTM process, the highest reported value for any molecule. There are two key aspects of the molecule that enable this remarkable observation. First, the molecule possesses a Dy^{3+} ion, which leverages a large spin state and spin-orbit coupling to produce a large potential activation energy. The spin orbit coupling in particular leads to a $^6H_{15/2}$ term ground state and

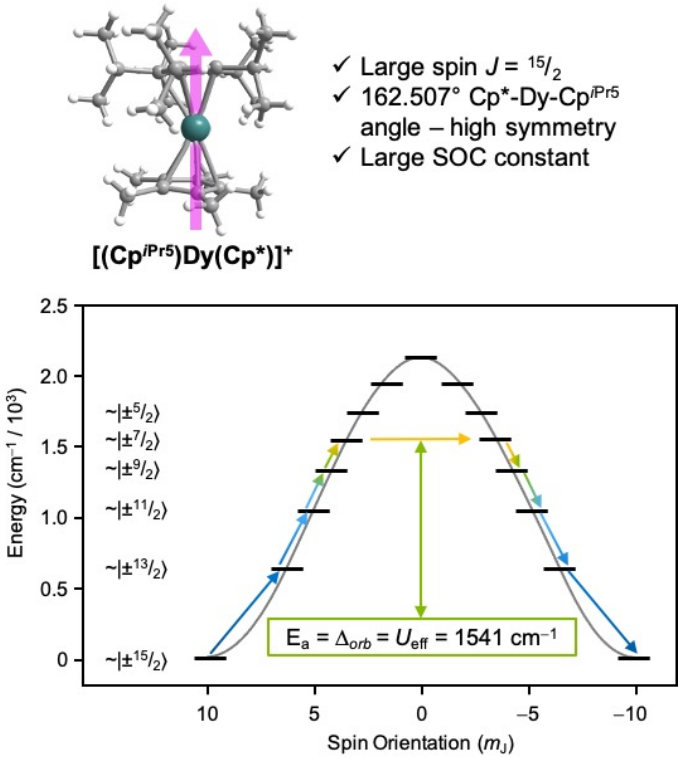

Figure 2.9. Recent ground-breaking system for targeting a long T_1. The highly axial geometry of the metal complex suppresses tunneling, which combines with the high spin state and large spin-orbit coupling to enable an exceptionally high activation energy to relaxation. Cp* = pentamethylcyclopentadiene ; Cp^{iPr5} = pentaisopropylcyclopentadiene. The levels in the bottom plot are labeled in "ket" notation, which here simply give the M_J values of the $^6H_{15/2}$ Dy^{3+} ion, which reach up to $M_J = \pm 15/2$.

magnetic orientations that are described with M_J values up to $\pm^{15}/_2$ (stemming from $J = L + S$, where J is the total angular momentum, L the orbital angular momentum, and S the spin).[44] Second, the species also possesses a highly pseudo-axial molecular symmetry. These two properties suppress tunneling in the ground state and lower lying levels. The result is a thermally assisted tunneling mechanism that is nearly the maximum possible activation energy for the molecule.

Complexes with Slow Spin-Spin Relaxation

Long T_2 values are common for open-shell defects in solid-state materials like the nitrogen vacancy center in diamond[65] or the double-vacancy site in silicon carbide.[66] All of these species exhibit extremely large T_2 values (~1 ms) because isotopic enrichment removes all environmental nuclear spins. Metal complexes are emerging as powerful alternative platforms to understand how to lengthen superposition lifetimes using synthetic chemistry, a strategy that is substantially more challenging in the solid state.

Of these, first-row transition metal complexes hold recent records for the longest spin-spin relaxation times. In 2015, Freedman and coworkers demonstrated the impact of using synthetic design to achieve near-complete removal of nuclear spins from the coordination shell of a metal ion. The resulting molecule, $(d^{20}\text{-}Ph_4P)_2[V(C_8S_8)_3]$, uses nearly nuclear-spin free ligands (^{12}C: I = 0, 98.9%; $^{32/34/36}S$: I = 0, 99.25%), deuterated counterions, and a remarkable solubility in CS_2, a relatively nuclear spin-free solvent, to achieve a near millisecond-length T_2 (Fig. 2.10). Together, these factors create a magnetically quiet environment, and hence a groundbreaking, millisecond T_2 is observed. This finding (the first for a metal complex) shows that controlling the properties of magnetic nuclei in the environment is critical to lengthen T_2, but there is much to learn about the exact role of ligand-based nuclei, and cutting-edge efforts reflect that.[48,53]

Another exciting strategy to lengthen T_2 is to design electronic structures that suppress environmental sensitivity. One method to do so is to create an EPR transition at an avoided-crossing point (Fig. 2.10). An avoided crossing point is where two M_S values would cross in energy at a given magnetic field. For an avoided crossing, however, there is an interaction between the wavefunctions of the M_S levels that strengthens as the levels become closer in energy. As a result, the M_S levels never actually cross and instead bow away from each other with increasing magnetic field. The result is an energy gap that is accessible with EPR spectroscopy. However, the transition is unconventional as the energies of the M_S levels (M_J in the case of the Ho^{3+}) are field-independent at the crossing point. The field independence of the energies translates into a relative

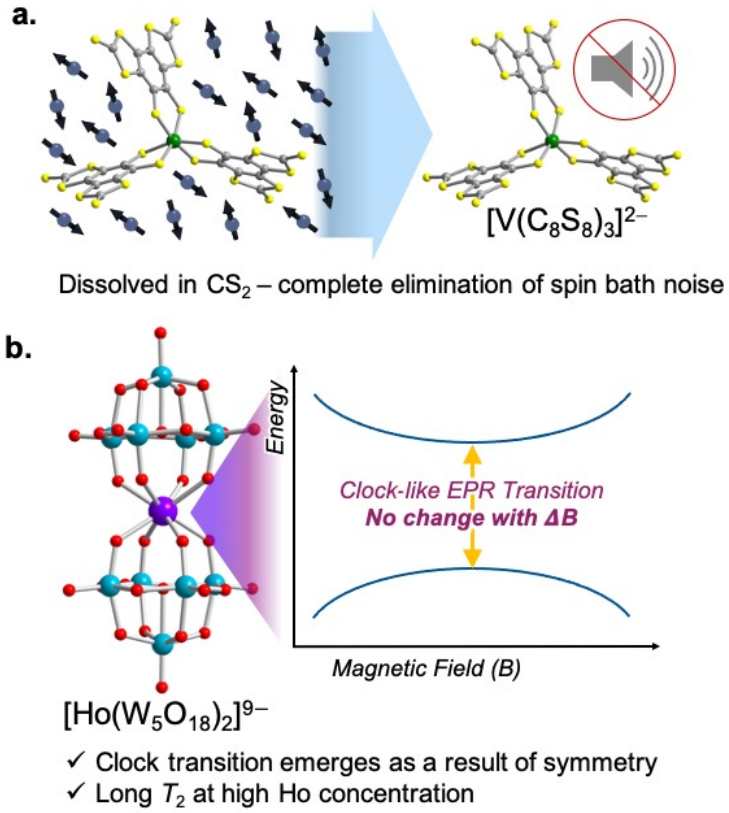

Figure 2.10. State-of-the-art molecules for lengthening T_2. (**a**) $[V(C_8S_8)_3]^{2-}$ is a predominantly nuclear-spin free complex that displays millisecond T_2 values when dissolved in the nuclear-spin free solvent CS_2. (**b**) $[Ho(W_5O_{18})_2]^{9-}$ exploits an almost perfect D_4 molecular symmetry to generate a clock-like EPR transition. These transitions have zero change in frequency with respect to changes in local magnetic field, and thus yield long T_2 values.

immunity toward local magnetism, and the superposition created at the avoided crossing point is consequently relatively long-lived. In fact, this mechanism for designing environmental immunity engenders the extraordinary frequency stability of the time-keeping transition of an atomic clock. It is for this reason that the EPR transition is “clock-like”. In the case of the molecule shown in Fig. 2.10, the symmetry, orbital angular momentum, and crystal field of the Ho^{3+} are what create the clock transition. However, other magnetic interactions in molecules can be used to create a clock transition, e.g. the hyperfine interaction.[67] It remains to be seen if this strategy will be able to achieve the near-millisecond T_2 values in molecules reported by the nuclear-spin-free strategy. Nevertheless, these studies represent a fascinating and rare intersection of coordination chemistry and atomic-clock physics.

Outlook

Magnetic molecules are an essential component of next-generation applications in quantum information processing to magnetic resonance imaging. But to reach that vision, we need a comprehensive understanding of how molecular structure and the environment control magnetic relaxation. In this review, we contextualized the relaxation process in a new analogy to a reaction-coordinate diagram, which enabled us to intuit relaxation phenomena in an accessible manner.

The question then is, where to next? There are of course many exciting directions, and we touched on a select few of these in the last section. We highlight one final area of particular opportunity: studying relaxation in highly magnetic and dynamic environments. Indeed, many of the proposed applications for magnetic metal complexes require long relaxation times in proton-rich biological environments, room-temperature solutions, or the stray-magnetic-field-rich interiors of electronic devices. Yet, as touched on herein, current studies of magnetic molecules focus almost exclusively on electron- and nuclear-spin-free conditions to suppress magnetic noise and very low temperatures to freeze out structural dynamics. These studies revealed that

extraordinarily long relaxation times are achievable. One pressing goal, then is the discovery of how to translate those proof-of-concept observations into noisy conditions. We are excited to see, then, more fundamental studies into controlling the interactions between spin baths and molecules via structural design.

Notes

‡ The transport integral is defined by the following equation:

$$J_8\left(\frac{\theta_D}{T}\right) = \int_0^{\theta_D/T} x^8 \frac{e^x}{(e^x-1)^2}\,dx$$

where T is the temperature and θ_D is the Debye temperature.

§ The correlation time for a thermally activated motion is described by the following equation:

$$\tau_c = \tau_0 e^{E_a/k_B T}$$

where the E_a is the activation energy for the thermally activated process, t_0 the preexponential factor, k_B is the Boltzmann constant, and T is the temperature.

References

1 G. Aromí, D. Aguilà, P. Gamez, F. Luis and O. Roubeau, *Chem. Soc. Rev.*, **2012**, *41*, 537–546.

2 M. J. Graham, J. M. Zadrozny, M. S. Fataftah and D. E. Freedman, *Chem. Mater.*, **2017**, *29*, 1885–1897.

3 A. Gaita-Ariño, F. Luis, S. Hill and E. Coronado, *Nat. Chem.*, **2019**, *11*, 301–309.

4 D. Gatteschi, R. Sessoli, J. Villain, *Molecular Nanomagnets*, Oxford University Press, Oxford, New York, 2006.

5 J. Wahsner, E. M. Gale, A. Rodríguez-Rodríguez and P. Caravan, *Chem. Rev.*, **2019**, *119*, 957–1057.

6 G. Tircs and Z. Baranyai , *The Chemistry of Contrast Agents in Medical Magnetic Resonance Imaging Stability and Toxicity of Contrast Agents*, John Wiley & Sons, 2013.

7 M. C. Heffern, L. M. Matosziuk and T. J. Meade, *Chem. Rev.*, **2014**, *114*, 4496–4539.
8 A. L. Buchachenko and V. L. Berdinsky, *Chem. Rev.* **2002**, *102*, 603-612.
9 D. Aravena and E. Ruiz, *Dalton Trans*., **2020**, *49*, 9916–9928.
10 S. Brooker, *Chem. Soc. Rev.*, **2015**, *44*, 2880–2892.
11 E. Coronado, *Nat. Rev. Mater.*, **2020**, *5*, 87–104.
12 S. T. Liddle and J. van Slageren, *Chem. Soc. Rev.*, **2015**, *44*, 6655–6669.
13 G. A. Craig and M. Murrie, *Chem. Soc. Rev.*, **2015**, *44*, 2135–2147.
14 L. Bogani and W. Wernsdorfer, *Nat. Mater.*, **2008**, *7*, 179–186.
15 L. J. Berliner, S. S. Eaton and G. R. Eaton, *Distance Measurements in Biological Systems by EPR*, Springer US, 2000.
16 L. J. Berliner, Ed., *In Vivo EPR (ESR): Theory and Application*, Springer US, 2003.
17 B. A. Reisner, S. R. Smith, J. L. Stewart, J. R. Raker, J. L. Crane, S. G. Sobel and L. L. Pesterfield, *Inorg. Chem.*, **2015**, *54*, 8859–8868.
18 J. R. Raker, B. A. Reisner, S. R. Smith, J. L. Stewart, J. L. Crane, L. Pesterfield and S. G. Sobel, *J. Chem. Educ.*, **2015**, *92*, 980–985.
19 L. J. Fox and G. H. Roehrig, *J. Chem. Educ.*, **2015**, *92*, 1456–1465.
20 F.-S. Guo, B. M. Day, Y.-C. Chen, M.-L. Tong, A. Mansikkamäki and R. A. Layfield, *Science*, **2018**, *362*, 1400–1403.
21 L. Tesi, A. Lunghi, M. Atzori, E. Lucaccini, L. Sorace, F. Totti and R. Sessoli, *Dalton Trans.*, **2016**, *45*, 16635–16643.
22 J. M. Frost, K. L. M. Harriman and M. Murugesu, *Chem. Sci.*, **2016**, *7*, 2470–2491.
23 D. Gatteschi and R. Sessoli, *Angew. Chem. Int. Ed*., **2003**, *42*, 268–297.
24 M. Vallone, *Phys. Status Solidi B*, **2020**, *257*, 1900443.
25 M. S. Fataftah, M. D. Krzyaniak, B. Vlaisavljevich, M. R. Wasielewski, J. M. Zadrozny and D. E. Freedman, *Chem. Sci*., **2019**, *10*, 6707–6714.
26 A. Schweiger and G. Jeschke, *Principles of Pulse Electron Paramagnetic Resonance*, Oxford University Press, 2001.
27 A. Lunghi, F. Totti, R. Sessoli and S. Sanvito, *Nat. Commun.,* **2017**, *8*, 14620.
28 Y. Zhou, B. E. Bowler, G. R. Eaton and S. S. Eaton, *J. Magn. Reson.*, **1999**, *139*, 165–174.
29 D. W. Feldman, J. G. Castle and J. Murphy, *Phys. Rev.*, **1965**, *138*, A1208–A1216.
30 P. G. Klemens, *Phys. Rev.*, **1962**, *125*, 1795–1798.
31 C. B. Harris, R. M. Shelby and P. A. Cornelius, *Phys. Rev. Lett.*, **1977**, *38*, 1415–1419.
32 N. V. Vugman and M. R. Amaral, *Phys. Rev. B*, **1990**, *42*, 9837–9842.

33 D. Goldfarb and S. Stoll, *EPR Spectroscopy: Fundamentals and Methods*, John Wiley & Sons, 2018.

34 J. Murphy, *Phys. Rev.*, **1966**, *145*, 241–247.

35 A. Abragam, B. Bleaney, *Electron Paramagnetic Resonance of Transition Ions*, Oxford University Press, Oxford, New York, 2012.

36 K. J. Standley, *Electron Spin Relaxation Phenomena in Solids*, Springer US, 1969.

37 A. J. Fielding, S. Fox, G. L. Millhauser, M. Chattopadhyay, P. M. H. Kroneck, G. Fritz, G. R. Eaton and S. S. Eaton, *J. Magn. Reson.*, **2006**, *179*, 92–104.

38 S. Gómez-Coca, A. Urtizberea, E. Cremades, P. J. Alonso, A. Camón, E. Ruiz and F. Luis, *Nat. Commun.*, **2014**, *5*, 4300.

39 W. M. Rogers and R. L. Powell, *Tables of Transport Integrals*, U.S. Government Printing Office, 1958.

40 L. Gu and R. Wu, *Phys. Rev. B*, **2021**, *103*, 014401.

41 J. M. Zadrozny and J. R. Long, *J. Am. Chem. Soc.*, **2011**, *133*, 20732–20734.

42 W. H. Harman, T. D. Harris, D. E. Freedman, H. Fong, A. Chang, J. D. Rinehart, A. Ozarowski, M. T. Sougrati, F. Grandjean, G. J. Long, J. R. Long and C. J. Chang, *J. Am. Chem. Soc.*, **2010**, *132*, 18115–18126.

43 V. A. Atsarkin, V. V. Demidov and G. A. Vasneva, *Phys. Rev. B*, **1997**, *56*, 9448–9453.

44 J.-L. Liu, Y.-C. Chen and M.-L. Tong, *Chem. Soc. Rev.*, **2018**, *47*, 2431–2453.

45 B. N. Figgis and M. A. Hitchman, *Ligand field theory and its applications*, Wiley-VCH, 2000.

46 E. Moreno-Pineda, M. Damjanović, O. Fuhr, W. Wernsdorfer and M. Ruben, *Angew. Chem. Int. Ed.*, **2017**, *56*, 9915–9919.

47 M. Atzori, E. Morra, L. Tesi, A. Albino, M. Chiesa, L. Sorace and R. Sessoli, *J. Am. Chem. Soc.*, **2016**, *138*, 11234–11244.

48 C.-J. Yu, M. J. Graham, J. M. Zadrozny, J. Niklas, M. D. Krzyaniak, M. R. Wasielewski, O. G. Poluektov, D. E. Freedman, *J. Am. Chem. Soc.*, **2016**, *138*, 14678-14685.

49 S. R. Cooper , Y. B. Koh and K. N. Raymond , *J. Am. Chem. Soc.*, **1982**, *104* , 5092–5102

50 M. Atzori and R. Sessoli, *J. Am. Chem. Soc.*, **2019**, *141*, 11339–11352.

51 M. A. Schlosshauer, *Decoherence: and the Quantum-To-Classical Transition*, Springer-Verlag, Berlin Heidelberg, 2007.

52 K. Bader, D. Dengler, S. Lenz, B. Endeward, S.-D. Jiang, P. Neugebauer and J. van Slageren, *Nat. Commun.*, **2014**, *5*, 5304.

53 C. E. Jackson, C.-Y. Lin, S. H. Johnson, J. van Tol and J. Zadrozny, *Chem. Sci.*, **2019**, *10*, 8447-8454.

54 M. Atzori, L. Tesi, E. Morra, M. Chiesa, L. Sorace and R. Sessoli, *J. Am. Chem. Soc.*, **2016**, *138*, 2154–2157.

55 J. M. Zadrozny, J. Niklas, O. G. Poluektov and D. E. Freedman, *ACS Cent. Sci.*, **2015**, *1*, 488–492.

56 K. Bader, M. Winkler and J. van Slageren, *Chem. Commun.*, **2016**, *52*, 3623–3626.

57 E. R. Canarie, S. M. Jahn and S. Stoll, *J. Phys. Chem. Lett.*, **2020**, *11*, 3396–3400.

58 W. E. Blumberg, *Phys. Rev.*, **1960**, *119*, 79–84.

59 J. Chen, C. Hu, J. F. Stanton, S. Hill, H.-P. Cheng and X.-G. Zhang, *J. Phys. Chem. Lett.*, **2020**, *11*, 2074–2078.

60 J. P. Wolfe, *Phys. Rev. Lett.*, **1973**, *31*, 907–910.

61 R. Hussain, G. Allodi, A. Chiesa, E. Garlatti, D. Mitcov, A. Konstantatos, K. S. Pedersen, R. De Renzi, S. Piligkos and S. Carretta, *J. Am. Chem. Soc.*, **2018**, *140*, 9814–9818.

62 J. P. Klare, *Biomed. Spectrosc. Imaging*, **2012**, *1*, 101–124.

63 R. Rahimi, H. J. Halpern and T. Takui, in *Oxygen Transport to Tissue XXXIX*, eds. H. J. Halpern, J. C. LaManna, D. K. Harrison and B. Epel, Springer International Publishing, Cham, 2017, pp. 335–339.

64 C. A. P. Goodwin, F. Ortu, D. Reta, N. F. Chilton and D. P. Mills, *Nature*, **2017**, *548*, 439–442.

65 F. Casola, T. van der Sar and A. Yacoby, *Nat. Rev. Mater.*, **2018**, *3*, 1–13.

66 A. Lohrmann, B. C. Johnson, J. C. McCallum and S. Castelletto, *Rep. Prog. Phys.*, **2017**, *80*, 034502.

67 J. M. Zadrozny, A. T. Gallagher, T. D. Harris and D. E. Freedman, *J. Am. Chem. Soc.*, **2017**, *139*, 7089–7094.

CHAPTER 3 – NUCLEAR-SPIN-PATTERN CONTROL OF ELECTRON-SPIN DYNAMICS IN A SERIES OF V(IV) COMPLEXES

Overview

Achieving control of phase memory relaxation times (T_m) in metal ions is an important goal of molecular spintronics. Herein we provide the first evidence that nuclear-spin patterning in the ligand shell is an important handle to modulate T_m in metal ions. We synthesized and studied a series of five V(IV) complexes with brominated catecholate ligands $[V(C_6H_{4-n}Br_nO_2)_3]^{2-}$ (n = 0, 1, 2, and 4), where the $^{79/81}$Br and ^{1}H nuclear spins are arranged in different patterns. High-field, high-frequency (120 GHz) pulsed electron paramagnetic resonance spectroscopic analysis of this series reveals a pattern-dependent variation in T_m for the V(IV) ion. Notably, we show that it is possible for two molecules to have starkly different (by 50%) T_m values despite the same chemical composition. Nuclear magnetic resonance analyses of the protons on the ligand shell suggest that relative chemical shift (δ), controlled by the patterning of nuclear spins, is an important underlying design principle. Here, having multiple ligand-based protons with nearly identical chemical shift values in the ligand shell will, ultimately, engender a short T_m for the bound metal ion.

Introduction

Magnetic molecules are next-generation components of many different technological arenas, ranging from magnetic resonance imaging (MRI)[1,2] to quantum information processing.[3–11] Utility in any of these applications requires long spin-lattice relaxation times (T_1 > 1 ms) and phase-memory relaxation times ($T_m^{\ddagger}$ > 100 μs). T_1 defines the lifetime of an excited spin and is the upper limit of T_m. In contrast, T_m is the lifetime of the electron spin superposition, or coherence time. Designing systems where both of these parameters are long is an acute challenge because of the ubiquitous spin bath (nearby

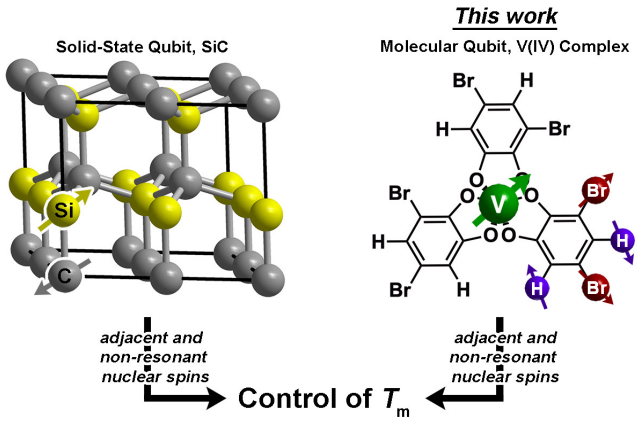

Figure 3.1. Defect qubits in SiC display a long T_m because only non-resonant spins can be adjacent in the structure, which disrupts nuclear spin diffusion. This manuscript tests whether such a design principle will affect T_m in molecular species, specifically by probing different patterns of ^{1}H and $^{79/81}$Br spins on catecholate ligands in V(IV) complexes.

electronic spins or nuclear spins), which produces a chaotic local magnetism that shortens T_1 and T_m from spin-spin interactions.[12–15] To circumvent the spin bath challenge, significant efforts are made to engineer environments with less noise from the spin bath. This engineering is done by dilution of the paramagnetic species, using smaller-magnetic-moment isotopic substitution (e.g. ^{2}H, μ = 0.86 μ_N for ^{1}H, μ = 2.79 μ_N), or complete elimination of nuclear spins.[3,16–20] However, large-moment environmental spins are a critical part of utility in nearly all applications. For example, MRI applications require function in proton-rich biological environments, and information processing applications will likely feature stray magnetic fields from moving charges or other proximate magnetic materials in a device. Hence, understanding how to design complexes with long T_1 and T_m in magnetic environments is a necessary advance for future technologies.

Herein, we demonstrate the first control of T_m via patterning of ligand-based nuclear spins in a metal complex (Fig. 3.1). In molecules, ligand nuclear spins are a critical component of the nuclear spin bath and control electron spin dynamics through nuclear spin diffusion.[14,15,21] In this phenomena, pairs of resonant nuclear spins (those that require identical quantities of energy to flip) engage in energy-conserving flip-flop motions, wherein two oppositely oriented spins simultaneously flip, or exchange spin.[22] This

process generates local magnetic noise and shortens T_m for a magnetic ion.[23–26] In the absence of a nuclear spin bath, T_m will approach and exceed millisecond lifetimes.[27–30] However, in spin-rich environments, lifetimes are typically less than 100 μs[31] and more frequently less than 10 μs.[19,23,50–52]

A recent breakthrough in the study of paramagnetic defects in SiC might hold the key to longer relaxation times in nuclear spin-rich baths (Fig. 3.1).[53–55] The defects in SiC display longer T_m values than nitrogen vacancy centers in diamond despite higher nuclear spin concentration in the former (1.1% ^{13}C and 4.7% ^{29}Si in SiC; 1.1% ^{13}C in diamond).[56] The relative enhancement in T_m stems from a particular structural feature – each Si atom is surrounded by C and each C atom is surrounded by Si.[53–55,57] This interstitial patterning increases T_m in two ways. First, two Si nuclear spins are never adjacent (likewise for C), and nuclear spin diffusion decreases for spins held far apart from one another.[12] Second, the difference in the nuclear g_n factors for C and Si ensures that, even when adjacent, spin diffusion will not occur between the nonresonant ^{13}C and ^{29}Si nuclei. These results suggest specific positioning of nuclear spins as a potential method of T_m control via synthetic chemistry.

Drawing inspiration from SiC, we address the questions: Can patterning of nuclear spins on ligand shells influence the electronic T_m of a ligated metal? Freedman and co-workers showed that separation between an open-shell ion and nuclear spins is important,[58] and there is significant literature demonstrating the impacts on replacement of ^1H (μ = 2.79 μ_N) with low-moment magnetic nuclei e.g. ^2H (μ = 0.86 μ_N).[19,42,46] In this paper we probe a different question: can the impacts of high-magnetic-moment nuclei on T_m be mitigated instead by controlling nuclear spin to nuclear spin interactions in a molecule? To address these questions, we prepared and investigated, via pulsed EPR spectroscopy, a series of Bu_3NH^+ salts of the canonical tris(catecholato)vanadate(IV)

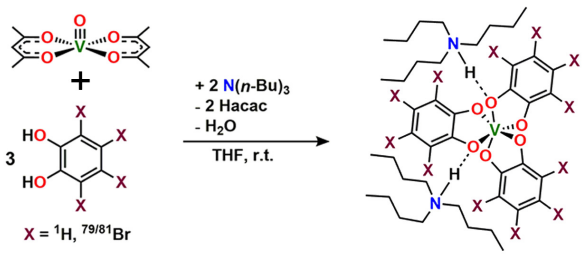

Ligand	Complex Formula and Label
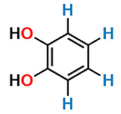	$(n\text{-}Bu_3NH)_2[V(C_6H_4O_2)_3]$ **1**
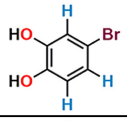	$(n\text{-}Bu_3NH)_2[V(C_6H_3BrO_2)_3]$ **2**
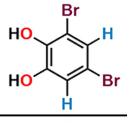	$(n\text{-}Bu_3NH)_2[V(C_6H_2Br_2O_2)_3]$ **3**
	$(n\text{-}Bu_3NH)_2[V(C_6H_2Br_2O_2)_3]$ **4**
	$(n\text{-}Bu_3NH)_2[V(C_6Br_4O_2)_3]$ **5**

Figure 3.2. General synthetic scheme for **1**–**5** and labelling scheme for the studied complexes in this manuscript. See Experimental section for additional synthetic information.

complex $[V(C_6H_4O_2)_3]^{2-}$: $(n\text{-}Bu_3NH)_2[V(C_6H_4O_2)_3]$ (**1**), $(n\text{-}Bu_3NH)_2[V(4\text{-}Br\text{-}C_6H_3O_2)_3]$ (**2**), $(n\text{-}Bu_3NH)_2[V(3,5\text{-}Br_2\text{-}C_6H_2O_2)_3]$ (**3**), $(n\text{-}Bu_3NH)_2[V(4,5\text{-}Br_2\text{-}C_6H_2O_2)_3]$ (**4**), and $(n\text{-}Bu_3NH)_2[V(C_6Br_4O_2)_3]$ (**5**). In this series, the specific pattern of ^{1}H v. $^{79/81}Br$ is varied on each ligand (Figs. 3.2 and 3.3). These nuclear spins have significantly different resonance frequencies,[56] and, on this basis, we hypothesized that ligand-based nuclear-spin diffusion would be modulated in **1**–**5**. Furthermore, we predicted that such change would lead to a variation in V(IV) T_m dependent on the exact substitutional pattern of H and Br on the ligand. In this report, we show for the first time that this patterning design strategy is an effective means of influencing T_m. Importantly, these studies also include the first investigation of the pulsed EPR spectroscopic properties of the V(IV) ion at very high field and frequency (> 4.0 T, 120 GHz).

Results and Discussion

Preparation of the targeted complexes proceeded via a simple ligand metathesis scheme using $VO(acac)_2$, tri-*n*-butylamine, and the ligands shown in Fig. 3.2 (see also Experimental section, Figs. 3.8-3.11). The general scheme for these syntheses follows previous reports of the triscatecholato complex of V(IV).[18,41,59–62] Recrystallization afforded crystals suitable for single crystal X-ray diffraction of **2**, **4**, and **5** (but not **3**, see Figs. 3.3, Tables 3.8-3.10, and ESI). Single crystal X-ray diffraction experiments on crystals of **1**,[40] **2**, **4**, and **5** (Fig. 3.3) reveal similar molecular structures of the VO_6 core. In these structures, all vanadium(IV) ions are in a six-coordinate environment, with average V–O bond lengths varying over a tight range across the series, from 1.938(4) Å for **1** to 1.943(9) Å for **5**. The continuous-shape-measurement (CSM) analyses using SHAPE 2.0 software[63,64] of **1**–**5** provide symmetry measures for an octahedron of 1.67, 2.39, 3.97, and 1.41 for **1**, **2**, **4**, and **5,** respectively (here, a value of 0 corresponds to a perfect

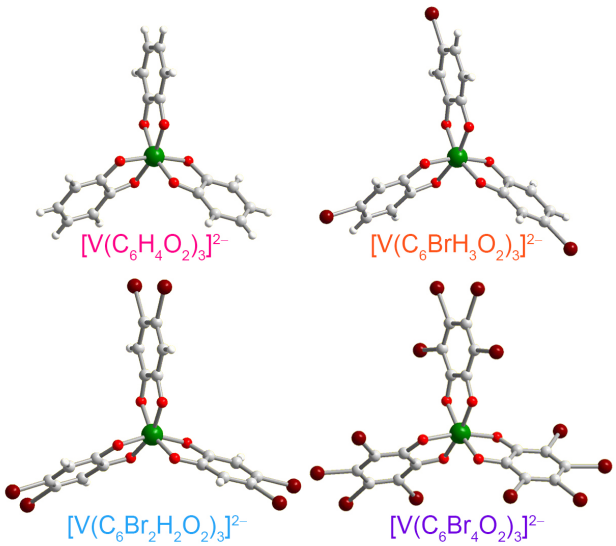

Figure 3.3 Molecular structures of the V(IV) complexes in **1** (ref. 40), **2**, **4**, and **5**, as determined from the crystal structures of these compounds. Counter ions are omitted for clarity. Green, maroon, red, gray, and white spheres represent vanadium, bromine, oxygen, carbon, and hydrogen atoms, respectively.

octahedron). The symmetry measures for a trigonal prismatic geometry are much higher (> 5), indicating that **1**, **2**, **4**, and **5** are better described as slightly distorted octahedra (Table 3.4). Beyond the first coordination sphere, all molecules exist hydrogen-bonded to two *n*-Bu_3NH^+ cations through the O atoms of the catecholate ligands (Fig. 3.12). This interaction is similar across **1**, **2**, **4**, and **5**, with an average V•••$HNBu_3^+$ distance of 2.99(6) Å. Prior experiments demonstrate that this association persists in solution (Fig. 3.12).[40]

One critical aspect of the tested design principle relies on the spin-flip energies of ^{1}H and $^{79/81}$Br to differ from one another. On this merit, high-field and high-frequency EPR (120 GHz) was selected for studying **1**–**5**. With this technique, the differences in Larmor frequencies between ^{1}H (ca. 187 MHz) and $^{79/81}$Br (ca. 47 and 51 MHz, respectively) at 4.4 T are large relative to those at the more conventional EPR frequency, X-band (0.4 T): ^{1}H (ca. 17.0 MHz) and $^{79/81}$Br (ca. 4.3 and 4.6 MHz, respectively).[65] Importantly, such conditions will decouple not only the ^{1}H and $^{79/81}$Br nuclear spins, but potentially ^{79}Br from ^{81}Br due to the bigger difference in Larmor frequencies (ca. 4 MHz) – rendering the Br atoms inert spin blocks to disrupt ^{1}H nuclear-spin diffusion. High-field, high-frequency investigations of the relaxation times of V(IV) are, to the best of our knowledge, unprecedented.

Echo-detected EPR spectra of **1**–**5** were collected to test for variation in the spin-Hamiltonian parameters as a function of ligand. To do so, **1**–**5** were dissolved in d^{14}-*o*-terphenyl (d^{14}-OTP) at a 1 mM concentration, leveraging the solubility in nonpolar media afforded from the presence of the tri-*n*-butylammonium cations.[40] The echo-detected, field-swept (EDFS) spectra of **1**–**5** were then collected at 5 K and 120 GHz (Fig. 3.4, Fig. 3.13, Table 3.5). The recorded spectra starkly differ in appearance from the 100 mT-wide, eight-line patterns observed at X-band frequency (Fig. 3.4). Instead, each 120 GHz spectrum reveals a single broad transition, spanning from 4.3–4.5 T. Such spectral width is attributed to enhanced broadening of the electronic *g*-factor ("*g*-strain") at high magnetic fields.[15]

Simulations of the spectra were performed using Easyspin[66] and the following spin Hamiltonian:

$$\hat{\boldsymbol{H}} = g_e\mu_B\boldsymbol{B}\hat{\boldsymbol{S}} - g_N\mu_N\boldsymbol{B}\hat{\boldsymbol{I}} + \hat{\boldsymbol{I}}\boldsymbol{A}\hat{\boldsymbol{S}} + \hat{\boldsymbol{I}}\boldsymbol{Q}\hat{\boldsymbol{I}}$$

Here, g_e and $\boldsymbol{A}$ correspond to rhombic electronic g factors and ^{51}V hyperfine coupling constants, respectively. $\boldsymbol{Q}$ is the nuclear quadrupolar constant for ^{51}V, $\hat{\boldsymbol{S}}$ and $\hat{\boldsymbol{I}}$ are electronic and nuclear spin operators, respectively, μ_B and μ_N are the Bohr and nuclear magnetons, respectively, g_n the nuclear g factor for ^{51}V and $\boldsymbol{B}$ the magnetic field. More simulation details and the exact spin Hamiltonian values extracted can be found in the Experimental section and Table 3.4. We note that the best simulations of the g-factors at 120 are only slightly different from those obtained at X-band.[40,41] We place higher confidence on the g-factors determined here, since greater accuracy on this parameter is a hallmark of high frequency EPR.[15,67–69] Most importantly, we note that the obtained parameters are similar in magnitude and anisotropy, demonstrating a relatively consistent electronic structure for the V(IV) ion in **1**–**5**. As the g and A values for V(IV) ions are also

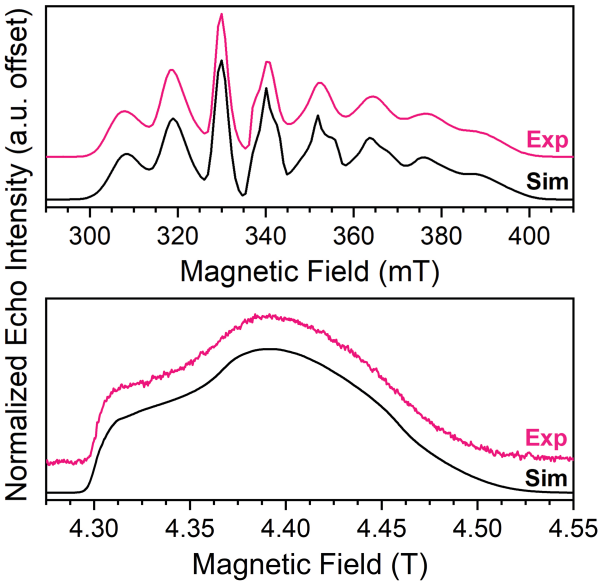

Figure 3.4. **(Top)** X-Band (9.460 GHz) echo-detected, field-swept spectra of **1** (1 mM in OTP, color line) at 5 K and simulation (black). Data taken from ref 40. **(Bottom)** 120 GHz echo-detected, field-swept spectra of 1 mM **1** in OTP solution (color) at 5 K and simulation (black).

extremely sensitive to the symmetry of the ligand field,[70] the similarity of these parameters

highlights a relatively consistent local coordination geometry for **1**–**5** when frozen in d^{14}-OTP.

Spin-lattice relaxation rates ($1/T_1$) were obtained as the first step toward understanding the impact of ligand nuclear-spin patterning on the V(IV) spin dynamics. To determine these rates for **1**–**5**, variable-temperature inversion recovery experiments were performed at the highest-intensity peaks in the 120 GHz EDFS spectra at 5 K, which is B_0 = 4.4 T for all five complexes (Figs. 3.5, 3.14-3.18, and Table 3.6). For **1**–**5**, $1/T_1$ is slowest at low temperature, with an average $1/T_1$ of 0.88(6) ms^{-1} at 5 K. With increasing temperature, T_1 rapidly decreases for **1**–**5**, a consequence of a rapidly hastening relaxation rate, $1/T_1$. Owing to instrumental limitations related to the deadtime, performance of these experiments was precluded above 40 K. An immediate observation from these data is the near-two-orders-of-magnitude enhancement of $1/T_1$ (average $1/T_1$ = 0.88(6) ms^{-1}) at 120 GHz versus the 5 K, 9.4 GHz $1/T_1$ of **1**: 0.0141(4) ms^{-1}.[40,41,43] Comparison of $1/T_1$ across the series of complexes, in contrast, reveals remarkable similarity between the temperature-dependent curves at this field/frequency.

The enhancement of spin-lattice relaxation rates ($1/T_1$) at high field/frequency gives valuable information about the dominant high-field relaxation process for V(IV). Indeed, there are a collection of different mechanisms potentially responsible for spin-lattice relaxation: direct, Raman, local-mode, tunneling, and thermally activated processes.[15,71] Yet, only direct, tunneling, and thermally activated processes are field-dependent. Of these, tunneling is typically suppressed under an applied field and thermally activated processes are likely precluded for V(IV) owing to the absence of low-lying excited states for this $S = {}^1/_2$ ion. Hence, we hypothesized that a dominant direct process is responsible for the stark shortening of T_1. To test this hypothesis, we modelled the temperature-dependence of the spin-lattice relaxation rate ($1/T_1$) at 120 GHz. We found that the data

for all complexes were readily modeled using the sum of a direct and Raman process in the following equation (See Figs 3.5, 3.19):[15]

$$\frac{1}{T_1} = A_{dir}B^2T + A_{Ram}\left(\frac{T}{\theta_D}\right)^9 J_8\left(\frac{\theta_D}{T}\right)$$

Here, T is temperature, A_{dir} is the direct process coefficient, B is the magnetic field, A_{Ram} is the Raman process coefficient, θ_D is the Debye temperature, $J_8(\theta_D/T)$ is the transport integral (see Experimental section for full expression and resulting fit parameters). Qualitatively, because the Raman process is field-independent, the two-

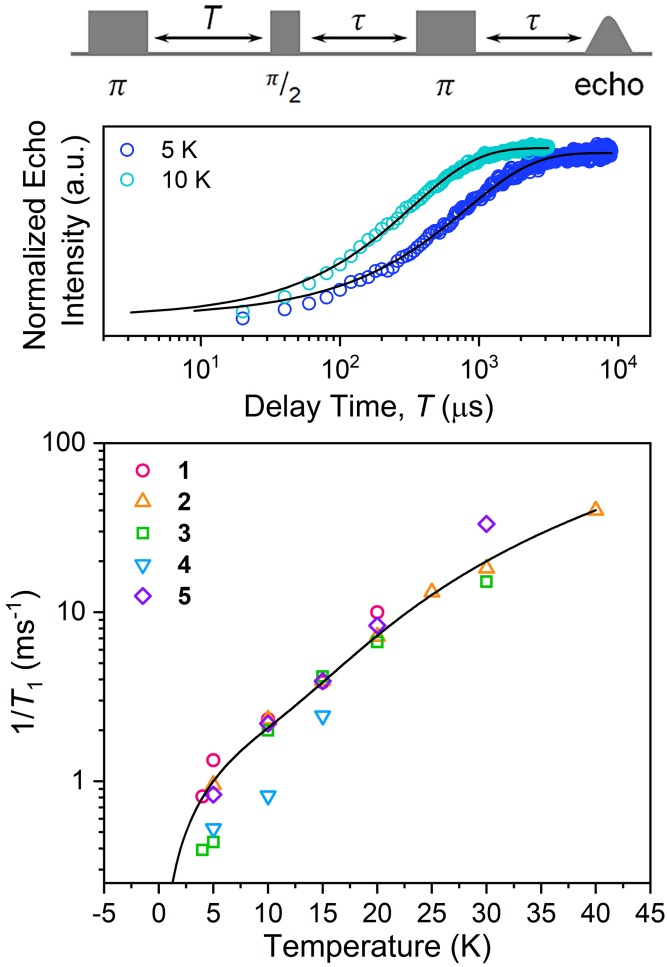

Figure 3.5. **(Top)** Selected variable temperature inversion recovery curves (color traces) and fits (black traces) for **1**. **(Bottom)** Variable-temperature $1/T_1$ data for **1**–**5**. Data were collected at 120 GHz frequency on samples of *ca.* 1 mM concentration in d^{14}-OTP glass. The black trace is the fit to the direct and Raman processes. Error bars are generally under the width of the symbols – exact uncertainties are tabulated and depicted in the EXPERIMENTAL SECTION.

order-of-magnitude shortening of T_1 at 120 GHz compared to 9.4 GHz is strongly suggestive of the direct process importance. Indeed, the two-order of magnitude difference in T_1 between these two data sets would be expected from the B^2 dependence of this process.[12] Furthermore, we can successfully simulate the T_1 data using the Raman process from X-band analyses and modulating only A_{dir}, (see EXPERIMENTAL SECTION). Finally, we note that the shortening of T_1 at the high fields of these analyses agrees with reported ac magnetic susceptibility studies.[41,43] The most important observation, however, is that the relaxation mechanisms for **1**–**5** appear invariant with ligand identity.

Nuclear spin diffusion is expected to exert the greatest impact on T_m, not T_1.[3,12,21,23] Hence, T_m was measured for **1**–**5** to test for a pattern-dependent effect. Variable-temperature, two-pulse Hahn echo experiments were performed on **1**–**5** in d^{14}-OTP at 1 mM concentration to evaluate the echo decay as a function of ligand (Figs. 3.6, 3.20-3.24). Stretched exponential functions were fit to these decays to extract T_m and the stretch parameter, β, (see Experimental, Table 3.6) which can give mechanistic insight into the decay of the superposition. All complexes display the longest T_m values at the lowest temperatures. At 5 K, the T_m values of **1**, **2**, **3**, and **5** range from 4.36(8) to 5.36(9) μs. For **4**, T_m is about 2 μs shorter, 2.75(3) μs. With increasing temperatures, T_m drops sharply for **1**–**5**. By 20 K, the T_m of **4** is 0.7(1) μs, which precluded pulsed measurements at any higher temperatures owing to low signal to noise. In contrast, T_m remains appreciable for **1**–**3** and **5** up to at least 30 K. Interestingly, above 20 K, T_m for **3** is slightly higher than the other complexes. The stretch parameters increase with increasing temperatures for **1**–**5**. For **1**–**3** and **5**, β ranges over 0.6 to 0.8 at the lowest temperatures, and venture closer to 1 at the highest temperatures. For **4**, however, β is close to 1 at the lowest temperature and only increases with higher temperatures.

The difference in T_m for **4** relative to **3**, and **3**, **4** relative to **1**, **2**, and **5**, represent two significant findings. First, these data particularly **3** (T_m = 4.36(8) μs) v. **4** (T_m = 2.75(3) μs) reveal for the first time that two substitutional isomers of the same magnetic metal complex can have significantly different T_m values. Second, the data for **3** v. the rest of the series highlight the possibility of enhancing T_m via patterns that avoid two adjacent protons (though that impact is modest in the present system). However, in that context, it is particularly puzzling that **4** demonstrates a significantly shorter T_m than **1** and **5**, which possess the highest number of adjacent ^{1}H and $^{79/81}$Br spins, respectively. It is further puzzling that **4** displays a shorter T_m than **3**, when the protons in **4** are clearly further separated than those of **3**. Changes in geometry of the coordination site and electronic

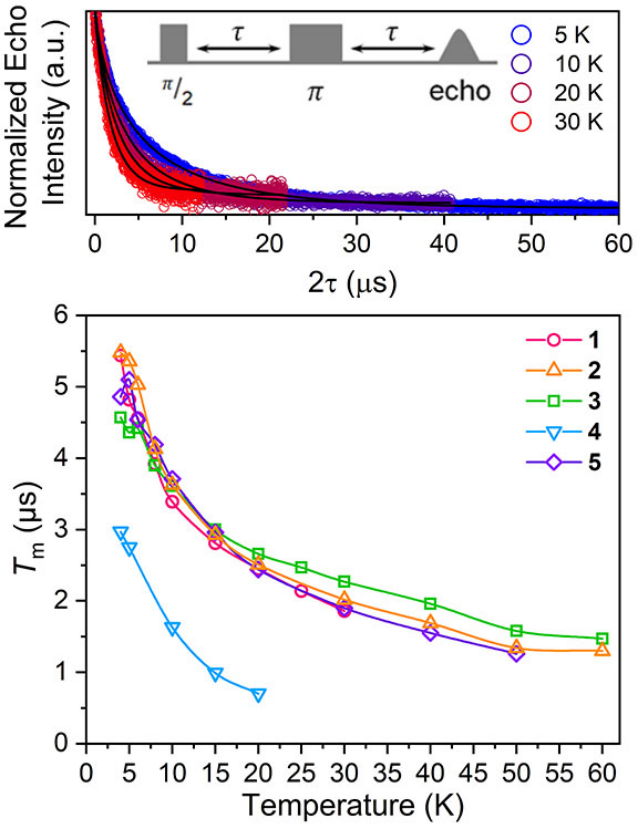

Figure 3.6. **(Top)** Selected variable temperature Hahn echo decay curves (color traces) and fits (black traces) for **1**. The pulse sequence is inset. **(Bottom)** Variable-temperature T_m data for **1**–**5**. Data were collected at 120 GHz frequency on samples of *ca.* 1 mM concentration *o*-terphenyl glass. Error values are generally within the width of the data symbols – exact uncertainties are tabulated and depicted in the EXPERIMENTAL SECTION.

structure are powerful mechanisms for adjusting T_m.[12] However, the similarity of the spin-Hamiltonian parameters, crystallographic data, and T_1 values for **1**–**5** suggests that the different substitutional patterns of the ligands do not affect these aspects of the complex. These results thus suggest that the impact of the pattern on T_m is truly magnetic in nature, stemming from the ^{1}H and $^{79/81}$Br ligand nuclear spins (*vide infra*).

For ligand-based nuclear spin diffusion to operate efficiently, the nuclear spins should have the same resonant NMR frequency (chemical shift). To probe the environment of nuclear spins for the molecules in this paper, we collected the ^{1}H NMR spectra of the ligands.[3,15] The 400 MHz (= 9.4 T field) ^{1}H NMR spectra of the ligands of **1**, **2**, and **3** demonstrate peaks of varying multiplicity over a range of chemical shifts (in frequency, 68, 93, and 61 Hz, respectively) (Figs. 3.7). The observed range of ^{1}H chemical shifts in the ligands of **1**–**3** is a consequence of two factors. First, the presence of different quantities and arrangements of bromine on the ligands adjust the ^{1}H chemical shifts. Second, *J*-coupling between the aromatic ^{1}H protons split the individual ^{1}H peaks into multiplets. In contrast, the aromatic protons of 4,5-dibromocatechol (the ligand of **4**) yield a single peak with a full-width half-maximum of 2 Hz. The protons in this ligand are constrained to a tight chemical shift window by the two-fold rotational symmetry and weak *J*-coupling (0-1 Hz) for aromatic 3,6 protons.[72,73]

On the basis of the NMR data, we rationalize the observed T_m data in terms of synthetic control via ligand-shell nuclear spin diffusion. First, the high symmetry of the 4,5-dibromocatechol and weak *J*-coupling ensure nearly identical chemical shifts for the aromatic ^{1}H nuclei. In the other ligands, in contrast, asymmetry and stronger ^{1}H-^{1}H *J*-coupling spread the ^{1}H chemical shifts out over > 60 Hz. Owing to the relatively tight range (2 Hz) of the ^{1}H frequencies in the ligand of **4** relative to **1**–**3**, we posit that a given ligand proton in **4** is significantly more likely to have a proximate nucleus (across the aromatic ring) with the same chemical shift. Hence, the ligand-based protons in **4** are more likely to

engage in nuclear spin diffusion and impact T_m. In the other complexes, *J*-coupling and differing chemical shifts spread the spin-flip frequencies of the ^{1}H protons over a wider range, ensuring a lower probability that a given ^{1}H will have a neighbor with precisely the same chemical shift. Hence, **1**–**3**, with non-resonant ^{1}H spins, would be expected to display less-efficient spin diffusion and show a longer T_m. This effect may also be operative for the ligand bromines, due to the different isotopes of bromine (^{79}Br and ^{81}Br). Hence, this argument may explain why **5** has a T_m in the same range of **1**–**3**. We note that the stretch parameters β are slightly higher for **4** relative to **1**–**3** and **5**, suggesting that nuclear spin-diffusion may be more operative for **4** (and consistent with our rationale).[21] However, the typical values of β for dominant nuclear-spin diffusion are closer to 2-2.5,[12] and this

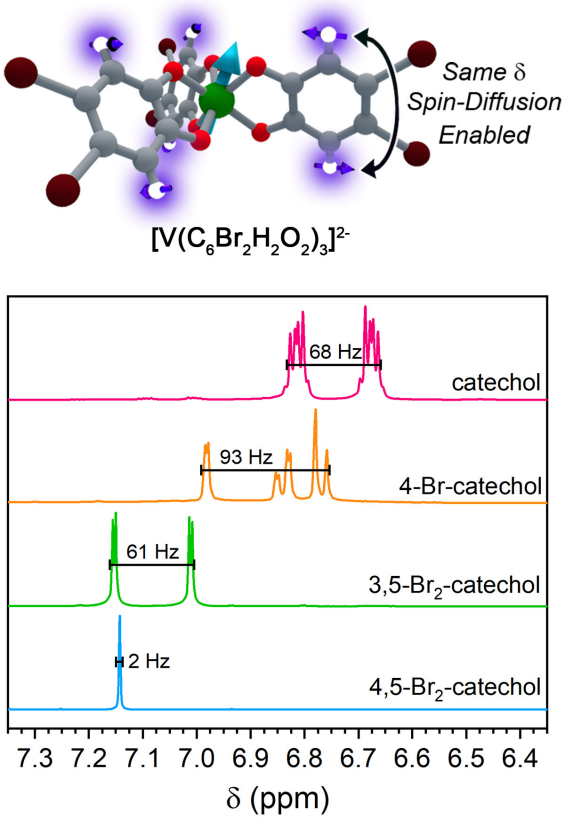

Figure 3.7. **(Top)** Hypothesized impact of patterning in the anomalously short T_m for **4**. **(Bottom)** Solution-phase, 400 MHz NMR spectra for the ligands in complexes **1**–**4**, focused explicitly on the aromatic region of chemical shift (δ). The relatively small spread in ^{1}H NMR frequencies for 4,5-dibromocatechol relative to the ^{1}H signals on the other ligands ensures that the protons in **4** always have a relatively proximate, resonant-spin neighbor. Hence, we hypothesize that these nuclei readily participate in nuclear spin diffusion and shorten T_m for the V(IV) ion.

discrepancy may be related to the limitation of T_m by the short T_1 in **1-5**. Given the fast spin-lattice relaxation at high field, lower-field measurements may engender stronger nuclear-spin-diffusion control by pushing ligand-based nuclear spin resonant frequencies closer together.[69,74–77] Such measurements are exciting next studies.

Conclusions

The foregoing results demonstrate, for the first time, that control of phase memory times is possible via nuclear-spin patterning within a molecule. Importantly, we interpret our data to suggest that tuning relative chemical shifts, which are dictated by the symmetry and chemical make-up of the molecule, are a key future design strategy for manipulating T_m in magnetic complexes. However, multiple new avenues of work are necessary to fully test the presented design strategy. In particular, learning how to harness said strategy to improve T_m is a pressing concern. Indeed, we note that the "optimally patterned" species 3 only exhibits a slight enhancement of T_m over a fully-protonated complex and the most dramatic impact is a shortening, not lengthening of T_m. Toward the understanding to use this mechanism to lengthen T_m, our future work spans studying the nuclear spin dynamics (in particular, the time constants for spin diffusion and spin-spin relaxation) of the ligands and metal complexes. In this context, an important absence in the above analyses is a direct picture of the spin dynamics of the $^{79/81}$Br nuclear spins, which is extremely challenging to address with solution-phase NMR. A system patterned with ^{19}F nuclei is in contrast particularly advantageous since ^{19}F NMR is readily performed.[78–80] It is in these directions that we are now working.

Notes

‡ In this paper, we use T_m to describe the time constant associated with the decay of the echo intensity in a Hahn-echo experiment. This parameter is frequently also labelled

T_2, the spin-spin relaxation. However, the T_2 designation is typically ascribed to relaxation in the xy-plane primarily from spin flip-flop motions. In contrast, T_m is a broader, all-encompassing term for all relaxation processes that affect relaxation in the xy-plane. The T_m designation is particularly appropriate in this manuscript because there may be other factors controlling T_m (e.g. a short T_1) under the experimental conditions. Further reading on this distinction can be found in reference 12.

Experimental

General Considerations. The complex (*n*-$Bu_3NH)_2[V(C_6H_4O_2)_3]$ (**1**) was reported to be air-sensitive.[40] Thus, all manipulations and syntheses of it and **2–5** were performed under a N_2 atmosphere with either a Vigor glovebox or Schlenk techniques. Glassware was either oven-dried at 150 °C for at least 4 h and/or flame-dried before bringing into the glovebox. Tetrahydrofuran (THF), diethyl ether (Et_2O), and hexanes were dried using a commercial solvent purification system from LC Technology Solutions and were stored over 4 Å molecular sieves prior to use. 4 Å molecular sieves were stored in a 150 °C oven and were activated at 280 °C under reduced pressure for at least 12 h prior to use. THF, Et_2O, and hexanes were subjected to a test with a standard purple solution of sodium benzophenone ketyl in THF to confirm low O_2 and H_2O content. Tri-*n*-butylamine (*n*-Bu_3N) and hexamethyldisiloxane (HMDSO) were purchased from commercial suppliers and dried by stirring over CaH_2 for at least 24 h then distilled over CaH_2. Tetrabromocatechol, 4-bromocatechol, and d^{14}-*o*-terphenyl were purchased from commercial suppliers and were used as received. Vanadyl acetylacetonate ($VO(acac)_2$),[81] 3,5-dibromocatechol,[82] 4,5-dibromocatechol,[83] and (*n*-$Bu_3NH)_2[V(C_6H_4O_2)_3]$ (**1**)[59,61] were prepared following the literature procedures.

(*n*-$Bu_3NH)_2[V(4\text{-}Br\text{-}C_6H_3O_2)_3]$ (2) In a N_2-filled glovebox, a 20-mL scintillation vial was charged with 0.135 g (0.509 mmol) $VO(acac)_2$, 0.283 g (1.49 mmol) 4-bromocatechol,

ca. 8 mL THF, and a Teflon-coated magnetic stir bar. A solution of 238 μL (1.00 mmol) *n*-Bu_3N was added to the mixture with gentle shaking, resulting almost immediately in an intensely dark blue solution. The reaction mixture was allowed to stir overnight. All volatile materials (THF, H_2O, and acetylacetone) were removed under reduced pressure. The resulting dark blue residue was washed twice with ca. 5 mL cold Et_2O (Note: the complex is slightly soluble in Et_2O) and twice with ca. 5 mL hexanes and then was dried under reduced pressure to yield 0.456 g of dark blue powder. The solid was further purified by slow evaporation of THF in the glovebox for 2 weeks to afford 0.472 g (0.479 mmol, 96 % yield) of large, shiny, dark blue crystals suitable for single-crystal X-ray diffraction. The ^1H NMR spectrum of **2** in $CDCl_3$ reveals extremely broadened signals that are depicted in Fig. 3.9. IR (KBr, cm^{-1}): 3086, 2959, 2928, 2874, 2775, 2673, 2608, 2555, 1590, 1555, 1537, 1510, 1467, 1402, 1353, 1347, 1289, 1288, 1261, 1213, 1197, 1116, 1070, 1047, 1023, 927, 892, 847, 795, 736, 658, 633, 578, 563, 517, 464, 442, 415. UV-vis (THF); λ_{max} (ε_M, $M^{-1}cm^{-1}$): 293 (16000); 462 (3400); 576 (5300); 682 (4800). LTQ-MS (m/z): positive ion mode: $\{(n\text{-}Bu_3NH)_3[V(C_6H_3BrO_2)_3]\}^+$, 1170.08; $\{(n\text{-}Bu_3NH)_2[HV(C_6H_3BrO_2)_3]\}^+$ (MeCN), 1024.00; negative ion mode: $\{(n\text{-}Bu_3NH)(n\text{-}Bu_3N)[HV(C_6H_3BrO_2)_3]\}^-$ (THF), 1291.58; $\{[V(C_6H_3BrO_2)_3]\}^-$, 612.91; $\{[VO(C_6H_3BrO_2)_2]\}^-$, 441.00; $\{[V(C_6H_3BrO_2)_2]\}^-$, 425.16. Combustion analyses calculated for $C_{42}H_{65}Br_3N_2O_6V$ (found): 51.21 (51.23) % C; 6.57 (6.65) % H; 2.27 (2.85) % N.

(n-$Bu_3NH)_2[V(3,5\text{-}Br_2\text{-}C_6H_2O_2)_3]$ (3) In a N_2-filled glovebox, a 20-mL scintillation vial was charged with 0.133 g (0.502 mmol) $VO(acac)_2$, 0.411 g (1.53 mmol) 3,5-dibromocatechol, ca. 8 mL THF, and a Teflon-coated magnetic stir bar. A solution of 238 μL (1.00 mmol) *n*-Bu_3N was added to the mixture with gentle shaking, resulting almost immediately in an intensely dark blue solution. The reaction mixture was allowed to stir overnight. All volatile materials (THF, H2O, and acetylacetone) were removed under

reduced pressure. The resulting dark blue residue was washed twice with ca. 5 mL cold Et_2O (Note: the complex is slightly soluble in Et_2O) and twice with ca. 5 mL hexanes and then was dried under reduced pressure to yield 0.518 g (0.424 mmol, 84 % yield) of pure dark blue powder indicated by elemental analysis. All crystallization attempts resulted in samples where crystals were too small for diffraction or amorphous solids. We hypothesize that crystals of high quality for **3** were unable to be obtained presumably due to extensive disorder of the three asymmetric 3,5-dibromocatecholate ligands on the V(IV) ion. The ^{1}H NMR spectrum of **3** in $CDCl_3$ reveals extremely broadened signals that are depicted in Fig. 3.10. IR (KBr, cm^{-1}): 3068, 2960, 2931, 2872, 1583, 1526, 1465, 1419, 1373, 1357, 1345, 1329, 1287, 1252, 1234, 1227, 1187, 1101, 1074, 1059, 995, 943, 923, 828, 798, 789, 754, 732, 716, 708, 668, 658, 624, 578, 536, 464. UV-vis (THF); λ_{max} (ε_M, $M^{-1}cm^{-1}$): 293 (15000); 391 (5000); 580 (8100); 682 (7200). LTQ-MS (m/z): positive ion mode: {[*n*-Bu_3NH][$C_6H_4Br_2O_2$]}$^+$, 453.33; negative ion mode: {[$V(C_6H_2Br_2O_2)_2$]}$^-$, 577.00; {[$VO(C_6H_2Br_2O_2)$]}$^-$, 328.91. Combustion analyses calculated for $C_{42}H_{62}Br_6N_2O_6V$ (found): 41.58 (41.30) % C; 5.44 (5.12) % H; 2.18 (2.29) % N.

(*n*-$Bu_3NH)_2$[$V(4,5\text{-}Br_2\text{-}C_6H_2O_2)_3$] (4) In a N_2-filled glovebox, a 20-mL scintillation vial was charged with 0.133 g (0.502 mmol) $VO(acac)_2$, 0.411 g (1.53 mmol) 4,5-dibromocatechol, ca. 8 mL THF, and a Teflon-coated magnetic stir bar. A solution of 238 μL (1.00 mmol) *n*-Bu_3N was added to the mixture with gentle shaking, resulting almost immediately in an intensely dark blue solution. The reaction mixture was allowed to stir overnight. All volatile materials (THF, H_2O, and acetylacetone) were removed under reduced pressure. The resulting dark blue residue was washed twice with ca. 5 mL cold Et_2O (Note: the complex is slightly soluble in Et_2O) and twice with ca. 5 mL hexanes and then was dried under reduced pressure to yield 0.556 g of dark blue powder. The solid was further purified by slow evaporation of THF in the glovebox for 2 weeks to afford 0.405 g (0.332 mmol, 66 % yield) of large, shiny, dark blue crystals suitable for single-crystal X-

ray diffraction. The ^{1}H NMR spectrum of **4** in $CDCl_3$ reveals extremely broadened signals that are depicted in Fig. 3.11. IR (KBr, cm^{-1}): 3094, 2961, 2933, 2872, 2746, 2659, 2540, 1556, 1536, 1493, 1462, 1355, 1337, 1257, 1226, 1186, 1080, 1026, 919, 873, 850, 836, 802, 734, 674, 656, 602, 535, 472, 412, 408. UV-vis (THF); λ_{max} (ε_M, $M^{-1}cm^{-1}$): 293 (11000); 579 (5100); 682 (45000). LTQ-MS (m/z): positive ion mode: {(*n*-$Bu_3NH)_3[V(C_6H_2Br_2O_2)]\}^+$, 1406.92; {[n-$Bu_3NH][C_6H_2Br_2O_2]\}^+$, 453.33; negative ion mode: {$[V(C_6H_2Br_2O_2)_3]\}^-$, 849.50; {$[V(C_6H_2Br_2O_2)_2]\}^-$, 582.92; {$[VO(C_6H_2Br_2O_2)_2]\}^-$, 598.75; {$[VO(C_6H_2Br_2O_2)]\}^-$, 328.91. Combustion analyses calculated for $C_{42}H_{62}Br_6N_2O_6V$ (found): 41.66 (41.30) % C; 5.24 (5.12) % H; 2.29 (2.29) % N.

(*n*-$Bu_3NH)_2[V(C_6Br_4O_2)_3]$ (5) In a N_2-filled glovebox, a 20-mL scintillation vial was charged with 0.0921 g (0.347 mmol) $VO(acac)_2$, 0.451 g (1.06 mmol) tetrabromocatechol, and a Teflon-coated magnetic stir bar. A solution containing 0.169 g (0.912 mmol) *n*-Bu_3N in 5 mL THF was added to the mixture with gentle shaking, resulting almost immediately in an intensely dark blue solution. The reaction mixture was allowed to stir overnight. All volatile materials (THF, H_2O, and acetylacetone) were removed under reduced pressure. The resulting dark blue residue was washed twice with ca. 5 mL Et_2O and then was dried under reduced pressure to yield 0.53 g of dark blue powder. The solid was further purified by crystallization with HMDSO/THF in a −35 °C freezer in the glovebox for 2−3 days to afford 0.451 g (0.266 mmol, 76.6 % yield) of large, shiny, dark blue crystals suitable for single-crystal X-ray diffraction (See Figure 3.12 for picture). The ^{1}H NMR spectrum of **5** in $CDCl_3$ reveals extremely broadened signals that are depicted in Fig. 3.9. IR (KBr, cm^{-1}): 3048, 2956, 2872, 1568, 1465, 1377, 1253, 1097, 1014, 870, 799, 733, 628, 537, 501, 412. UV-vis (CH_3CN); λ_{max} (ε_M, $M^{-1}cm^{-1}$): 289 (17000), 347 (5000), 559 (8000), 658 (7100). LTQ-MS (m/z): positive ion mode: {*n*-$Bu_3NH\}^+$, 186.25 (base); {(*n*-$Bu_3NH)_2[V(C_6H_4O_2)_3]\}^+$, 748.46; negative ion mode: {$H[V(C_6H_4O_2)_3]\}^-$, 376.08. Combustion analyses calculated for $C_{42}H_{56}Br_{12}N_2O_6V$ (found): 29.77 (29.94) % C; 3.33 (3.17) % H; 1.65 (1.46) % N.

Determination of Density of d^{14}-*o*-terphenyl. 1 g d^{14}-*o*-terphenyl was placed in a 20-mL scintillation vial and the mass was recorded. Next, the vial was heated to 60 °C for d^{14}-*o*-terphenyl to melt. 0.1 mL d^{14}-*o*-terphenyl was removed via a micropipette. The mass difference was recorded and the density of d^{14}-*o*-terphenyl could be calculated. This process was repeated two more times to yield an average density of 1.29(5) g/cm^3.

X-ray Data Collection, Structure Solution and Refinement for 2, 4, and 5. The diffraction data were collected at the X-Ray Diffraction facility of the Central Instrument Facility at Colorado State University. Data for **2, 4,** and **5** were collected on a Bruker D8 Quest ECO single-crystal X-ray diffractometer equipped with Mo Kα (λ = 0.71073 Å). Data were collected and integrated using Bruker Apex 3 software. Absorption correction were applied using SADABS.[84] Space group assignments were determined by examination of systematic absences, E-statistics, and successive refinement of the structures. Crystal structures were solved using SHELXT and refined with the aid of successive difference Fourier maps by SHELXL operated in conjunction with OLEX2 software.[85-87] None of the crystals demonstrated decay by X-ray radiation over the course of the experiment. Hydrogen atoms were placed in ideal positions and refined using a riding model for all structures. In **2**, two of the alkyl chains were each disordered over two positions and were modeled using free variables. In one of the alkyl chains the disordered carbons freely modeling the two positions yielded occupancies of 0.393(14) and 0.607(14), respectively. The methyl group on the end of the other alkyl chain yielded occupancies of 0.504(14) and 0.496(14), respectively. One of the 4,5-dibromocatecholate ligands in **2** was disordered over two positions by rotational symmetry and was modeled using free variables yielding occupancies 0.65(5), 0.64(4), 0.56(3), 0.55(4), and 0.528(3) for C1, C1A, C2A, C2B, and Br, respectively. In **4**, two of the alkyl chains on the counteraction was disordered over two positions and were modeled using free variables yielding occupancies of 0.69(3) and 0.31(3). In **5** one of the alkyl chains on the counteraction was disordered over two positions

and were modeled using free variables yielding occupancies of 0.66(3) and 0.34(3). See Tables 3.1–3.4 for refinement details. Crystallographic information files for **2**, **4**, and **5** are available in the CSD at accession numbers 1921675-1921677.

Electron Paramagnetic Resonance. EPR spectra collected herein were simulated using Easyspin[88] with the function pepper (frozen solution and solid) and were refined using the function esfit or simulations of the experimental data. All samples were prepared under an inert atmosphere. Samples **1**, **2**, **3**, and **5** for pulsed EPR studies (1 mM) were prepared by first loading 20 μL 1 mM THF solution of **1** by a micropipette into a 4 mm OD quartz EPR tube. Following removal of THF under reduced pressure, 0.0232 g *o*-terphenyl or 0.0258 g d^{14}-*o*-terphenyl (20 μL when molten) was loaded into the same tube. Sample **4** is less soluble in non-polar solvents, so the aforementioned preparation was unsuccessful. Sample **4** for pulsed EPR studies was prepared by first loading 0.0258 g d^{14}-*o*-terphenyl (20 μL when molten), then adding a 1 mM solution of **4** in THF to the same tube and them removing THF under reduced pressure. These tubes were flame sealed under dynamic vacuum (< 50 mTorr) and placed in a 65−70 °C oil bath until a clear dark blue solution formed. While sample tubes prepared in this manner can be stored at room temperature for an extended period without compound decomposition, the quality of glass appeared to decay with extended time on the basis of spectral quality. Hence, prior to each measurement, the samples were remelted and frozen.

All pulsed EPR data were collected at the National High Magnetic Field Laboratory (NHMFL, Tallahassee, FL, USA) on a custom built 120/240/336 GHz EPR spectrometer.[89,90] Sample tubes were gently melted using a heat gun to afford a homogeneous dark blue solution, then quickly inserted into the resonator to ensure glassing behavior. The data collected were processed using an EPR measurement program locally developed at NHMFL, Matlab 2018b, and Origin Pro 2018b software packages.[91,92]

T_1 data were collected on the most intense resonance of the EDFS spectra at 4.4 T at 120 GHz, via an inversion recovery sequence (π − T − $\pi/2$ − τ − π − τ − echo). The length of the three pulses, π − $\pi/2$ − π, are 900− 600 − 900 ns with a starting T value of 10300 ns and τ of 700 ns. The inversion recovery data were fit accounting for spectral diffusion with the following equation:

$$\mathrm{I}(t) = -A\left[e^{-\left(\frac{t}{T_1}+\sqrt{\frac{t}{q}}\right)} - \mathrm{I}(0) - 1\right]$$

The temperature-dependent T_1 data were fit using the following equation performed in Matlab software:

$$\frac{1}{T_1} = A_{\mathrm{dir}}T + A_{\mathrm{Ram}}\left(\frac{T}{\theta_{\mathrm{D}}}\right)^9 J_8\left(\frac{\theta_{\mathrm{D}}}{T}\right)$$

Here, T is temperature, A_{dir} is the direct process coefficient, A_{Ram} is the Raman process coefficient, θ_{D} is the Debye temperature, and $J_8\left(\frac{\theta_{\mathrm{D}}}{\mathrm{T}}\right)$ is the transport integral:

$$J_8\left(\frac{\theta_{\mathrm{D}}}{T}\right) = \int_0^{\theta_{\mathrm{D}}/T} x^8 \frac{\mathrm{e}^x}{(\mathrm{e}^x - 1)^2}\,\mathrm{d}x$$

Variable temperature T_1 data presented challenges in fitting. Due to the enhanced relaxation rate of spin-lattice relaxation with 120 GHz frequencies, measurements were restricted to below 40 K. Furthermore, **4** has a much shorter T_{m} than the rest of the series, precluding higher temperature measurements of T_1 at 120 GHz. We successfully fit the data using the Raman and direct processes, using Raman parameters (A_{Ram} and θ_{D} to 1.8 × 10^6 (s^{-1}) and 95 K, respectively) close to those obtained from the X-band analyses previously reported by some of us and others.[16] Since the Raman process is *field-independent,* this method was done to see how the A_{dir} value changed. By restricting A_{Ram} and θ_{D} to the X-band values, we obtain an A_{dir} value of 197(82) $K^{-1}s^{-1}$. When A_{Ram} and θ_{D} values were unrestricted, we obtained equivalent values within the error of the parameters (see Table 3.6).

The discrepancy between the direct process coefficients (A_{dir}) between this study and the X-band analyses of $(Bu_3NH)_2[V(C_6H_4O_2)_3]$ (**1**) deserves additional comment. The direct process field dependence is B^2, hence:

$$\frac{1}{T_1} = A_{\mathrm{dir}} B^2 T$$

On account of this equation, one might expect that a fit of the T_1 temperature-dependent data would yield the same A_{dir} between the X-band and 120 GHz data of **1** following a switch of B, considering that the measurements are of samples of the same concentration in the same frozen matrix. The values of A_{dir}, between X-band data and the present data are close, but not the same, from this approach (27(2) $K^{-1}s^{-1}T^{-2}$ for the X-band data and 10(4) $K^{-1}s^{-1}T^{-2}$ for the 120 GHz data). Note that the original reported 3.2(2) $K^{-1}s^{-1}$ value of A_{dir} in ref. 16 does not account for the field strength. Additional analyses are required to understand why this change in A_{dir} is observed between the two fields for the same complex. However, we note that the nature of the probed resonances at 120 GHz and X-band change substantially, because the transitions are heavily overlapped at high-field versus low-field (Fig. 3.25). Such overlap might (1) change the A_{dir} parameter or (2) enable the operation of other relaxation processes. In this latter case, the effect of such unmodeled processes on the fit could be manifest in a change to A_{dir}. A clear solution to this problem is the ability to collect far more detailed T_1 data sets – but extremely low signal-to-noise and limited instrument time deem this experimental design unfeasible for now.

T_m data were collected on the most intense resonance (4.4 T at 120 GHz) in the EDFS spectra via a Hahn echo sequence ($\pi/2 - \tau - \pi - \tau -$ echo) with a 4-step phase cycle with microwave pulses of 600 ($\pi/2$) and 900 ns (π) and an interpulse time (τ) of 700 ns. The Hahn echo decay data were fit using the stretched exponential equation:

$$\mathrm{I}(\tau) = I(0) - Ae^{-\left(\frac{2\tau}{T_m}\right)^{\beta}}$$

Here, β is the stretch parameter. The low temperature data were better fit with stretched exponential equation due to the dominant nuclear spin diffusion. We found that β approached 1 as the temperature increased, indicating that a conventional single exponential fit could be used. Nevertheless, we used the stretched exponential fit throughout the whole temperature range for consistency.

Owing to the long pulse lengths and 100 ns deadtime, T_m values below 200-300 ns were in general extremely difficult to observe, requiring prohibitively long data acquisition times. This factor limited the temperature range for a usable echo to only the lowest temperatures, hence all analyses generally stopped by 40 K, lower for **4**, which displayed much shorter T_m values than the rest of the series.

Other Physical Measurements. ^{1}H NMR spectra were collected on a Bruker Avance NEO 400 MHz spectrometer. The spectra were referenced using residual protiated solvent signal as an internal standard ($CDCl_3$, 7.26 ppm). Combustion analyses were performed by Midwest Microlab (Indianapolis, IN, USA). Infrared spectra were recorded on a Bruker TENSOR II FTIR spectrometer. Electronic absorption spectra were recorded on acetonitrile solutions of **1**−**5** with a Hewlett-Packard 8453 spectrophotometer using air-free quartz cuvettes with a 1 cm path length. Linear trap quadruple mass spectrometry (LTQ-MS) measurements were performed on acetonitrile solutions of **1**−**5** with a Thermo-Finnigan LTQ LC/MS-MS at the Central Instrument Facility (CIF) of the Colorado State University.

Table 3.1. Crystallographic information for the structural refinement of **2**.

Empirical formula	$H_{64}C_{42}N_2Br_3O_6V$
Formula weight	983.62
Temperature	116(2)
Crystal system	tetragonal
Space group	$P4_32_12$
a	14.6090(13) Å
b	14.6090(13) Å
c	21.144(2) Å
α	90°
β	90°
γ	90°
Volume	4512.6(9) $Å^3$
Z	4
ρ_{calc}	1.448 g/cm^3
μ	2.921 mm^{-1}
F(000)	2024
Crystal color	Dark blue
Crystal size	$0.185 \times 0.162 \times 0.159$ mm^3
Radiation	MoKα (λ = 0.71073 Å)
2θ range for data collection	3.388 to 60.068°
Index ranges	$-19 \leq h \leq 19$, $-14 \leq k \leq 19$, $-28 \leq l \leq 20$
Reflections collected	16717
Independent collections	5621 [R_{int} = 0.0274, R_{sigma} = 0.0546]
Data/restraints/parameters	5621/2/276
Goodness-of-fit on F^2	1.131
Final R indexes [$I \geq 2\sigma$ (I)]	R_1 = 0.0376, wR_2 = 0.0955
Final R indexes [all data]	R_1 = 0.0566, wR_2 = 0.1261
Largest diff. peak/hole	0.86/–0.61 e $Å^{-3}$
Flack parameter	0.000(4)

Table 3.2. Crystallographic information for the structural refinement of **4**.

Empirical formula	$H_{62}C_{42}N_2Br_6O_6V$
Formula weight	1221.33
Temperature	120(2)
Crystal system	tetragonal
Space group	$P4_32_12$
a	10.7250(6) Å
b	10.7250(6) Å
c	42.298(3) Å
α	90°
β	90°
γ	90°
Volume	4865.3(6) $Å^3$
Z	4
ρ_{calc}	1.667 g/cm^3
μ	5.176 mm^{-1}
F(000)	2436
Crystal color	Dark blue
Crystal size	$0.156 \times 0.154 \times 0.146$ mm^3
Radiation	MoKα (λ = 0.71073 Å)
2θ range for data collection	3.852 to 51.358°
Index ranges	$-13 \leq h \leq 13$, $-13 \leq k \leq 13$, $-51 \leq l \leq 51$
Reflections collected	408403
Independent collections	4625 [R_{int} = 0.0872, R_{sigma} = 0.0223]
Data/restraints/parameters	4625/2/261
Goodness-of-fit on F^2	1.148
Final R indexes [$I \geq 2\sigma$ (I)]	R_1 = 0.0508, wR_2 = 0.1459
Final R indexes [all data]	R_1 = 0.0522, wR_2 = 0.1500
Largest diff. peak/hole	0.95/–0.69 e $Å^{-3}$
Flack parameter	0.059(5)

Table 3.3. Crystallographic information for the structural refinement of **5**.

Empirical formula	$H_{56}C_{42}N_2Br_{12}O_6V$
Formula weight	1694.63
Temperature	145 (2)
Crystal system	triclinic
Space group	*P*–1
a	12.039(5) Å
b	12.432(6) Å
c	37.11(2) Å
α	83.93(3)°
β	89.04(2)°
γ	84.219(19)°
Volume	5495(5) $Å^3$
Z	4
ρ_{calc}	2.048 g/cm^3
μ	8.950 mm^{-1}
F(000)	51
Crystal color	Dark blue
Crystal size	0.372 × 0.235 × 0.142 mm^3
Radiation	MoKα (λ = 0.71076 Å)
2θ range for data collection	7.566 to 52.988°
Index ranges	$-15 \leq h \leq 15$, $-15 \leq k \leq 15$, $-46 \leq l \leq 46$
Reflections collected	46089
Independent collections	21824 [R_{int} = 0.0494, R_{sigma} = 0.0757]
Data/restraints/parameters	21824/0/1148
Goodness-of-fit on F^2	1.154
Final R indexes [$I \geq 2\sigma(I)$]	R_1 = 0.0653, wR_2 = 0.1662
Final R indexes [all data]	R_1 = 0.0829, wR_2 = 0.1685
Largest diff. peak/hole	1.24/–1.54 e $Å^{-3}$
Flack parameter	0.060(5)

Table 3.4. Continuous-shape-measurement (CSM) (SHAPE 2.0 software) analysis results for **1**, **2**, **4** and **5**.

Complex	SHAPE analysis octahedral	SHAPE analysis trigonal prismatic
1	1.67	8.83
2	2.39	7.64
4	3.97	5.45
5	1.41	10.52

Table 3.5. EDFS spin Hamiltonian parameters for **1**–**5** in d^{14}-*o*-terphenyl collected at 5 K. The standard errors for these parameters were not available from the simulating process.

Complex	**1**	**2**	**3**	**4**	**5**
g_x	1.939	1.938	1.938	1.943	1.934
g_y	1.923	1.920	1.921	1.924	1.914
g_z	1.990	1.990	1.990	1.991	1.989
g_x strain	0.0042	0.0045	0.0045	0.0052	0.0042
g_y strain	0.0129	0.028	0.028	0.020	0.0190
g_z strain	0	0	0	0	0
A_x (MHz)	301	280	280	285	285
A_y (MHz)	348	365	365	375	355
A_z (MHz)	53	60	60	50	70

*Changes in *A*-strain resulted in no change in the simulated spectrum.

Table 3.6. Fit T_1 values from the fitting function: $I\,(t) = -A\left[e^{-\left(\frac{t}{T_1}+\sqrt{\frac{t}{q}}\right)} - I(0) - 1\right]$. The standard error for each fit is reported in parentheses.

1 in d^{14}-*o*-terphenyl:

T (K)	T_1 (ms)	q	T(K)	T_1 (ms)	q
4	1.23(6)	7(1)	15	0.26(1)	0.8(1)
5	1.15(3)	5.6(6)	20	0.09(1)	14(40)
10	0.43(1)	3.8(5)			

2 in d^{14}-*o*-terphenyl:

T (K)	T_1 (ms)	q	T(K)	T_1 (ms)	q
5	1.05(2)	7.0(6)	25	0.076(4)	3(3)
10	0.43(1)	3.0(3)	30	0.055(4)	5(9)
15	0.254(9)	1.0(1)	40	0.025(4)	15(172)
20	0.139(7)	2.0(9)			

3 in d^{14}-*o*-terphenyl:

T (K)	T_1 (ms)	q	T(K)	T_1 (ms)	q
4	2.55(9)	15(2)	15	0.24(2)	4(2)
5	2.3(1)	9(1)	20	0.15(2)	3(3)
10	0.50(2)	2.4(4)	30	0.066(3)	3(1)

4 in d^{14}-*o*-terphenyl:

T (K)	T_1 (ms)	q	T(K)	T_1 (ms)	q
5	1.91(8)	3.9(4)	15	0.41(16)	0.9(3)
10	1.22(7)	1.4(1)			

5 in d^{14}-*o*-terphenyl:

T (K)	T_1 (ms)	q	T(K)	T_1 (ms)	q
5	1.20(3)	3.2(4)	20	0.12(3)	0.5(8)
10	0.456(8)	2.5(2)	30	0.03(1)	0.2(2)
15	0.256(9)	0.1(3)			

Table 3.7. Fit parameters for the temperature dependence of T_1; see "EPR measurements" section for fitting equation. The standard error for each fit is reported in parentheses.

A_{dir} ($K^{-1}\,s^{-1}\,T^{-2}$)	197(82)
A_{Ram} (s^{-1})	$1.8(1)\times10^6$
θ_D (K)	95(5)

Table 3.8. Fit T_m values (in μs) and the stretch parameters (β) from the stretched exponential fitting function: $I(2\tau) = I(0) - Ae^{-(\frac{2\tau}{T_m})^{\beta}}$. The standard error for each fit is reported in parentheses.

1 in d^{14}-*o*-terphenyl:

T (K)	T_m (μs)	β	T(K)	T_m (μs)	β
4	5.44(2)	0.660(2)	15	2.81(4)	0.80(1)
5	4.82(3)	0.678(3)	20	2.45(4)	0.86(2)
6	4.56(2)	0.707(3)	25	2.14(4)	0.91(2)
8	3.92(3)	0.740(4)	30	1.86(3)	0.94(2)
10	3.39(3)	0.769(6)			

2 in d^{14}-*o*-terphenyl:

T (K)	T_m (μs)	β	T(K)	T_m (μs)	β
4	5.48(8)	0.659(7)	20	2.51(4)	0.81(1)
5	5.36(9)	0.70(1)	30	2.02(5)	0.87(3)
6	5.03(7)	0.708(7)	40	1.69(6)	0.89(5)
8	4.13(6)	0.737(9)	50	1.34(9)	0.82(7)
10	3.63(5)	0.78(1)	60	1.3(1)	1.1(2)
15	2.93(4)	0.82(1)			

3 in d^{14}-*o*-terphenyl:

T (K)	T_m (μs)	β	T(K)	T_m (μs)	β
4	4.57(8)	0.629(7)	20	2.66(7)	0.78(2)
5	4.36(8)	0.646(8)	25	2.47(9)	0.79(3)
6	4.42(7)	0.75(1)	30	2.27(5)	0.85(2)
8	3.90(7)	0.69(1)	40	1.96(4)	0.86(2)
10	3.61(6)	0.72(1)	50	1.58(5)	0.90(3)
15	3.00(6)	0.76(1)	60	1.47(9)	0.96(7)

4 in d^{14}-*o*-terphenyl:

T (K)	T_m (μs)	β	T(K)	T_m (μs)	β
4	2.97(3)	1.05(2)	10	1.63(7)	1.12(6)
5	2.75(4)	1.03(2)	15	0.99(9)	1.1(1)

5 in d^{14}-*o*-terphenyl:

T (K)	T_m (μs)	β	T(K)	T_m (μs)	β
4	4.86(4)	0.591(3)	15	2.96(2)	0.802(5)
4.5	5.27(3)	0.666(2)	20	2.44(2)	0.833(8)
5	5.10(4)	0.651(3)	30	1.90(4)	0.87(2)
6	4.54(3)	0.696(3)	40	1.55(7)	0.97(5)
8	4.19(2)	0.729(3)	50	1.26(6)	1.03(6)
10	3.71(2)	0.750(3)			

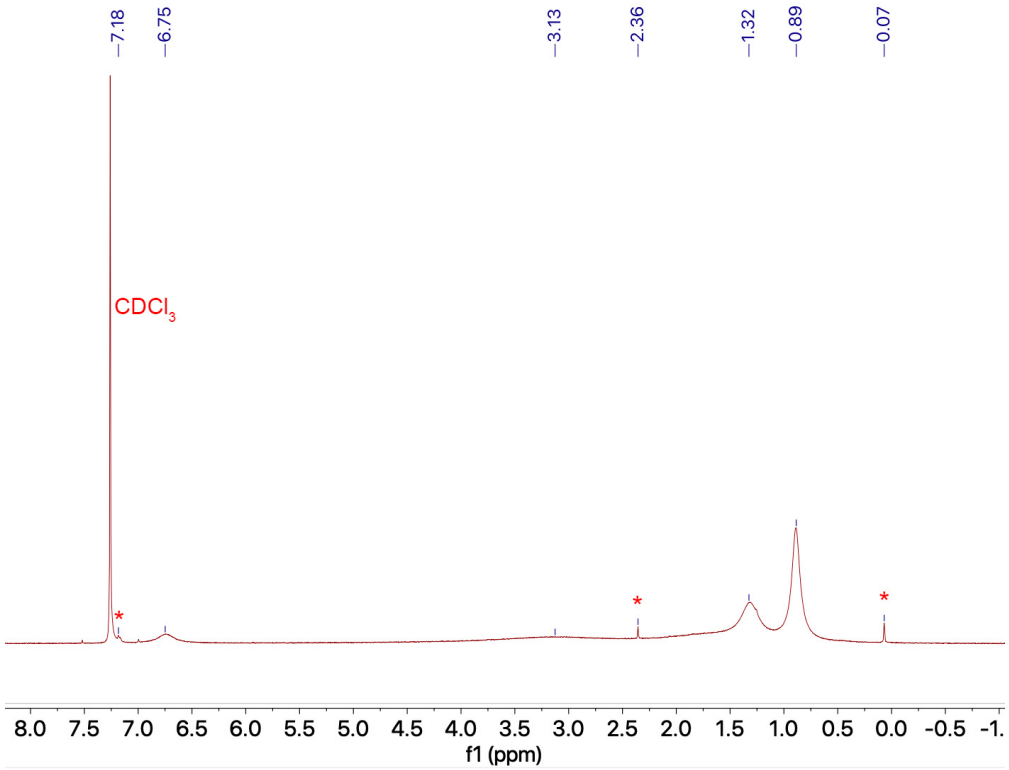

Figure 3.8 ^{1}H NMR spectrum of **2** in $CDCl_3$. No signal was observed outside this spectral range. Asterisks denote impurities in the NMR solvent.

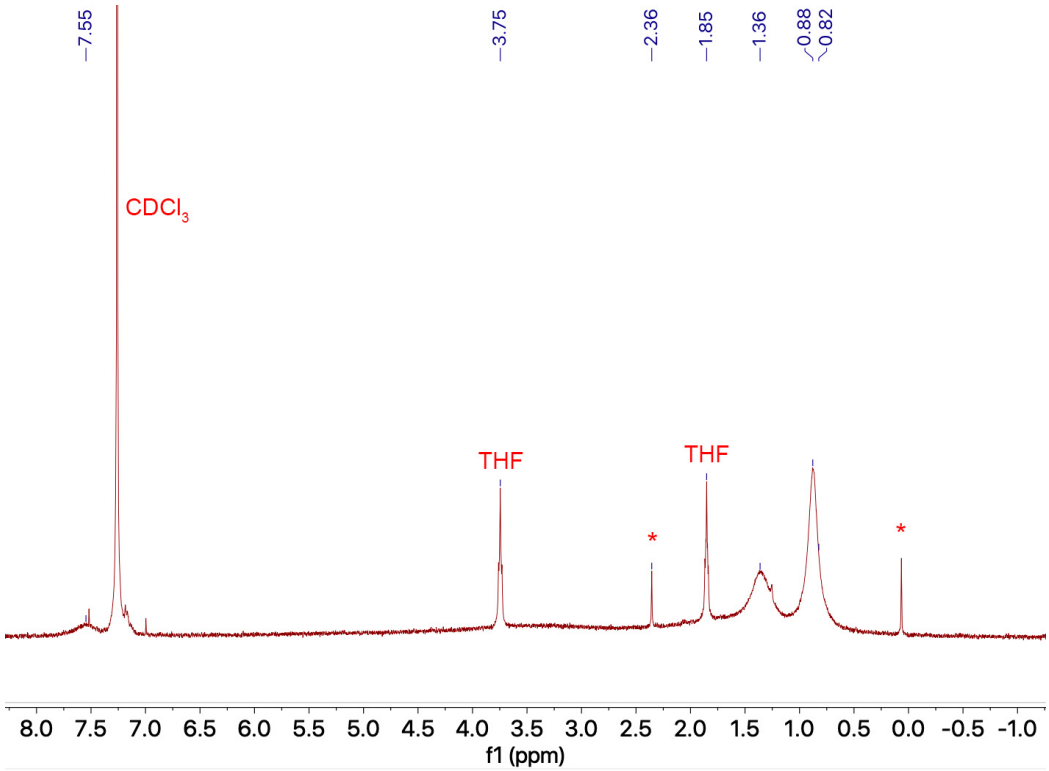

Figure 3.9. ^{1}H NMR spectrum of **3** in $CDCl_3$. No signal was observed outside this spectral range. Asterisks denote impurities in the NMR solvent.

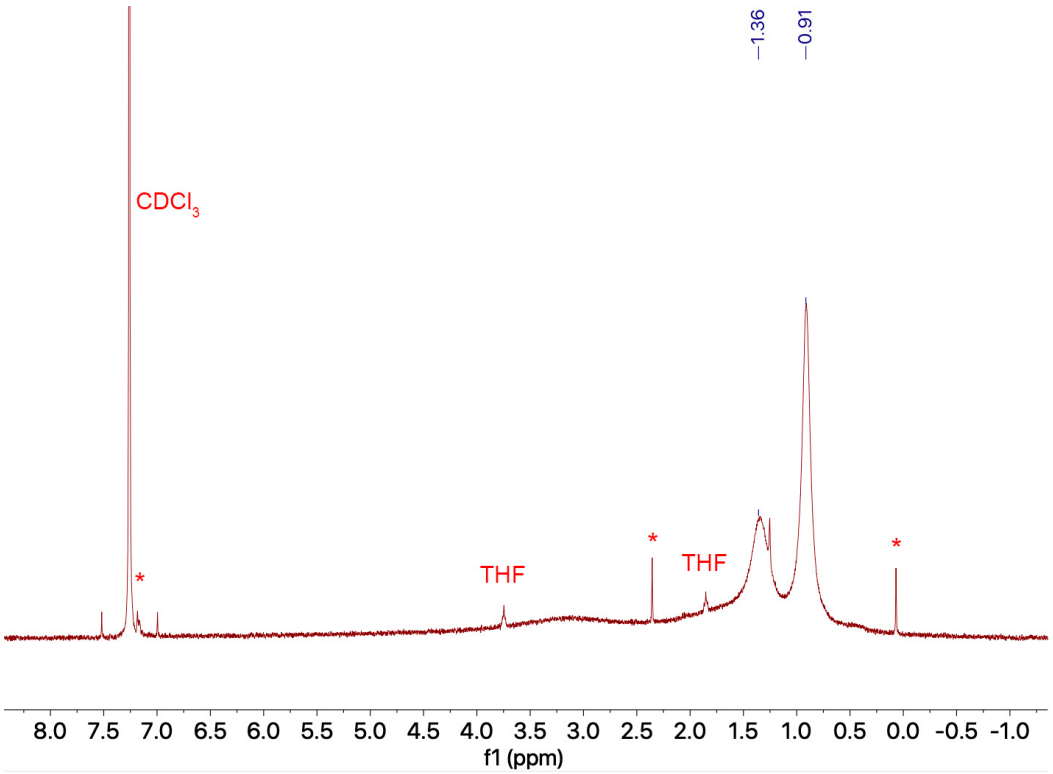

Figure 3.10. ^{1}H NMR spectrum of **4** in $CDCl_3$. No signal was observed outside this spectral range. Asterisks denote impurities in the NMR solvent.

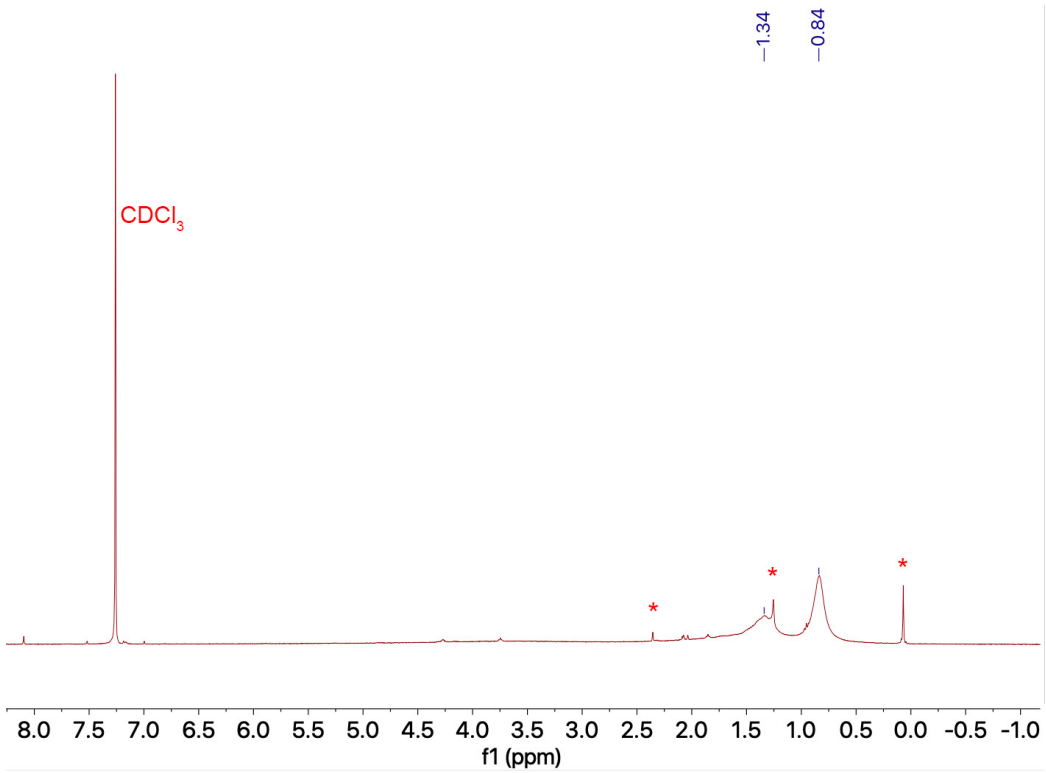

Figure 3.11. ^{1}H NMR spectrum of **5** in $CDCl_3$. No signal was observed outside this spectral range. Asterisks denote impurities in the NMR solvent.

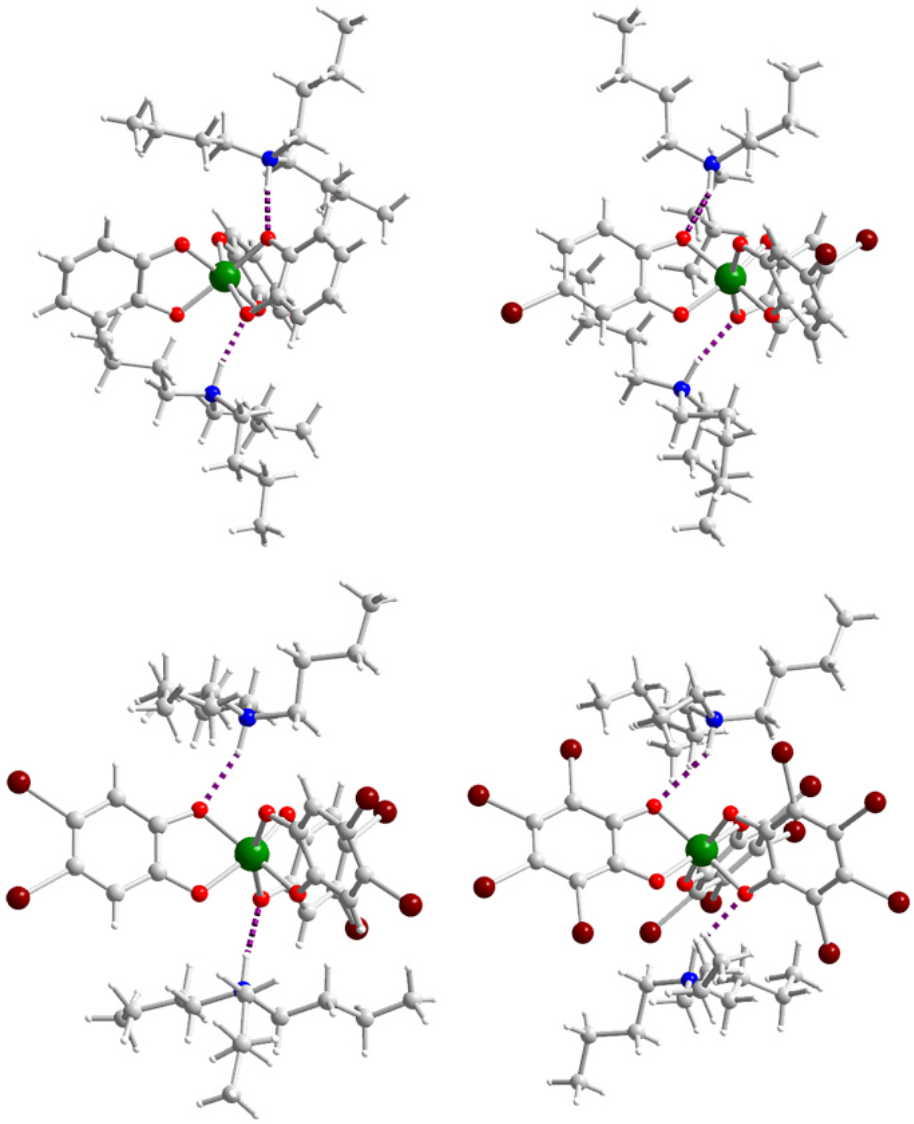

Figure 3.12. Depiction of hydrogen bonding interactions in **1**, **2**, **4**, and **5**. Molecular structures of the V(IV) complexes in **1** (top left) (ref. 16), **2** (top right), **4** (bottom left), and **5** (bottom right), as determined from the crystal structures of these compounds. Green, maroon, red, gray, and white spheres represent vanadium, bromine, oxygen, carbon, and hydrogen atoms, respectively. Dashed lines represent the hydrogen bonding interactions.

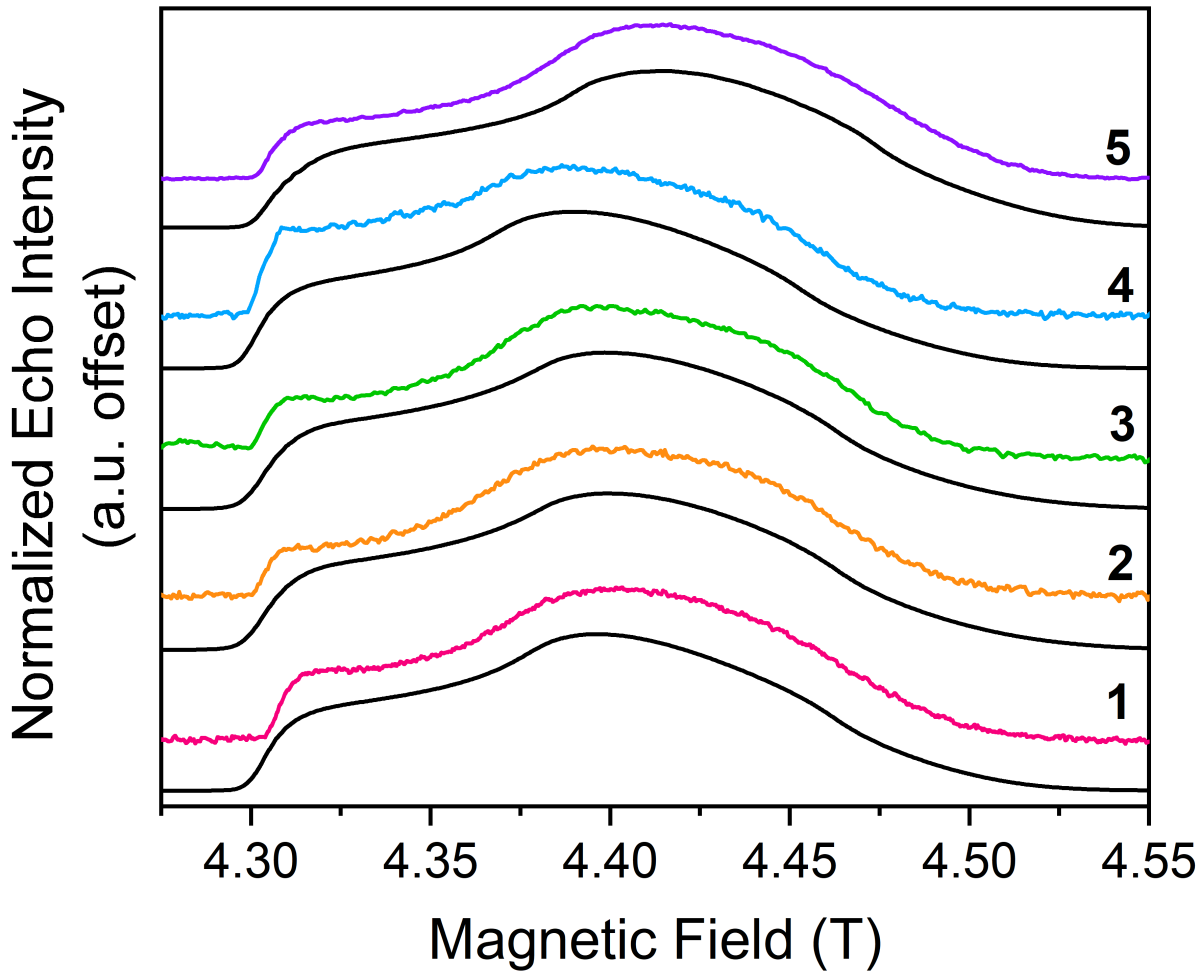

Figure 3.13. Echo-detected, field-swept spectra at 120 GHz of **1**–**5** in d^{14}–*o*–terphenyl solutions (color) at 5 K and simulations (black). Simulated spin Hamiltonian parameters are given in Table 3.6.

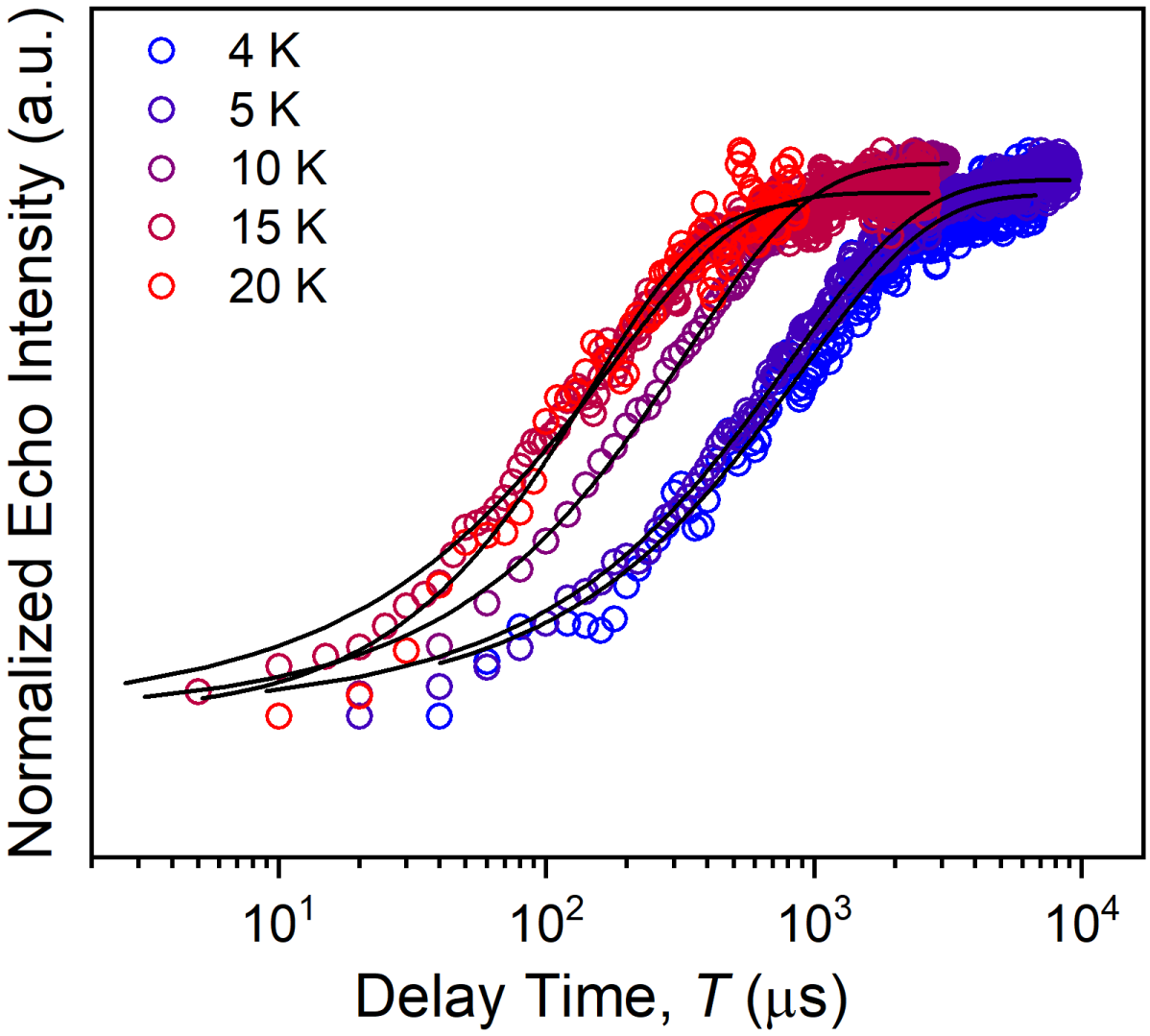

Figure 3.14. Selected variable temperature inversion recovery curves (color traces) and fits (black traces) for **1** in d^{14}-*o*-terphenyl.

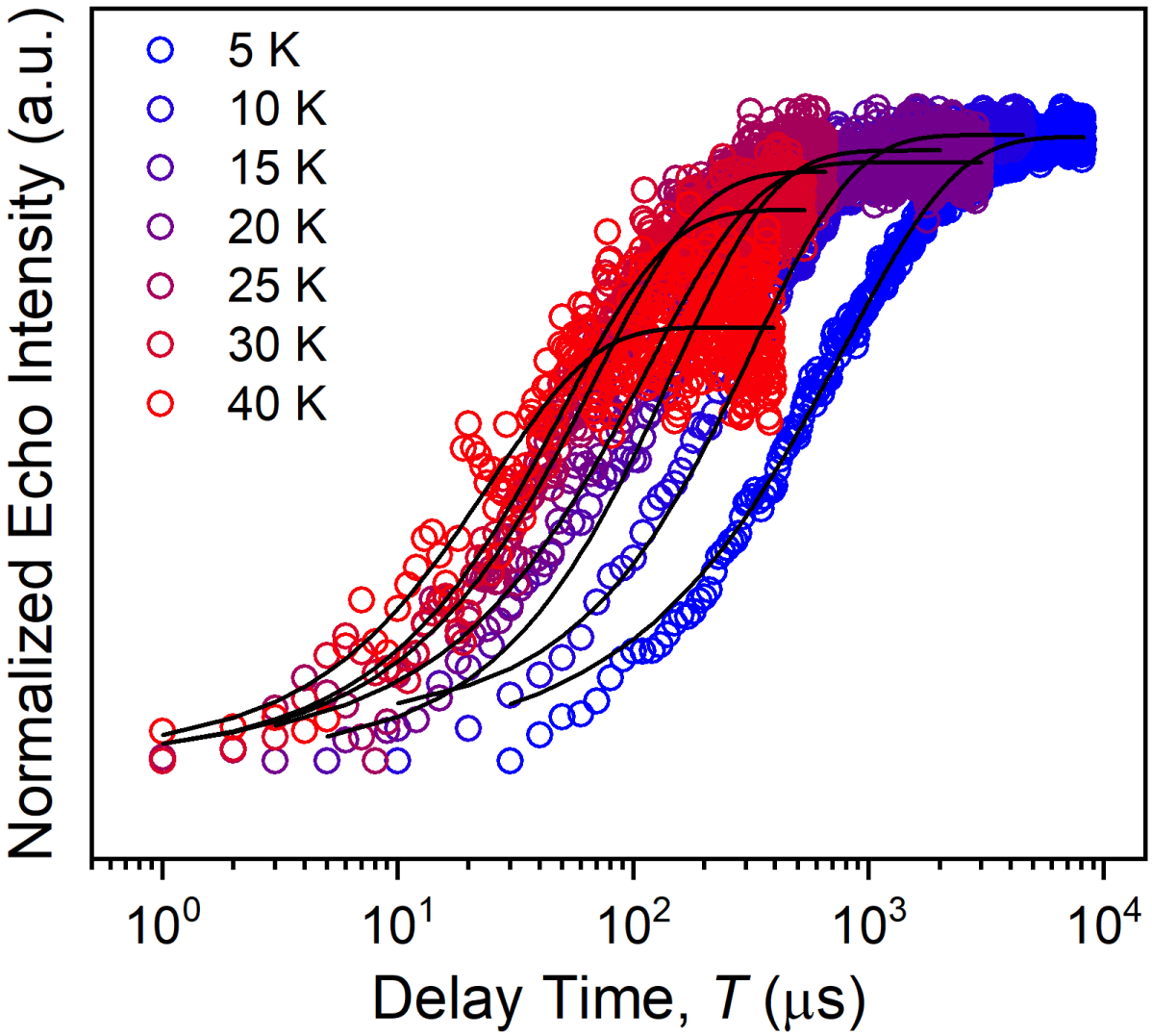

Figure 3.15. Selected variable temperature inversion recovery curves (color traces) and fits (black traces) for **2** in d^{14}-*o*-terphenyl.

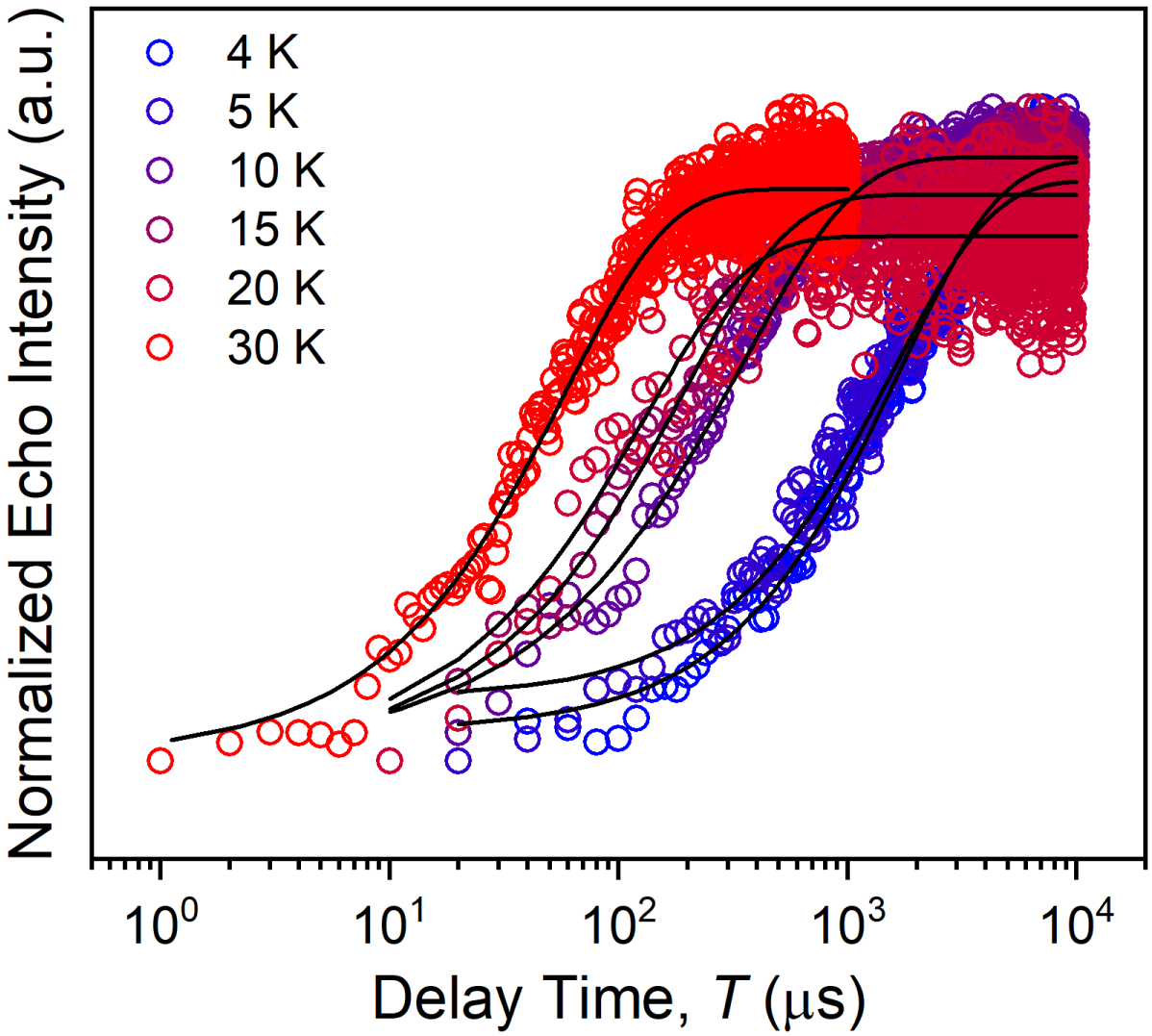

Figure 3.16. Selected variable temperature inversion recovery curves (color traces) and fits (black traces) for **3** in d^{14}-*o*-terphenyl.

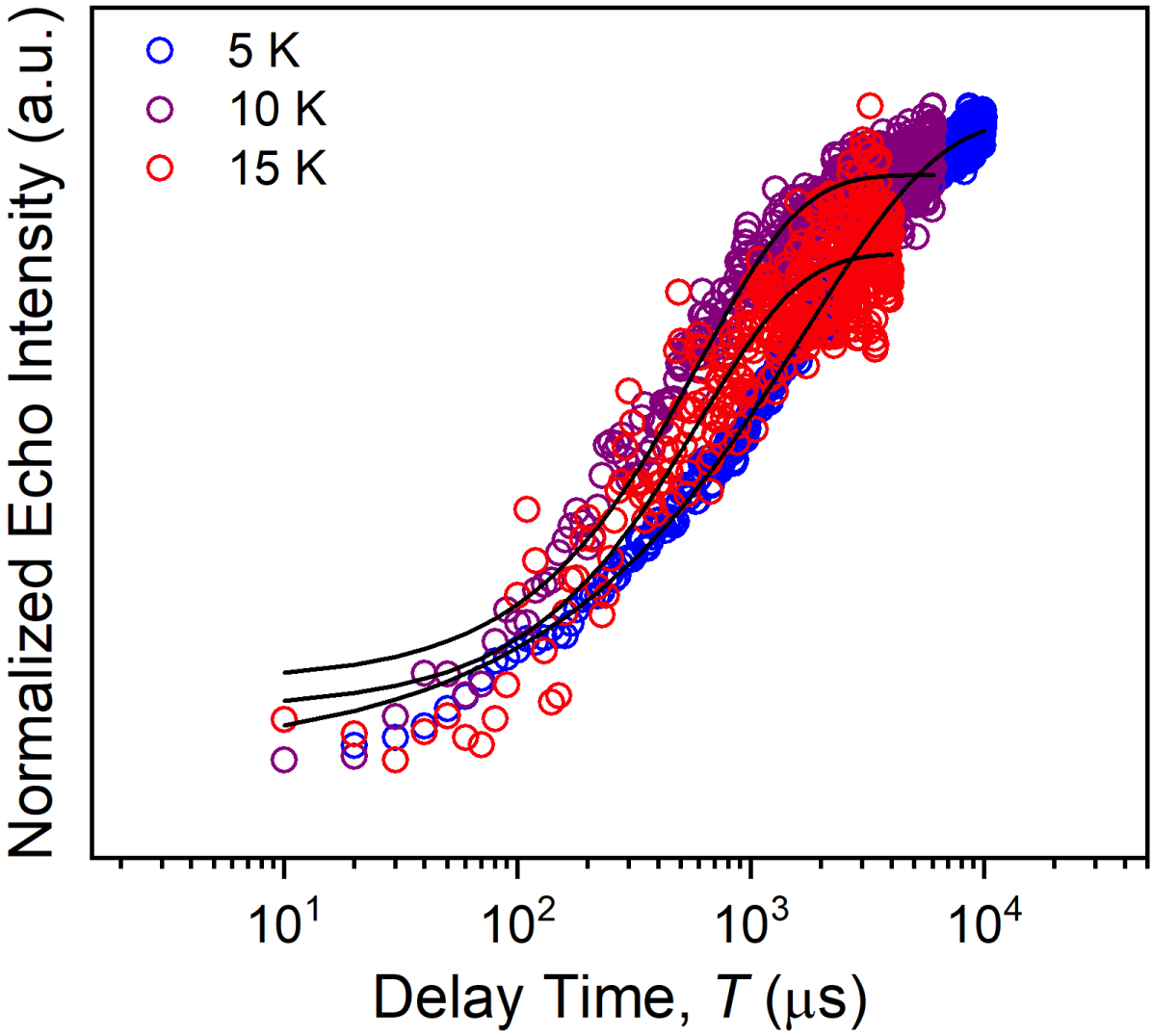

Figure 3.17. Selected variable temperature inversion recovery curves (color traces) and fits (black traces) for **4** in d^{14}-*o*-terphenyl.

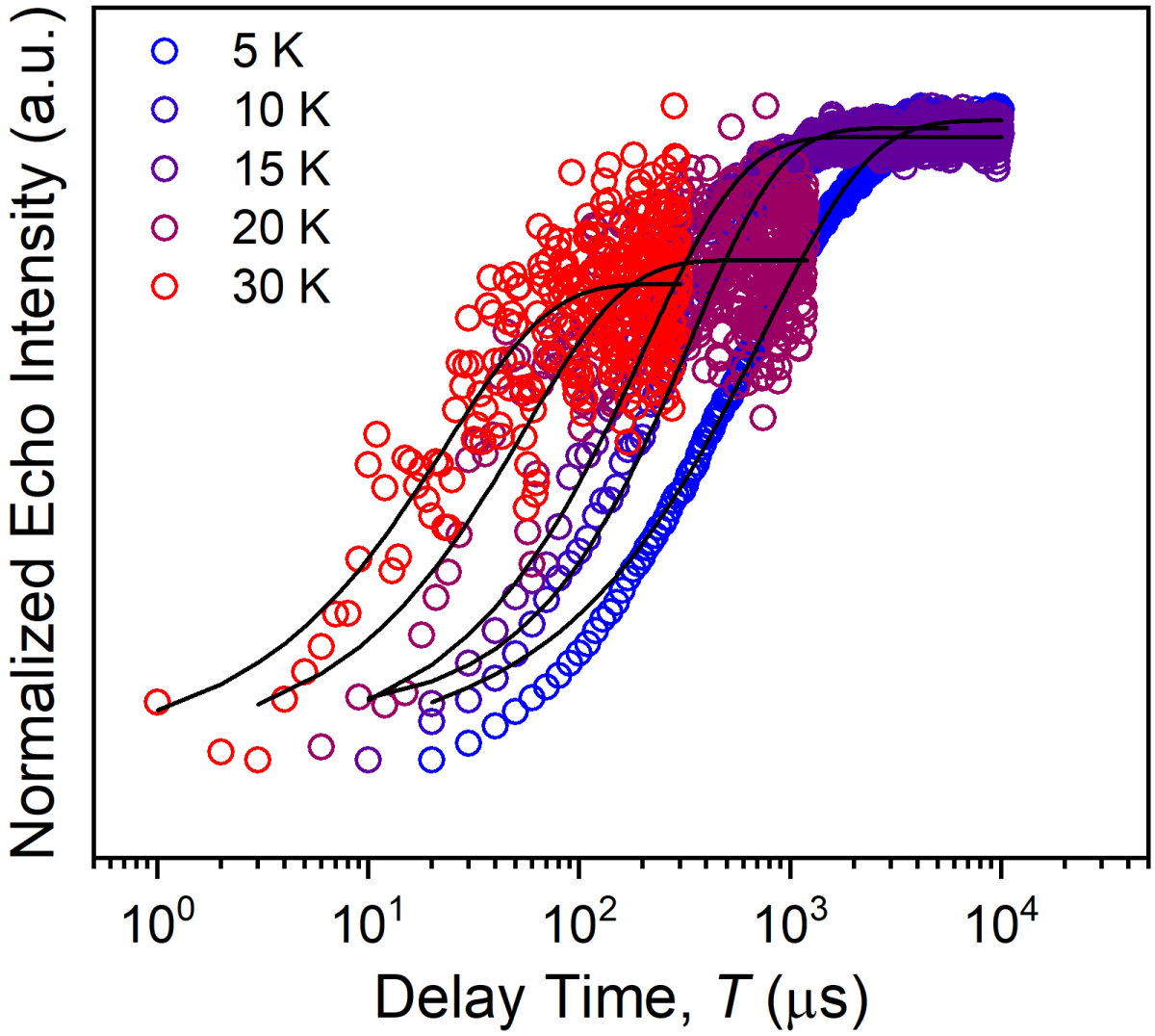

Figure 3.18. Selected variable temperature inversion recovery curves (color traces) and fits (black traces) for **5**.

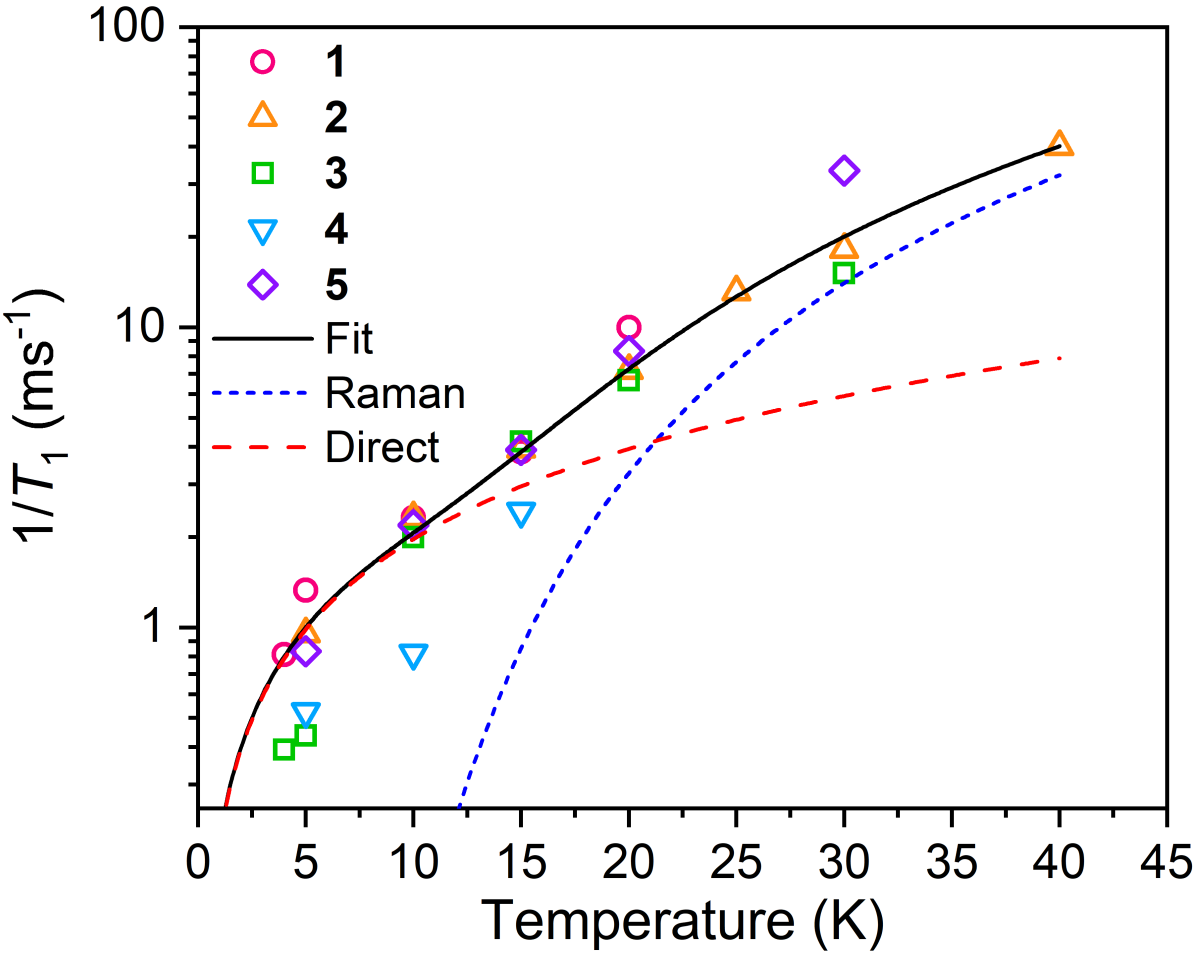

Figure 3.19. Variable temperature T_1 data showing the individual relaxation processes for **1**–**5**. Black line represents the best fit to the data as a sum of the direct and Raman processes. The individual components are shown in dashed lines. The equation for modelling the temperature dependent T_1 data is in the Electron Paramagnetic Resonance section of the Experimental with the fit parameters in Table 3.6.

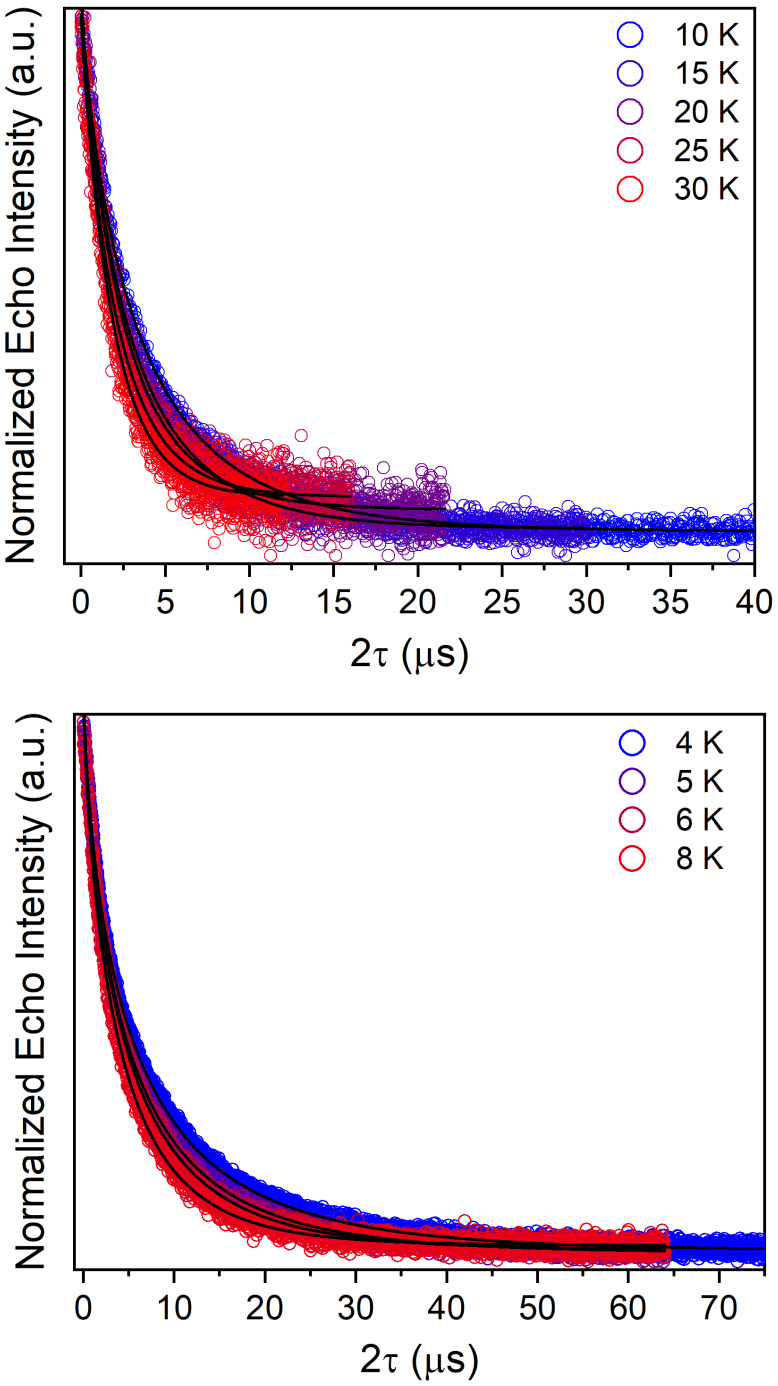

Figure 3.20. Selected variable temperature Hahn echo decay curve (color traces) and fits (black traces) for **1** in d^{14}-*o*-terphenyl at 120 GHz.

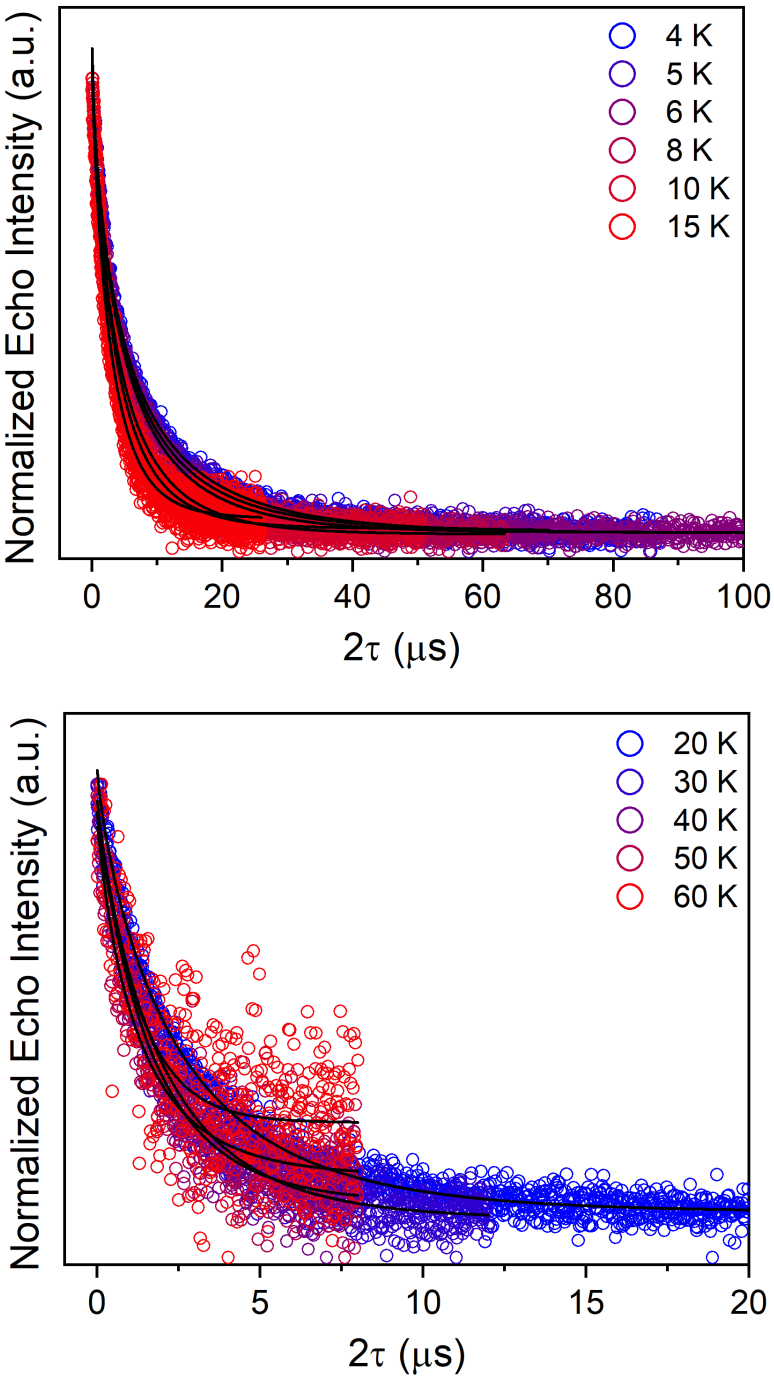

Figure 3.21. Selected variable temperature Hahn echo decay curve (color traces) and fits (black traces) for **2** in d^{14}-*o*-terphenyl at 120 GHz.

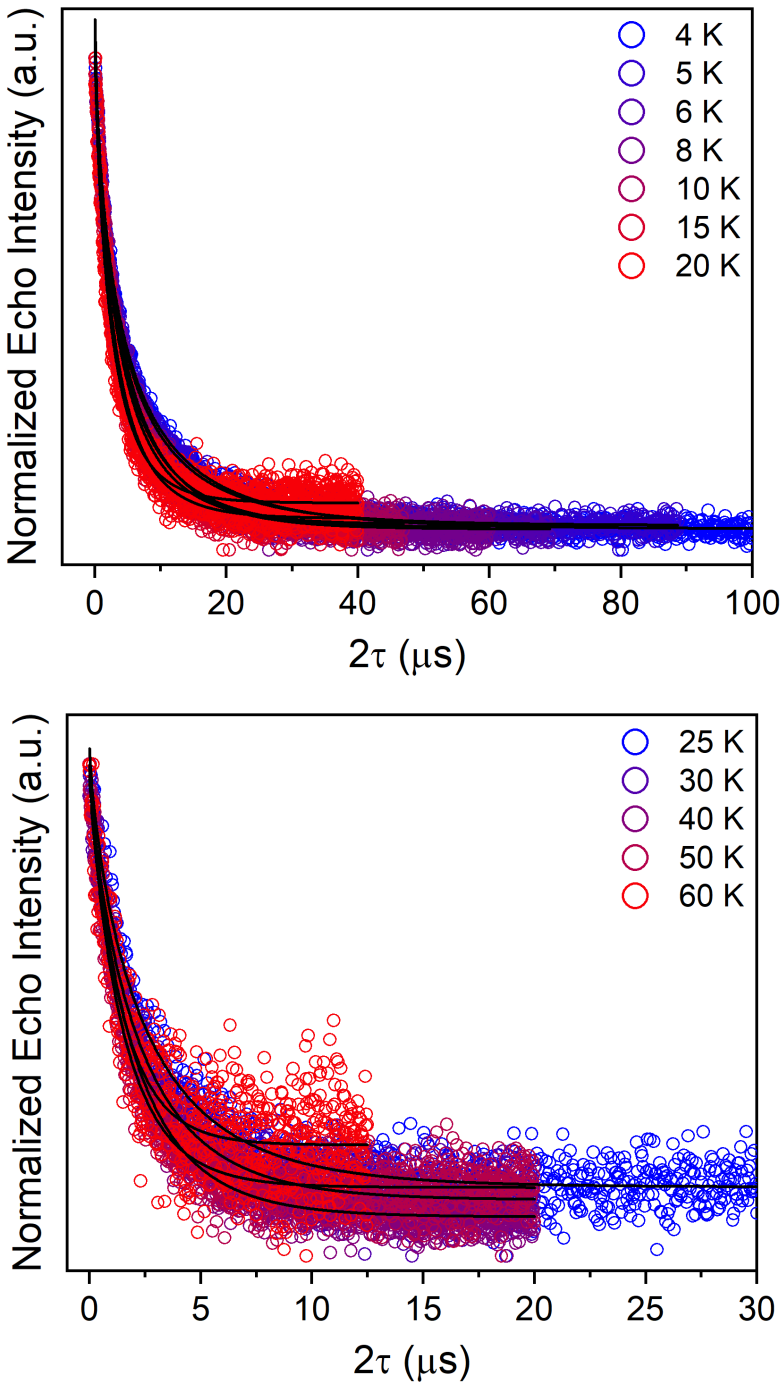

Figure 3.22. Selected variable temperature Hahn echo decay curve (color traces) and fits (black traces) for **3** in d^{14}-*o*-terphenyl at 120 GHz.

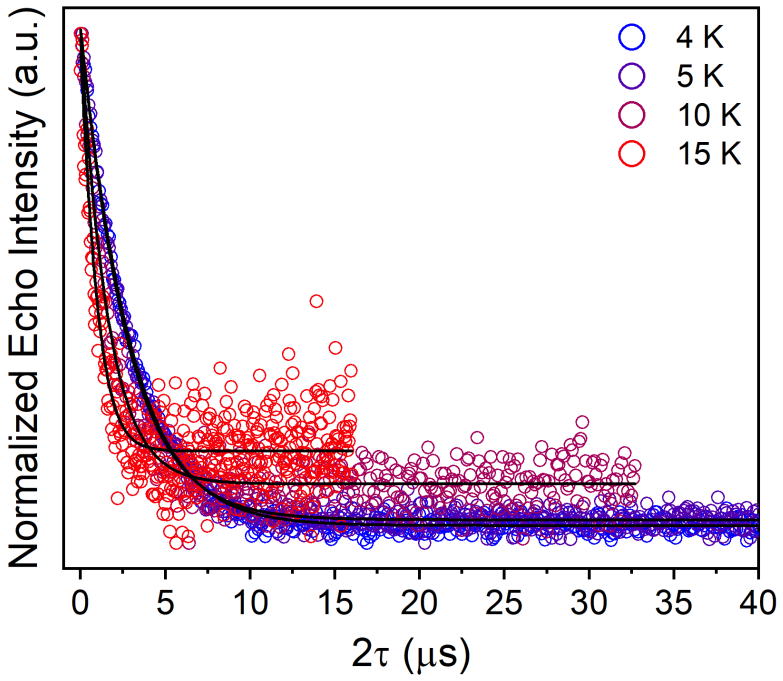

Figure 3.23. Selected variable temperature Hahn echo decay curve (color traces) and fits (black traces) for **4** in d^{14}-*o*-terphenyl at 120 GHz.

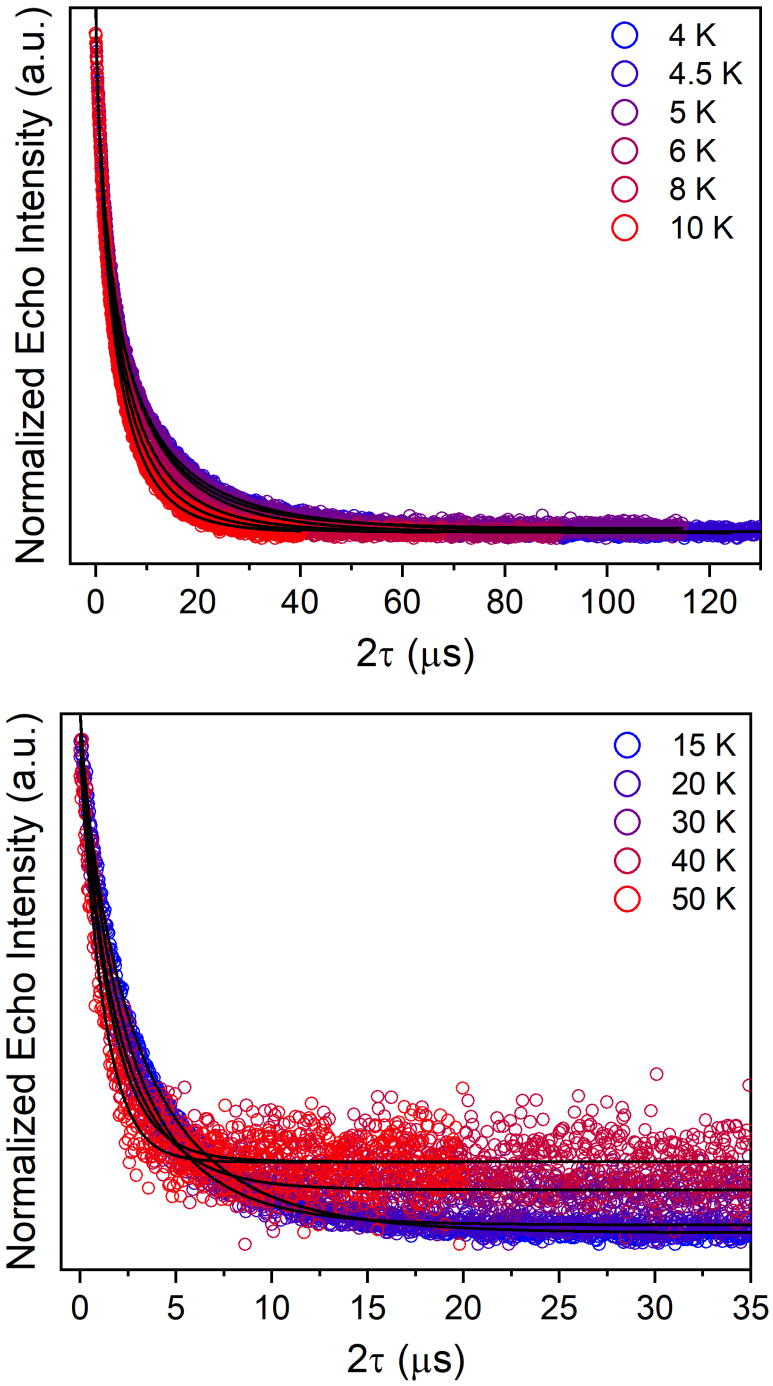

Figure 3.24. Selected variable temperature Hahn echo decay curve (color traces) and fits (black traces) for **5** in d^{14}-*o*-terphenyl at 120 GHz.

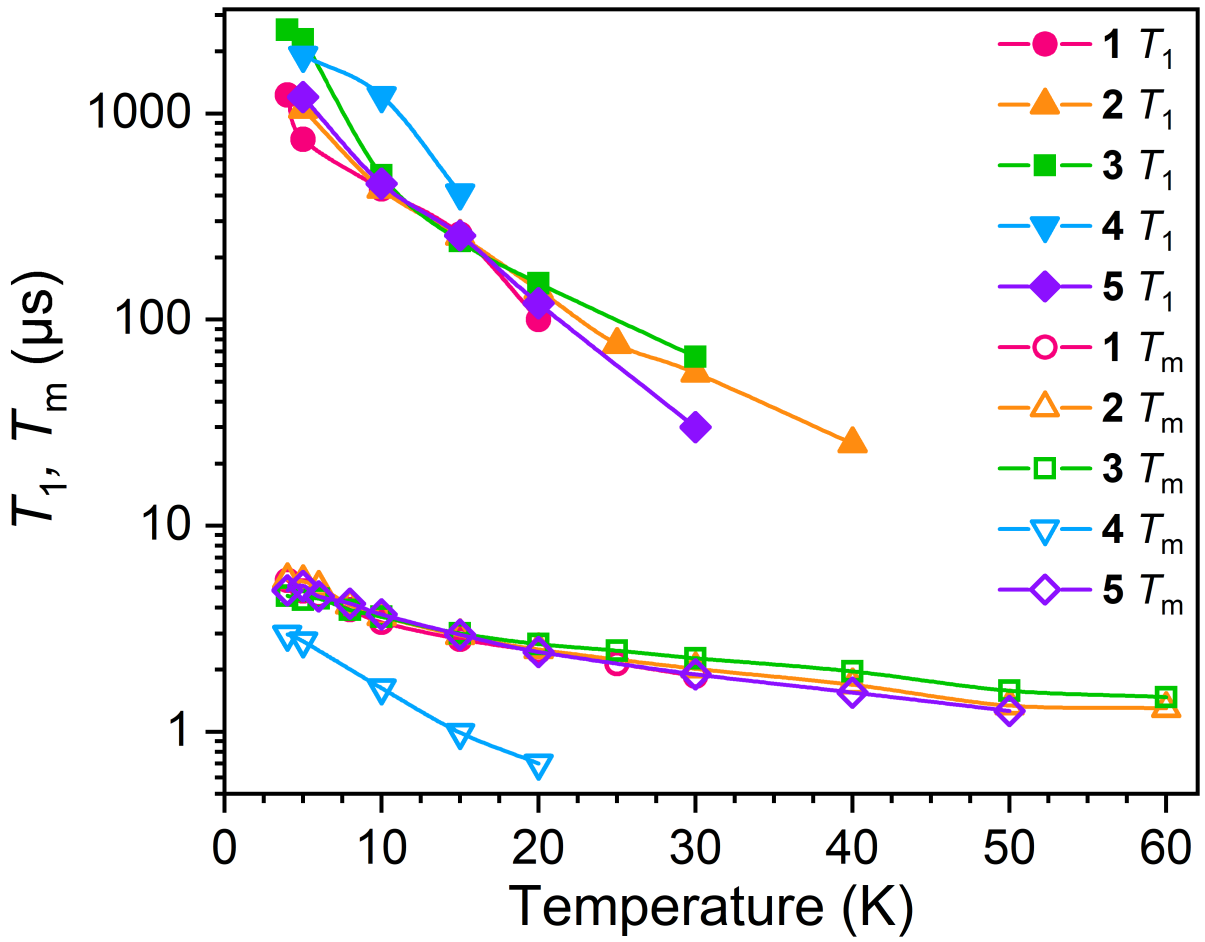

Figure 3.25. Variable temperature T_1 and T_m plot for **1**–**5**.

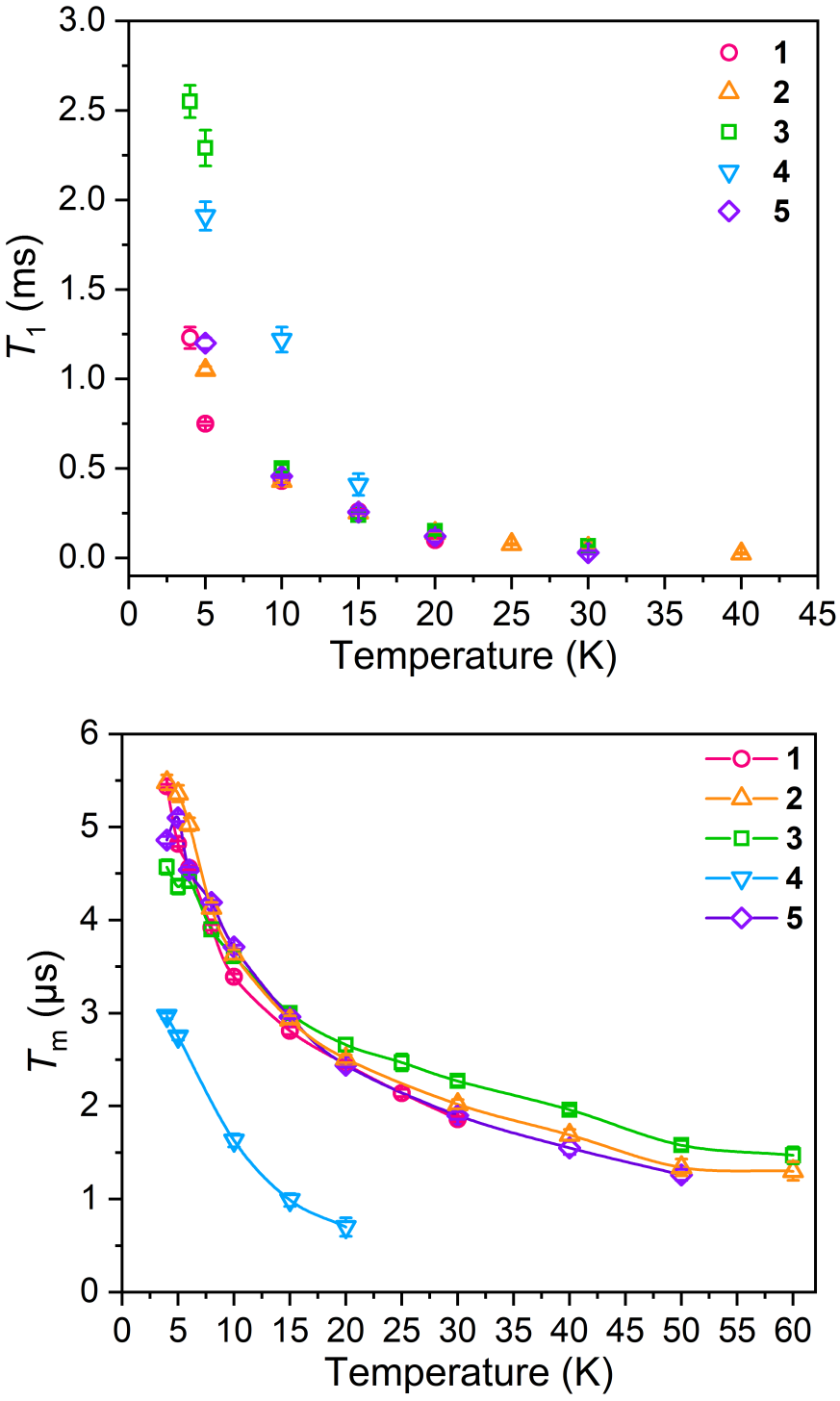

Figure 3.26. Variable temperature T_1 (**top**) plot for **1**–**5** with the error in T_1 shown. Variable temperature T_m (**bottom**) plot for **1**–**5** with error in T_m shown.

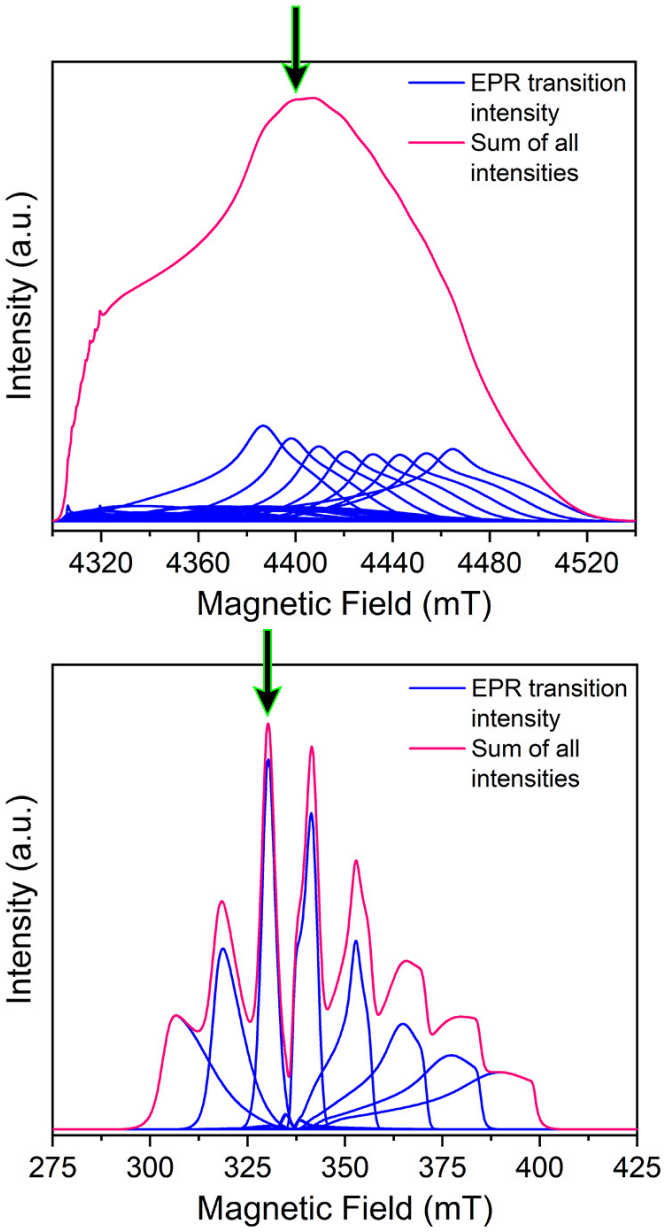

Figure 3.27. Comparison of probed transitions at X-band and 120 GHz. The glowing black arrow indicates the field of analysis. **Top:** Individual transitions that combine to yield the X-band spectrum. **Bottom:** Separate transitions at 120 GHz for **1** using the *g* and A values listed in Table 3.5. Transitions were simulated using Easyspin. The pink lines in both plots represent the sums of the intensities of all the simulated transitions for that frequency.

References

1 M. C. Heffern, L. M. Matosziuk and T. J. Meade, *Chem. Rev.*, **2014**, *114*, 4496–4539.

2 G. Tircs and Z. Baranyai, The Chemistry of Contrast Agents in Medical Magnetic Resonance Imaging Stability and Toxicity of Contrast Agents, John WIley & Sons, 2013.

3 M. J. Graham, J. M. Zadrozny, M. S. Fataftah and D. E. Freedman, *Chem. Mater.*, **2017**, *29*, 1885–1897.

4 M. Affronte, F. Troiani, A. Ghirri, A. Candini, M. Evangelisti, V. Corradini, S. Carretta, P. Santini, G. Amoretti, F. Tuna, G. Timco and R. E. P. Winpenny, *J. Phys. D. Appl. Phys.*, **2007**, *40*, 2999–3004.

5 G. Aromí, D. Aguilà, P. Gamez, F. Luis and O. Roubeau, *Chem. Soc. Rev.*, **2012**, *41*, 537–546.

6 F. Troiani and M. Affronte, *Chem. Soc. Rev.*, **2011**, *40*, 3119.

7 L. Escalera-Moreno, J. J. Baldoví, A. Gaita-Ariño and E. Coronado, *Chem. Sci.*, **2018**, *9*, 3265–3275.

8 P. C. E. Stamp and A. Gaita-Ariño, *J. Mater. Chem.*, **2009**, *19*, 1718–1730.

9 A. Gaita-Ariño, F. Luis, S. Hill and E. Coronado, *Nat. Chem.*, **2019**, *11*, 301–309.

10 R. E. P. Winpenny, *Angew. Chem. Int. Ed.*, **2008**, *47*, 7992–7994.

11 M. A. Nielsen and I. L. Chuang, Quantum Computation and Quantum Information, Cambridge University Press, Cambridge, 2010.

12 L. J. Berliner, G. R. Eaton and S. S. Eaton, Distance Measurements in Biological Systems by EPR, Springer US, 2002.

13 S. K. Misra, Multifrequency Electron Paramagnetic Resonance: Theory and Applications, Wiley-VCH, 2011.

14 S. S. Eaton, G. R. Eaton and L. J. Berliner, Biomedical EPR. Part A, Free radicals, Metals, Medicine and Physiology, Springer, 2011.

15 D. Goldfarb and S. Stoll, EPR Spectroscopy: Fundamentals and Methods, Wiley, 2018 .

16 K. Bader, S. H. Schlindwein, D. Gudat and J. van Slageren, *Phys. Chem. Chem. Phys.*, **2017**, *19*, 2525–2529.

17 K. Bader, D. Dengler, S. Lenz, B. Endeward, S.-D. Jiang, P. Neugebauer and J. van Slageren, *Nat. Commun.*, **2014**, *5*, 5304.

18 J. J. L. Morton, A. M. Tyryshkin, A. Ardavan, K. Porfyrakis, S. A. Lyon and G. A. D. Briggs, *Phys. Rev. B*, **2007**, *76*, 085418.

19 C. J. Wedge, G. A. Timco, E. T. Spielberg, R. E. George, F. Tuna, S. Rigby, E. J. L. McInnes, R. E. P. Winpenny, S. J. Blundell and A. Ardavan, *Phys. Rev. Lett.*, **2012**, *108*, 107204.

20 A. Ardavan, O. Rival, J. J. L. Morton, S. J. Blundell, A. M. Tyryshkin, G. A. Timco and R. E. P. Winpenny, *Phys. Rev. Lett.*, **2007**, *98*, 057201.

21 G. R. Eaton and S. S. Eaton, in Characterization of Materials, John Wiley & Sons, Inc., Hoboken, NJ, USA, 2012, pp. 1–13.

22 S. S. Eaton and G. R. Eaton, in eMagRes, John Wiley & Sons, Ltd, Chichester, UK, 2016, pp. 1543–1556.

23 S. Lenz, K. Bader, H. Bamberger and J. van Slageren, *Chem. Commun.*, **2017**, *53*, 4477–4480.

24 W. M. Witzel and S. Das Sarma, *Phys. Rev. B*, **2007**, *76*, 241303.

25 W. M. Witzel, R. de Sousa and S. Das Sarma, *Phys. Rev. B*, **2005**, *72*, 161306.

26 W. M. Witzel and S. Das Sarma, *Phys. Rev. B*, **2006**, *74*, 035322.

27 J. M. Zadrozny, J. Niklas, O. G. Poluektov and D. E. Freedman, *ACS Cent. Sci.*, **2015**, *1*, 488–492.

28 C.-J. Yu, M. J. Graham, J. M. Zadrozny, J. Niklas, M. D. Krzyaniak, M. R. Wasielewski, O. G. Poluektov and D. E. Freedman, *J. Am. Chem. Soc.*, **2016**, *138*, 14678–14685.

29 G. Balasubramanian, P. Neumann, D. Twitchen, M. Markham, R. Kolesov, N. Mizuochi, J. Isoya, J. Achard, J. Beck, J. Tissler, V. Jacques, P. R. Hemmer, F. Jelezko and J. Wrachtrup, *Nat. Mater.*, **2009**, *8*, 383–387.

30 G. Wolfowicz, A. M. Tyryshkin, R. E. George, H. Riemann, N. V. Abrosimov, P. Becker, H.-J. Pohl, M. L. W. Thewalt, S. A. Lyon and J. J. L. Morton, *Nat. Nanotechnol*., **2013**, *8*, 561–564.

31 A. M. Ariciu, D. H. Woen, D. N. Huh, L. Nodaraki, A. Kostopoulos, C. Goodwin, N. Chilton, E. J. L. Mcinnes, R. Winpenny, W. J. Evans and F. Tuna, *Nat. Commun.*, **2019**, *10*, 3330-3337.

32 J. Yang, Y. Wang, Z. Wang, X. Rong, C.-K. Duan, J.-H. Su and J. Du, *Phys. Rev. Lett.*, **2012**, *108*, 230501.

33 F. Moro, D. Kaminski, F. Tuna, G. F. S. Whitehead, G. A. Timco, D. Collison, R. E. P. Winpenny, A. Ardavan and E. J. L. McInnes, *Chem. Commun.*, **2014**, *50*, 91–93.

34 G. Mitrikas, Y. Sanakis, C. P. Raptopoulou, G. Kordas and G. Papavassiliou, *Phys. Chem. Chem. Phys.*, **2008**, *10*, 743–748.

35 M. Warner, S. Din, I. S. Tupitsyn, G. W. Morley, A. M. Stoneham, J. A. Gardener, Z. Wu, A. J. Fisher, S. Heutz, C. W. M. Kay and G. Aeppli, *Nature*, **2013**, *503*, 504–508.

36 K. S. Pedersen, A.-M. Ariciu, S. McAdams, H. Weihe, J. Bendix, F. Tuna and S. Piligkos, *J. Am. Chem. Soc.*, **2016**, *138*, 5801–5804.

37 D. Aguilà, L. A. Barrios, V. Velasco, O. Roubeau, A. Repollés, P. J. Alonso, J. Sesé, S. J. Teat, F. Luis and G. Aromí, *J. Am. Chem. Soc.*, **2014**, *136*, 14215–14222.

38 M. Shiddiq, D. Komijani, Y. Duan, A. Gaita-Ariño, E. Coronado and S. Hill, *Nature*, **2016**, *531*, 348–351.

39 M. S. Fataftah, J. M. Zadrozny, S. C. Coste, M. J. Graham, D. M. Rogers and D. E. Freedman, *J. Am. Chem. Soc.*, **2016**, *138*, 1344–1348.

40 C.-Y. Lin, T. Ngendahimana, G. R. Eaton, S. S. Eaton and J. M. Zadrozny, *Chem. Sci.*, **2019**, *10*, 548–555.

41 M. Atzori, S. Benci, E. Morra, L. Tesi, M. Chiesa, R. Torre, L. Sorace and R. Sessoli, *Inorg. Chem.*, **2018**, *57*, 731–740.

42 S. Lenz, H. Bamberger, P. P. Hallmen, Y. Thiebes, S. Otto, K. Heinze and J. van Slageren, *Phys. Chem. Chem. Phys.*, **2019**, *21*, 6976–6983.

43 M. Atzori, E. Morra, L. Tesi, A. Albino, M. Chiesa, L. Sorace and R. Sessoli, *J. Am. Chem. Soc.*, **2016**, *138*, 11234–11244.

44 G. R. Eaton and S. S. Eaton, *J. Magn. Reson.*, **1999**, *136*, 63–68.

45 J. J. Baldoví, S. Cardona-Serra, J. M. Clemente-Juan, E. Coronado, A. Gaita-Ariño and H. Prima-García, *Chem. Commun.*, **2013**, *49*, 8922.

46 K. Bader, M. Winkler and J. van Slageren, *Chem. Commun.*, **2016**, *52*, 3623–3626.

47 M. J. Martínez-Pérez, S. Cardona-Serra, C. Schlegel, F. Moro, P. J. Alonso, H. Prima-García, J. M. Clemente-Juan, M. Evangelisti, A. Gaita-Ariño, J. Sesé, J. van Slageren, E. Coronado and F. Luis, *Phys. Rev. Lett.*, **2012**, *108*, 247213.

48 C. Schlegel, J. van Slageren, M. Manoli, E. K. Brechin and M. Dressel, *Phys. Rev. Lett.*, **2008**, *101*, 147203.

49 J. P. S. Walsh, S. B. Meadows, A. Ghirri, F. Moro, M. Jennings, W. F. Smith, D. M. Graham, T. Kihara, H. Nojiri, I. J. Vitorica-Yrezabal, G. A. Timco, D. Collison, E. J. L. McInnes and R. E. P. Winpenny, *Inorg. Chem.*, **2015**, *54*, 12019–12026.

50 J. Ferrando-Soria, E. Moreno Pineda, A. Chiesa, A. Fernandez, S. A. Magee, S. Carretta, P. Santini, I. J. Vitorica-Yrezabal, F. Tuna, G. A. Timco, E. J. L. McInnes and R. E. P. Winpenny, *Nat. Commun.*, **2016**, *7*, 11377.

51 A. J. Fielding, S. Fox, G. L. Millhauser, M. Chattopadhyay, P. M. H. Kroneck, G. Fritz, G. R. Eaton and S. S. Eaton, *J. Magn. Reson.*, **2006**, *179*, 92–104.

52 Y. Krupskaya, R. Zaripov, E. Vavilova, V. Miluykov, I. Bezkishko, D. Krivolapov, O. Kataeva, O. Sinyashin, E. Hey-Hawkins, V. Voronkova, K. Salikhov, V. Kataev and B. Büchner, *Phys. Rev. B*, **2011**, *84*, 092402.

53 A. L. Falk, B. B. Buckley, G. Calusine, W. F. Koehl, V. V. Dobrovitski, A. Politi, C. A. Zorman, P. X.-L. Feng and D. D. Awschalom, *Nat. Commun.*, **2013**, *4*, 1819.

54 J. R. Weber, W. F. Koehl, J. B. Varley, A. Janotti, B. B. Buckley, C. G. Van de Walle and D. D. Awschalom, *J. Appl. Phys.*, **2011**, *109*, 102417.

55 W. F. Koehl, B. B. Buckley, F. J. Heremans, G. Calusine and D. D. Awschalom, *Nature*, **2011**, *479*, 84–87.

56 J. R. Rumble, D. R. Lide and T. J. Bruno, CRC Handbook of Chemistry and Physics: a Ready-Reference Book of Chemical and Physical Data, 99th Edition; CRC Press: Boca Raton, 2018.

57 G. Pacchioni, *Nat. Rev. Mater.*, **2017**, *2*, 17052.

58 M. J. Graham, C.-J. Yu, M. D. Krzyaniak, M. R. Wasielewski and D. E. Freedman, *J. Am. Chem. Soc.*, **2017**, *139*, 3196–3201.

59 S. R. Cooper, Y. B. Koh and K. N. Raymond, *J. Am. Chem. Soc.*, **1982**, *104*, 5092–5102.

60 M. Branca, G. Micera, A. Dessi, D. Sanna and K. N. Raymond, *Inorg. Chem.*, **1990**, *29*, 1586–1589.

61 C. Milsmann, A. Levina, H. H. Harris, G. J. Foran, and P. Turner and P. A. Lay , *Inorg. Chem.,* **2006**, *45*, 4743–4754.

62 B. A. Borgias, S. R. Cooper, Y. B. Koh and K. N. Raymond, *Inorg. Chem.*, **1984**, *23*, 1009–1016.

63 S. Alvarez, P. Alemany, D. Casanova, J. Cirera, M. Llunell and D. Avnir, *Coord. Chem. Rev.*, **2005**, *249*, 1693–1708.

64 S. Alvarez, D. Avnir, M. Llunell and M. Pinsky, *New J. Chem.*, **2002**, *26*, 996–1009.

65 N. J. Stone, *At. Data Nucl. Data Tables*, **2005**, *90*, 75–176.

66 S. Stoll and A. Schweiger, *J. Magn. Reson.* **2006**, *178*, 42-55.

67 J. Telser, J. Krzystek and A. Ozarowski, *J. Biol. Inorg. Chem.*, **2014**, *19*, 297–318.

68 J. van Tol, G. W. Morley, S. Takahashi, D. R. McCamey, C. Boehme and M. E. Zvanut, *Appl. Magn. Reson.*, **2009**, *36*, 259–268.

69 S. Takahashi, R. Hanson, J. van Tol, M. S. Sherwin and D. D. Awschalom, *Phys. Rev. Lett.*, **2008**, *101*, 047601.

70 B. N. Figgis and M. A. Hitchman, Ligand Field Theory and Its Applications, Wiley-VCH, 2000.
71 D. Gatteschi and R. Sessoli, *Angew. Chem. Int. Ed.*, **2003**, *42*, 268–297.
72 E. L. Hahn, A. Abragam and D. M. S. Bagguley, Pulsed Magnetic Resonance: NMR, ESR, and Optics: A Recognition of E.L. Hahn, Clarendon Press, 1992.
73 L. M. Jackman; S. Sternhell, Application of Nuclear Magnetic Resonance Spectroscopy in Organic Chemistry, 2nd ed.; Pergamon press: New York, 1969.
74 S. Takahashi, I. S. Tupitsyn, J. van Tol, C. C. Beedle, D. N. Hendrickson and P. C. E. Stamp, *Nature*, **2011**, *476*, 76–79.
75 T. D. Ladd, D. Press, K. De Greve, P. L. McMahon, B. Friess, C. Schneider, M. Kamp, S. Höfling, A. Forchel and Y. Yamamoto, *Phys. Rev. Lett.*, **2010**, *105*, 107401.
76 N. V Prokof'ev and P. C. E. Stamp, *Reports Prog. Phys.*, **2000**, *63*, 669–726.
77 P. C. E. Stamp, *Stud. Hist. Philos. Mod. Phys.*, **2006**, *37*, 467–497.
78 C. Dalvit and A. Vulpetti, *J. Med. Chem.*, **2019**, *62*, 2218–2244.
79 A. H. Schmieder, S. D. Caruthers, J. Keupp, S. A. Wickline and G. M. Lanza, *Engineering*, **2015**, *1*, 475–489.
80 H. Kovacs and Ē. Kupče, *Magn. Reson. Chem.*, **2016**, *54*, 544–560.
81 Bryant, B. E.; Fernelius, W. C.; Busch, D. H.; Stoufer, R. C.; Stratton, W. Vanadium(IV) Oxy(Acetylacetonate). In Inorganic Syntheses; 1957; Vol. 5, pp 113–116.
82 Saikia, B.; Borah, P.; Chandra Barua, N. H_2O_2 in WEB: A Highly Efficient Catalyst System for the Dakin Reaction. *Green Chem.* **2015**, *17*, 4533–4536.
83 Kohn, M. Bromination of Catechol. *J. Am. Chem. Soc.*, **1951**, *73*, 480–480.
84 Sheldrick, G. M. Program for Empirical Absorption Correction of Area Detector Data. SADABS 1996.
85 Sheldrick, G. M. *Acta Crystallogr. Sect. Found. Adv.* **2015**, *71*, 3–8.
86 Sheldrick, G. M. *Acta Crystallogr. Sect. C Struct.* Chem. 2015, 71 (1), 3–8.
87 Sheldrick, G. M. *Acta Crystallogr. A* **2008**, *64*, 112–122.
88 Stoll, S.; Schweiger, A. EasySpin, *J. Magn. Reson.* **2006**, *178*, 42–55.
89 Van Tol, J.; Brunel, L.-C.; Wylde, R. J. *Rev. Sci. Instrum.* **2005**, *76*, 074101.
90 Morley, G. W.; Brunel, L.-C.; van Tol, J. *Rev. Sci. Instrum.* **2008**, *79*, 064703.
91 Matlab; The MathWorks Inc.: Natick, MA, 2018.
92 Origin; OriginLab: Northampton, MA, 2018.

CHAPTER 4 – ORIENTATION DEPENDENCE OF PHASE MEMORY RELAXATION IN THE V(IV) ION AT HIGH FREQUENCIES

Overview

Understanding how magnetic relaxation depends on molecular orientation is a fundamental parameter for designing magnetic molecules for application. Herein we report the first use of pulsed high-frequency electron paramagnetic resonance spectroscopy (HFEPR, 120 and 240 GHz) to define the orientation dependence of phase memory relaxation in the $S = {}^1/_2$ V(IV) complex $(n\text{-}Bu_3NH)_2[V(C_6H_4O_2)_3]$. We demonstrate a variation of 20 % of the phase memory relaxation time (T_m) as a function of the orientation of the $[V(C_6H_4O_2)_3]^{2-}$ molecule in the applied magnetic field. Ultimately, this work underlines an important design strategy for molecule-based quantum computing architectures.

Introduction

Molecular qubits are a potential centrepiece in next stage quantum information processing and sensing schemes.[1–4] Molecular species are highly tuneable platforms for gaining insight into engineering long-lived superpositions. Indeed, spin-based superpositions can be engineered via molecular design to be exceedingly stable in these molecular species as indicated by phase-memory relaxation times (T_m) on millisecond timescales.[5,6] Prominent proposals for building actual molecule-scale quantum computers to seize upon these discoveries are predominantly surface-based.[7–10] Here, qubits are oriented in precise arrays to encourage entanglement and individual manipulation, effectively generating small test-scale spin-based quantum computing devices. Toward this goal, understanding molecular qubit properties upon surface deposition is essential.[7–13]

One important piece of that information pertains to the orientation of the molecule on the surface. Designing surface-based molecular computers hinges on knowing precisely how magnetic orientation affects properties. Indeed, many recent reports propose extremely precise surface orientations of metal ions,[14,15] or highly structurally anisotropic metal complexes that could be readily envisioned to lodge onto surface materials.[6,11,12,16] Yet, orientation-dependent studies of spin-based properties are relatively rare in the present explosion of interest in metal-ion molecular qubits, despite their necessity in identifying the optimal orientations to target.

In this manuscript, we use high-field/high-frequency (120 and 240 GHz) electron paramagnetic resonance for the first time to define how molecular orientation affects T_m in the candidate molecular qubit (n-$Bu_3NH)_2[V(C_6H_4O_2)_3]$ (**1**) (Fig. 4.1).[17] HFEPR enables the high resolution of resonances from molecules at specific alignments in magnetic field (when g_z, g_x, and g_y are coincident with B_0).[18] This resolution is higher than typically possible at the frequencies of conventional EPR (X-band, ca. 3500 G), wherein other magnetic interactions (e.g. hyperfine coupling or zero-field splitting) engender overlapping peaks. Hence, HFEPR is indispensable for

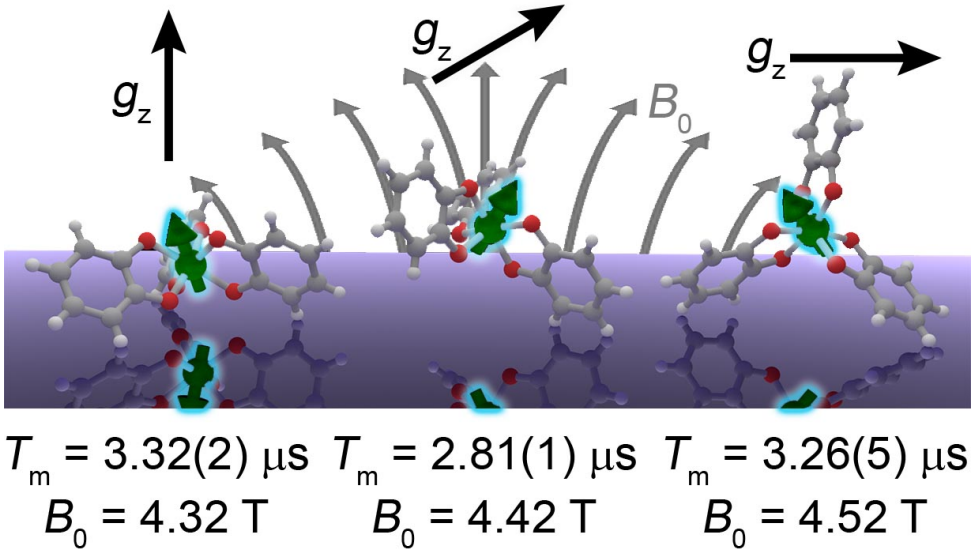

Fig 4.1. Graphical depiction of orientation dependence of phase memory relaxation in $[V(C_6H_4O_2)_3]^{2-}$ relative to B_0. Selected T_m values are shown under select orientations of **1**, as determined from frozen-solution spectra.

orientation-dependent investigations of T_m. Furthermore, high fields enhance spin polarization,[19,20] facilitate qubit initialization,[21] suppress environmental magnetic noise,[22] and are typical for dynamic nuclear polarization (DNP).[23,24] These points underscore the broader importance of using the technique to understand the high-field magnetic properties of molecular qubits, particularly containing metal ions.

We focus on the extremely promising V(IV) ion – molecular qubits of V(IV) enable synthetic control, long-lived phase memory relaxation (T_m), and long spin-lattice relaxation times (T_1) in select species, e.g. $[V(C_8S_8)_3]^{2-}$.[5,6,25–30] Yet, to the best of our knowledge, only one previous report of the coherent spin dynamics of V(IV) properties at high field exists.[28] Hence, the impact of both the chemical environment and molecular orientation on V(IV) electron spin coherence at high field remains untested – critical information to design future qubits using this ion. Herein we use **1** for an initial test of orientation dependence at high field, not because of a unique or large T_m, but because of the well-studied nature of its low-field relaxation and, hence, facility of comparison with the present high-field conditions.[25,28,29] These studies demonstrate a smaller T_m-dependence on solvent deuteration at high field for the V(IV) ion (relative to low field). Furthermore, we demonstrate a significant change in T_m (ca. 20%) as a function of orientation. Importantly, our results reveal the highest T_m for canonical orientations (Fig. 4.1). These results, the first of which for a V(IV) complex, support many of the recent surface-based proposals for highly oriented molecules in spin-based quantum computing architecture.[10,15]

Methods

General Considerations. The complex $(n\text{-}Bu_3NH)_2[V(C_6H_4O_2)_3]$ (**1**) was reported to be air-sensitive.[29] Thus, all manipulations and syntheses of it were performed under a N_2 atmosphere with either a Vigor glovebox or Schlenk techniques. Both *o*-terphenyl (98%, Alfa Aesar) and d^{14}-*o*-terphenyl (98% ^2H, Cambridge isotopes) were used as received. The complex $(n\text{-}Bu_3NH)_2[V(C_6H_4O_2)_3]$ (**1**) was prepared following the literature procedures.[29]

Electron Paramagnetic Resonance Measurements. EPR spectra collected herein were simulated using Easyspin[31] with the function pepper (frozen solution and solid) and were refined using simulations of the experimental data. All samples were prepared under an inert atmosphere of N_2. Sample **1** for pulsed EPR studies (1 mM) were prepared by first loading 20 μL 1 mM THF solution of **1** by a micropipette into a 4 mm OD quartz EPR tube. Following removal of THF under reduced pressure, 0.0232 g o-terphenyl or 0.0258 g deuterated o-terphenyl (20 μL when molten) was loaded into the same tube. These tubes were flame sealed under dynamic vacuum (< 50 mTorr) and placed in a 65−70 °C oil bath until a clear dark blue solution formed. Sample tubes prepared in this manner can be stored at room temperature for an extended period without compound decomposition, but the OTP will slowly crystallize. Hence, prior to each measurement, the samples were remelted and refrozen to produce a high-quality glass.

All pulsed EPR data were collected at the National High Magnetic Field Laboratory (NHMFL, Tallahassee, FL, USA) on a custom built 120/240/336 GHz EPR spectrometer.[32,33] Sample tubes were gently melted using a heat gun to afford a homogeneous dark blue solution, then quickly inserted into the cold same chamber to ensure glass formation. The collected data were processed using an EPR measurement program locally developed at NHMFL, Matlab 2018b, and Origin Pro 2018b software packages.[34,35]

T_1 data were collected on the most intense resonance of the EDFS spectra at 4.4 T at 120 GHz, via an inversion recovery sequence (π − *T* − π/2 − τ − π − τ − echo). The length of the three pulses, π − π/2 − π, are 900− 600 − 900 ns with a starting *T* value of 10300 ns and τ of 700 ns. The inversion recovery data were fit accounting for spectral diffusion with the following equation:

$$I(t) = -A[e^{\left(-\frac{t}{T_1}+\sqrt{\frac{t}{q}}\right)} - I(0) - 1]$$

Here, *A* is a preexponential factor, T_1 is the spin lattice relaxation time, *t* is the delay following the inversion pulse, *q* is a parameter specifically related to the presence of spectral diffusion,[36] and *I*(0) is the intensity at zero delay. Variable-temperature T_1 data presented challenges in fitting due

to the enhanced relaxation rate of spin-lattice relaxation with 120 GHz frequencies. As a result, measurements were restricted to below 40 K.

T_m data for 120 GHz were collected on the most intense resonance (4.4 T at 120 GHz) in the EDFS spectra via a Hahn echo sequence (π/2 − τ − π − τ − echo) with a 4-step phase cycle with microwave pulses of 600 (π/2) and 900 ns (π) and a starting interpulse delay (τ) of 700 ns. T_m data for 240 GHz were collected on the most intense resonance (8.8 T at 120 GHz) in the EDFS spectra via a Hahn echo sequence (π/2 − τ − π − τ − echo) with a 4-step phase cycle with microwave pulses of 1000 (π/2) and 1200 ns (π) and a starting interpulse time (τ) of 800 ns. The Hahn echo decay data were fit using the stretched exponential equation:

$$I(\tau) = I(0) - Ae^{\left(\frac{2\tau}{T_m}\right)^{\beta}}$$

Here, $I(0)$ is the echo intensity at $\tau = 0$, A is a preexponential factor, τ is the interpulse delay time, T_m is the phase memory relaxation time, and β is the stretch parameter. The low temperature data were better fit with this stretched exponential equation as opposed to a simple monoexponential decay. Indeed, we found that β approached 1 as the temperature increased for our samples, indicating that a conventional single exponential fit could be used. Nevertheless, we used the stretched exponential fit throughout the whole temperature range for consistency.

Owing to the long pulse lengths and 100 ns deadtime, T_m values below 200-300 ns were in general extremely difficult to observe, requiring prohibitively long data acquisition times. This factor limited the temperature range for a usable echo to only the lowest temperatures, hence all analyses generally stopped by 40 K.

Results and Discussion

Echo-detected, field-swept (EDFS) EPR spectra of (*n*-$Bu_3NH)_2[V(C_6H_4O_2)_3]$ (**1**) (Fig 2, Tables 4.5, 4.2) reveal a singular broad peak using 120 and 240 GHz frequencies. As previously shown, these spectra are extremely wide compared to the sharp eight-line spectrum at X-band,

likely attributable to g-strain.[28] Simulation of the spectra are nevertheless possible with the rhombic g (g_x = 1.941, g_y = 1.925, and g_z = 1.992) and A values (A_x = 313, A_y = 363, and A_z = 60 MHz) (Tables 4.1 and 4.2).[28,29] While broad, the spectral signals nevertheless contain important, resolvable features – the sharp, low-field feature results from molecules with g_z aligned to the magnetic field (B_0), while the more intense, high-field feature stems from molecules where $g_{x,y}$ is parallel to B_0. In contrast, at X-band frequencies (B_0 ~ 3400 G), the signals from these three orientations are entirely overlaid.[29]

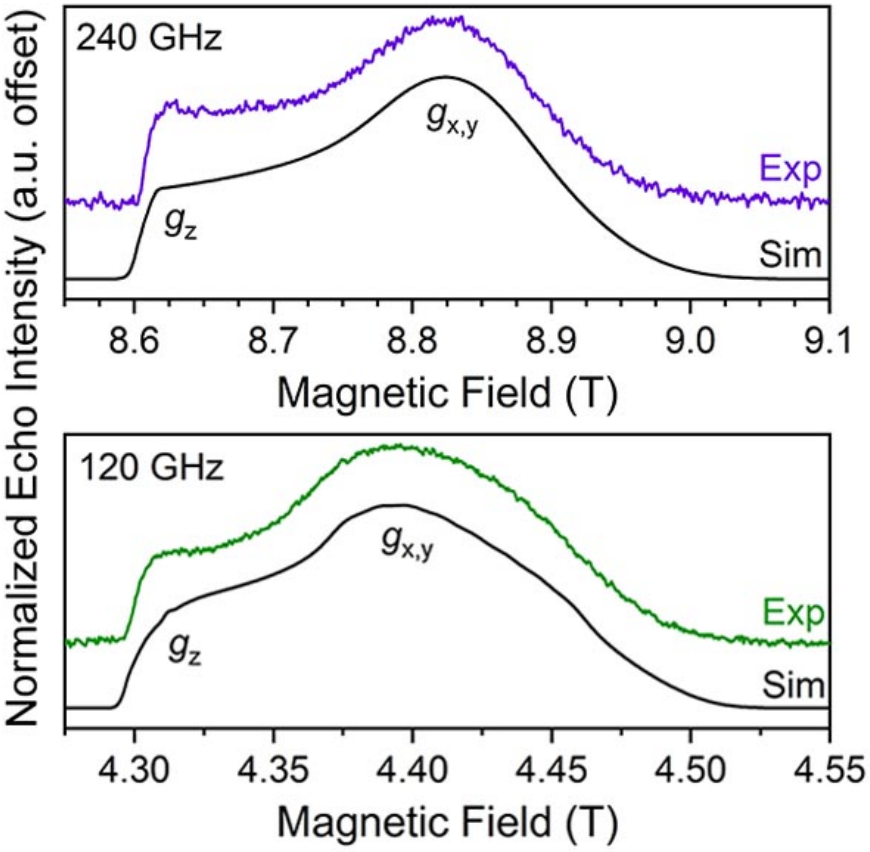

Fig 4.2. Echo-detected, field-swept (EDFS) EPR spectra collected with 120 and 240 GHz microwave radiation at 4 and 4.5 K, respectively. Samples were 1 mM in frozen OTP glass. Coloured lines are experimental data, black lines are simulations for a rhombic system with $g_z > g_x > g_y$, and $A_z < A_x < A_y$ (see main text).

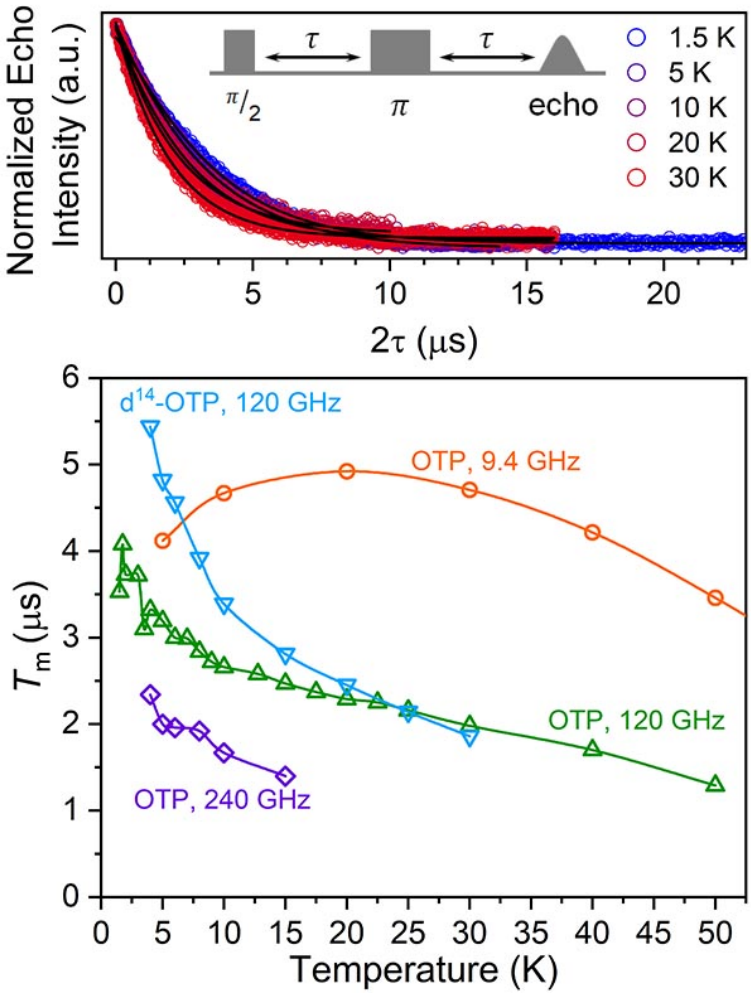

Fig 4.3. (Top) Selected Hahn-echo decay curves (coloured circles) and exponential fit (black trace) for **1** in OTP at 120 GHz. (Bottom) Variable-temperature T_m data at 9.4, 120, and 240 GHz for **1** in OTP or d^{14}-OTP glass. The 9.4 GHz data were taken from refs. 28,29. Error bars are within the width of the data points.

Preliminary evaluation of the spin dynamics of **1** proceeded by analysis of the spin-lattice relaxation times using inversion recovery experiments at the strongest-intensity peak in the EDFS. These experiments were performed at 120 GHz for **1** dissolved to 1 mM concentration in protiated and deuterated *o*-terphenyl (OTP). The values of T_1 are essentially the same between the two matrices (Figs. 4.5-4.6, Table 4.3, 4.4), demonstrating that environmental deuteration impacts T_1 negligibly at these frequencies.

Next, we investigated the temperature and matrix dependence of phase memory time, or T_m. Here, we performed two-pulse Hahn echo experiments at the strongest peak in the EDFS as

a function of temperature (Figs. 4.3, 4.7, 4.8) to extract T_m in OTP and d^{14}-OTP. At 120 GHz and 5 K, T_m of **1** in d^{14}-OTP is 4.82(3) μs and is temperature dependent in the regime measured. When compared to the T_m of **1** in OTP at 120 GHz and 5 K, T_m is shorter with a value of 3.192(9) μs. With increasing temperature T_m drops, reaching the same T_m as **1** in OTP by 25 K. In comparison to both 120 GHz data sets, T_m of **1** in OTP at 240 GHz is relatively much shorter, with a T_m of 2.00(5) μs at 5 K, dropping to 1.40(4) μs at 15 K. When compared to T_m collected at X-band frequency in OTP, we notice a similar T_m of 4.12(3) μs at 5 K, yet T_m here is not as temperature-dependent (Fig 3).[29] Note that these data were successfully fit without a noticeable stretch parameter, implying that methyl group rotation on the counterion is not a governing factor in T_m here (Table 4.5, 4.9).

The temperature and matrix dependence of T_m highlights the environmental role in controlling phase memory relaxation. The use of a deuterated solvent typically increases T_m by a factor of about two or more in metal complexes,[5,37,38] due to the lower nuclear magnetic dipole moment of deuterium (0.86 μ_N) relative to the proton (2.79 μ_N).[39,40] Yet, we observe a slightly smaller enhancement, by a factor of 1.5. This relatively smaller enhancement factor may suggest that other mechanisms of decoherence are operative at high frequency (rather than common interactions with the nuclear spin bath). Indeed, the T_m of the probed spins is strongly temperature dependent in the studied window, potentially highlighting the impact of a short, temperature-dependent T_1 from other V(IV) spins in the sample.[41] However, another factor may be the relatively small density of nuclear spins in OTP (45 $^1H/nm^3$) versus other solvents (e.g. H_2O, 66 $^1H/nm^3$). Furthermore, we do not detect a low temperature downturn of T_m of **1** as was seen when rotation of $–CH_3$ groups on the *n*-Bu_3NH^+ counterions directed T_m.[29] Finally, T_m decreases from 120 to 240 GHz in the same sample, in trend with the expected field dependence of T_1 for this ion.[28]

The nearly 0.3 T separation of signals from $[V(C_6H_4O_2)_3]^{2-}$ molecules with g_z oriented parallel and perpendicular to the magnetic field suggested that HFEPR would be ideal for testing

the orientation dependence of T_m. This prospect is especially tantalizing relative to conventional X-band EPR, where peaks corresponding to different orientations are extremely close (~0.01 T) and overlap. Since **1** is approximately axial, we hypothesized that T_m would be longer where g_z for $[V(C_6H_4O_2)_3]^{2-}$ is parallel or perpendicular to B_0. Indeed, simulations of the resonant field (B) as a function of angle between g_z and B_0 (θ) suggested a stable EPR frequency to small motions at these alignments (i.e. dB/dθ is small, Fig. 4.4). As small changes in resonant frequency induce relaxation, orientations where dB/dθ is small (here, where g_z, g_x, and g_y are parallel to B_0) might therefore exhibit the highest T_m – providing a clear design principle for surface attachment of molecular qubits.

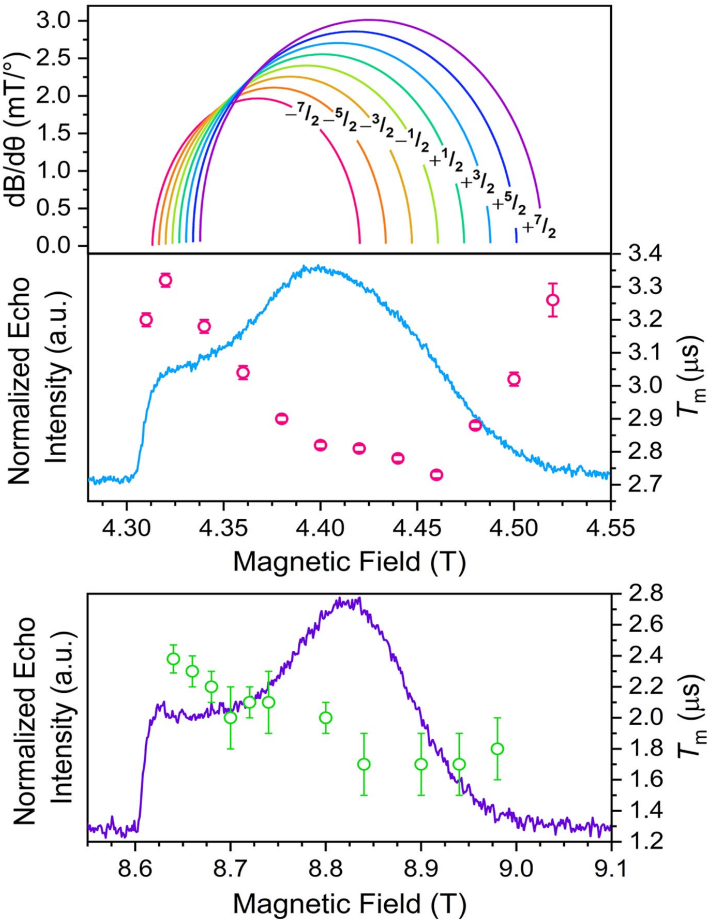

Figure 4.4 (Top) Derivative of the resonant field (B) with respect to orientation as a function of background applied magnetic field for each of the transitions in the 120 GHz EDFS. The dB/dθ values were calculated using microwave frequency = 120 GHz and *g*- and *A*-parameters listed in Table 4.1. (Middle) EDFS and orientation dependence of T_m for **1** at 120 GHz and 4 K. (Bottom) EDFS and orientation dependence of T_m for **1** at 240 GHz and 4.5 K. All measurements here were in OTP.

To test this hypothesis, we evaluated T_m via Hahn-echo experiments as a function of magnetic field at 120 and 240 GHz (Figs. 4.4, S7, Tables 4.7, 4.8). At 120 GHz and 5 K in OTP, we see T_m reach a maximum of 3.32(2) μs at 4.32 T (where g_z for the molecule is coincident with B_0), then drop with increasing field, reaching 2.73(1) at 4.46 T, before climbing to 3.26(5) μs at 4.52 T (where g_x, g_y are coincident and g_z is perpendicular to B_0). Overall, the variation in T_m is about 20% as a function of orientation. At 240 GHz and 5 K, also in OTP, similar behaviour is seen, wherein T_m is 2.38(9) μs at 8.64 T, drops with increasing field, then climbs again to 1.8(2) μs at 8.98 T (Fig. 4.8). These results demonstrate a smaller variation in T_m as a function of orientation than the 41% observed for this same molecule at X-band frequency.[29] Although modest, the orientation-dependent data nevertheless shows how specific orientations of molecular species can enhance T_m.

Our results show that T_m is longer along the edges of the EDFS spectrum, when g_x and g_y, or g_z are coincident to B_0. This observation is consistent with a scenario where slight changes in molecular geometry (via librations) dictate only small changes in resonant field ($dB/d\theta \approx 0$), as is well-established.[42,43] The results of the small $dB/d\theta$ are emphasized at 4.32 T and 4.52 T in the 120 GHz data, where there is likely only one hyperfine transition being probed (Fig 4). This observation of high T_m only at the spectral extrema likely stems from the inability to resolve the individual hyperfine peaks relative to the X-band data. Hence, the only places in the EDFS spectrum where most of the spins exhibit a small $dB/d\theta$ are the edges of the spectrum. This aspect is in contrast to the X-band data where the longest T_m times occur in the middle of the EDFS spectrum owing to highly overlapping peaks.

Reported orientation dependence studies of metal complexes are largely limited to X-band frequencies. For example, other groups report large variations (> 40%) of T_m at X-band for vanadyl,[44] Cu(II),[43,45,46] Mo(V),[47] and Cr(V)[48] systems. The relatively lower variation observed in this study may stem from the use of a new magnetic field, which are likely changing the dominant

relaxation processes in **1**. One possibility for the weaker orientation dependence is that T_m is being shortened via the decreased T_1 for $[V(C_6H_4O_2)_3]^{2-}$ at high frequency. However, even though the recorded high frequency T_1 for **1** is short (~1 ms), it's still ~3 orders of magnitude higher than T_m at the temperature of the orientation dependence studies (5 K). Hence, future studies are ultimately required to truly understand the mechanisms responsible for magnetic relaxation in **1** at high frequency.

Conclusions

The foregoing results constitute the first orientation-dependent study of T_m in V(IV) using pulsed, high-frequency EPR. Importantly, we observe a 20% variation in T_m as a function of magnetic field, with peak T_m values when g_z is parallel and perpendicular to B_0. Hence, these data provide a precise design principle for molecular alignment in addressing the challenge of scaling in spin-qubit processors. We note that these results were obtained by studying frozen glass solutions, not surface-mounted molecules, and the molecular dynamics should be significantly different in the latter scenario. Hence, additional studies of molecules directly bound to surfaces will ultimately be needed to evaluate whether the orientation dependence observed here translates to surface-based architectures. Finally, the extent to which other promising $S = {}^1/_2$ qubits (e.g. V(IV) vanadyl or Cu(II) species) demonstrate the same orientation dependence at high magnetic fields is an open question, and these studies will be reported in due course.

Experimental

Table 4.1. Spin Hamiltonian parameters for **1** in *o*-terphenyl collected at 120 GHz and 5 K. The standard errors for these parameters were obtained by varying the parameter to determine when the simulation significantly dropped in quality.

Complex and frequency	**1 at 120 GHz**
g_x	1.941(2)
g_y	1.925(1)
g_z	1.992(1)
g_x strain	0.0044(3)
g_y strain	0.012(2)
g_z strain	0.001(2)
A_x (MHz)	313(5)
A_y (MHz)	363(8)
A_z (MHz)	60(8)

*Changes in *A*-strain resulted in no change in the simulated spectrum.

Table 4.2. Spin Hamiltonian parameters for **1** in *o*-terphenyl collected at 240 GHz and 5 K. The standard errors for these parameters were obtained by varying the parameter to determine when the simulation significantly dropped in quality.

Complex and frequency	**1 at 240 GHz**
g_x	1.941(1)
g_y	1.922(1)
g_z	1.992(1)
g_x strain	0.012(1)
g_y strain	0.022(9)
g_z strain	0.001(1)
A_x (MHz)	313(9)
A_y (MHz)	363(30)
A_z (MHz)	60(9)

*Changes in *A*-strain resulted in no change in the simulated spectrum.

Table 4.3. Fit T_1 values from the fitting function: $I\,(t) = -A\left[e^{-\left(\frac{t}{T_1}+\sqrt{\frac{t}{q}}\right)} - I(0) - 1\right]$. The standard error for each fit is reported in parentheses.

T (K)	T_1 (ms)	q
5	1.23(3)	2.7(1)
10	0.47(2)	1.3(1)
15	0.23(2)	7(5)
20	0.20(3)	0.5(1)

Table 4.4. Fit T_m values (in μs) measured at 120 GHz and the stretch parameters (β) from the stretched exponential fitting function: $I(2\tau) = I(0) - Ae^{(\frac{2\tau}{Tm})^{\beta}}$. The standard error for each fit is reported in parentheses.

1 in *o*-terphenyl at 120 GHz:

T (K)	T_m (μs)	β	T(K)	T_m (μs)	β
1.5	3.53(2)	1.17(1)	10	2.66(2)	1.07(1)
1.75	4.08(1)	1.170(5)	12.75	2.58(1)	1.075(7)
2	3.73(2)	1.18(1)	15	2.47(1)	1.062(8)
3	3.719(9)	1.201(4)	17.5	2.37(2)	1.00(2)
3.5	3.10(2)	1.07(1)	20	2.29(3)	1.00(2)
4	3.322(9)	1.128(4)	22.5	2.25(3)	1.03(2)
5	3.192(9)	1.077(5)	25	2.16(2)	1.10(2)
6	3.00(1)	1.079(5)	30	1.98(1)	1.037(9)
7	2.99(1)	1.106(6)	40	1.70(3)	1.00(2)
8	2.84(1)	1.089(6)	50	1.29(5)	0.91(4)
9	2.72(1)	1.065(8)			

Table 4.5. Fit T_m values (in μs) measured at 240 GHz and the stretch parameters (β) from the stretched exponential fitting function: $I(2\tau) = I(0) - Ae^{(\frac{2\tau}{Tm})^{\beta}}$. The standard error for each fit is reported in parentheses.

1 in *o*-terphenyl at 240 GHz:

T (K)	T_m (μs)	β	T (K)	T_m (μs)	β
4	2.34(4)	1.13(3)	8	1.92(6)	0.99(4)
5	2.00(5)	1.06(4)	10	1.67(4)	0.98(3)
6	1.96(4)	0.99(3)	15	1.40(4)	1.10(5)

Table 4.6. Fit T_m values (in μs) measured at 120 GHz and the stretch parameters (β) from the stretched exponential fitting function: $I(2\tau) = I(0) - Ae^{(\frac{2\tau}{Tm})^{\beta}}$. The standard error for each fit is reported in parentheses.

1 in *o*-terphenyl at 120 GHz:

B (T)	T_m (μs)	β	B (T)	T_m (μs)	β
4.31	3.20(2)	1.10(1)	4.42	2.81(1)	1.113(7)
4.32	3.32(2)	1.12(1)	4.44	2.78(1)	1.125(6)
4.34	3.18(2)	1.08(1)	4.46	2.73(1)	1.113(8)
4.36	3.04(1)	1.09(1)	4.48	2.88(1)	1.186(7)
4.38	2.90(1)	1.074(9)	4.50	3.02(2)	1.23(1)
4.40	2.82(1)	1.055(9)	4.52	3.26(5)	1.25(3)

Table 4.7. Fit T_m values (in μs) measured at 240 GHz and the stretch parameters (β) from the stretched exponential fitting function: $I(2\tau) = I(0) - Ae^{(\frac{2\tau}{Tm})^{\beta}}$. The standard error for each fit is reported in parentheses.

1 in *o*-terphenyl at 240 GHz:

B (T)	T_m (μs)	β	B (T)	T_m (μs)	β
8.64	2.38(9)	1.18(6)	8.8	2.0(1)	1.00(7)
8.66	2.3(1)	1.09(7)	8.84	1.7(2)	0.79(7)
8.68	2.2(1)	1.01(7)	8.9	1.7(2)	0.81(8)
8.7	2.0(2)	0.92(8)	8.94	1.7(2)	0.83(9)
8.72	2.1(1)	1.00(9)	8.98	1.8(2)	0.9(1)
8.74	2.1(2)	0.92(7)			

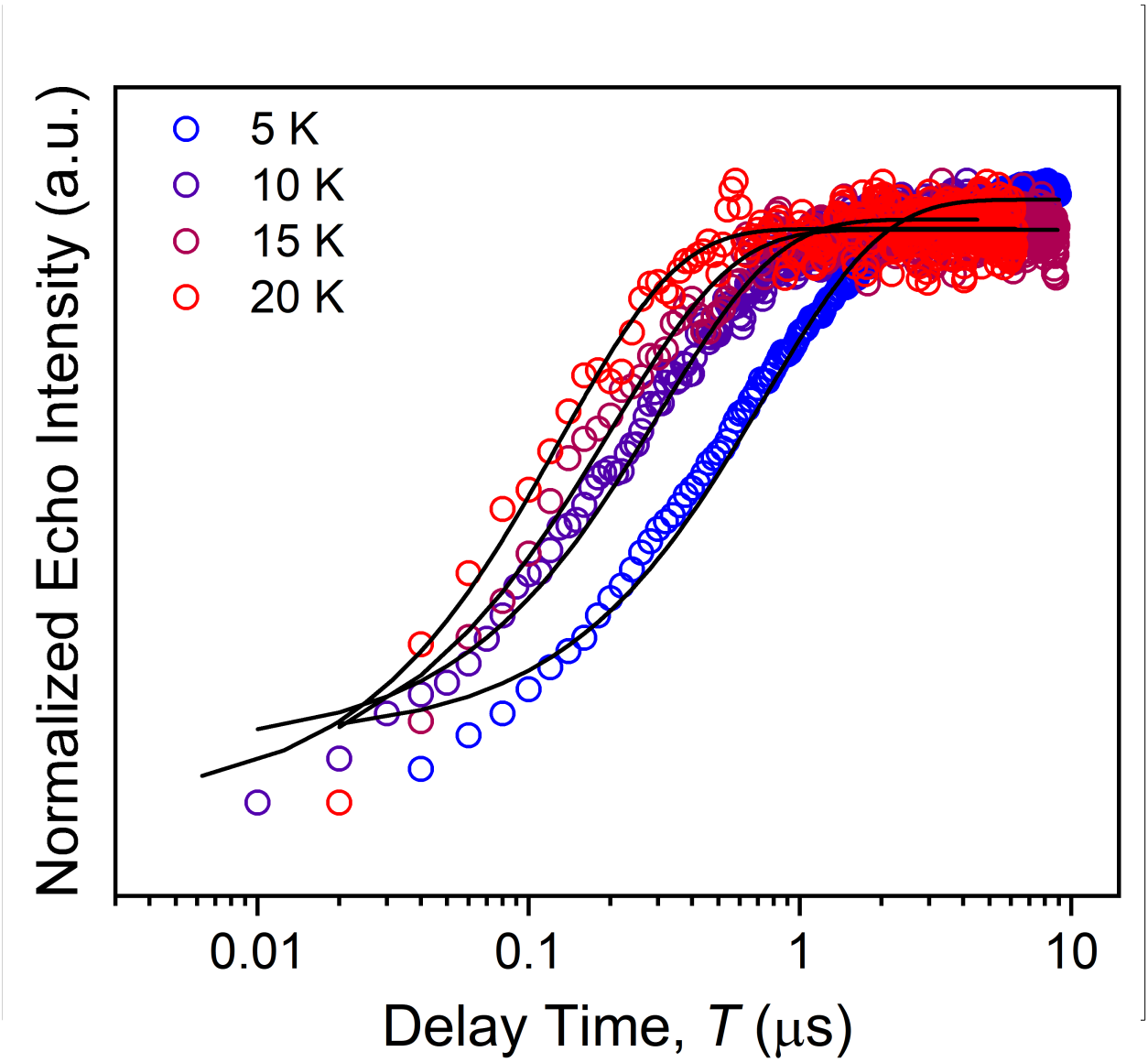

Figure 4.5. Selected variable temperature inversion recovery curves (color traces) and fits (black traces) for **1** in *o*-terphenyl at 120 GHz.

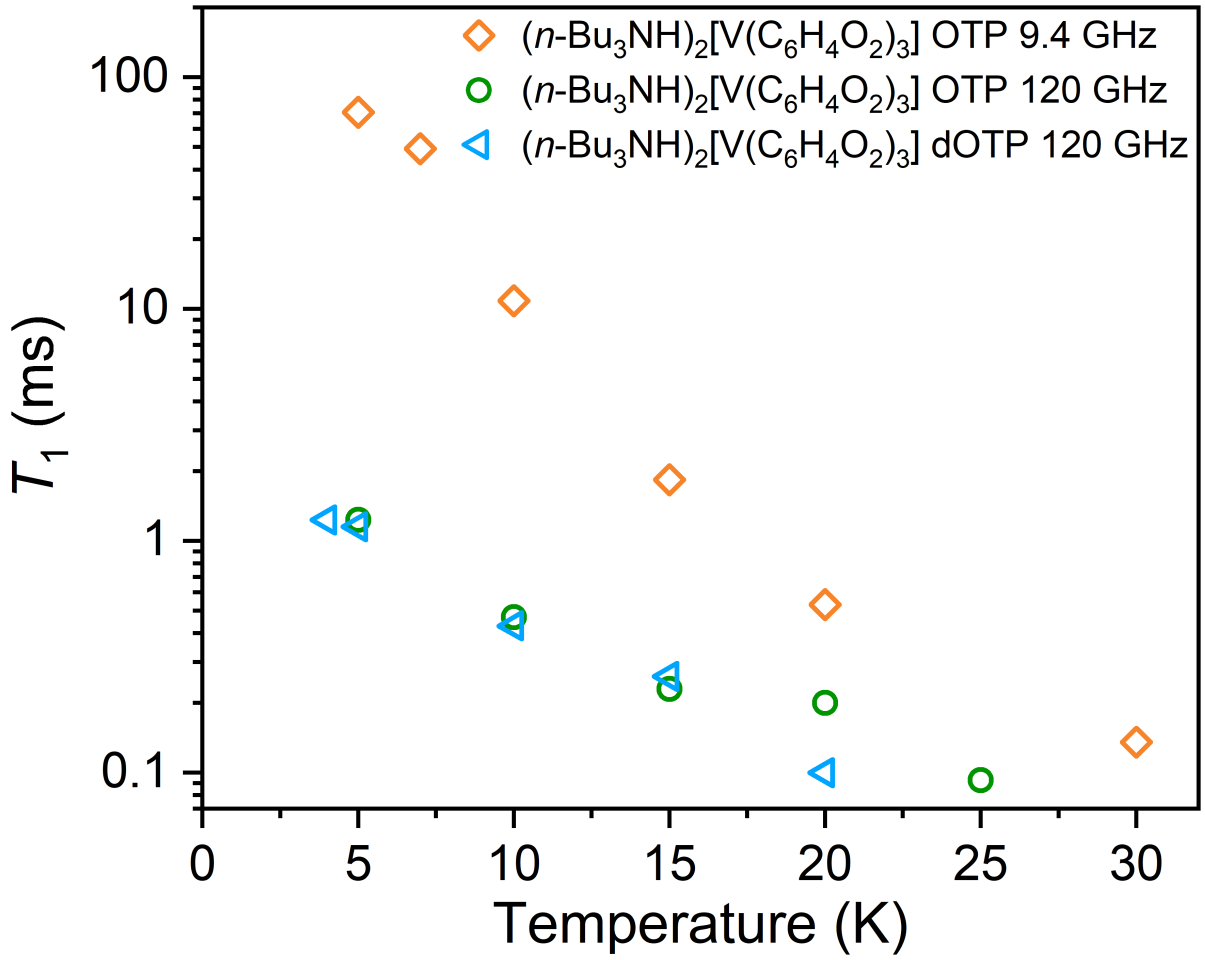

Figure 4.6. Variable-temperature T_1 and data for **1**. Data were collected on samples of ca. 1 mM concentration in *o*-terphenyl or d^{14}-*o*-terphenyl glass.

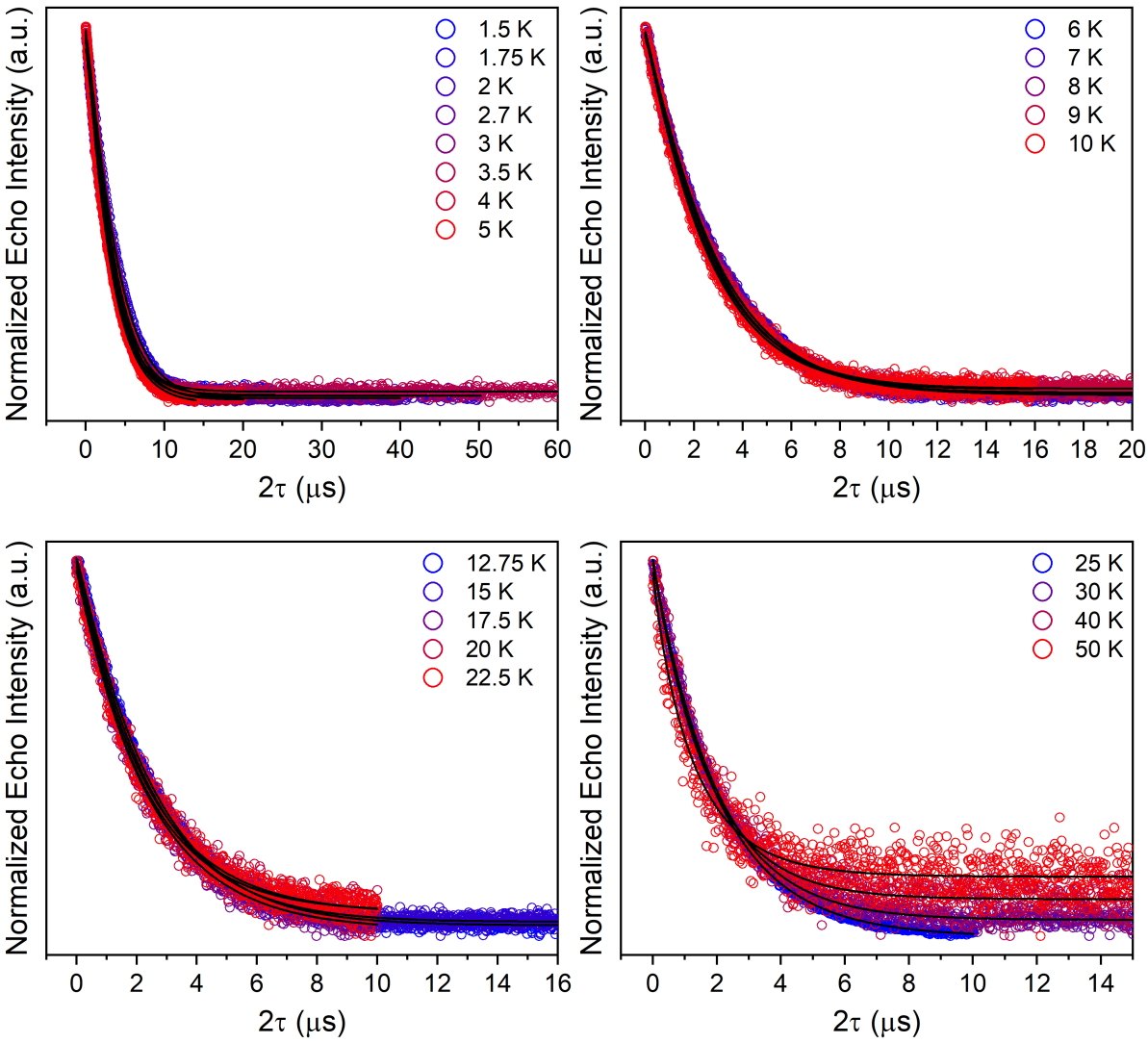

Figure 4.7. Selected variable temperature Hahn echo decay curve (color traces) and fits (black traces) for **1** in *o*-terphenyl at 120 GHz.

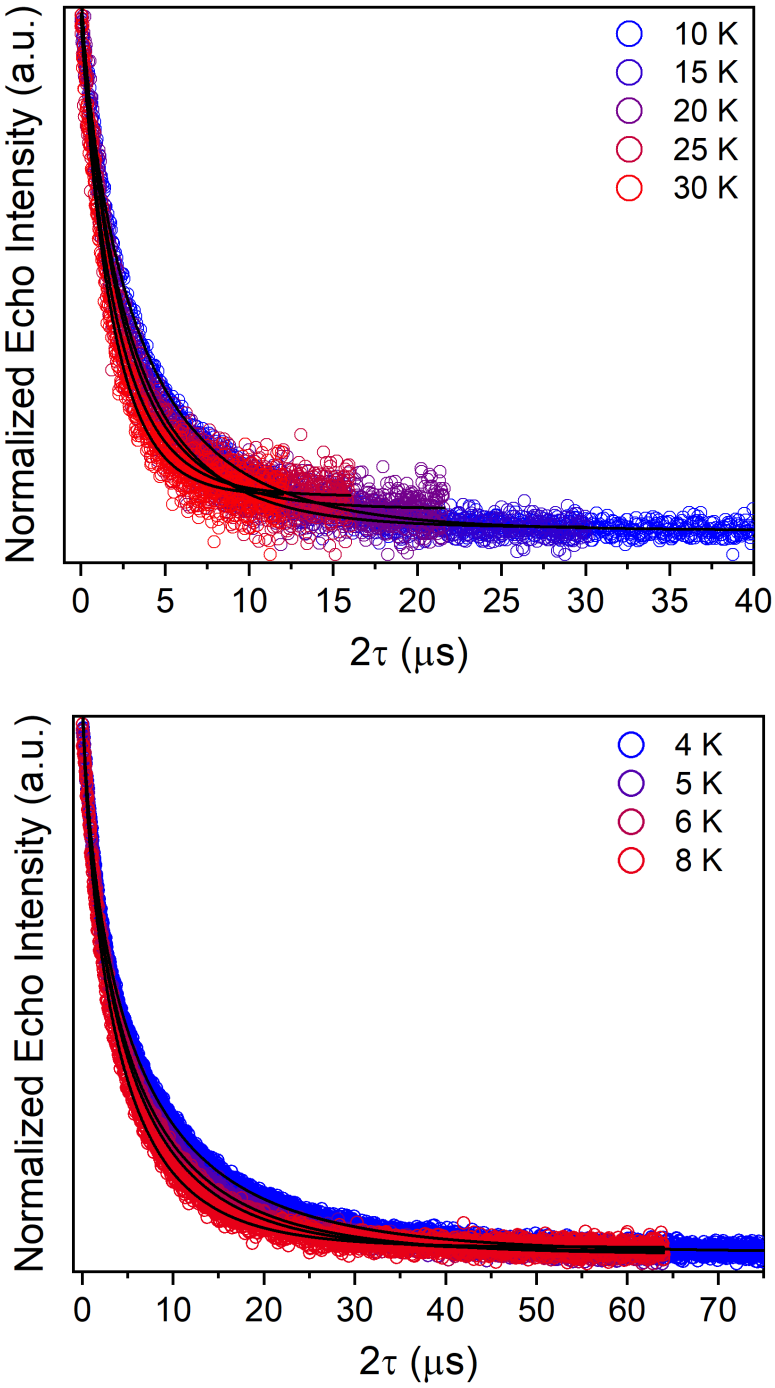

Figure 4.8. Selected variable temperature Hahn echo decay curve (color traces) and fits (black traces) for **1** in *o*-terphenyl at 240 GHz.

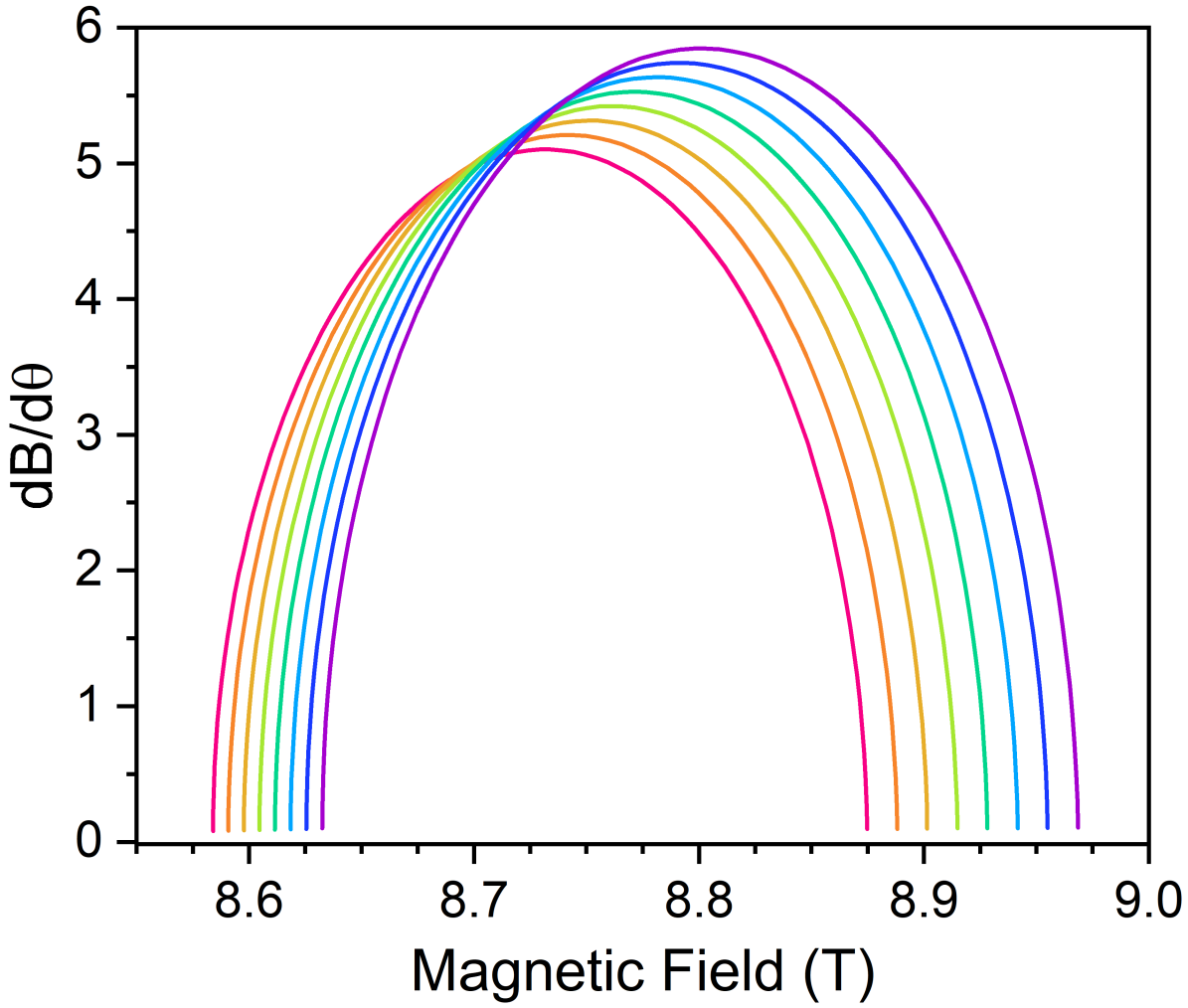

Figure 4.9. Derivative of the resonant field (here, B) with respect to orientation as a function of field for each of the transitions in the EDFS. The dB/dθ values were calculated using microwave frequency = 240 GHz and *g*- and *A*-parameters listed in Table 4.2. The transitions are going from low field to high field: M_s = $-^7/_2$ (pink), $-^5/_2$ (dark orange), $-^3/_2$ (light orange), $-^1/_2$ (light green), $+^1/_2$ (dark green), $+^3/_2$ (blue), $+^5/_2$ (indigo), and $+^7/_2$ (violet).

References

1 M. Atzori and R. Sessoli, *J. Am. Chem. Soc.*, **2019**, *141*, 11339–11352.

2 M. Affronte, F. Troiani, A. Ghirri, A. Candini, M. Evangelisti, V. Corradini, S. Carretta, P. Santini, G. Amoretti, F. Tuna, G. Timco and R. E. P. Winpenny, *J. Phys. D: Appl. Phys*, **2007**, *40*, 2999–3004.

3 A. Gaita-Ariño, F. Luis, S. Hill and E. Coronado, *Nat. Chem.*, **2019**, *11*, 301–309.

4 M. J. Graham, J. M. Zadrozny, M. S. Fataftah and D. E. Freedman *Chem. Mater.* **2017**, *29*, 1885-1897.

5 J. M. Zadrozny, J. Niklas, O. G. Poluektov and D. E. Freedman, *ACS Cent. Sci.*, **2015**, *1*, 488–492.

6 C.-J. Yu, M. J. Graham, J. M. Zadrozny, J. Niklas, M. D. Krzyaniak, M. R. Wasielewski, O. G. Poluektov and D. E. Freedman, *J. Am. Chem. Soc.*, **2016**, *138*, 14678–14685.

7 A. Ghirri, V. Corradini, V. Bellini, R. Biagi, U. del Pennino, V. De Renzi, J. C. Cezar, C. A. Muryn, G. A. Timco, R. E. P. Winpenny and M. Affronte, *ACS Nano*, **2011**, *5*, 7090–7099.

8 Y. Bae, K. Yang, P. Willke, T. Choi, A. J. Heinrich and C. P. Lutz, *Sci. Adv.*, **2018**, *4*, eaau4159.

9 A. Hofmann, Z. Salman, M. Mannini, A. Amato, L. Malavolti, E. Morenzoni, T. Prokscha, R. Sessoli and A. Suter, *ACS Nano*, **2012**, *6*, 8390–8396.

10 D. Gatteschi, A. Cornia, M. Mannini and R. Sessoli, *Inorg. Chem.*, **2009**, *48*, 3408–3419.

11 M. Warner, S. Din, I. S. Tupitsyn, G. W. Morley, A. M. Stoneham, J. A. Gardener, Z. Wu, A. J. Fisher, S. Heutz, C. W. M. Kay and G. Aeppli, *Nature*, **2013**, *503*, 504–508.

12 L. Tesi, E. Lucaccini, I. Cimatti, M. Perfetti, M. Mannini, M. Atzori, E. Morra, M. Chiesa, A. Caneschi, L. Sorace and R. Sessoli, *Chem. Sci.*, **2016**, *7*, 2074–2083.

13 M. Mannini, F. Bertani, C. Tudisco, L. Malavolti, L. Poggini, K. Misztal, D. Menozzi, A. Motta, E. Otero, P. Ohresser, P. Sainctavit, G. G. Condorelli, E. Dalcanale and R. Sessoli, *Nat. Commun.*, **2014**, *5*, 4582.

14 L. Malavolti, M. Briganti, M. Hänze, G. Serrano, I. Cimatti, G. McMurtrie, E. Otero, P. Ohresser, F. Totti, M. Mannini, R. Sessoli and S. Loth, *Nano Lett.*, **2018**, *18*, 7955–7961.

15 M. D. Jenkins, D. Zueco, O. Roubeau, G. Aromí, J. Majer and F. Luis, *Dalton Trans.*, **2016**, *45*, 16682–16693.

16 J. McGuire, H. N. Miras, E. Richards and S. Sproules, *Chem. Sci.* **2019**, *10*, 1483-1491.

17 S. R. Cooper, Y. B. Koh and K. N. Raymond, *J. Am. Chem. Soc.*, **1982**, *104*, 5092–5102.

18 J. van Tol, G. W. Morley, S. Takahashi, D. R. McCamey, C. Boehme and M. E. Zvanut, *Appl. Magn. Reson.*, **2009**, *36*, 259–268.

19 Molecular Nanomagnets, Oxford University Press, Oxford, New York, 2006.

20 S. S. Eaton, G. R. Eaton and L. J. Berliner, Biomedical EPR - Part A: Free Radicals, Metals, Medicine and Physiology, Springer Science & Business Media, 2004.
21 D. P. Vincenzo, Fortschr. *Phys.*, **2000**, *48*, 771–783.
22 S. Takahashi, R. Hanson, J. Van Tol, M. S. Sherwin and D. D. Awschalom, *Phys. Rev. Lett.*, **2008**, *101*, 1–4.
23 M. D. Lingwood and S. Han, *Annu. Rep. NMR Spectrosc.* **2011**, *73*, 83-126.
24 T. Maly, G. T. Debelouchina, V. S. Bajaj, K.-N. Hu, C.-G. Joo, M. L. Mak–Jurkauskas, J. R. Sirigiri, P. C. A. van der Wel, J. Herzfeld, R. J. Temkin and R. G. Griffin, *J. Chem. Phys.*, **2008**, *128*, 052211.
25 M. S. Fataftah, M. D. Krzyaniak, B. Vlaisavljevich, M. R. Wasielewski, J. M. Zadrozny and D. E. Freedman, *Chem. Sci.*, **2019**, *10*, 6707–6714.
26 M. Atzori, S. Benci, E. Morra, L. Tesi, M. Chiesa, R. Torre, L. Sorace and R. Sessoli, *Inorg. Chem.*, **2018**, *57*, 731–740.
27 M. Atzori, L. Tesi, S. Benci, A. Lunghi, R. Righini, A. Taschin, R. Torre, L. Sorace and R. Sessoli, *J. Am. Chem. Soc.*, **2017**, *139*, 4338–4341.
28 M. Atzori, E. Morra, L. Tesi, A. Albino, M. Chiesa, L. Sorace and R. Sessoli, *J. Am. Chem. Soc.*, **2016**, *138*, 11234–11244.
29 C. E. Jackson, C.-Y. Lin, S. H. Johnson, J. van Tol and J. M. Zadrozny, *Chem. Sci.*, **2019**, *10*, 8447-8454.
30 C.-Y. Lin, T. Ngendahimana, G. R. Eaton, S. S. Eaton and J. M. Zadrozny, *Chem. Sci.*, **2019**, *10*, 548-555.
31 S. Stoll and A. Schweiger, *J. Magn. Reson.*, **2006**, *178*, 42–55.
32 J. van Tol, L.-C. Brunel and R. J. Wylde, *Rev. Sci. Instrum.* **2005**, *76*, 074101.
33 G. W. Morley, L.-C. Brunel and J. van Tol, *Rev. Sci. Instrum.* **2008**, *79*, 064703.
34 Matlab; The MathWorks Inc.: Natick, MA, 2018.
35 Origin; OriginLab: Northampton, MA, 2018.
36 H. Chen, A. G. Maryasov, O. Y. Rogozhnikova, D. V. Trukhin, V. M. Tormyshev and M. K. Bowman, *Phys. Chem. Chem. Phys.*, **2016**, *18*, 24954–24965.
37 J. M. Zadrozny and D. E. Freedman, *Inorg. Chem.* **2015**, *54*, 12027-12031.
38 K. Bader, M. Winkler and J. van Slageren, *Chem. Comm.* **2016**, 52, 3623-3626.
39 W. M. Haynes, T. J. Bruno and D. R. Lide, CRC Handbook of Chemistry and Physics: A Ready-reference Book of Chemical and Physical Data, CRC Press, 2014.
40 N. J. Stone, *At. Data Nucl. Data Tables* **2005**, *32*, 75-176.
41 K. M. Salikhov, S. A. Dzuba and A. M. Raitsimring *J. Magn. Reson.* **1981**, *42*, 255-276.

42 M. Rohrer, P. Gast, K. Möbius and T. F. Prisner *Chem. Phys. Lett.* **1996**, *259*, 523-530.

43 S. A. Dzuba *Phys. Lett. A* **1996**, *213*, 77-84.

44 J.-L. Du, K. M. More, S. S. Eaton and G. R. Eaton, *Isr. J. Chem.*, **1992**, *32*, 351–355.

45 J.-L. Du, G. R. Eaton and. S. S. Eaton, *J. Magn. Reson. Ser. A* **1995**, *117*, 67-72.

46 A. J. Fielding, S. Fox, G. L. Millhauser, M. Chattopadhyay, P. M. H. Kroneck, G. Fritz, G. R. Eaton and S. S. Eaton, *J. Magn. Reson*., **2006**, *179*, 92–104.

47 R. Husted, J.-L. Du, G. R. Eaton and S. S. Eaton, *Magn. Reson. Chem.*, **1995**, *33*, S66–S69.

48 R. Konda, J.-L. Du, S. S. Eaton and G. R. Eaton, *Appl. Magn. Reson.*, **1994**, *7*, 185–193.

CHAPTER 5 – PROGRAMMABLE NUCLEAR-SPIN DYNAMICS IN TI(IV) COORDINATION COMPLEXES

Overview

Interstitial patterning of nuclear spins is a nascent design principle for controlling electron spin superposition lifetimes in open-shell complexes and solid-state defects. Herein we report the first test of the impact of the patterning principle on ligand-based nuclear spin dynamics. We test how substitutional patterning of ^{1}H and $^{79/81}$Br nuclear spins on ligands modulates proton nuclear spin dynamics in the ligand shell of metal complexes. To do so, we studied the ^{1}H nuclear magnetic resonance relaxation times (T_1 and T_2) of a series of eight polybrominated catechol ligands and six complexes formed by coordination of the ligands to a Ti(IV) ion. These studies reveal that ^{1}H T_1 values can be enhanced in the individual ligands by a factor of 4 (from 10.8(3) to 43(5) s) as a function of substitution pattern, reaching the maximum value for 3,4,6-tribromocatechol. The T_2 for ^{1}H is also enhanced by a factor of 4, varying by ~14 s across the series. When complexed, the impact of the patterning design strategy on nuclear spin dynamics is amplified and ^{1}H T_1 and T_2 values vary by over an order of magnitude. Importantly, the general trends observed in the ligands also match those when complexed. Hence, these results demonstrate a new design principle to control ^{1}H spin dynamics in metal complexes through pattern-based design strategies in the ligand shell.

Introduction

Next-generation applications of open shell magnetic complexes rely on long-lived electronic spin superposition lifetimes. Applications for sustained molecule-based spin superpositions span quantum sensing,[1,2] quantum computation,[3,4] and dynamic nuclear polarization.[5] Toward utility in these applications, chemical design principles for lengthening

superposition lifetime are critically important.[6-11] However, the realization of useful lifetimes (> 100 μs) in molecules are still only achieved in environments engineered to be free of a spin bath, both in terms of nuclear and electronic spins.[12,13] Special environments like these are disjoint from applications, wherein highly active local spin environments are likely to be present. Hence, testing new design strategies to prolong spin superposition lifetime in dynamic magnetic surroundings is a pressing concern.

One prominent origin of short-lived spin superpositions in open-shell molecules is the dynamic nuclear spin bath.[14] Rapid and numerous fluctuations in the orientations of these nuclear spins, when close to an electronic spin, impose a fluctuating local magnetic field on the electron, which accelerates the collapse of electronic spin superpositions. The extent to which environmental nuclear spins impart this fluctuating local field depends on their respective nuclear relaxation dynamics. In turn, these dynamics stem (in part) from the respective interactions between the nuclear spins.[15-18] Hence, controlling the spin-spin interactions between bath nuclear spins may be a powerful method for manipulating the dynamic field and producing long-lived molecular electronic spin superpositions.

In this context, a set of chemical design principles to tune the magnetic environment imposed by the nuclei in a molecule would be extremely useful. Here, manipulation of the impact of this proximate “edge” of the larger nuclear spin bath could be achieved via synthetic modification of interspin distances, relative arrangements, and identity of nuclear spins on the molecule itself. Indeed, recent breakthroughs from our group on V(IV) complexes[19] and others on the solid-state defects in SiC[20-22] provide preliminary demonstrations of manipulating nuclear spin position/arrangements to control nearby electronic spin superpositions. Extensive literature exists on the fundamental mechanisms governing nuclear spin relaxation,[15-18] providing a foundational backbone for translating the aforementioned breakthroughs into broadly applicable design principles. Yet, generalizable synthetic strategies to tailor nuclear spin relaxation in the ligand shell of metal complexes are still absent.

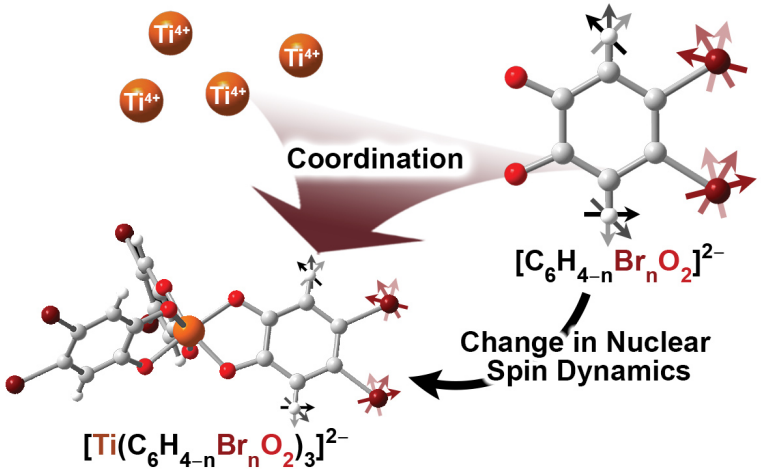

Figure 5.1. In this manuscript, we perform the first tests of how different substitutional patterns of ^{1}H and $^{79/81}$Br nuclear spins on ligands impact the ligand ^{1}H T_1 and T_2 and how the effect changes upon coordination.

Toward that knowledge, we herein test the dependence of ^{1}H nuclear-spin dynamics on substitutional patterning in a series of brominated catechol derivatives and upon coordination to Ti(IV) (Fig. 5.1). We hypothesized that different patterns of Br functional groups on the ligand would enable a significant synthetic variation in ^{1}H spin dynamics in the isolated catechols, as bromine and hydrogen have significantly different nuclear magnetic moments (^{1}H, μ = 2.79 μ_N, ^{79}Br, μ = 2.11 μ_N, ^{81}Br, μ = 2.27 μ_N) and Larmor frequencies (at 9.4 T, ^{1}H = 400 MHz, ^{79}Br = 101 MHz, ^{81}Br = 108 MHz). We thus reasoned that different substitutional patterns on the ligand shell would modulate the interspin dipole-dipole interactions, thereby impacting T_1 and T_2.[23] The difference in Larmor frequencies was also viewed as particularly advantageous for suppressing the impact of nuclear Overhauser effects on relaxation and simplifying the analysis.[24] Finally, we predicted that these trends would be reproduced when the ligands were part of the coordination shell. This last prediction is on the basis of the distance dependence of the dipolar interactions between nuclei, which weaken with r^{-6} (where r is the distance separating nuclei).[37-39]

To test the foregoing hypotheses, we investigated the ^{1}H spin-lattice relaxation (T_1) and spin-spin relaxation (T_2) times for eight catechol molecules: pyrocatechol (**1**), 3-bromocatechol

(**2**), 4-bromocatechol (**3**), 3,5-dibromocatechol (**4**), 4,5-dibromocatechol (**5**), 3,4,5-tribromocatechol (**6**), 3,4,6-tribromocatechol (**7**), and tetrabromocatechol (**8**) (Fig. 5.2). We also selected six specific titanium complexes from this set of ligands for investigation: $[Ti(C_6H_4O_2)_3]^{2-}$ (**1a**), $[Ti(C_6H_3\text{-}4\text{-}BrO_2)_3]^{2-}$ (**3a**), $[Ti(C_6H_2\text{-}3,5\text{-}Br_2O_2)_3]^{2-}$ (**4a**), $[Ti(C_6H_2\text{-}4,5\text{-}Br_2O_2)_3]^{2-}$ (**5a**), $[Ti(C_6H\text{-}3,4,5\text{-}Br_3O_2)_3]^{2-}$ (**6a**), and $[Ti(C_6Br_4O_2)_3]^{2-}$ (**8a**) (Fig. 5.2), all isolated as the $Me_2NH_2^+$ salts. We found that substituting $^{79/81}$Br in a ^{1}H spin system extends ^{1}H T_1 by a factor of 4 and T_2 by a factor of *ca*. 7, depending on the pattern of the substitution. When complexed with Ti(IV), the ligand protons mimic the relaxation trends of the uncomplexed ligands. Yet, the relative variation is considerably more dramatic in the studied complexes, as ^{1}H T_1 and T_2 are enhanced by an order of magnitude depending on substitutional pattern. These data provide the first evidence of a synthetic design principle for modifying nuclear spin dynamics via substitutional patterning, and that coordination enhances the relative impact of the pattern design principle.

Results and Discussion

Isolation of the studied molecules proceeded with little difficulty. Indeed, many of the brominated catechols are available commercially (**1**, **2**, **3**, **8**) and all others were prepared via slight modifications of reported procedures (**4**, **5**, **6**, **7**).[25-27] Overnight reactions of 3.3 eq. of the catechols **1**, **3**, **4**, **5**, **6** and **8** with 1 eq of $Ti(NMe_2)_4$ in THF yielded dark red solutions containing **1a**, **3a**, **4a**, **5a**, **6a**, or **8a** (Fig. 5.2), which can be isolated as orange powders. These reactions produce $Me_2NH_2^+$ counterions, suggesting that the Me_2N^- ligands of the Ti(IV) starting material $Ti(NMe_2)_4$ are deprotonating the catechol ligands during reaction progression. This same counterion formation by ligand deprotonation characterizes the synthesis of the analogous V(IV) complexes.[28,29]

Single-crystal X-ray diffraction of crystals resulting from the reactions of **1** and **5** with $Ti(NMe_2)_4$ reveal an octahedral geometry for the TiO_6 coordination environment (Figs. 5.3, 5.9, Tables 5.3-5.5). These experiments reveal a general 3-to-1 ligand-to-metal stoichiometry and two

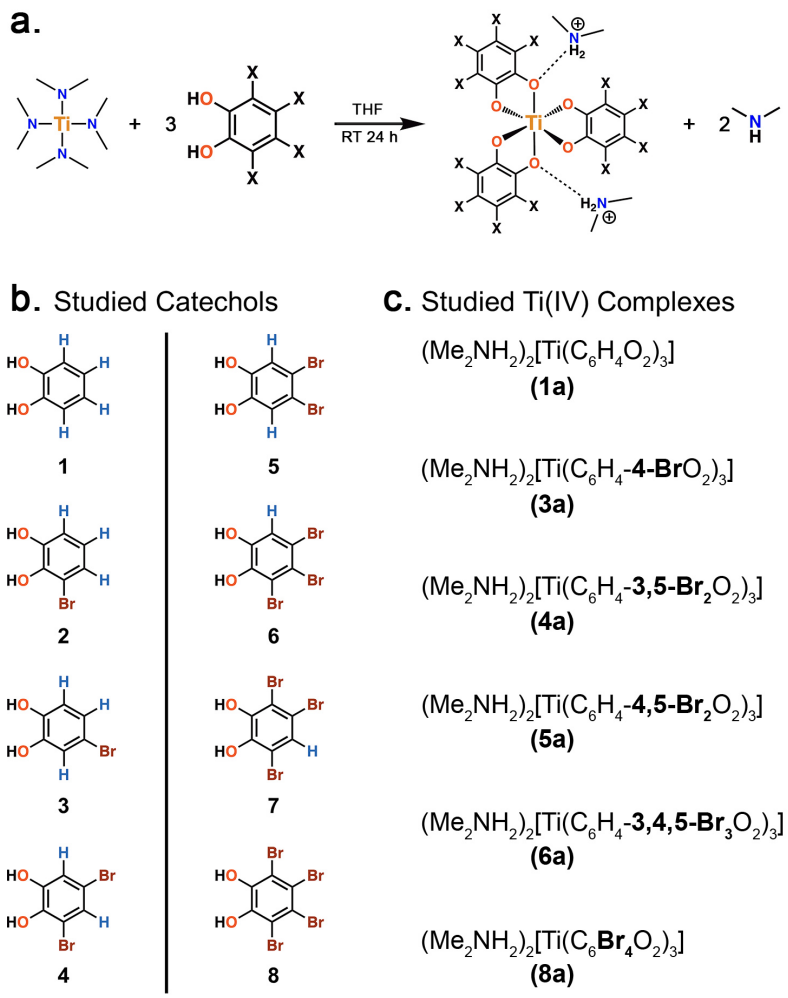

Figure 5.2. Synthetic scheme and complexes. **(a)** The general synthetic scheme to produce the titanium complexes is depicted. **(b)** The series of ten brominated ligands used in this study. **(c)** Ligands **1**, **3-5**, and **8** were reacted to form five Ti(IV) coordination complexes following the scheme shown in **(a)**.

$Me_2NH_2^+$ counterions. All other characterization data for the metal complexes match this general stoichiometry, though isolating high-quality single crystals of **3a**, **4a**, **6a**, and **8a** was significantly more challenging (see Experimental section). Bond metrics taken from the obtained structures match literature expectations. For example, the average Ti–O distances in **1a** and **5a** are 1.9640(3) and 1.993(5) Å, respectively, close to those of known Ti-catecholate analogue.[30-32] Furthermore, C–O bond distances in the ligands are 1.345(8) Å which match those for the fully reduced catecholate, suggesting closed-shell ligands (as opposed to possible semiquinones,

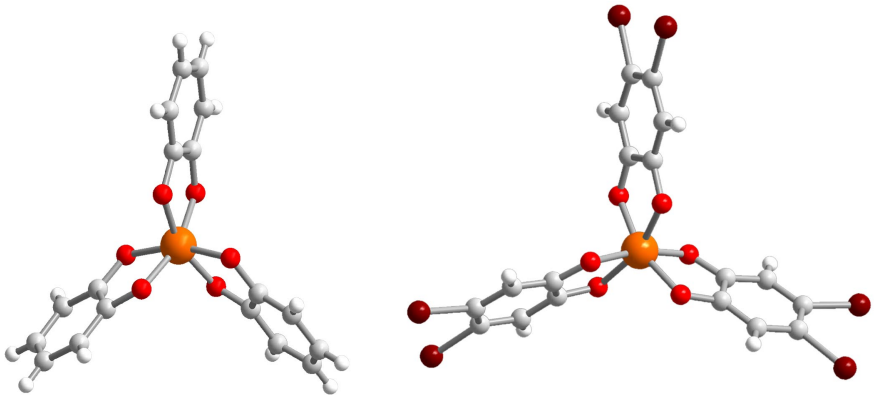

Figure 5.3. Molecular structures of $[Ti(C_6H_4O_2)_3]^{2-}$ (left) and $[Ti(C_6H_2Br_2O_2)_3]^{2-}$ (right), as determined in the crystal structures of **1a** and **5a**. Hydrogen bonding contacts with the $Me_2NH_2^+$ counterions are omitted for clarity. Orange, maroon, blue, red, gray, and white spheres represent titanium, bromine, nitrogen, oxygen, carbon, and hydrogen atoms, respectively.

where C–O is 1.302(11) Å).[33] These data establish these molecules as closed-shell Ti(IV) complexes.

Proton NMR spectroscopy (400 MHz, 9.4 T) was applied to the ligands and complexes to locate and identify the chemical shifts of the nuclei of interest. All ligands and complexes depict ^{1}H peaks in the aromatic region (save for **8** and **8a**, which have only aromatic $^{79/81}$Br nuclear spins). Here, the peaks appear to be shifted downfield by proximity to either hydroxy or bromine groups. Furthermore, these peaks are split by *J*-coupling, where *J* is largest for 1,2-coupling between *ortho* protons (5.86-8.43 Hz) and decreasing as the protons are spaced apart on the catechol ring (2.05-3.57 Hz for 1,3-coupling between *meta* ^{1}Hs).[34] The 1,4-coupling strength between *para* ^{1}Hs was too small to observe for **1**, **3**, and **5** in our spectrometer. Peaks corresponding to OH groups for the free ligand show up from 7.76-9.22 ppm. The $Me_2NH_2^+$ counterions show peaks at 2.60 and 8.09-8.60 ppm for the $-CH_3$ and NH_2 protons, respectively, in the complexes. Upon complexation to Ti(IV), the catecholate ^{1}H aromatic peaks move slightly upfield, but otherwise retain the same relative δ values and *J* couplings. The exception to the spectral similarity is complex **3a**, which exhibits rearranged peaks due to the removal of the shifting effect from the hydroxyl protons (Figs. 5.9 and 5.15 in the ESI).

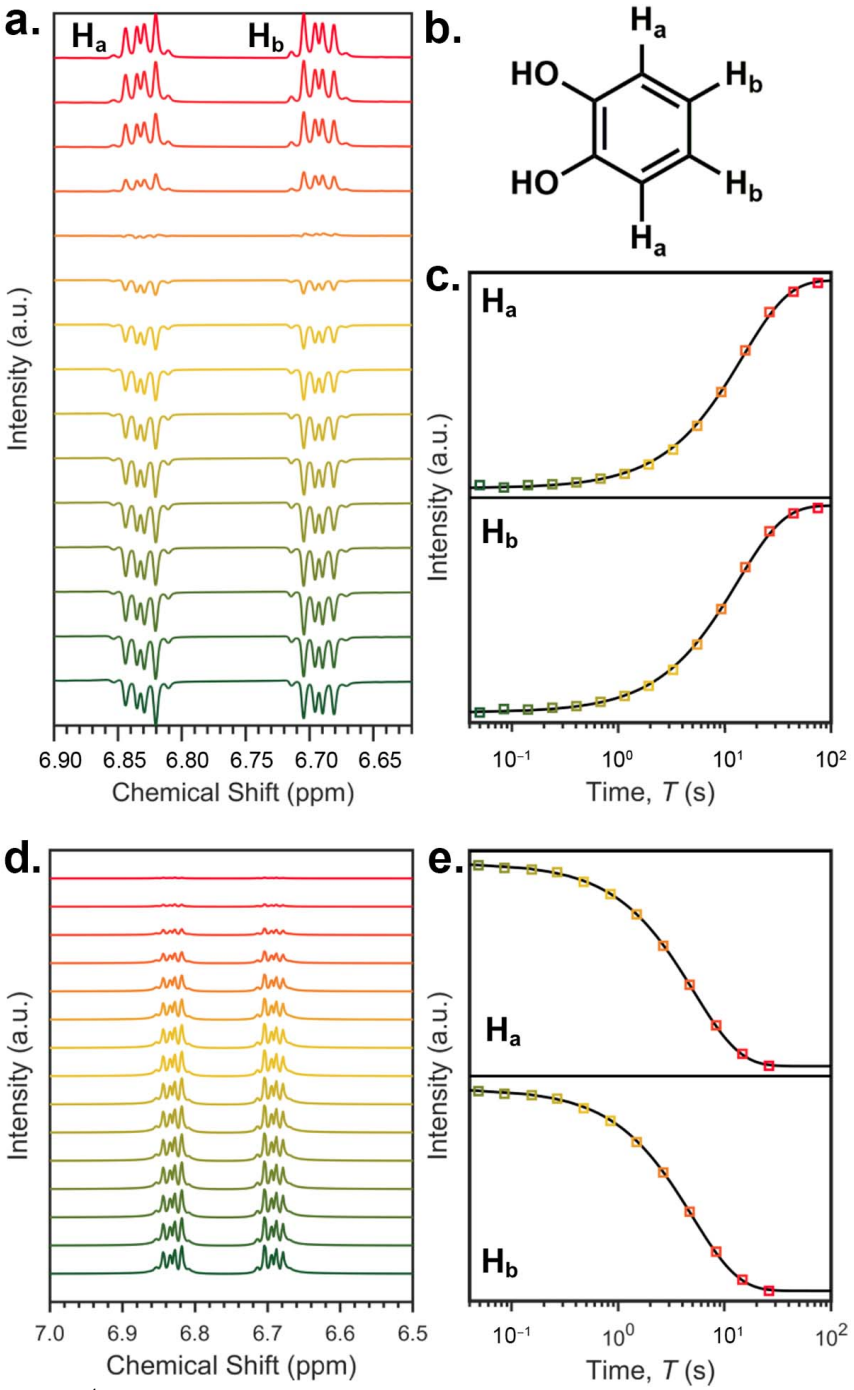

Figure 5.4. Example ^{1}H NMR analyses of a catechol molecule, here **1**. **(a)** Inversion-recovery spectra – the offset spectra represent different delay times between inversion and measurement, with the shortest delays at the bottom in green. **(b)** Depiction of ^{1}H peak assignment. **(c)** Peak intensity as a function of delay following inversion. The black line is a fit to an exponential recovery to yield T_1 for a given peak. **(d)** CPMG experimental results – the offset spectra represent different numbers of applied π pulses: the green spectrum at the bottom was collected with one π pulse and the red spectrum at the top was collected with 12 π pulses. **(e)** ^{1}H peak intensity versus total time after the π /2 pulse. The black line is a fit to an exponential decay to yield T_2 for the indicated peak.

Table 5.1. Tabulated aromatic ^{1}H spin-lattice relaxation times (T_1) determined via inversion recovery experiments.[a,b,c]

Ligands	Ring Position			
	3	4	5	6
1	14.8(7)	13.3(6)	13.3(6)	14.8(7)
2	-	17.9(4)	10.8(4)	11.9(2)
3	27(3)	-	13.7(6)	13.4(7)
4	-	30(5)	-	31(5)
5	28(4)	-	-	28(4)
6	-	-	-	32(4)
7	-	-	43(5)	-

Complexes	Ring Position			
	3	4	5	6
1a	1.32(2)	2.11(6)	2.11(6)	1.32(2)
3a	0.48(2)	-	0.74(8)	0.38(3)
4a	-	6.3(5)	-	6.8(3)
5a	6.0(5)	-	-	6.0(5)
6a	-	-	-	7.1(2)

[a]All T_1 values given in units of s. [b]There are no aromatic protons for **8** and **8a**, hence the omission. [c]T_1 values for OH groups and $Me_2NH_2^+$ counterions can be found in the SI.

Spin-lattice relaxation times were determined by standard ^{1}H-NMR inversion-recovery experiments at room temperature (see Figs. 5.4, 5.8-5.13, and SI) for all ligands and complexes. These experiments proceeded with π pulses of 22 μs, and all catechol solutions were 200 mM in acetone-d_6. All Ti(IV) complexes were measured at 100 mM in DMSO-d_6 (solubility challenges precluded the use of acetone – see Experimental section). NMR spectra were then collected following the initial π pulse and a variable-delay period, *T*. For all ligands and complexes, the initial spectra following the π pulses are inverted, eventually recovering to the expected positive signal intensity. All recoveries were successfully fit with monoexponential functions, suggesting that only a single relaxation process dominates for each peak. Importantly, the timescale of this recovery is peak-dependent (Figs. 5.4 and 5.8-5.14).

Our results show that, with minor exceptions, the substitution of Br atoms for H atoms engenders longer ^{1}H T_1 times (Table 5.1), based on four key observations. First, the shortest T_1

values are observed for protons that are adjacent to other protons. For example, the adjacent protons of **2** have T_1 times of 10.8(4) and 11.9(2) s, respectively, the shortest of **1**–**8**. This general trend holds true for the adjacent protons in **1** and **3**, which exhibit aromatic ^{1}H T_1 values only slightly longer compared to **2**, *ca*. 13-14 s. Second, the presence of a Br atom adjacent to a ^{1}H (versus another proton) appears to have a slight lengthening effect on T_1. Indeed, in **2**, the proton in the 4-position (which has one adjacent proton and one adjacent bromine) exhibits a slightly longer T_1 (17.9(4) s) than the other two protons of this ligand, which lack a neighboring Br atom (10-12 s). Third, T_1 is further lengthened when the Br atom isolates a given proton from other protons. For example, the ^{1}H in the 3-position of **3**, which is separated from the other protons, exhibits a relaxation time of 27(3) s, nearly twice as long as the proton in the corresponding position on **1**. Similarly, for **4** and **5**, which have no adjacent protons, the ^{1}H T_1 values are extended to 28-31 s. Finally, fourth, when only one aromatic ^{1}H is present (as in the triply brominated **6** and **7**), T_1 can become even longer (32(4) and 43(5) s). In summary, these data demonstrate that T_1 can be varied by a factor of approximately four depending on the substitutional pattern.

The aromatic ^{1}H signals for the ligands display shorter *overall* T_1 values when coordinated to Ti(IV) (Figs. 5.5, 5.15-5.19, and Table 5.1). However (and importantly), the same trends in ^{1}H T_1 values as a function of Br substitution patterns are seen for both the complexes and the lone ligands. For example, the adjacent protons in **3a** display the shortest T_1 values among the studied complexes, 0.48(2) and 0.38(3) s. In contrast, **4a**–**6a**, which have ^{1}H nuclear spins isolated from one another by Br atoms, exhibit T_1 values that are an order of magnitude greater (6.0(5) to 7.1(2) s).

Tests of the effects of substitutional pattering on ^{1}H T_2 were determined through application of Carr-Purcell-Meiboom-Gill (CPMG) experiments (Figs. **4**, **5**, 5.8-5.13, and 5.15-5.18).[35,36] This experiment is similar to a Hahn-echo experiment, however, the time separating sequential π pulses is fixed, and the number of π pulses is varied, such that the total delay time is the sum of repeated pulses and fixed delays. Application of the CPMG sequence to obtain T_2

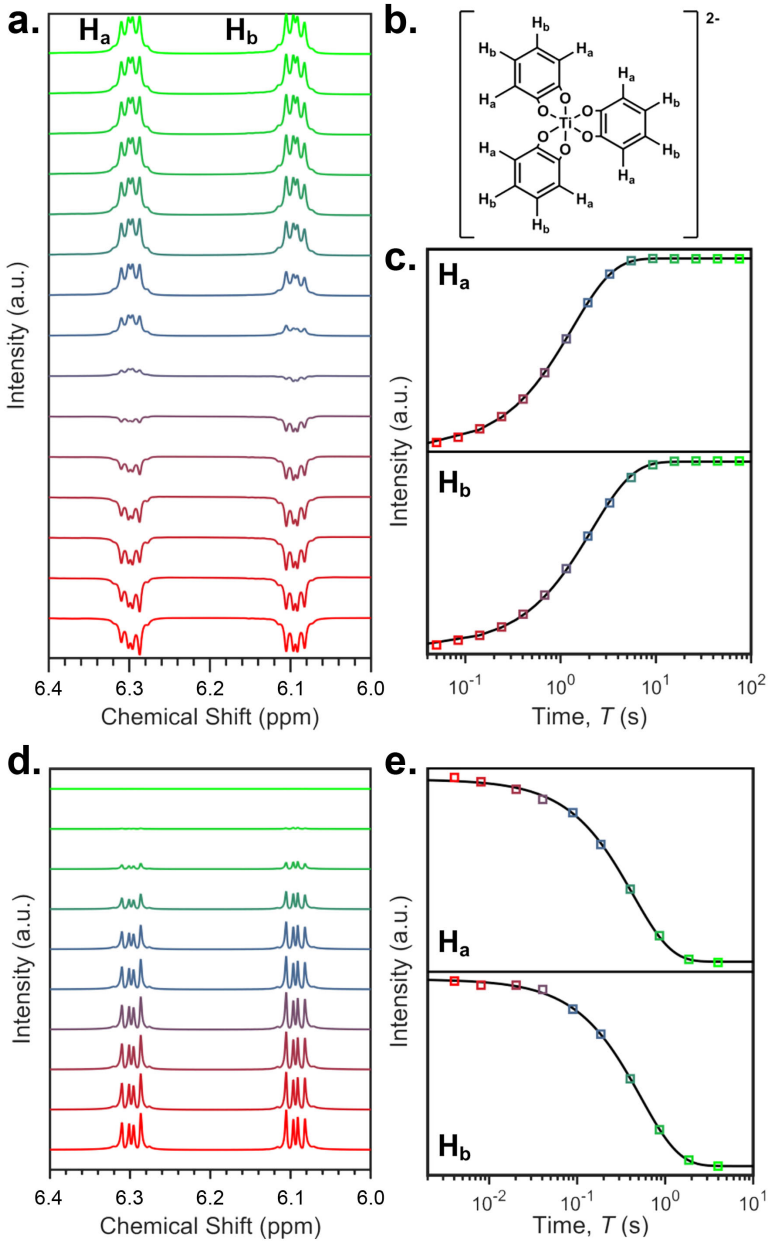

Figure 5.5. Example ^{1}H NMR analyses of a Ti(IV) catecholate complex molecule, here **1a**. **(a)** Inversion-recovery spectra – the offset spectra represent different delay times between inversion and measurement, with the shortest delays at the bottom in green. **(b)** Depiction of ^{1}H peak assignment. **(c)** Peak intensity as a function of delay following inversion. The black line is a fit to an exponential recovery to yield T_1 for a given peak. **(d)** CPMG experimental results – the offset spectra represent different numbers of applied π pulses: the red spectrum at the bottom was collected with one π pulse and the fluorescent green spectrum at the top was collected with 10 π pulses. **(e)** ^{1}H peak intensity versus total time after the π /2 pulse. The black line is a fit to an exponential decay to yield T_2 for the indicated peak.

Table 5.2. Tabulated aromatic ^{1}H spin-spin relaxation times (T_2) determined with CPMG pulse sequences.[a,b,c]

Ligands	Ring Position			
	3	4	5	6
1	5.1(2)	5.0(2)	5.0(2)	5.1(2)
2	-	6.3(6)	5.4(6)	6.0(3)
3	6.8(2)	-	6.5(2)	6.3(2)
4	-	10.9(9)	-	9.8(6)
5	6.5(3)	-	-	6.5(3)
6	-	-	-	4.30(4)
7	-	-	18(1)	-

Complexes	Ring Position			
	3	4	5	6
1a	0.85(7)	0.9(3)	0.9(3)	0.85(7)
3a	0.22(1)	-	0.22(2)	0.23(1)
4a	-	3.42(4)	-	2.87(1)
5a	2.65(4)	-	-	2.65(4)
6a	-	-	-	2.88(5)

[a] T_2 values given in units of seconds. [b] There are no aromatic protons for **8** and **8a**, hence the omission. [c] T_2 values for OH groups and $Me_2NH_2^+$ counterions can be found in the SI.

removes field inhomogeneities as a potential impact on spin-spin relaxation – ensuring any determined trends are attributable to the studied complexes and not extrinsic effects. As with T_1, the time-dependent data set could be effectively modeled with a single exponential function, implying a single relaxation process is dominant. Critically, as with T_1, T_2 is peak-dependent.

The T_2 times of the aromatic protons in **1**–**8** broadly follow the trends seen in the T_1 data – greater degrees of bromination produce longer ^{1}H T_2 values (see Table 5.2). For example, the adjacent ligand ^{1}Hs on **1** were found to have T_2 parameters of approximately 5 s, which are the shortest of the series (second to **6**, see below). The singly brominated ligands **2** and **3** both have T_2 values that are larger than **1**, again consistent with T_1 trends. Furthermore, protons in **3** and **5** that are isolated from the others by bromination show similar T_2 values. The doubly brominated **5**'s T_2 values fall within the range of **3**'s relaxation times. In contrast, the compositional isomer to **5**, with relatively closer ^{1}H spins, **4**, shows > 60% relative lengthening of T_2. The two triply brominated ligands also display radically different T_2 values. **6** was found to have a T_2 of 4.30(4) s, shorter even than **1**. In contrast, **7** exhibits the longest T_2 of all the ligands, 18(1) s, exceeding

the T_1 of pyrocatechol. In summary, these data show substantial variation in T_2 with substitutional patterning that mimics the trends in T_1.

As with T_1, the spin-spin relaxation times of the aromatic ^{1}H ligand peaks all decrease upon complexation and generally follow the trends in T_1. For example, the ligand ^{1}Hs in **1** exhibit the second-shortest T_2 values (~0.9 s), generally smaller than complexes where ^{1}H spins are separated by bromines, which have T_2 parameters ranging from 2.65(4) s in **5a** to 3.42(4) s in **4a**. But, there are a few important exceptions in the correlation to T_1. For example, the aromatic ^{1}H

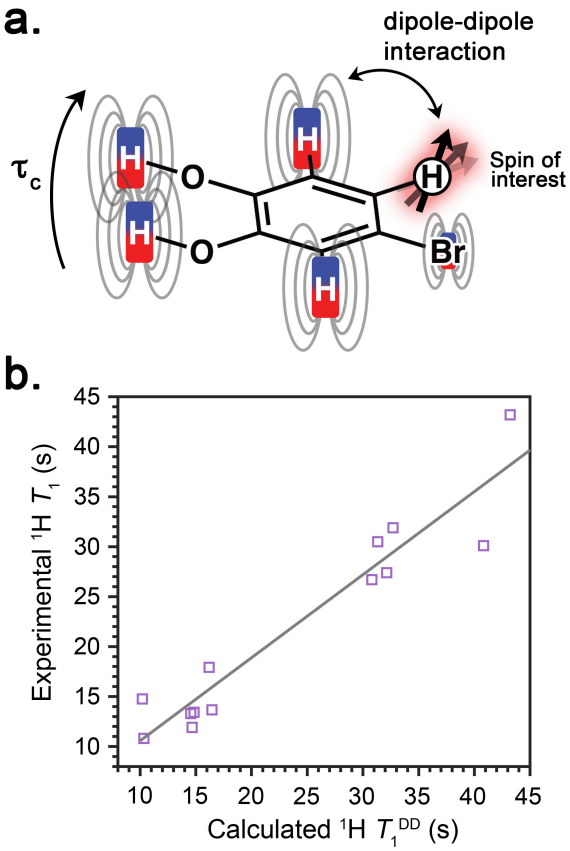

Figure 5.6. **(a)** Each proton in the ligand experiences dipolar interactions with other nuclear spins in its vicinity. Rotation of the molecule (on a timescale called the correlation time, τ_c) impacts the T_1 and T_2 of a spin of interest through dipolar coupling between the spin of interest and other nuclear spins in the environment. **(b)** Comparison of the experimental ^{1}H ligand T_1 relaxation times with the computed T_1 considering only dipole-dipole interactions, T_1^{DD} and assuming the same τ_c, 9 ps, for **1-7** (**8** has no protons on the ligand shell). The high correlation between the two data sets (gray line, R^2 = 0.91) suggests that spin-lattice relaxation in these systems is governed predominantly by dipole-dipole effects between a given proton and its nearest neighbors.

peaks of **3a** have the shortest T_2 values of the studied complexes (0.22(1) to 0.23(1)) s, despite having a Br atom. Second, the complex with triply brominated ligands, **6a**, has a T_2 that is within the range of the other complexes (2.88(5) s), when the ligand for this complex, **6**, has the longest T_2 of all the ligands. These few exceptions point to more complicated relaxation dynamics in the complexes than dipole effects from only the ligand shell, in contrast to the pure ligands.

The collected NMR data paint a rich picture of the ^{1}H nuclear spin dynamics within the studied species, also revealing a path toward bespoke nuclear magnetization dynamics in the ligand shell. The results further point toward dipole-driven relaxation processes as the synthetically tunable feature. Here, whenever a proton is replaced by a $^{79/81}$Br nucleus in a given ligand, the strong ^{1}H•••^{1}H interaction of that proton with neighboring ones is replaced by the relatively weaker coupling to the bromine (as $^{79/81}$Br have a smaller magnetic moment). This switch results in the general lengthening of both T_1 and T_2 for the ^{1}H spins with increasing bromine content across the series of tested ligands. In the following analyses, note that we ignore the impact of potential ^{13}C nuclear spins in the ligands, as this $I = {}^1/_2$ isotope is only 1% naturally abundant.[23]

We tested the correlation between ^{1}H relaxation times and dipolar interactions to better quantitate the T_1/T_2 trends for the studied species. For this test, we computed the ^{1}H dipole-driven spin-lattice (T_1^{DD}) and spin-spin (T_2^{DD}) relaxation times which stem from a sum of dipole-dipole interactions with all surrounding magnetic nuclei and a rotational correlation time (Fig. 5.6), τ_c[37-39] (see Experimental for detailed equations and interpretation). Comparison of the experimental T_1 and T_2 values with the computed values are shown in Figs. 6 and 5.20. Relatively good linear correlations are seen for T_1 (R^2 = 0.91), when the τ_c values for all protonated catechol ligands (**1-7**) are assumed to be 9 ps, as is typical of small molecules.[36] Low correlation with T_2 is observed, however, which may stem from the CPMG sequence, as well as the fundamental assumption of the same τ_c for all ligands (see Experimental section). When the experimental T_1 is set as T_1^{DD},

numerical solutions for τ_c are obtained. The determined τ_c values via this method range from ca. 6 to 12 ps, well within the bounds of what is reasonable for small organic molecules (Table 5.7).[40-42] This slight variation in τ_c for protons in ligands/complexes with the nearly the same chemical composition likely stems from differences in mass distributions (owing to the heavy Br atoms), which will affect motion in solution.[43,44]

Similar comparison of experimental ^{1}H T_1/T_2 with T_1^{DD}/T_2^{DD} for the metal complexes is of lower quality, and τ_c cannot be extracted in some cases, unlike the ligands (Table 5.7). When τ_c times can be extracted, they are categorically longer than those for the ligands, consistent with the picture of decreased relaxation times for longer τ_c values in small molecules. Furthermore, the general trend in spin dynamics from the ligands carries over to the metal complexes: when protons are separated by Br atoms, ^{1}H spin relaxation becomes slower. On this basis, we conclude that the general mechanism of ^{1}H spin relaxation in the ligands is likely also present in the metal complexes. Precise modeling of T_1 and T_2 here would require explicit intramolecular association (as is known for catechol),[45] and ligand-to-ligand and ligand-to-$H_2NMe_2^+$ interactions. We posit that the impact of the counterion is relatively weak. Otherwise, T_1 and T_2 would be smaller for every ^{1}H in the 3 and 6 positions of the studied complexes, as these positions are closest to the hydrogen-bonded counterion. In this light, **3a** and **4a** are important, as the 3- and 6-position protons here have T_1 or T_2 values that are comparable or longer than protons in the 4 and 5 positions. Other factors that prevent perfect correlation include lengthening of T_2 via the quantum zeno effect[46] and other relaxation processes, e.g. scalar, or chemical shift anisotropy processes, though they are relatively minor contributions to ^{1}H T_1 and T_2 compared to the dipolar mechanism.[36,37] Future studies by us will test many of the foregoing ideas, especially counterion effects.

As one final point, the impact of the bromination in the ligands and complexes could be linked to manipulation of τ_c, not control of dipolar interactions. However, the trends in τ_c do not

follow the trends in T_1 or T_2. For example, the longest T_1 observed in the ligands is 17.8(3) s for **7** yet this ligand exhibits a correlation time (τ_c = 8.8 s) well within the range of all of the other ligands (6.1 to 12 s). Furthermore, the shortest τ_c times for the metal complexes was found for **1a**, yet this complex does not display the shortest T_1 and T_2 for the studied complexes. We take this observation and the correspondence of the trends in the ligands and complexes as the final evidence that the operative mechanism by which spin patterning affects relaxation is through dipolar interactions.

It is noteworthy that comparison of the foregoing results with trends in ^{1}H T_1 and T_2 for other ligand systems is nearly impossible, since explicit studies targeting ligand nuclear spin dynamics via synthetic design are, to the best of our knowledge, unrepresented in the literature. We can, however, compare our results with studies of proton spin dynamics in simple haloalkanes. Here, our results agree with these previous studies, which found increasing T_1 and T_2 with increasing degree of halogenation via weakening the overall ^{1}H•••^{1}H dipolar interactions.[38,39] These studies found relative variation in T_1 of up to a factor of sixteen, slightly lower than we found for our metal complexes, but beyond what we observed for the isolated ligands. This benchmark underscores the high tunability in the nuclear spin-dynamics of ligands (given the discovery of the right design strategies) and also the importance of coordination.

Conclusions

The dynamics of nuclear spins close to metal-based electronic spins are profoundly important for determining electronic spin relaxation times. Yet, understanding how to control those nuclear spin dynamics to precisely direct the magnetic properties of metal ions is a significant fundamental challenge. This paper represents an important step toward that goal by clearly demonstrating (1) the possibility of controlling the dynamics of ligand-based nuclei via patterning and (2) that design principles for isolated ligands can be translated directly to metal complexes (if

that metal is closed-shell). Importantly these results also demonstrate that the design principles for T_1 and T_2 are enhanced upon coordination, suggesting that future studies of nuclear spin dynamics in the ligand shell will yield significant fundamental insight. An enormous body of knowledge targets understanding how coordination geometry, symmetry, donor atom strength, etc, affect electron spin relaxation in metal complexes (e.g. refs 47-53). But, to the best of our knowledge, none has tested direct synthetic manipulation of the nuclear spin dynamics within the ligand shell as a potential design parameter for lengthening electron spin relaxation. We thus hope that this work and others from our group will inspire future studies in this undoubtedly rich area.

Experimental

General Considerations. Syntheses and handling of catechols **1–8** proceeded without precaution for air sensitivity unless otherwise indicated below. In contrast, all manipulations of the titanium complexes **9**−**14** were performed under a N_2 atmosphere with a Vigor glovebox and Schlenk techniques. Glassware was either oven-dried at 150 °C for at least 4 h and/or flame-dried before bringing into the glovebox. Tetrahydrofuran (THF), diethyl ether (Et_2O), and DMF were dried using a commercial solvent purification system from LC Technology Solutions and were stored over 4 Å molecular sieves prior to use. 4 Å molecular sieves were stored in a 150 °C oven and activated at 280 °C under reduced pressure for at least 12 h prior to use. Deuterated solvents acetone-d_6 and DMSO-d_6 were purchased from Cambridge Isotopes, dried, and degassed prior to use. Catechol **(1)**, 3-bromocatechol **(2)**, 4-bromocatechol **(3)**, and tetrabromocatechol **(8)** were purchased from commercial suppliers, purified, and thoroughly characterized prior to use. $Ti(NMe_2)_4$ was purchased from Strem, moved into the glovebox, and used as received.

Pyrocatechol ($C_6H_6O_2$) (1) Catechol was purchased from a commercial supplier and sublimed prior to characterization. Melting point: 106.5-109 °C. ^{1}H NMR (acetone-d_6): 6.68 (dd, J = 3.6, 5.9 Hz, 2H), 6.82 (dd, J = 3.6, 5.9 Hz, 2H), and 7.76 (s, 2H) ppm. ^{13}C NMR (acetone-d_6): 115.3, 119.9,

and 145.1 ppm; IR (ATR, cm^{-1}): 3445, 3320, 1619, 1512, 1468, 1362, 1279, 1254, 1239, 1186, 1094, 1040, 936, 848, 769, 740, 630, 554, 491, and 448.

3-Bromocatechol ($C_6H_5BrO_2$) (2) 3-Bromocatechol was purchased from a commercial supplier and used as purchased. Melting point: 37.5-38.0 °C. ^{1}H NMR (acetone-d_6): 8.58 (s, 1H), 7.89 (s, 1H), 6.97 (d, J = 8.1 Hz, 1H), 6.84 (d, J = 7.9 Hz, 1H), and 6.63 (td, J = 8.1, 2.1 Hz, 1H) ppm. ^{13}C NMR (acetone-d_6): 145.98, 142.99, 123.50, 120.59, 114.45, and 109.36 ppm. IR (ATR, cm^{-1}): 3363, 1594, 1459, 1350, 1315, 1253, 1232, 1182, 1157, 1124, 1063, 872, 814, 758, 717, 705, 624, 561, and 459.

4-Bromocatechol ($C_6H_5BrO_2$) (3) 4-Bromocatechol was purchased from a commercial supplier and sublimed prior to characterization. Melting point: 86.5-87.5 °C. ^{1}H NMR (acetone-d_6): 8.27 (s, 1H), 8.13 (s, 1H), 6.99 (d, J = 2.2 Hz, 1H), 6.85 (dd, J = 8.4, 2.2 Hz, 1H), and 6.77 (d, J = 8.4 Hz, 1H) ppm. ^{13}C NMR (acetone-d_6): 123.38, 119.10, 119.03, 117.66, 117.59, and 111.49 ppm. IR (ATR, cm^{-1}): 3485, 3283, 1602, 1500, 1447, 1430, 1330, 1268, 1232, 1202, 1165, 1108, 923, 880, 853, 839, 794, 776, 631, 572, and 445.

3,5-Dibromocatechol ($C_6H_4Br_2O_2$) (4) 3,5-Dibromocatechol was synthesized by a slightly modified literature procedure for the Dakin oxidation of salicylaldehyde,[25] with this procedure using 3,5-Dibromosalicylaldehyde as starting material. Melting point: 64.5-67.5 °C. ^{1}H NMR (acetone-d_6): 9.13 (s, 1H), 8.28 (s, 1H), 7.16 (d, J = 2.3 Hz, 1H), and 7.02 (d, J = 2.3 Hz, 1H) ppm. ^{13}C NMR (acetone-d_6): 147.66, 143.70, 126.17, 118.25, 111.49, and 110.77 ppm. IR (ATR, cm^{-1}): 3447, 3306, 3081, 1599, 1579, 1470, 1427, 1331, 1315, 1261, 1244, 1219, 1136, 909, 881, 856, 833, 690, 597, 568, and 455.

4,5-Dibromocatechol ($C_6H_4Br_2O_2$) (5) 4,5-Dibromocatechol was synthesized by aromatic bromination of **(1)** following the literature procedure of Kohn et al.[54] Melting point: 121.0-123.0 °C. ^{1}H NMR (acetone-d_6): 8.56 (s, 2H) and 7.15 (s, 4H) ppm. ^{13}C NMR (acetone-d_6): 146.59, 120.50, and 113.47 ppm. IR (ATR, cm^{-1}): 3492, 3442, 3320, 1606, 1592, 1493, 1408, 1333, 1310, 1261, 1228, 1204, 1152, 1098, 912, 861, 831, 797, 698, 631, 518, 462, 413.

3,4,5-Tribromocatechol ($C_6H_3Br_3O_2$) (6) 3,4,5-Tribromocatechol was synthesized following the literature procedure of Kohn et al.[54] Melting point: 135.3-137.3 °C. ^{1}H NMR (400 MHz, acetone-d_6): 9.22 (s, 1H), 8.53 (s, 2H), and 7.25 (s, 1H) ppm. ^{13}C NMR (acetone-d_6): 146.27, 145.07, 119.31, 117.05, 114.05, and 113.92 ppm. IR (ATR, cm^{-1}): 3507, 3477, 3074, 1591, 1577, 1452, 1395, 1335, 1315, 1287, 1251, 1224, 1205, 1152, 113, 923, 855, 849, 794, 740, 713, 635, 554, and 438.

3,4,6-Tribromocatechol ($C_6H_3Br_3O_2$) (7) 3,4,6-Tribromocatechol was synthesized following a literature procedure by refluxing tetrabromocatechol in the presence of zinc dust.[55] Melting point: 97.6-98.7 °C. ^{1}H NMR (acetone-d_6) 8.86 (s, 2H) and 7.41 (s, 1H) ppm. ^{13}C NMR (acetone-d_6): 145.91, 143.74, 127.14, 115.16, 112.84, and 110.02 ppm. IR (ATR, cm^{-1}): 3538, 3419, 3176, 3076, 1643, 1579, 1464, 1403, 1317, 1286, 1247, 1167, 1136, 910, 891, 844, 779, 712, 636, 542, 487, and 420.

Tetrabromocatechol ($C_6H_2Br_4O_2$) (8) Tetrabromocatechol was purchased from a commercial supplier and sublimed prior to characterization. Melting point: 195.5-198.9 °C. ^{1}H NMR (Acetone-d_6): 8.97 (s, 2H) ppm. ^{13}C NMR (Acetone-d_6): 144.65, 118.14, and 113.63 ppm. IR (ATR, cm^{-1}): 3464, 3414, 1564, 1552, 1446, 1375, 1315, 1287, 1262, 1237, 1151, 933, 902, 738, 684, 608, 574, 481, 436, and 410.

$(Me_2NH_2)_2[Ti(C_6H_4O_2)_3]$ (1a) In an N_2-filled glovebox, catechol (0.175 g, 1.59 mmol) was loaded into a 20 mL scintillation vial with 10 mL of THF and allowed to stir until combined. To this solution, $Ti(NMe_2)_4$ (118 µL, 0.500 mmol) was added with a micropipette, and the tip rinsed with the mixture to ensure all starting material was incorporated. The vial was then sealed and stirred overnight. The following day, the mother-liquor was dried under high vacuum, and solid powder collected. This powder was washed with Et_2O (10 mL) to yield **1a** (0.114 g, 61 % yield). Crystals suitable for X-ray diffraction were grown from Et_2O vapor diffusion into a concentrated solution of **1a** in DMF. ^{1}H NMR (DMSO-d_6): 8.61 (s, 4H), 6.29 (dd, J = 3.5, 5.6 Hz, 6H), 6.09 (dd, J = 3.5, 5.6 Hz, 6H), and 2.62 (s, 12H) ppm. ^{13}C NMR (DMSO-d_6): 159.75, 116.36, 110.35, and 34.73 ppm. IR (ATR,

cm^{-1}): 3004, 2748, 2476, 1469, 1325, 1241, 1100, 1022, 913, 863, 795, 747, 731, 624, 597, and 496. LTQ-MS (m/z), positive ion mode: $\{(Me_2NH_2)[H(Ti(C_6H_4O_2)_3](DMF)_2\}^+$, 610.171; negative ion mode: 373.017, $\{Ti(C_6H_4O_2)_3\}^{1-}$; 186.005, $\{Ti(C_6H_4O_2)_3\}^{2-}$. Combustion Analysis: Calcd for $C_{22}H_{28}N_2O_6Ti$•DMF, 55.87 %C; 6.56 %H; 7.82 %N. Found: 56.21 %C; 6.56 %H; 7.79 %N.

$(Me_2NH_2)_2[Ti(C_6H_3BrO_2)_3]$ (3a) In an N_2-filled glovebox, 4-bromocatechol (0.5587 g, 2.96 mmol) was loaded into a 20 mL scintillation vial with 10 mL of THF and allowed to stir until combined. To this solution, $Ti(NMe_2)_4$ (212 µL, 0.896 mmol) was added with a micropipette, and the tip rinsed with the mixture to ensure all starting material was incorporated. The vial was then sealed and stirred overnight. The following day, the mother-liquor was dried under high vacuum, and solid powder collected. This powder was washed with Et_2O (10 mL) to yield **3a** (0.547 g, 87 % yield). ^1H NMR (DMSO-d_6): 8.44 (s, 2H), 6.41 (dd, J = 8.1, 2.2 Hz, 3H), 6.20 (d, J = 2 Hz, 3H), 5.98 (d, J = 8.1 Hz, 3H), and 2.59 (s, 12H) ppm. ^{13}C NMR (DMSO-d_6): 161.41, 159.43, 118.07, 112.88, 110.66, 107.27, and 34.51 ppm. IR (ATR, cm^{-1}): 3894, 3675, 3475, 3303, 3137, 2424, 2234, 2058, 1990, 1962, 1718, 1541, 1410, 1336, 1294, 1137, 1067, 1030, 945, 853, 829, 745, 719, 597, 545, and 481. LTQ-MS (m/z): positive ion mode: $\{(Me_2NH_2)_3[Ti(C_6H_3BrO_2)_3]\}^+$, 747.917; $\{(Me_2NH_2)_2[HTi(C_6H_3BrO_2)_3]\}^+$, 700.864. Combustion Analysis: Calcd for $C_{22}H_{25}Br_3N_2O_6Ti$, 37.69 %C; 3.59 %H; 4.00 %N. Found: 37.68 %C; 3.56 %H; 3.80 %N.

$(Me_2NH_2)_2[Ti(C_6H_2Br_2O_2)_3]$ (4a) In an N_2-filled glovebox, 3,5-dibromocatechol (0.865 g, 3.229 mmol) was loaded into a 20 mL scintillation vial with 10 mL of THF and allowed to stir until combined. To this solution, $Ti(NMe_2)_4$ (237 µL, 1.00 mmol) was added with a micropipette, and the tip rinsed with the mixture to ensure all starting material was incorporated. The vial was then sealed and stirred overnight. The following day, the mother-liquor was dried under high vacuum, and solid powder collected. This powder was washed with Et_2O (10 mL) to yield **4a** (0.604 g, 64 % yield). In our hands, we found it difficult to remove all reaction solvent even by evacuation at high temperature. Hence, prior to combustion analyses, the powder was lyophilized with benzene. A small amount of this benzene remains, which could be located in the NMR spectrum and is

required to match the combustion analysis. ^{1}H NMR (DMSO-d_6): 8.17 (s, 2H), 6.65 (d, J = 2.3 Hz, 3H), 6.18 (dd, J = 2.2, 1.0 Hz, 3H), and 2.57 (s, 12H) ppm. ^{13}C NMR (DMSO-d_6): 161.17, 156.08, 120.43, 112.39, 107.48, 102.91, and 34.46 ppm. IR (ATR, cm^{-1}): 3036, 2773, 1611, 1546, 1450, 1396, 1244, 1171, 1018, 922, 845, 827, 715, 644, 578, 522, 510, and 431. LTQ-MS (m/z): positive ion mode: $\{(Me_2NH_2)_3[Ti(C_6H_2Br_2O_2)_3](THF)\}^+$, 1010.281; $\{(Me_2NH_2)_3[Ti(C_6H_2Br_2O_2)_3]\}^+$, 983.582; $\{(Me_2NH_2)_2[HTi(C_6H_2Br_3O_2)_3]\}^+$, 938.582; $\{(Me_2NH_2)[H_2Ti(C_6H_2Br_3O_2)_3]\}^+$, 893.520; negative ion mode: $\{HTi(C_6H_2Br_3O_2)_3\}^-$, 846.80. Combustion Analysis: Calcd for $C_{22}H_{22}Br_6N_2O_6Ti \bullet 0.35C_6H_6$, 29.99 %C; 2.52 %H; 2.90 %N. Found: 29.99 %C; 2.57 %H; 2.87 %N.

$(Me_2NH_2)_2[Ti(C_6H_2Br_2O_2)_3]$ (5a) In an N_2-filled glovebox, 4,5-dibromocatechol (0.424 g, 1.58 mmol) was loaded into a 20 mL scintillation vial with 10 mL of THF and allowed to stir until combined. To this solution, $Ti(NMe_2)_4$ (118 µL, 0.500 mmol) was added with a micropipette, and the tip rinsed with the mixture to ensure all starting material was incorporated. The vial was then sealed and stirred overnight. The following day, the mother-liquor was dried under high vacuum, and solid powder collected. This powder was washed with Et_2O (10 mL) to yield **5a** (0.228 g, 49 % yield). Crystals suitable for X-ray diffraction were grown from Et_2O vapor diffusion into a concentrated DMF solution of **5a**. ^{1}H NMR (DMSO-d_6): 8.21 (s, 4H), 6.00 (s, 6H), and 2.58 (s, 12H) ppm. ^{13}C NMR (DMSO-d_6): 160.46, 113.64, 108.68 and 34.54 ppm. IR (ATR, cm^{-1}): 3043, 2770, 2362, 2337, 1463, 1349, 1319, 1243, 1191, 1082, 1018, 930, 656, 528, 437, and 410. LTQ-MS (m/z), negative ion mode: 422.732 (base), $\{Ti(C_6H_2Br_2O_2)_3\}^{2-}$; 846.474, $\{Ti(C_6H_2Br_2O_2)_3\}^{1-}$. Combustion Analysis: Calcd for $C_{22}H_{22}Br_6N_2O_6Ti$, 31.08 %C; 3.35 %H; 5.17 %N. Found: 30.95 %C; 3.24 %H; 4.94 %N.

$(Me_2NH_2)_2[Ti(C_6HBr_3O_2)_3]$ (6a) In an N_2-filled glovebox, 3,4,5-dibromocatechol (0.940 g, 2.71 mmol) was loaded into a 20 mL scintillation vial with 10 mL of THF and allowed to stir until combined. To this solution, $Ti(NMe_2)_4$ (187 µL, 0.790 mmol) was added with a micropipette, and the tip rinsed with the mixture to ensure all starting material was incorporated. The vial was then sealed and stirred overnight. The following day, the mother-liquor was dried under high vacuum,

and solid powder collected. This powder was washed with Et_2O (10 mL) to yield **6a** (0.696 g, 75 % yield). ^{1}H NMR (DMSO-d_6): 8.34 (s, 4H), 6.46 (s, 3H), and 2.57 (s, 12H) ppm. ^{13}C NMR (DMSO-d_6): 159.24, 157.36, 113.22, 111.36, 109.73, 106.05, and 34.49 ppm. IR (ATR, cm^{-1}): 3476, 3289, 3130, 2984, 2835, 2686, 2357, 2155, 2016, 1979, 1635, 1568, 1508, 1260, 1280, 1138, 959, 911, 763, 692, 627, and 493. LTQ-MS (m/z), negative ion mode: 344.759 (base), $\{H(C_6HBr_3O_2)\}^{1-}$; 541.594, $\{Ti(C_6HBr_3O_2)_3\}^{2-}$; 1082.197 $\{Ti(C_6HBr_3O_2)_3\}^{1-}$. Combustion Analysis: Calcd for $C_{22}H_{19}Br_9N_2O_6Ti$, 22.50 %C; 1.63 %H; 2.39 %N. Found: 22.41 %C; 1.84 %H; 2.42 %N.

$(Me_2NH_2)_2[Ti(C_6Br_4O_2)_3]$ (8a) In an N_2-filled glovebox, tetrabromocatechol (0.609 g, 1.43 mmol) was loaded into a 20 mL scintillation vial with 10 mL of THF and allowed to stir until combined. To this solution, $Ti(NMe_2)_4$ (117 µL, 0.494 mmol) was added with a micropipette, and the tip rinsed with the mixture to ensure all starting material was incorporated. The vial was then sealed and stirred overnight. The following day, the mother-liquor was dried under high vacuum, and solid powder collected. This powder was washed with Et_2O (10 mL) to yield **8a** (0.495 g, 71 % yield). ^{1}H NMR (DMSO-d_6): 8.09 (s, 4H) and 2.59 (s, 12H) ppm. ^{13}C NMR (DMSO-d_6): 156.07, 112.72, 105.89, and 34.65 ppm. IR (ATR, cm^{-1}): 3465, 3302, 3140, 2425, 2234, 2058, 1996, 1559, 1489, 1362, 1274, 1250, 1072, 1030, 971, 816, 766, 614, 481, and 440. LTQ-MS (m/z), negative ion mode: 1319.800 $\{HTi(C_6Br_4O_2)_3\}^{1-}$; 1364.458 $\{(Me_2NH_2)[Ti(C_6Br_4O_2)_3]\}^{1-}$. Combustion Analysis: Calcd for $C_{22}H_{16}Br_{12}N_2O_6Ti$, 18.73 %C; 1.14 %H; 1.99 %N. Found: 18.56 %C; 1.24 %H; 1.83 %N.

Nuclear Magnetic Resonance Experiments. All samples were prepared in an N_2 glovebox and loaded into Teflon-sealed J-Young tubes for analysis. For relaxation studies of individual ligands, 200 mM solutions of **1-8** were prepared with dry, degassed acetone-d_6. For relaxation studies of the metal complexes, 100 mM solutions of **1a, 3a-6a, 8a** were prepared with dry, degassed DMSO-d_6. Catecholates were sublimed for purity prior to analysis. Preliminary ligand analyses conducted in both DMSO-d_6 and acetone revealed only ±0.1 ppm changes in aromatic ^{1}H δ as a function of solvent. Hence, solvent selection was dependent largely on solubility to enhance

signal/noise (see below). Spectra collected in DMSO-d_6 were referenced to δ = 2.50 ppm for ^{1}H analysis and δ = 39.52 ppm for ^{13}C analysis. ^{13}C spectra were proton decoupled. Spectra in acetone-d_6 were referenced to δ = 2.05 ppm for ^{1}H analyses and δ = 29.84 ppm for ^{13}C spectra.[56] All NMR spectra and nuclear spin relaxation dynamics data were collected on a Bruker NEO 400 MHz NMR spectrometer equipped with a broad-band BBFO probe. Individual spectra were processed with MestreNova,[57] and relaxation data were processed with Matlab,[58] using simple monoexponential decay/growth functions to extract T_2 and T_1. Spin-lattice relaxation times were collected via inversion recovery pulse sequences via free-induction-decay measurement, π – delay – $\pi/2$ – collect. Here, π and $\pi/2$ pulse lengths were 11 and 5.5 μs, respectively, and the starting delay was 50 ms for **1-8** and 10 ms for **1a**, **3a-6a**, and **8a**. Spin-spin relaxation times were collected by the Carr-Purcell-Meiboom-Gill (CPMG)[35,36] sequence: $\pi/2$ – delay – $[\pi$ – delay$]_n$ – collect, which n values ranging 0 to 12 steps. For these analyses, π and $\pi/2$ pulse lengths were 22 and 11 μs, respectively, and the delay length was fixed at 1 ms. For **1-8**, the recycle delays were 150 s for both T_1 and T_2 measurements. For metal complexes **1a, 3a-6a, 8a**, the recycle delays were 60 s for both T_1 and T_2 measurements.

Owing to solubility considerations, sample concentrations were changed between the ligands (200 mM) and their corresponding metal complexes (100 mM). Tests of the concentration dependence of the relaxation times (Figs. 5.22 and 5.23) demonstrate a concentration dependence for –OH, $–NH_2^+$, and $–CH_3$ protons. For the aromatic protons (the main foci of this report), however, the variation in concentration is less than (1) the variation in T_1 and T_2 as a function of different spin patterns and (2) the variation is less than the difference in T_1 and T_2 as a function of coordination. Hence, the variations are truly molecular in identity, and not stemming from a simple variation in concentration.

X-ray Diffraction Data Collection, Solution, and Refinement. Diffraction data on single crystals of **1a** and **5a** were collected at the X-Ray Diffraction facility of the Central Instrument Facility at Colorado State University. Data were collected on a Bruker D8 Quest ECO single-crystal X-ray diffractometer equipped with Mo Kα (λ = 0.71073 Å). Data were collected and integrated using Bruker Apex 3 software.[59] Absorption correction were applied using SADABS.[60] Space group assignments were determined by examination of systematic absences, E-statistics, and successive refinement of the structures. Crystal structures were solved using SHELXT[61] and refined with the aid of successive difference Fourier maps by SHELXL[62] operated in conjunction with OLEX2 software.[63] None of the crystals demonstrated decay by X-ray radiation over the course of the experiment. Hydrogen atoms were placed in ideal positions and refined using a riding model for all structures. All other atoms were refined anisotropically. See Tables 5.3 and 5.4 for refinement details. Structural pictures for the main manuscript were generated with Diamond,[64] while ellipsoid plots for Fig. 5.9 were generated with Mercury.[65]

All Other Physical Characterization. Melting point data were acquired on powder samples in glass capillaries with a Barnstead International Mel-temp Electrothermal Melting Point Apparatus. IR spectroscopic data were collected in attenuated total reflectance mode on neat powders with a Bruker Tensor II FTIR spectrometer. Mass spectrometry measurements were performed on acetonitrile solutions of **1a** and **3a-6a** with an Agilent Technologies 6224 TOF LC/MS with Dual ESI Ion Source. The Mass spectral analyses of **8a** were performed a Thermo-Finnigan linear trap quadrupole LC/MS-MS at the Central Instrument Facility (CIF) of the Colorado State University. All samples were examined in both positive and negative ion mode, and peak assignment was on the basis of m/z, interpeak spacing, and isotopic distributions.

Description of T_1 and T_2 modeling via dipolar interactions. Scripts were written in MATLAB to calculate the dipolar contribution to relaxation time. The primary spin-bearing nuclei on the studied molecules are $^{79/81}$Br ($I = {}^3/_2$) and ^{1}H ($I = {}^1/_2$). These nuclei are the only spins considered in our calculations. The $^{79/81}$Br impact was treated as a weighted average, using the relative natural

abundances of these two isotopes.[66] The abundance of other spin-bearing nuclei in the present system, i.e. ^{2}H (I = 1, 0.015%), ^{13}C (I = $^{1}/_{2}$, 1.108%), and ^{17}O (I = $^{5}/_{2}$, 0.037%), are small enough that their contributions to dipolar relaxation are likely insignificant, and were thus neglected.[67] The relative positions of each nucleus were taken from X-ray crystallographic data for catechol,[68] or the metal complexes from the Cambridge Crystallographic Database and used to calculate the internuclear distances between spin bearing nuclei. Incorporating Br substitutions into the calculations was accomplished by simply switching the H for Br, while keeping the C–Br distance the same as that for C–H (when crystal structures for complexes or ligands were not available). T_1 and T_2 are calculated using the canonical formulae for dipolar relaxation (eqs 1 and 2). For the case of two like nuclei, i.e. two protons, the following expressions were used:

$$\frac{1}{T_1^{DDL}} = \frac{1}{5}\gamma^4\hbar^2 I(I+1)\sum_i r_i^{-6}\left(\frac{2}{1+\omega^2\tau_c^2}+\frac{8}{1+4\omega^2\tau_c^2}\right)\tau_c \qquad \text{(eq 1)}$$

$$\frac{1}{T_2^{DDL}} = \frac{1}{5}\gamma^4\hbar^2 I\left(I+\frac{1}{2}\right)\sum_i r_i^{-6}\left(3+\frac{5}{1+\omega^2\tau_c^2}+\frac{2}{1+4\omega^2\tau_c^2}\right)\tau_c \quad \text{(eq 2)}$$

where γ is the proton gyromagnetic ratio, I is the spin quantum number, r_i is the distance between a particular proton and its i^{th} interaction partner, ω is the Larmor frequency, and τ_c is the rotational correlation time. The contribution to a proton's relaxation by interaction with a Br nucleus is determined with the following expressions (eqs 3 and 4):

$$\frac{1}{T_1^{DDU}} = \frac{1}{15}\gamma_X^2\gamma_S^2 I_S(I_S+1)\sum_S r_{XS}^{-6}\left(\frac{12}{\tau_c^2(\omega_S+\omega_X)^2+1}+\frac{6}{\tau_c^2\omega_X^2+1}\right.$$
$$\left.+\frac{2}{\tau_c^2(\omega_S-\omega_X)^2+1}\right)\tau_c \qquad \text{(eq 3)}$$

$$\frac{1}{T_2^{DDU}} = \frac{1}{15}\gamma_X^2\gamma_S^2 I_S(I_S+1)\sum_S r_{XS}^{-6}\left(\frac{6}{\tau_c^2(\omega_S+\omega_X)^2+1}+\frac{6}{\tau_c^2\omega_S^2+1}+\frac{3}{\tau_c^2\omega_X^2+1}+\frac{1}{\tau_c^2(\omega_S-\omega_X)^2+1}\right.$$

$$\left.+4\right)\tau_c \quad \text{(eq 4)}$$

where X is the proton of interest and S is the nucleus causing relaxation (here, one of the Br atoms). Separate analyses of only ^{1}H interactions, then including $^{79/81}$Br found that the contribution from Br was significant enough that we needed to include those atoms in our model. Finally, the total predicted relaxation time is calculated as the sum of the reciprocals of the like and unlike dipole-dipole terms (eq 5):[39,69,70]

$$\frac{1}{T_{1,2}^{DD}} = \frac{1}{T_{1,2}^{DDL}} + \frac{1}{T_{1,2}^{DDU}} \quad \text{(eq 5)}$$

Initial analyses relevant to Fig. 5.6 in the main manuscript were carried out with τ_c held constant cross the series of ligands, which, when compared to the experimental values, showed a strong positive correlation with T_1. The fits for T_2 were somewhat less conclusive, but the CPMG experiments used to determine T_2 may artificially lengthen the measurements, resulting in poorer fits.[69,71]

From the above expression for T_1, exact solutions for τ_c were found (Table 5.7). The solutions for τ_c were in the form of real and complex roots. The complex roots were discarded outright. The remaining two solutions for τ_c were of different orders of magnitude (ns and ps, respectively). The nanosecond results were discarded, as the rotation of small molecules in room-temperature solutions is typically on the order of picoseconds, and hence we deemed these more realistic.[69] Furthermore, we place additional confidence in using T_1 to compute τ_c rather than T_2 because of the potential impact of artificial lengthening via the CPMG sequence.[71]

The same analysis was applied to the series of measurements taken with the Ti(IV) metal complexes. The r^{-6} distance dependence of dipole-dipole interactions implies that the interaction

between dipoles on neighboring ligands in a coordination complex from the tested series is likely vanishingly small. For this reason, the dipolar analysis of the metal complexes considered only relaxation effects from nuclei on a single ligand. When applied to the complexes the model omits the impact of ligand hydroxyl protons as they leave the ligands upon complexation (as observed in ref. 31 and the structures of this manuscript). Computation of the τ_c values, as for the ligands, yielded real and complex roots. In some cases (e.g. **1a** and **3a**) certain protons *only* had imaginary roots. Clearly those values are unrealistic, and they stem from the fact that within the ligand-only, dipole-only description of relaxation, there is no way to change τ_c to make T_1^{DD} low enough to match the experimental T_1 for the "problematic" protons. Certainly, there are possible improvements to be made to the description of relaxation (see main text) though some of them would be extremely tough to establish, e.g. the impact of the counterion. Even then, we expect the counterion to wield minimal influence on T_1 and T_2. The counterion is likely mobile, and thus held close enough to impact a given ligand-based proton for only a short amount of time. Furthermore, if the counterion were a clear originator for T_1 and T_2 relaxation, then every proton in the 3 or 6 position of the catechol ligands would have a shorter T_1/T_2 than those further away in the 4 and 5 positions. Yet we see clear examples where this is not the case. In **4a**, for example, the proton "closer" to the potential counterion (in the 6-position) has a longer $T_{1\ \text{than}}$ the proton further away, in the 4 position. Additionally, in **3a**, all protons have nearly the same T_2 values, despite two of them being close to the counterion (3 and 6 position) and one further away (in the 4 position).

However, for all the fits that yield real values, the results are realistic – all τ_cs are larger than the individual ligands, which is expected, as a relatively larger Ti(IV) complex should tumble in solution more slowly than an individual catechol. A more complete model incorporating the counterion as well as changing inertial moments as a function of bromination may yield more accurate results and is a topic of further study from us.[35,72]

Table 5.3. Refinement Details for the Crystal Structure of **1a**•DMF**.**

Molecular formula	$(Me_2NH_2)_2[Ti(C_6H_4O_2)_3]\bullet C_3H_7NO$
Empirical formula	$C_{25}H_{35}N_3O_7Ti$
Formula weight	537.43
Temperature/K	120
Crystal system	Monoclinic
Space group	$P\,2_1/n$
a	12.6791(10) Å
b	11.2864(9) Å
c	18.7823(15) Å
α	90°
β	94.005(3)°
γ	90°
Volume	2681.2(4) Å^3
Z	4
ρ_{calc}	1.331
μ	0.366 mm^{-1}
F(000)	1136.0
Crystal size	0.32 × 0.87 × 0.28 mm^3
Radiation	MoKα (λ = 0.71073)
2θ range for collection	4.214 to 66.284°
Index ranges	$-19 \le h \le 19$, $-17 \le k \le 17$, $-28 \le l \le 28$
Reflections collected	313618
Independent reflections	10189 [R_{int} = 0.0556, $R_{\square}$ = 0.0145]
Data/restraints/parameters	10189/0/331
Goodness-of-fit on F^2	1.092
Final *R* indices [I ≥ 2σ (I)]	R_1 = 0.0472, wR_2 = 0.1231
Final *R* indices [all data]	R_1 = 0.0574, wR_2 = 0.1359
Largest diff. peak/hole	0.53/–0.86 eÅ^{-3}

Table 5.4. Refinement Details for the Crystal Structure of **5a**•2DMF**.**

Molecular formula	$(Me_2NH_2)_2[Ti(C_6H_2Br_2O_2)_3]\bullet 2C_3H_7NO$
Empirical formula	$C_{28}H_{36}Br_6N_4O_8Ti$
Formula weight	1083.88
Temperature/K	120
Crystal system	Monoclinic
Space group	*C* 2/c
a	22.2028(10) Å
b	15.0920(10) Å
c	11.2756(6) Å
α	90°
β	95.269(4) °
γ	90°
Volume	3762.3(4) $Å^3$
Z	4
ρ_{calc}	1.914 g/cm^3
μ	6.649 mm^{-1}
F(000)	2112.0
Crystal size	0.29 × 0.18 × 0.17 mm^3
Radiation	MoKα (λ = 0.71073)
2θ range for data collection	4.756 to 66.846°
Index ranges	$-34 \leq h \leq 34$, $-23 \leq k \leq 23$, $-17 \leq l \leq 17$
Reflections collected	251954
Independent reflections	7273 [R_{int} = 0.0718, $R_{\square}$ = 0.0176]
Data/restraints/parameters	7271/0/217
Goodness-of-fit on F^2	1.016
Final *R* indices [I ≥ 2σ (I)]	R_1 = 0.0241, wR_2 = 0.0676
Final *R* indices [all data]	R_1 = 0.0304, wR_2 = 0.0707
Largest diff. peak/hole	0.74/–0.91 $eÅ^{-3}$

Table 5.5. Interatomic Distances (Å) and Angles (°) for **1a** and **5a**.

	1a	**5a**
Ti–O	1.9785(9)	1.9738(9)
	1.9694(9)	1.9738(9)[e]
	1.9307(9)	1.9663(9)
	1.9818(9)	1.9663(9)[e]
	1.9684(9)	1.9517(9)
	1.9471(9)	1.9517(9)[e]
C–O[a]	1.3516(14)	1.3418(15)
	1.3457(15)	1.3356(15)
	1.3478(14)	1.3351(15)
	1.3429(14)	1.3418(15)[e]
	1.3479(15)	1.3356(15)[e]
	1.3457(15)	1.3351(15)[e]
C–C[b]	1.4072(18)	1.4139(17)
	1.4092(17)	1.4130(17)
	1.4083(17)	
O–Ti–O[c]	79.88(4)	80.09(4)
	79.40(4)	80.09(4)[e]
	80.47(4)	80.85(5)
O•••H–$NHMe_2$[d]	1.915	1.952
	1.922	1.952[e]
Ti•••H–$NHMe_2$[d]	3.313	2.995
	3.334	2.995[e]

[a]C–O bonds involving the coordinated catechol O atoms. [b]C–C bond for the O-attached C atoms on catechol. [c]Bite angle for catecholate ligands. [d]Computed in Mercury.[e]Generated by symmetry operation of the other unique parameters.

Table 5.6. Summary of relaxation times for OH peaks in free ligands and counterions in the metal complexes.

	T_1 (s)		T_2 (ms)	
Ligands	**OH**		**OH**	
1	12(1)		680(60)	
2	5.15(5), 5.04(5)		18(1), 20(1)	
3	13.4(7), 13.5(7)		100(1), 100(1)	
4	17(4), 15(3)		20(2), 24(1)	
5	13(2)		20(1)	
6[a]	8(3), 9(3)		1.6(1), 0.8(1)	
7[a]	-		1.3(1)	
8[a]	17(6)		0.74(1)	
Complexes	**NH_2**	**CH_3**	**NH_2**	**CH_3**
1a	0.58(1)	1.51(5)	28(1)	970(70)
3a	0.31(1)	0.82(9)	50(1)	440(2)
4a	0.76(4)	1.7(1)	36(5)	1060(60)
5a	0.53(2)	1.2(1)	50(1)	220(1)
6a	0.030(1)	0.16(1)	10(1)	100(1)
8a	0.52(1)	1.40(6)	11.6(3)	460(1)

[a]Hydroxyl protons on **6**,**7**, and **8** are too labile to measure with the chosen pulse sequence. Hence, we report here T_2* values, taken from the linewidth (fwhm = $1/\pi T_2^*$).

Table 5.7. Correlation time data determined by analyses of the ligand ^{1}H relaxation times for protonated ligands and complexes in this manuscript. All τ_cs are in units of ps.[a]

	Proton position			
Ligands	3	4	5	6
1	9.7	6.1	6.1	9.7
2	-	8.0	8.4	10.9
3	10.2	-	10.6	9.8
4	-	12.0	-	9.0
5	10.3	-	-	10.3
6	-	-	-	9.0
7	-	-	8.8	-
	Proton position			
Complexes[b]	3	4	5	6
1a	*	44.5	44.5	*
3a	*	*	*	-
4a	-	61.8	-	112
5a	150	-	-	150
6a	-	-	-	126

[a]Hyphens indicate not measured at this site, as the proton position was brominated. [b]Asterisks indicate only complex values of τ_c were obtained for these protons (see text above).

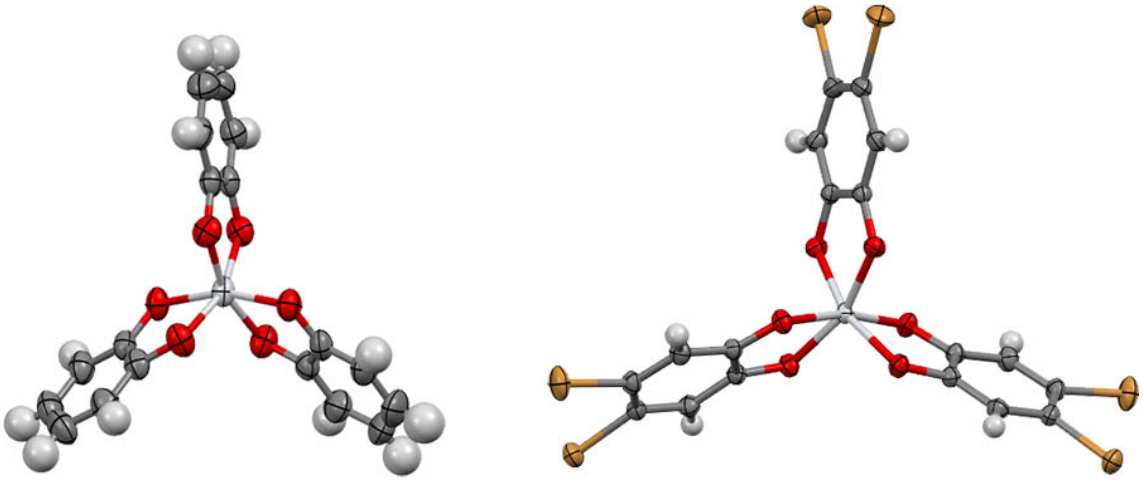

Figure 5.7. Thermal ellipsoid plots for the structures of the $[Ti(C_6H_4O_2)_3]^{2-}$ (left) and $[Ti(C_6H_2Br_2O_2)_3]^{2-}$ (right) moieties in the crystal structures of **1a** and **5a**, respectively. Ellipsoids are shown at the 75% probability level. Light gray, yellow/orange, dark gray, and red ellipsoids represent electron density from Ti, Br, C, and O atoms, respectively. The light gray spheres represent H atoms, which were refined isotropically.

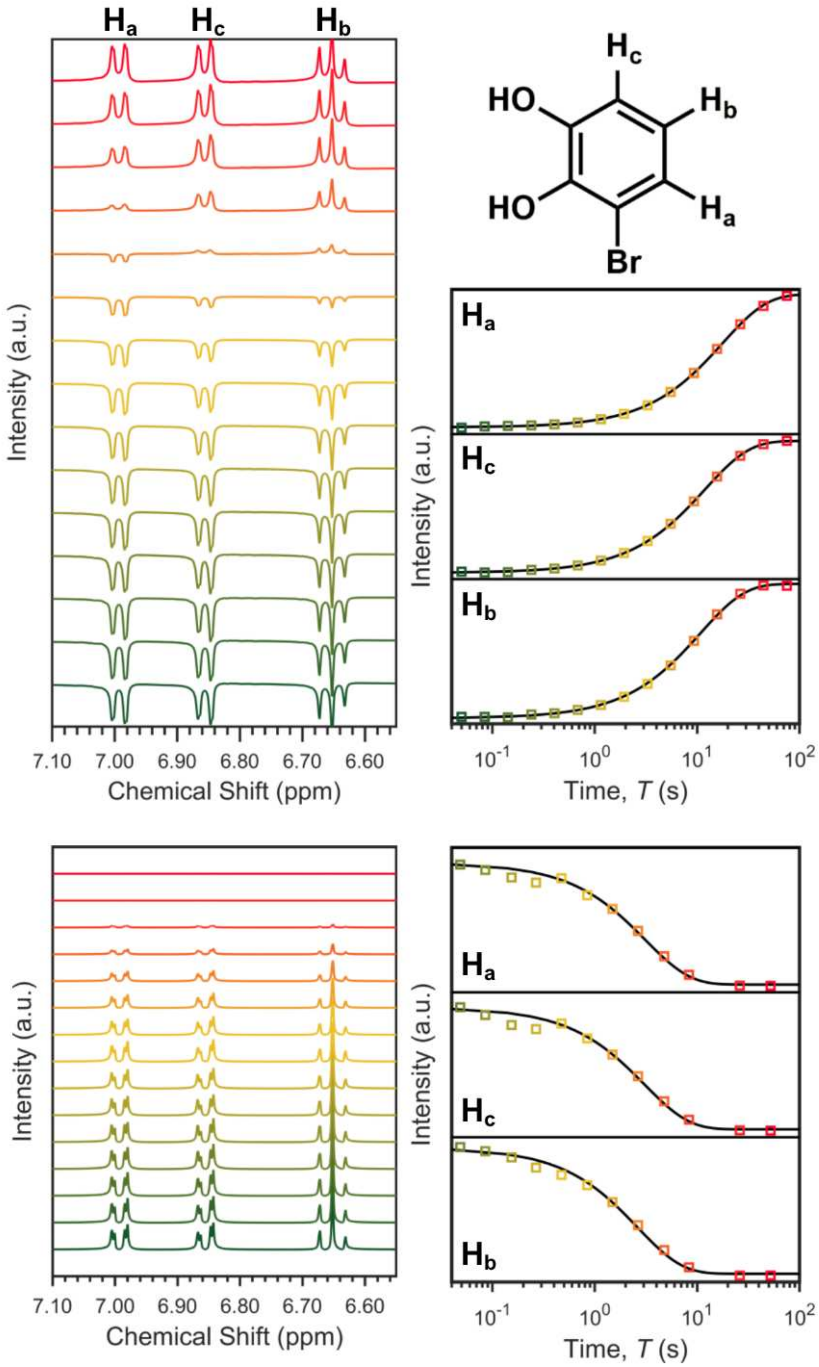

Figure 5.8. NMR analyses and assignments for **2**. **Top: Inversion recovery data.** Aromatic region of the ^{1}H NMR spectrum for **2** as a function of time after the initial inversion recovery pulse is shown. Integrals of these peaks generated the depicted intensity v. time plots. Black lines represent fits of the data to an exponential recovery. Peaks are labeled according to the depicted diagram for **2**. **Bottom: CPMG data.** ^{1}H NMR data from the aromatic region as a function of the number of pulses is shown. Intensities of these peaks are plotted as a function of time and fit to yield T_2.

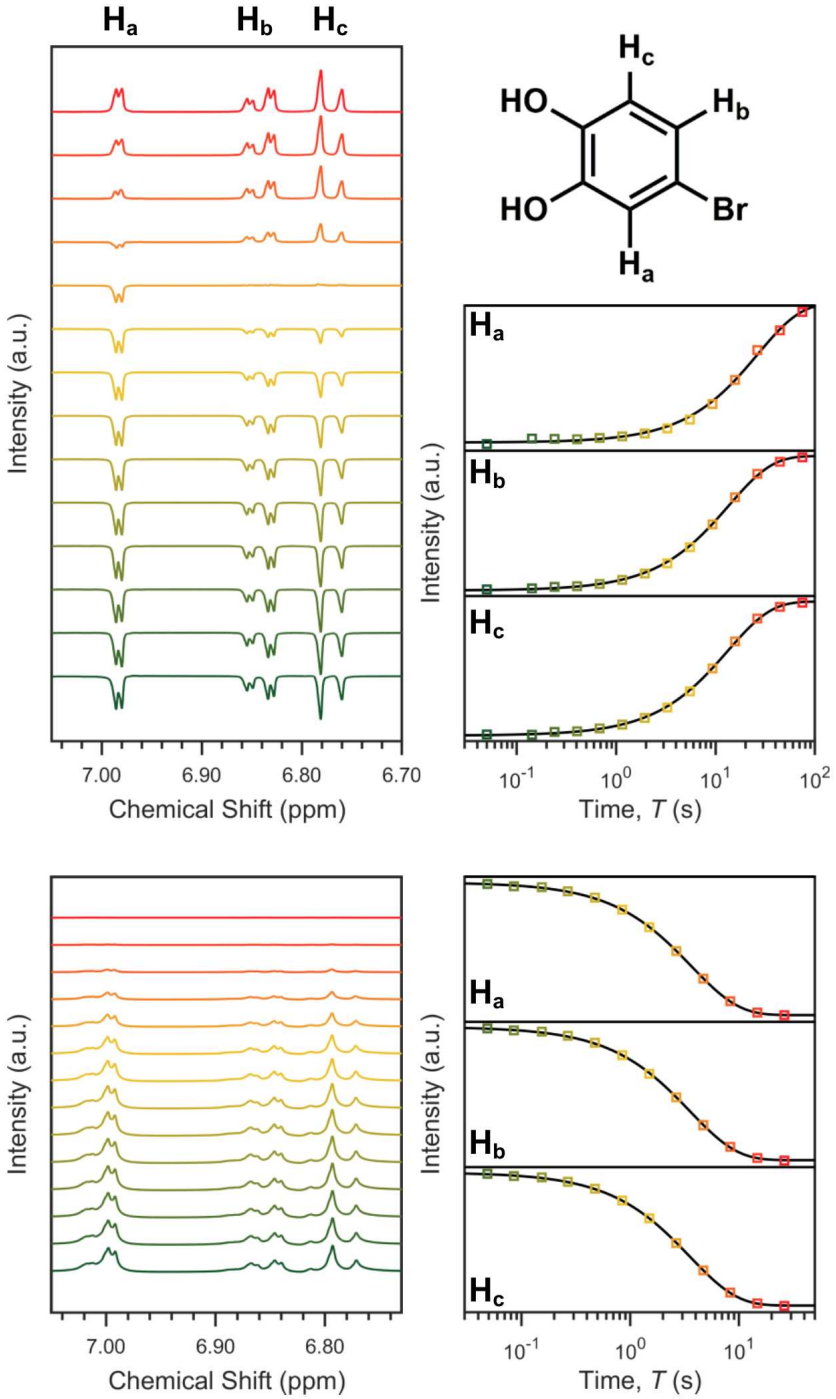

Figure 5.9. NMR analyses and assignments for **3**. **Top: Inversion recovery data.** Aromatic region of the ^{1}H NMR spectrum for **3** as a function of time after the initial inversion recovery pulse is shown. Integrals of these peaks generated the depicted intensity v. time plots. Black lines represent fits of the data to an exponential recovery. Peaks are labeled according to the depicted diagram for **3**. **Bottom: CPMG data.** ^{1}H NMR data from the aromatic region as a function of the number of pulses is shown. Intensities of these peaks are plotted as a function of time and fit to yield T_2.

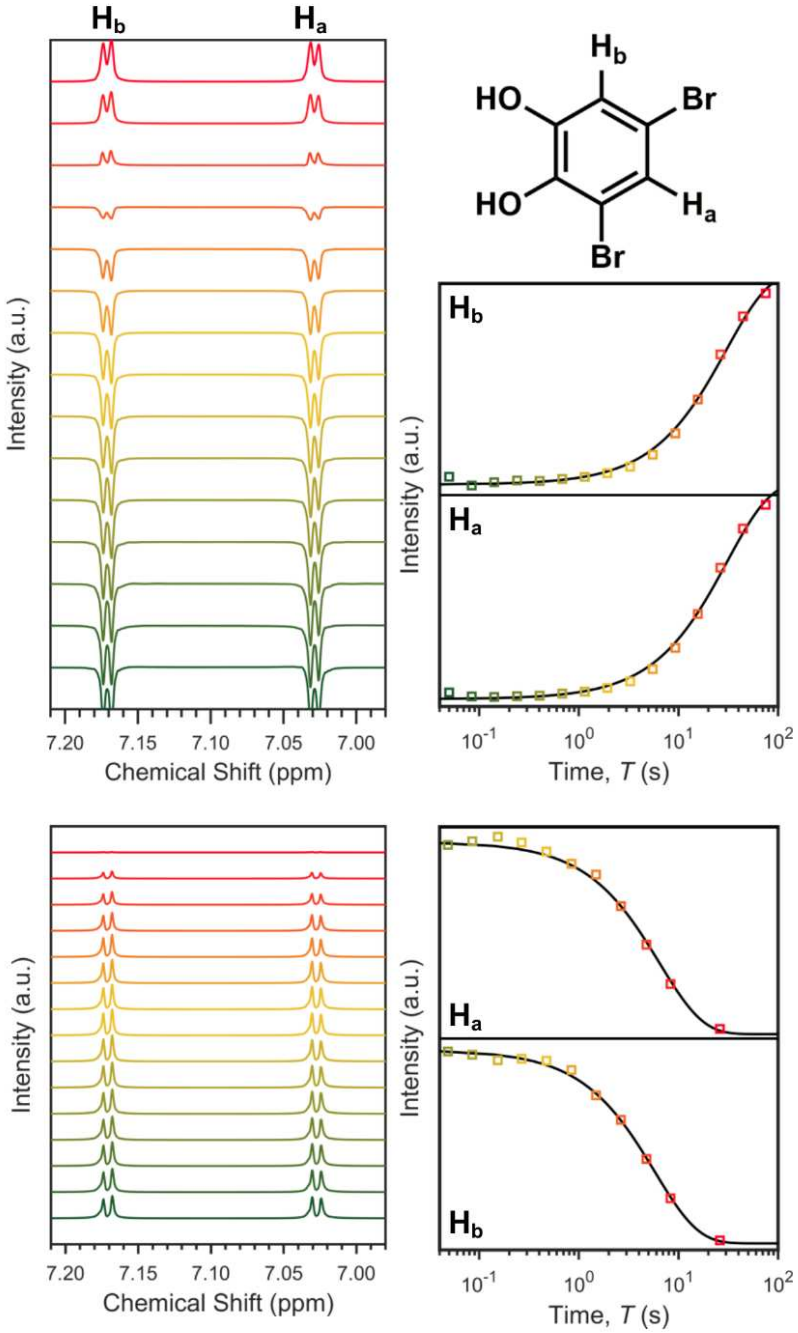

Figure 5.10. NMR analyses and assignments for **4**. **Top: Inversion recovery data.** Aromatic region of the ^{1}H NMR spectrum for **4** as a function of time after the initial inversion recovery pulse is shown. Integrals of these peaks generated the depicted intensity v. time plots. Black lines represent fits of the data to an exponential recovery. Peaks are labeled according to the depicted diagram for **4**. **Bottom: CPMG data.** ^{1}H NMR data from the aromatic region as a function of the number of pulses is shown. Intensities of these peaks are plotted as a function of time and fit to yield T_2.

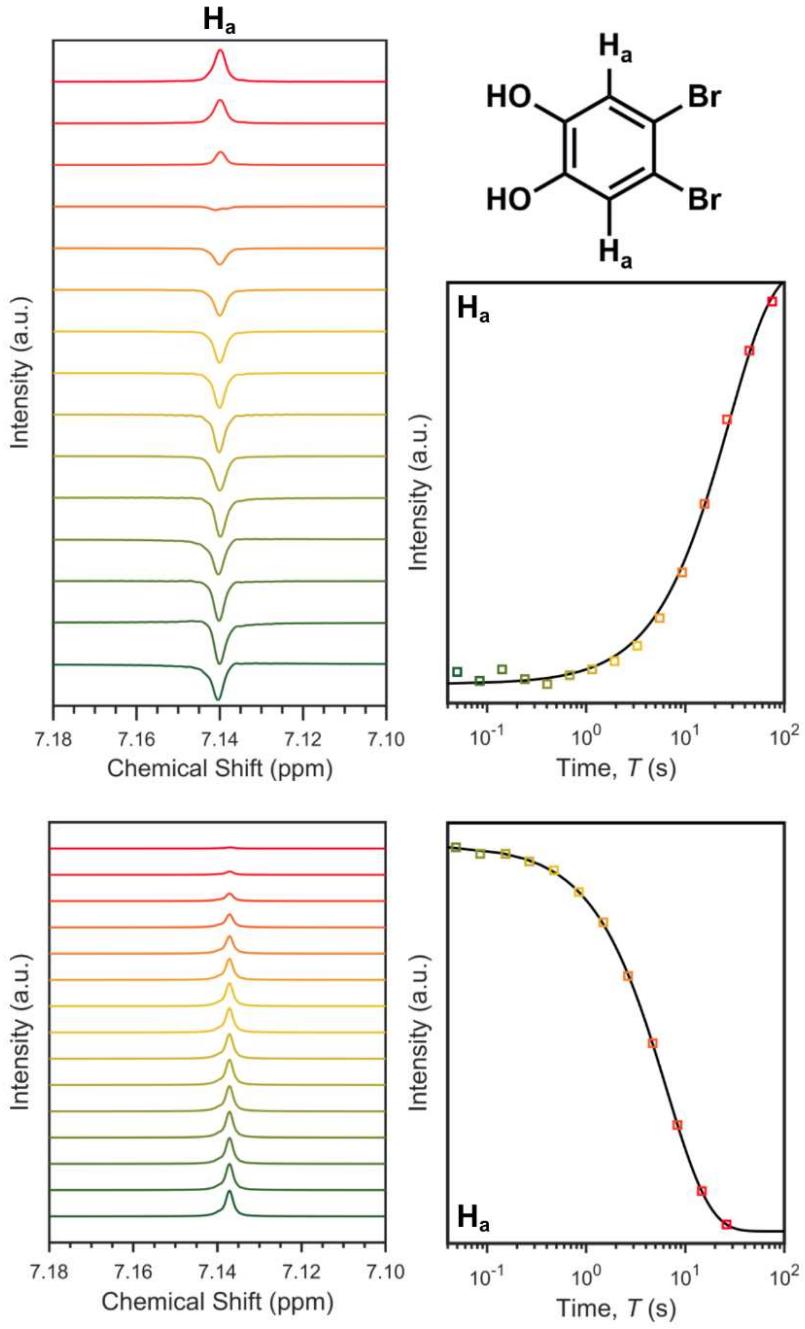

Figure 5.11. NMR analyses and assignments for **5**. **Top: Inversion recovery data.** Aromatic region of the ^{1}H NMR spectrum for **5** as a function of time after the initial inversion recovery pulse is shown. Integrals of these peaks generated the depicted intensity v. time plots. Black lines represent fits of the data to an exponential recovery. Peaks are labeled according to the depicted diagram for **5**. **Bottom: CPMG data.** ^{1}H NMR data from the aromatic region as a function of the number of pulses is shown. Intensities of these peaks are plotted as a function of time and fit to yield T_2.

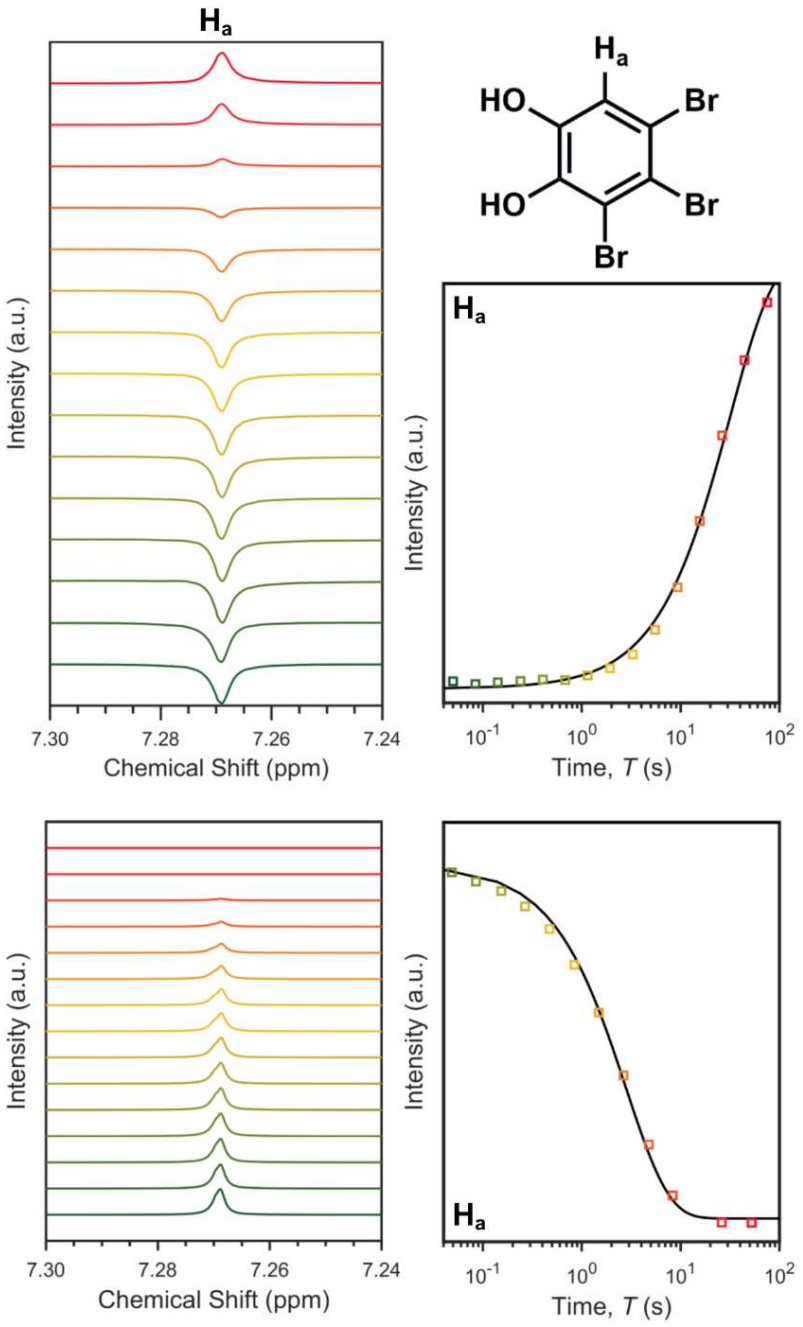

Figure 5.12. NMR analyses and assignments for **6**. **Top: Inversion recovery data.** Aromatic region of the ^{1}H NMR spectrum for **6** as a function of time after the initial inversion recovery pulse is shown. Integrals of these peaks generated the depicted intensity v. time plots. Black lines represent fits of the data to an exponential recovery. Peaks are labeled according to the depicted diagram for **6**. **Bottom: CPMG data.** ^{1}H NMR data from the aromatic region as a function of the number of pulses is shown. Intensities of these peaks are plotted as a function of time and fit to yield T_2.

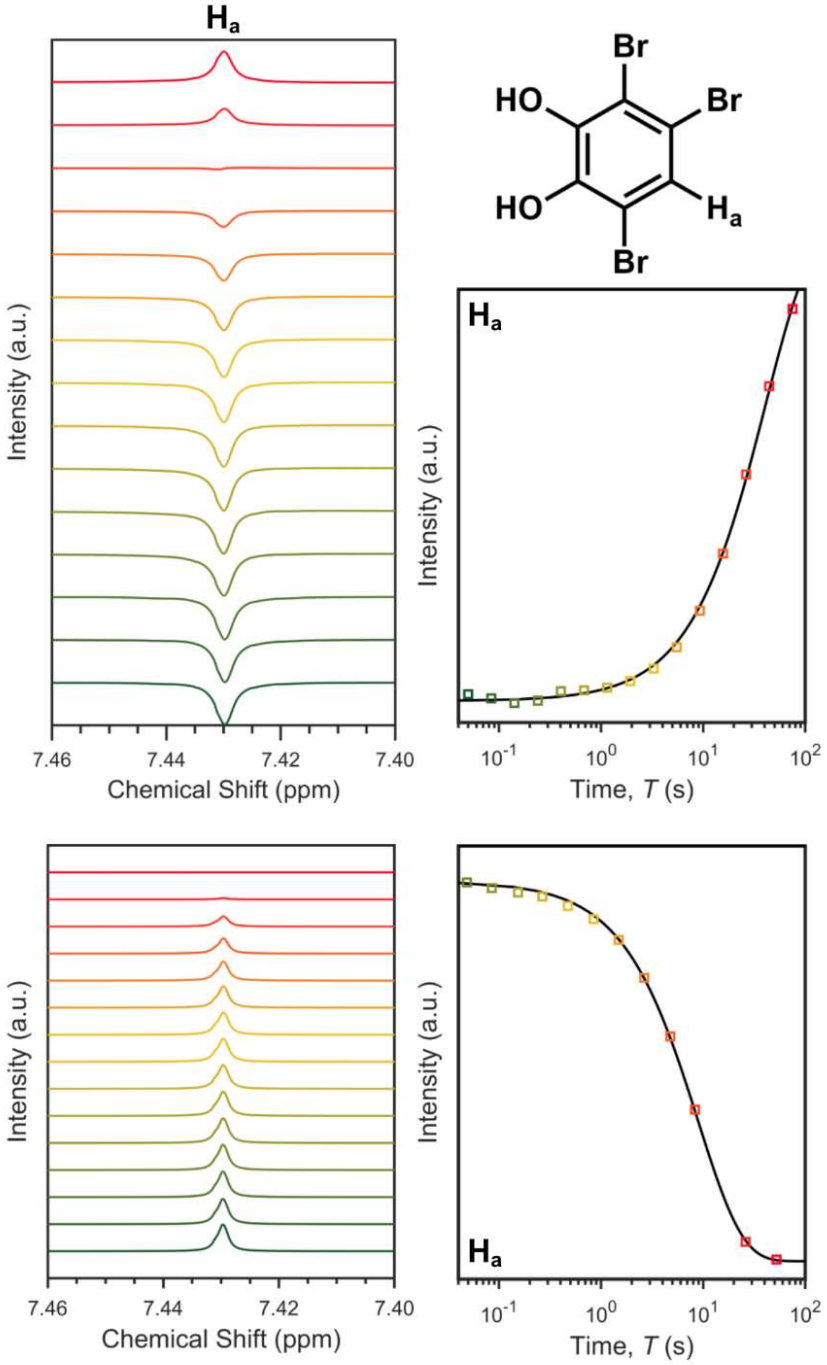

Figure 5.13. NMR analyses and assignments for **7**. **Top: Inversion recovery data.** Aromatic region of the ^{1}H NMR spectrum for **7** as a function of time after the initial inversion recovery pulse is shown. Integrals of these peaks generated the depicted intensity v. time plots. Black lines represent fits of the data to an exponential recovery. Peaks are labeled according to the depicted diagram for **7**. **Bottom: CPMG data.** ^{1}H NMR data from the aromatic region as a function of the number of pulses is shown. Intensities of these peaks are plotted as a function of time and fit to yield T_2.

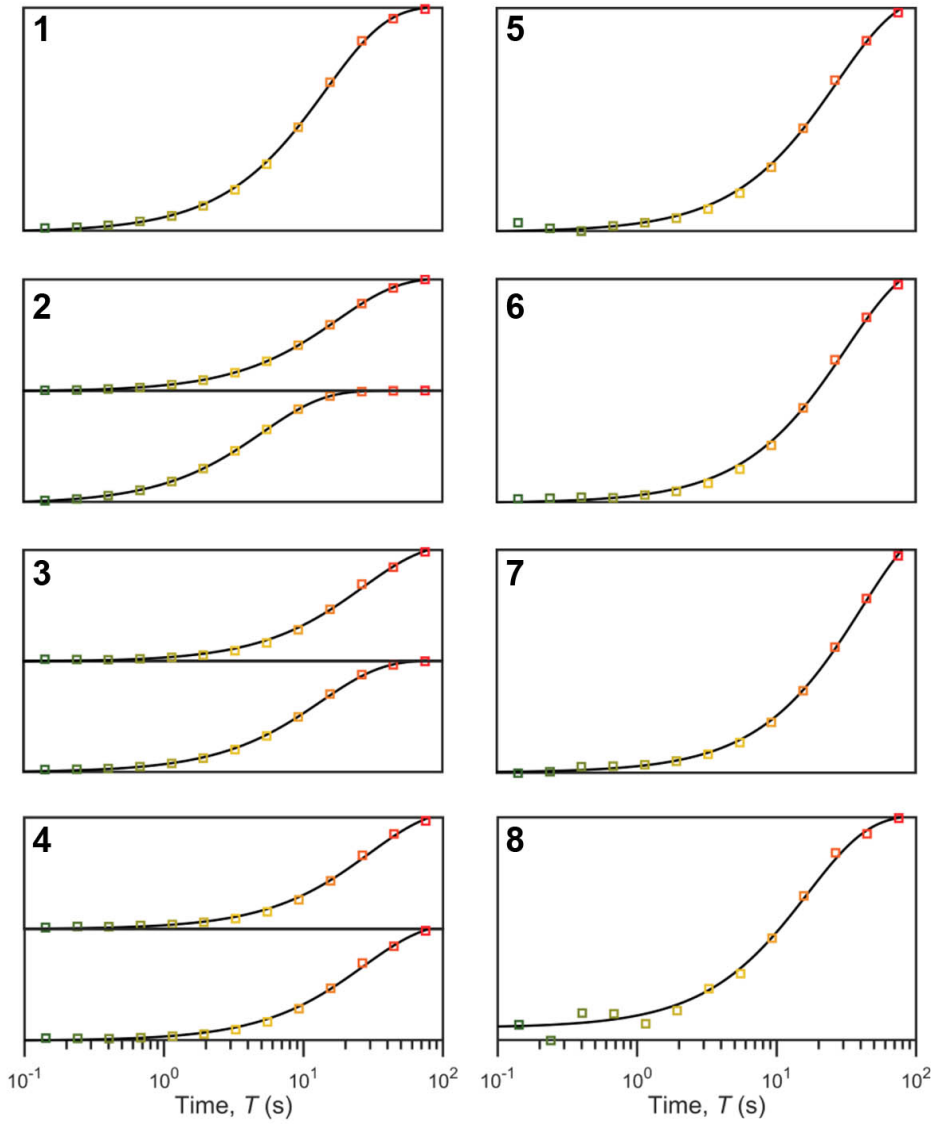

Figure 5.14: ^{1}H inversion recovery data for the O–H protons in ligands **1**-**8**. Ligands displaying only one OH peak have only one curve, ligands with two discernable OH peaks have the two curves presented. Black lines represent fits of the recovery to exponential recovery functions. The T_1 parameters resulting from these fits are given in Table 5.2 of the main manuscript.

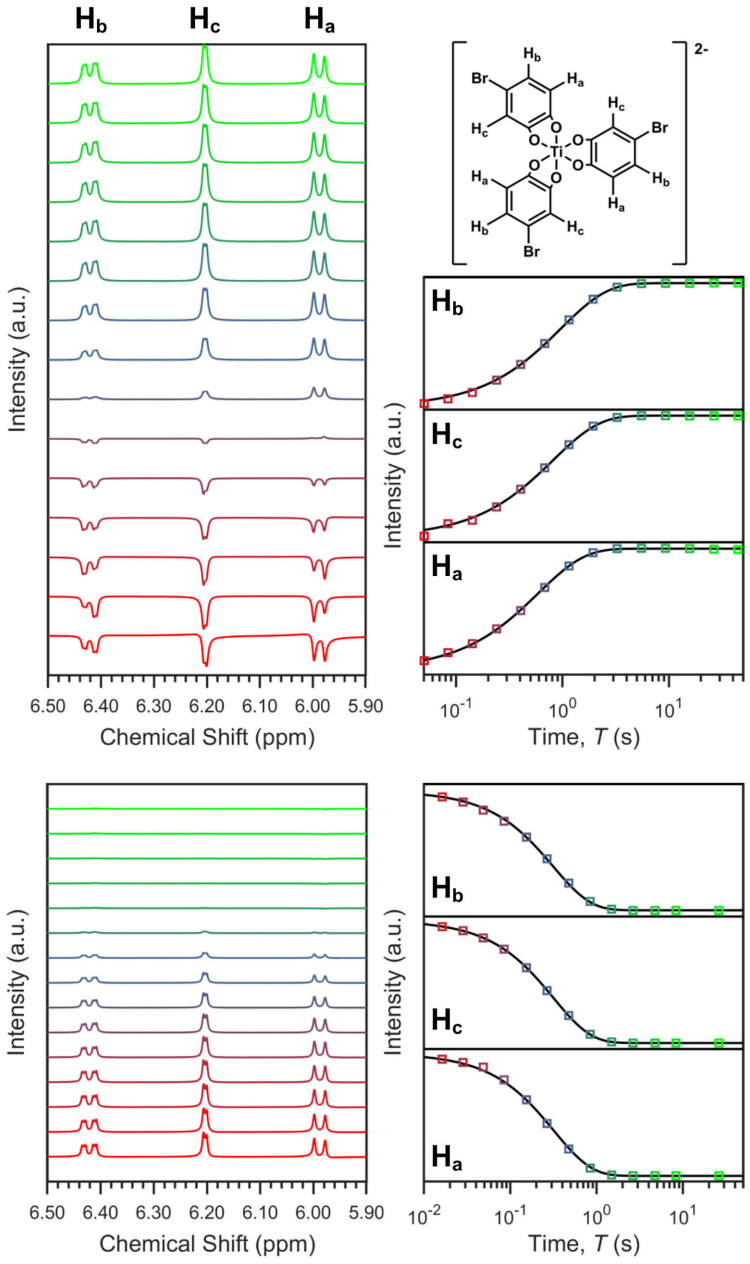

Figure 5.15. NMR analyses and assignments for **3a**. **Top: Inversion recovery data.** Aromatic region of the ^{1}H NMR spectrum for **3a** as a function of time after the initial inversion recovery pulse is shown. Integrals of these peaks generated the depicted intensity v. time plots. Black lines represent fits of the data to an exponential recovery. Peaks are labeled according to the depicted diagram for **3a**. **Bottom: CPMG data.** ^{1}H NMR data from the aromatic region as a function of the number of pulses is shown. Intensities of these peaks are plotted as a function of time and fit to yield T_2.

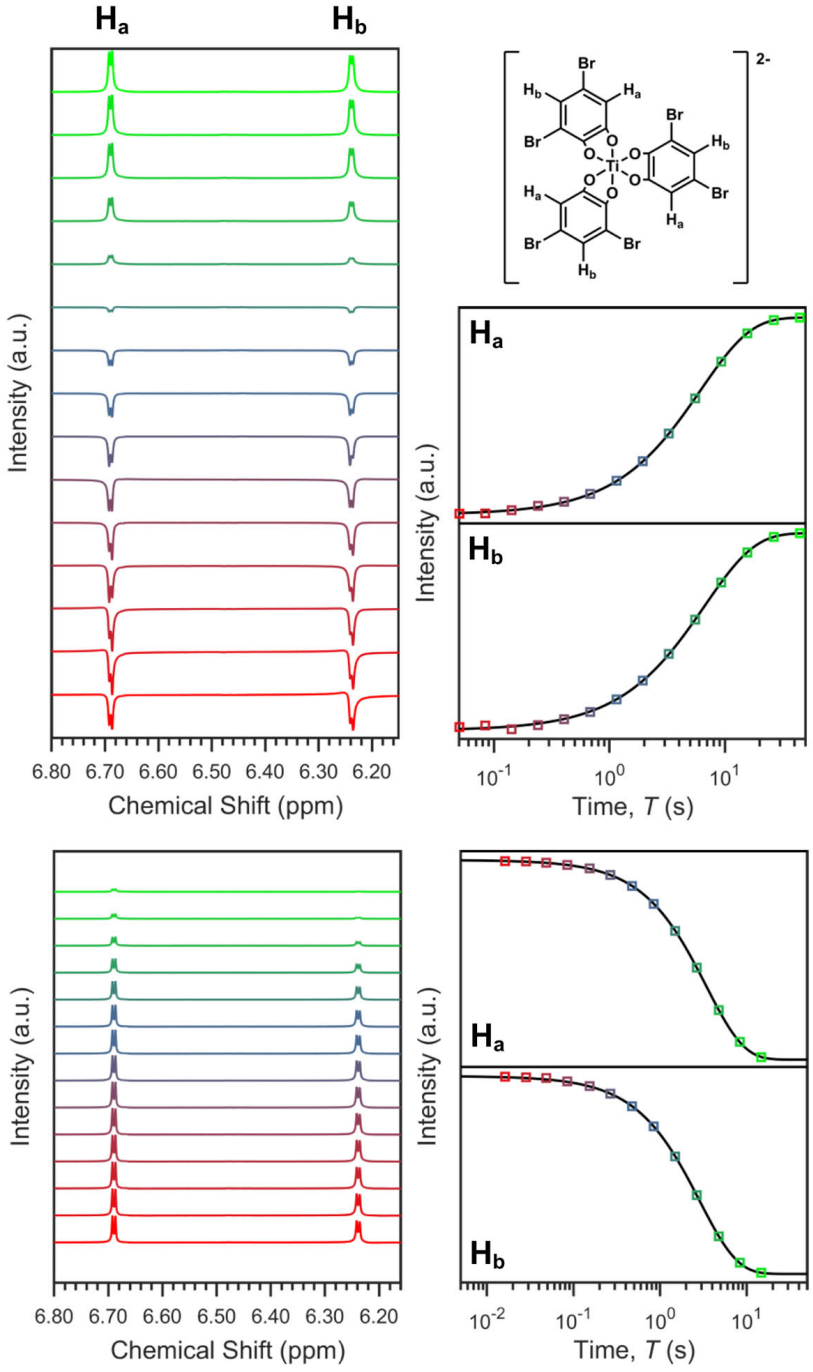

Figure 5.16. NMR analyses and assignments for **4a**. **Top: Inversion recovery data.** Aromatic region of the ^{1}H NMR spectrum for **4a** as a function of time after the initial inversion recovery pulse is shown. Integrals of these peaks generated the depicted intensity v. time plots. Black lines represent fits of the data to an exponential recovery. Peaks are labeled according to the depicted diagram for **4a**. **Bottom: CPMG data.** ^{1}H NMR data from the aromatic region as a function of the number of pulses is shown. Intensities of these peaks are plotted as a function of time and fit to yield T_2.

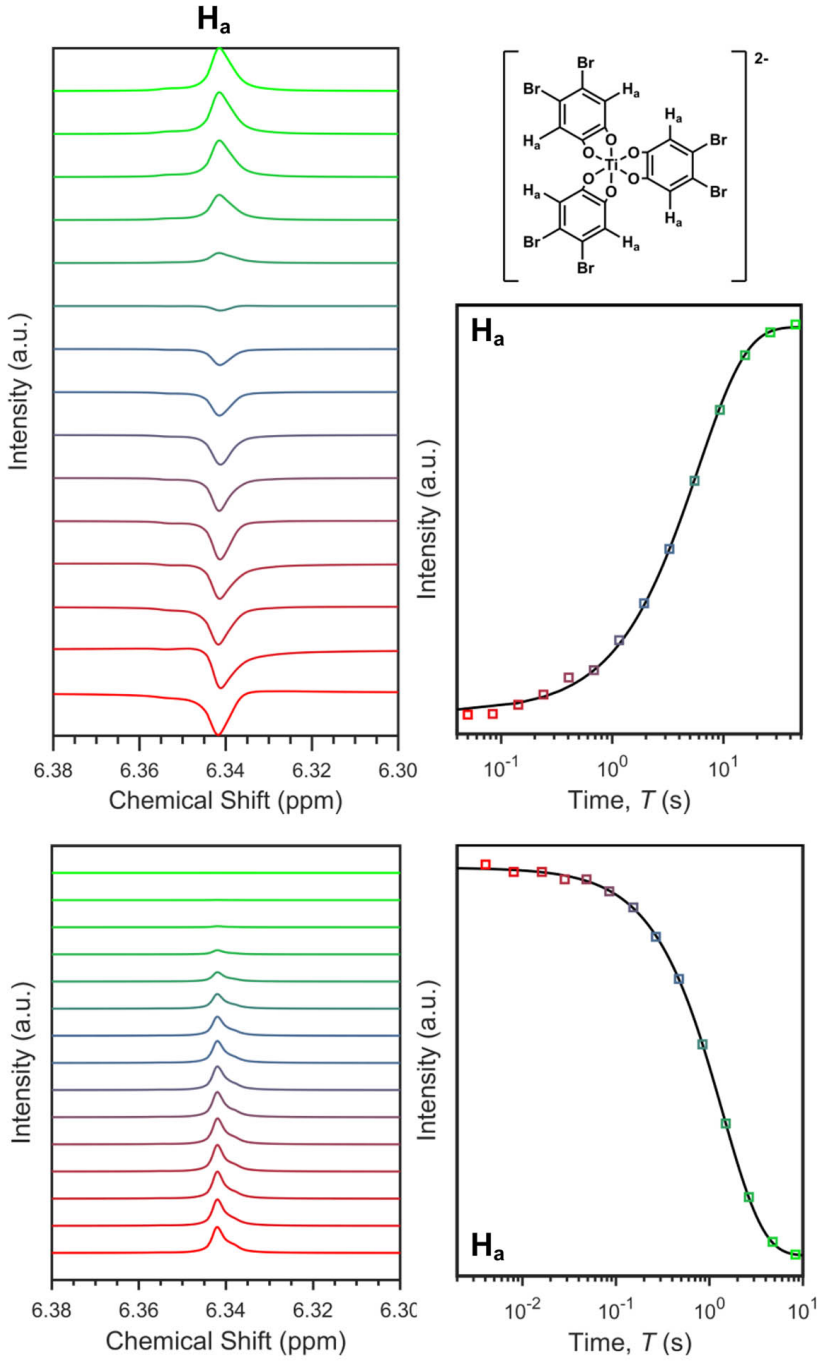

Figure 5.17. NMR analyses and assignments for **5a**. **Top: Inversion recovery data.** Aromatic region of the ^{1}H NMR spectrum for **5a** as a function of time after the initial inversion recovery pulse is shown. The integrals of the peaks generate the depicted intensity v. time plots. Black lines represent fits of the data to an exponential recovery. The peak are labeled according to the depicted diagram for **5a**. **Bottom: CPMG data.** ^{1}H NMR data from the aromatic region as a function of the number of pulses is shown. Intensities of the peak are plotted as a function of time and fit to yield T_2.

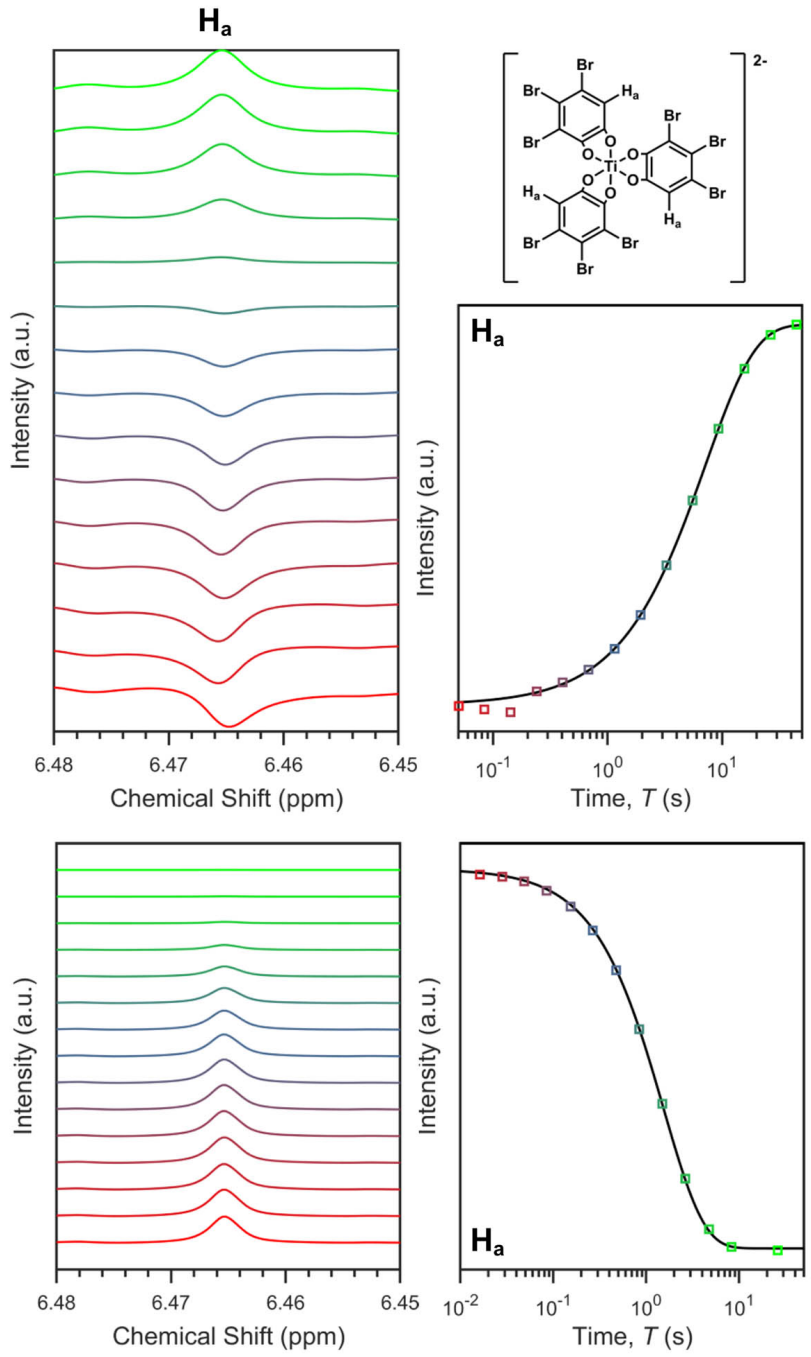

Figure 5.18. NMR analyses and assignments for **6a**. **Top: Inversion recovery data.** Aromatic region of the ^{1}H NMR spectrum for **6a** as a function of time after the initial inversion recovery pulse is shown. The integrals of the peaks generate the depicted intensity v. time plots. Black lines represent fits of the data to an exponential recovery. The peak are labeled according to the depicted diagram for **6a**. **Bottom: CPMG data.** ^{1}H NMR data from the aromatic region as a function of the number of pulses is shown. Intensities of the peak are plotted as a function of time and fit to yield T_2.

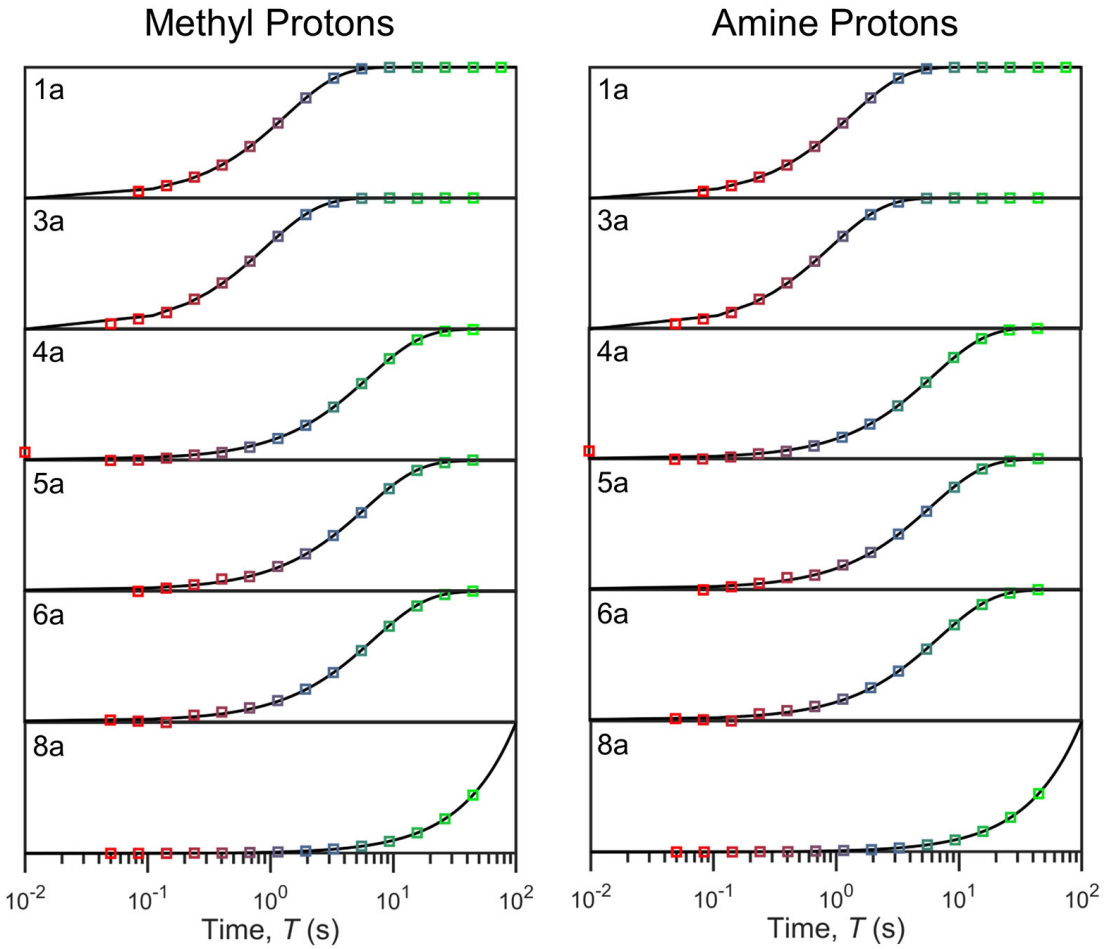

Figure 5.19. Inversion recovery curves for the counterion ^{1}H peaks in metal complexes **1a**, **3a-6a**, and. **8a**. Black lines result from exponential recovery fits – the T_1 values resulting from these fits are given in Table 5.2 of the main manuscript.

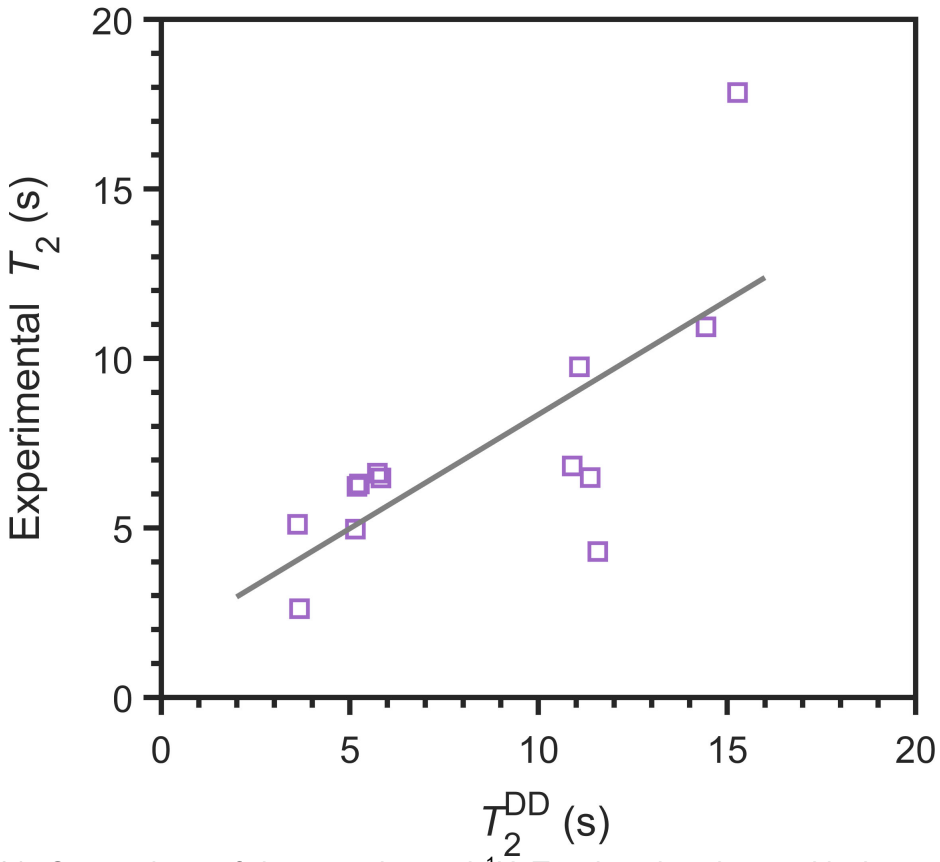

Figure 5.20. Comparison of the experimental ^1H T_2 relaxation times with the computed T_2 considering only dipole-dipole interactions as the mediators of relaxation, T_2^{DD}, assuming a correlation time of 25 ps. The low correlation between the two data sets (gray line, R^2 = 0.5) suggests that spin-spin relaxation in these systems highlights the importance of varying τ_c between the ligands on T_2, but could also be affected by the quantum Zeno effect through the use of the CPMG sequence.[22]

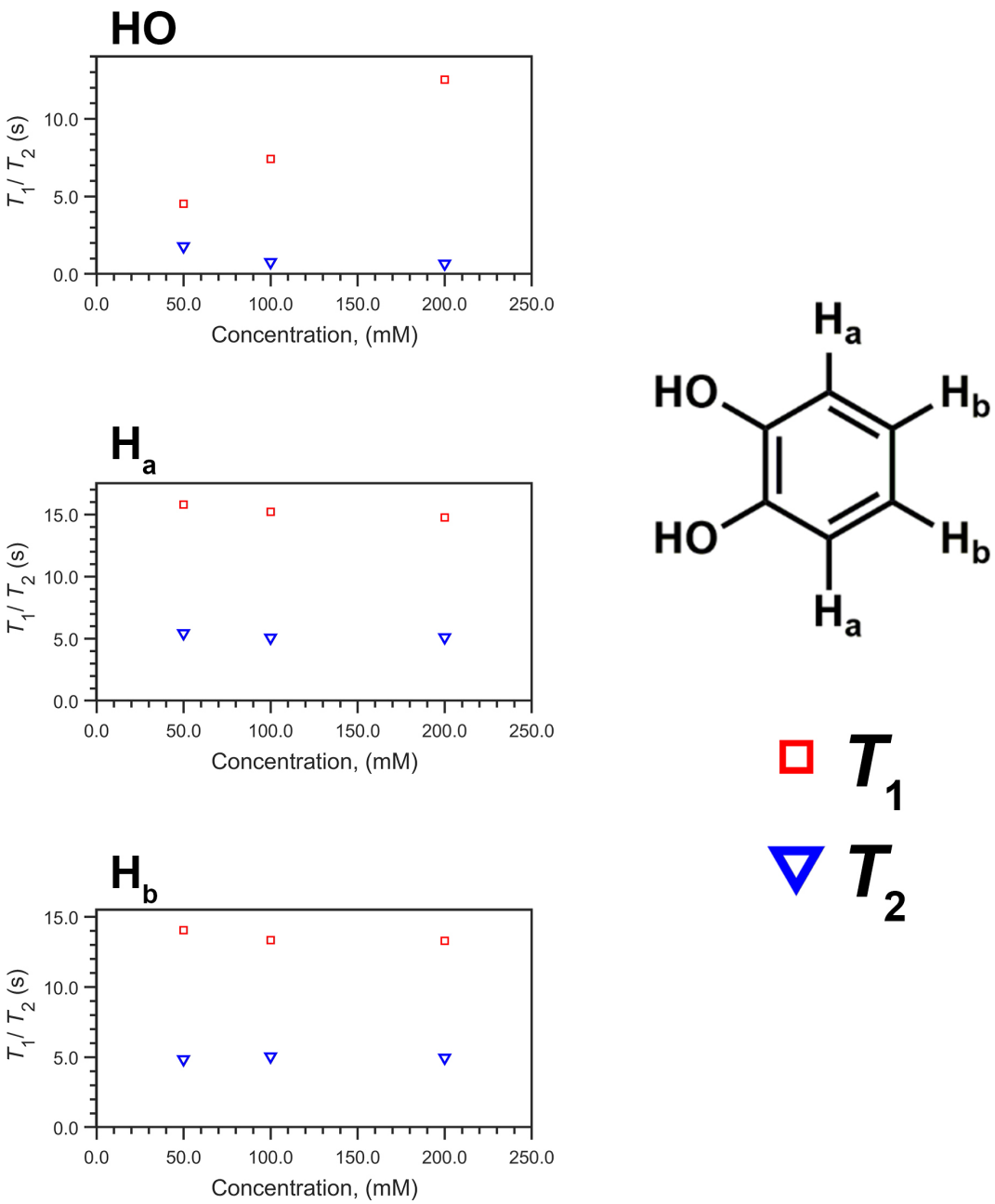

Figure 5.21. Concentration dependence of T_1 and T_2 for **1** in acetone-d_6. T_1 and T_2 parameters were obtained via the same sequences and parameters used throughout the report. The legend and peak labels are given for convenience.

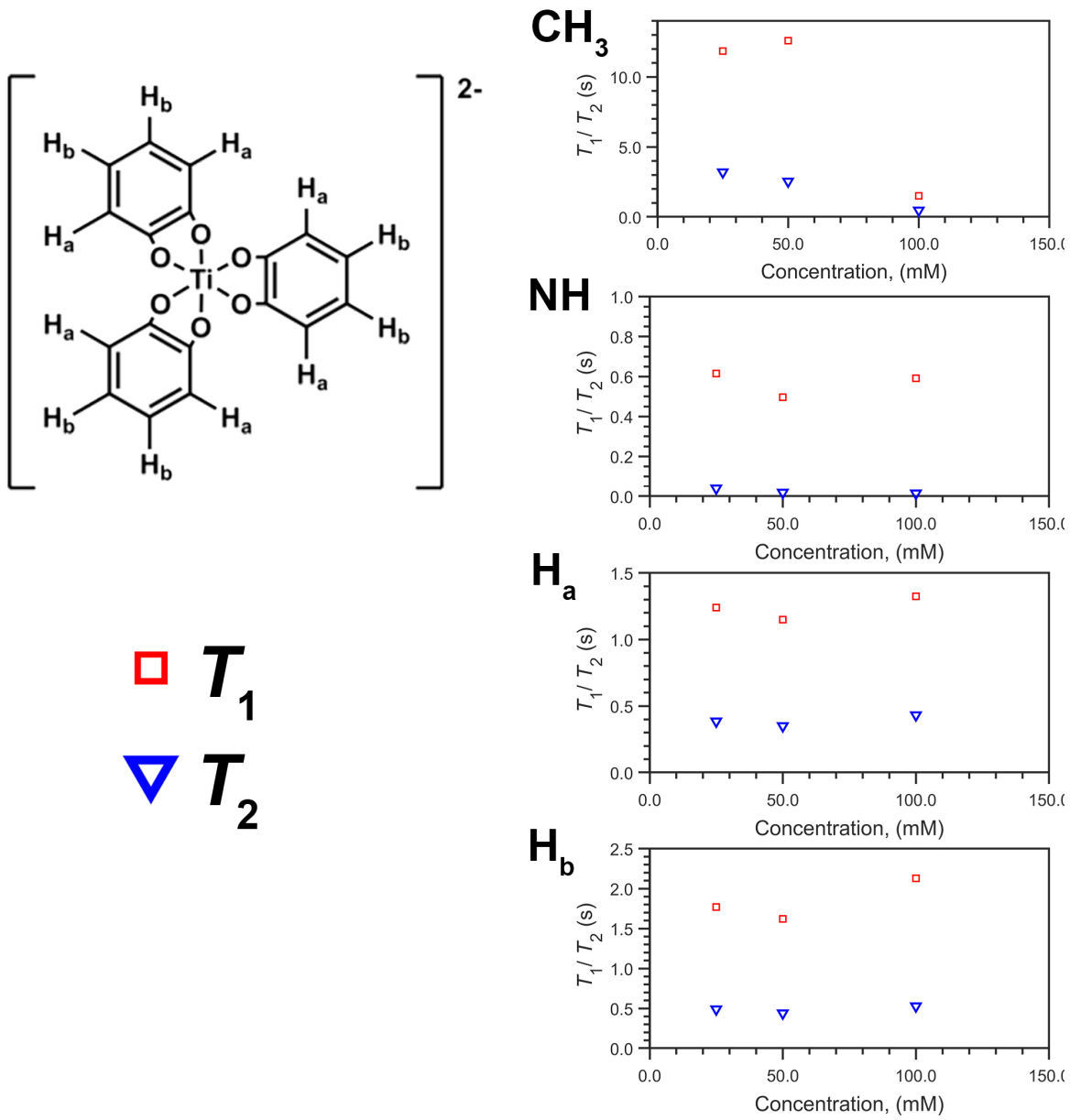

Figure 5.22. Concentration dependence of T_1 and T_2 for **1a** in DMSO-d_6. T_1 and T_2 parameters were obtained via the same sequences and parameters used throughout the report. The legend and peak labels are given for convenience. NH and CH_3 protons correspond to the protons of the $Me_2NH_2^+$ counterions.

References

1 Schirhagl, R.; Chang, K.; Loretz, M.; Degen, C. L. Nitrogen-Vacancy Centers in Diamond: Nanoscale Sensors for Physics and Biology. *Annu. Rev. Phys. Chem.* **2013**, *65* (1), 83–105.

2 Lovchinsky, I.; Sushkov, A. O.; Urbach, E.; de Leon, N. P.; Choi, S.; De Greve, K.; Evans, R.; Gertner, R.; Bersin, E.; Müller, C.; McGuinness, L.; Jelezko, F.; Walsworth, R. L.; Park, H.; Lukin, M. D. Nuclear Magnetic Resonance Detection and Spectroscopy of Single Proteins Using Quantum Logic. *Science* **2016**, *351* (6275), 836–841.

3 Stolze, J.; Dieter, S. *Quantum Computing: A Short Course from Theory to Experiment*; Wiley-VCH, Weinheim, 2004.

4 Nielsen, M. A.; Chuang, I. L. *Quantum Computation and Quantum Information*; Cambridge University Press, Cambridge, 2011.

5 Griffin, R.; Prisner, T. High Field Dynamic Nuclear Polarization–the Renaissance. *Phys. Chem. Chem. Phys* **2010**, *12*, 5737–5740.

6 Winpenny, R. E. P. Quantum Information Processing Using Molecular Nanomagnets as Qubits. *Angew. Chem. Int. Ed.* **2008**, *47* (42), 7992–7994.

7 Ardavan, A.; Rival, O.; Morton, J. J. L.; Blundell, S. J.; Tyryshkin, A. M.; Timco, G. A.; Winpenny, R. E. P. Will Spin-Relaxation Times in Molecular Magnets Permit Quantum Information Processing? *Phys. Rev. Lett.* **2007**, *98* (5), 1–4.

8 Bader, K.; Winkler, M.; Van Slageren, J. Tuning of Molecular Qubits: Very Long Coherence and Spin-Lattice Relaxation Times. *Chem. Commun.* **2016**, *52* (18), 3623–3626.

9 Lehmann, J.; Gaita-Ariño, A.; Coronado, E.; Loss, D. Quantum Computing with Molecular Spin Systems. *J. Mater. Chem.* **2009**, *19* (12), 1672–1677.

10 Aromí, G.; Aguilà D.; Gamez, P.; Luis, F.; Roubeau, O. Design of magnetic coordination complexes for quantum computing. *Chem. Soc. Rev.* **2012**, *41*, 537−546.

11 Atzori, M.; Sessoli, R. The Second Quantum Revolution: Role and Challenges of Molecular Chemistry. *J. Am. Chem. Soc.* **2019**, *141* (29), 11339–11352.

12 Zadrozny, J. M.; Niklas, J.; Poluektov, O. G.; Freedman, D. E. Millisecond Coherence Time in a Tunable Molecular Electronic Spin Qubit. *ACS Cent. Sci.* **2015**, *1* (9), 488–492.

13 Yu, C.-J.; Graham, M. J.; Zadrozny, J. M.; Niklas, J.; Krzyaniak, M.; Wasielewski, M. R.; Poluektov, O. G.; Freedman, D. E. Long Coherence Times in Nuclear Spin-Free Vanadyl Qubits. *J. Am. Chem. Soc.* **2016**, *138*, 14678–14685.

14 S. S. Eaton and G. R. Eaton, in Biological Magnetic Resonance, ed. L. J. Berliner, S. S. Eaton and G. R. Eaton, Kluwer academic/Plenum publishers, New York, 2002, Vol. 19, pp. 29–154.

15 Bloembergen, N.; Purcell, E. M.; Pound, R. V. Relaxation effects in nuclear magnetic resonance absorption. *Phys. Rev.* **1948**, *73*, 679–712.

16 Solomon, I. Relaxation processes in a system of two spins. *Phys. Rev.* **1955**, 99, 559–565

17 Levitt, M. H. *Spin Dynamics*, 2nd ed.; John Wiley & Sons, Ltd: West Sussex, 2008.

18 Carrington, A.; McLachlan, A. D. *Introduction to Magnetic Resonance*, 2nd ed.; Harper & Row: New York, 1969.

19 Jackson, C. E.; Lin, C.-Y.; Johnson, S. H.; van Tol, J.; Zadrozny, J. M. Nuclear-spin-pattern control of electron-spin dynamics in a series of V(IV) complexes. *Chem. Sci.* **2019**, *10*, 8447–8454.

20 Falk, A. L.; Buckley, B. B.; Calusine, G.; Koehl, W. F.; Dobrovitski, V. V.; Politi, A.; Zorman, C. A.; Feng, P. X.-L.; Awschalom, D. D. Polytype control of spin qubits in silicon carbide. *Nat. Commun.*, **2013**, *4*, 1819.

21 Weber, J. R.; Koehl, W. F; Varley, J. B.; Janotti, A.; Buckley, B. B.; Van de Walle, C. G.; Awschalom, D. D. Defects in SiC for quantum computing. *J. Appl. Phys.*, **2011**, *109*, 102417.

22 Koehl, W. F.; Buckley, B. B.; Heremans, F. J.; Calusine, G.; Awschalom, D. D. Room temperature coherent control of defect spin qubits in silicon carbide. *Nature*, **2011**, *479*, 84–87.

23 CRC Handbook of Chemistry and Physics, ed, J. Rumble, CRC Press, 99th edn, 2018.

24 Chaffin, J. H.; Hubbard, P. S. Nuclear magnetic relaxation and Overhauser effectsin liquid CHF_3. *J. Chem. Phys.* **1967**, *46*, 1511-1520.

25 Dakin, H. D. Synthesis of Catechol. *Org. Synth.* **1923**, *3*, 28.

26 Kohn, M. Bromination of Catechol. *J. Am. Chem. Soc.* **1951**, *73* (1), 480.

27 Kohn, M.; Steiner, L. The Reduction of Bromo Derivatives of Catechol, Resorcinol, and Pyrogallol. *J. Org. Chem.* **1947**, *12* (1), 30–33.

28 Lin, C. Y.; Ngendahimana, T.; Eaton, G. R.; Eaton, S. S.; Zadrozny, J. M. Counterion Influence on Dynamic Spin Properties in a V(IV) Complex. *Chem. Sci.* **2019**, *10* (2), 548–555.

29 Cooper, S. R.; Koh, Y. B.; Raymond, K. N. Synthetic, Structural, and Physical Studies of Bis(Triethylammonium) Tris(Catecholato)Vanadate(IV), Potassium

Bis(Catecholato)Oxovanadate(IV), and Potassium Tris(Catecholato)Vanadate(III). *J. Am. Chem. Soc.* **1982**, *104* (19), 5092–5102.

30 Assi, H.; Haouas, M.; Mouchaham, G.; Martineau-Corcos, C.; Allain, C.; Clavier, G.; Guillou, N.; Serre, C.; Devic, T. $MgTi(Cat)_3$, a Promising Precursor for the Preparation of Ti–MOFs? *Polyhedron* **2018**, *156*, 111–115.

31 Borgias, B. A.; Cooper, S. R.; Koh, Y. B.; Raymond, K. N. Synthetic, Structural, and Physical Studies of Titanium Complexes of Catechol and 3,5-Di-Tert-Butylcatechol. *Inorg. Chem.* **1984**, *23* (8), 1009–1016.

32 Dong, G.-L.; Wang, L.; Fang, W.-H.; Zhang, L. Hydrothermal synthesis, structures and visible light harvest of three titanium complexes. *Inorg. Chem. Commun.* **2018**, *93*, 61-64.

33 Brown, S. N. Metrical Oxidation States of 2-Amidophenoxide and Catecholate Ligands: Structural Signatures of Metal–Ligand π Bonding in Potentially Noninnocent Ligands. *Inorg. Chem.* **2012**, *51*, 1251–1260.

34 Silverstein, R. M.; Webster, F. X.; Kiemle, D. J. *Spectrometric Identification of Organic Compounds*, 7th ed.; John Wiley & Sons: Hoboken, 2005.

35 Carr, H. Y.; Purcell, E. M. Effects of Diffusion on Free Precession in Nuclear Magnetic Resonance Experiments. *Phys. Rev.* **1954**, *94* (3), 630–638.

36 Meiboom, S.; Gill, D. Modified spin-echo method for measuring nuclear relaxation times *Rev. Sci. Instrum.* **1958,** *29,* 688–691.

37 Sudmeier, J. L.; Anderson, S. E.; Frye, J. S. Calculation of Nuclear Spin Relaxation Times. *Concepts Magn. Reson.* **1990**, *2* (4), 197–212.

38 Farrar, T. C.; Becker, E. D. Relaxation Mechanisms. In *Pulse and Fourier Transform NMR*; 1971; pp 46–65.

39 Abragam, A. Thermal Relaxation in Liquids and Gases. In *The Principles of Nuclear Magnetism*; The Clarendon Press: Oxford, 1961; pp 264–353.

40 Miller, C. R.; Gordon, S. L. Proton Spin Relaxation in the Chloroethanes. *J. Chem. Phys.* **1970**, *53* (9), 3531–3538.

41 Brown, P. M.; Krishna, N. R.; Gordon, S. L. Proton Spin Relaxation in the Halomethanes. *J. Magn. Reson.* **1975**, No. 20, 540–543.

42 Lee, D. H.; McClung, R. E. D. Nuclear Relaxation and Molecular Motion of 1,3,5-Trifluorobenzene-d_3 in Liquid Solutions. *Chem. Phys.* **1987**, *116* (1), 101–111.

43 Steele, W. A. Molecular Reorientation in Liquids. II. Angular Autocorrelation Functions. *J. Chem. Phys.* **1963**, *38* (10), 2411–2418.

44 Díez, E.; Bermejo, F. J.; Guilleme, J. Molecular Reorientation from NMR Relaxation Times in Planar Molecules. *J. Chem. Phys.* **1985**, *83* (1), 58–69.

45 Kuhn, L. The Hydrogen Bond. I. Intra- and Intermolecular hydrogen bonds in alcohols. *J. Am. Chem. Soc.* **1952**, *74*, 2492–2499.

46 Xiao, L.; Jones, J. A. NMR Analogues of the quantum zeno effect. *Phys. Lett. A* **2006**, *359*, 424–427.

47 Sessoli, R.; Powell, A. K. Strategies toward single molecule magnets based on lanthanide ions. *Coord. Chem. Rev.* **2009**, *253*, 2328–2341.

48 Craig, G. A.; Murrie, M. 3d single-ion magnets. *Chem. Soc. Rev.* **2015**, *44*, 2135–2147.

49 Liddle, S. T.; van Slageren, J. Improving f-element single molecule magnets. *Chem. Soc. Rev.* **2015**, *44*, 6655–6669.

50 Frost, J. M.; Harriman, K. L. M.; Murugesu, M. The rise of 3-d single-ion magnets in molecular magnetism: toward materials from molecules? *Chem. Sci.* **2016**, *7*, 2470–2491.

51 Meng, Y.-S.; Jiang, S.-D.; Wang, B.-W.; Gao, S. Understanding the magnetic anisotropy toward single-ion magnets. *Acc. Chem. Res.* **2016**, *49*, 2381–2389.

52 Rinehart, J. D.; Long, J. R. Exploiting single-ion anisotropy in the design of f-element single-molecule magnets. *Chem. Sci.* **2011**, *2*, 2078–2085.

53 Feng, M.; Tong, M.-L. Single ion magnets from 3d to 5f: developments and strategies. *Chem.-Eur. J.* **2018**, *24*, 7574–7594. (1) Dakin, H. D. Catechol. *Org. Synth.* **1923**, *3*, 28.

54 Kohn, M.; Steiner, L. The Reduction of Bromo Derivatives of Catechol, Resorcinol, and Pyrogallol. *J. Org. Chem.* **1947**, *12*, 30–33.

55 Fulmer, G. R.; Miller, J. M.; Sherden, N. H.; Gottlieb, H. E.; Nudelman, A.; Stoltz, B. M.; Bercaw, J. E.; Goldberg, K. I. NMR Chemical Shifts of Trace Impurities: Common Laboratory Solvents, Organics, and Gases in Deuterated Solvents Relevant to the Organometallic Chemist. *Organometallics* **2010**, *29*, 2176-2179.

56 *MestreNova*; Mestrelab Research: Escondido, CA, USA, 2019.

57 *Matlab*; The MathWorks Inc.: Natick, MA, USA, 2018.

58 *APEX3;* Bruker AXS Inc., Madison, Wisconsin, USA, 2016.

59 *SADABS.* Bruker AXS Inc., Madison, Wisconsin, USA, 2001.

60 Sheldrick, G. M. SHELXT – Integrated space-group and crystal-structure determination. *Acta Crystallogr. Sect. A Found. Crystallogr.* **2015,** *71*, 3-8.

61 Sheldrick, G. M. Crystal Structure Refinement with SHELXL. *Acta Crystallogr. Sect. C Struct. Chem.*, **2015**, *71*, 3-8.

62 Dolomanov, O. V.; Bourhis, L. J.; Gildea, R. J.; Howard, J. A. K.; Puschmann, H. OLEX2: a complete structure solution, refinement and analysis program. *J. Appl. Cryst.* **2009,** *42*, 339-341.

63 *Diamond.* Crystal Impact GbR, Bonn, Germany, 1999.

64 Macrae, C. F.; Edgington, P. R.; McCabe, P.; Pidcock, E.; Shields, G. P.; Taylor, R.; Towler, M.; van de Streek, J. Mercury: Visualization and Analysis of Crystal Structures. *J. Appl. Cryst.* **2006**, *39*, 453-457.

65 CRC Handbook of Chemistry and Physics, ed, J. Rumble, CRC Press, 99th edn, 2018.

66 Hore, P. J. *Nuclear Magnetic Resonance*, 1st ed.; Oxford University Press: Oxford, 1995.

67 Polyanskaya, T. M.; Khaldoyanidi, K. A; Smolentsev, A. I. Supramolecular architecture of catechol and its 2:1 complex with dimethylsulfoxide. *Zh. Strukt. Khim.* **2010**, *51*, 342.

68 Farrar, T. C.; Becker, E. D. Relaxation Mechanisms. In *Pulse and Fourier Transform NMR*; 1971; pp 46–65.

69 L. Sudmeier, J.; E. Anderson, S.; S. Frye, J. Calculation of nuclear spin relaxation times. *Concepts Magn. Reson.* **1990**, *2*, 197–212.

70 Moniz, W. B.; Steele, W. A.; Dixon, J. A. Nuclear spin relaxation in liquids. Spheroidal molecules. *J. Chem. Phys.* **1963**, *38*, 2418–2426.

CHAPTER 6 –IMPACT OF COUNTERION METHYL GROUPS ON SPIN RELAXATION IN $[V(C_6H_4O_2)_3]^{2-}$

Overview

A detailed understanding of how methyl groups on counterions of magnetic molecules affect electron spin relaxation is key to using these chemical species in the design of new molecular qubits. Here we study the coherent spin dynamics of the V(IV) complex $[V(C_6H_4O_2)_3]^{2-}$ with five different counter-cations: $(Et_3NH)^+$ (**1**), $(n\text{-}Bu_3NH)^+$ (**2**), $(n\text{-}Hex_3NH)^+$ (**3**), $(n\text{-}Oct_3NH)^+$ (**4**), and $(n\text{-}Bu_3N^2H)^+$ (**2-*d*^{2}**). These counterions systematically increase the distance between the V(IV) spin and the methyl group of the alkyl chains. Pulsed EPR investigations in both glassy solution and solid-state dilutions show: (1) that the counterions are bound via hydrogen bonding to the $[V(C_6H_4O_2)_3]^{2-}$ unit, even in solution, and that (2) the methyl group of the counterion has a dominant role in dictating the spin-spin relaxation. We can reproduce the rate of the spin echo decay with a model that is based on the distance-dependent impact from the counterion methyl groups. For the ethyl derivative **1** the methyl groups also generate a modulation of the echo decay. Finally, we show that an important instrumental setting of the spin echo measurement, the shot repetition time, can have a dramatic impact on the shape of the echo decay curve and thus the measured relaxation times. The spin-lattice relaxation times are independent of cation and are the same, within experimental uncertainty, in glassy OTP and for the V(IV) complexes doped into the closed-shell Ti(IV) analogue, $(n\text{-}Bu_3NH)_2[Ti(C_6H_4O_2)_3]$ (**2-Ti**).

Introduction

Slowing electron spin relaxation of open-shell metal complexes is a fundamental goal that is essential to applications in quantum computing[1–3] and magnetic resonance imaging.[4–6] In particular, understanding what and how specific chemical features of a molecule affect the relaxation times T_1 (spin-lattice relaxation time) and T_2 or T_m (spin-spin or phase memory

relaxation time, respectively) is vital to designing future useful species. An important advantage of metal complexes is the extraordinary chemical tunability,[7,8] which enables the study of how aspects of the primary, secondary, and tertiary coordination spheres affect these relaxation times.[9–13] In the secondary coordination shell, many molecules experience direct (e.g. hydrogen-bonded) interactions with counterions. These interactions can be magnetic (from ambient magnetic nuclei) or physical (e.g. librations), and change as a function of matrix/molecular identity (**Fig. 6.1**). The same species in different chemical environments may exhibit different relaxation times. Understanding the origins of these variations is vital toward the broader goal of slowing relaxation processes.

Toward that understanding, our groups recently tested the role of counterion in V(IV) spin dynamics through pulsed electron paramagnetic resonance (EPR) studies of a series of V(IV) complexes, $(R_3NH)_2[V(C_6H_4O_2)_3]$ (R = Et, **1**; *n*-Bu, **2**; *n*-Hex, **3**; *n*-Oct, **4**). These species synthetically varied V(IV)•••CH_3 distance[14] by varying the counterion. The results showed that T_m

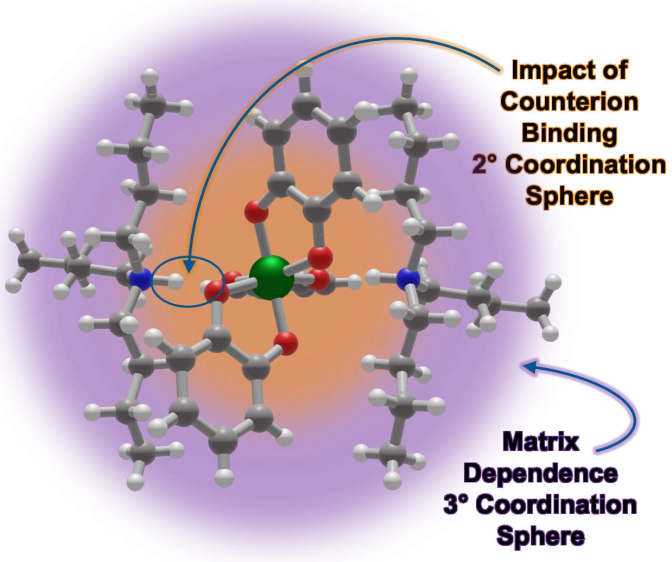

Figure 6.1. Role of counterion binding for $(n\text{-}Bu_3NH)_2[V(C_6H_4O_2)_3]$. Here we examine in detail the impact on V(IV) spin echo dephasing from methyl groups in counterions directly bound to the molecule (2° coordination sphere) and in cations of neighboring molecules (3° coordination sphere).

decreased as the distance between the CH_3 and the V(IV) ion decreased. The key finding of the paper is that the type/position of magnetic nuclei in the first and secondary coordination shell matter more for T_m than simply the quantity, since complex **1** displayed a shorter T_m than **4**, despite **4** possessing 72 more protons per molecular unit than **1**. Furthermore, we showed an apparent downturn in T_m (by as much as 33%) at low temperature which also increased in magnitude when the CH_3 group was closer to the V(IV) ion as observed for the $(Et_3NH)^+$ counter-cation. This phenomenon was not explained.

We speculated on possible correlations between the observed spectroscopic data and the CH_3 groups, but there were many important questions that remained. First, how many and how close are the counterions in solution versus the solid state? As crystallized, all complexes showed hydrogen-bonding with both R_3NH^+ counterions, but EPR measurements were performed as glassy solutions in *o*-terphenyl (OTP), wherein dissociation may occur. Second, what is the nature of the low-temperature downturn of T_m? What phenomena might be contributing? Finally, third, how important, are the methyl groups of the counterion to T_m relative to the spins in the environment? Spin diffusion processes between magnetic nuclei (e.g. ^1H) in a spin's local chemical environment are widely considered to be the controlling factor in T_m. Hence, strategies to minimize nuclear spin content (via deuteration[15], isotopic enrichment[11], or nuclear-spin-free strategies[16]) in the local environment are widely employed. If the methyl groups in the molecule itself were revealed to be the dominant factor, that would be critical supporting evidence for molecular design strategies as a viable route to longer T_m times.

Herein we provide answers to the foregoing questions via a detailed spectroscopic investigation of pulsed EPR relaxation times for **1**-**4**. We show that: (1) one or more counterions are bound to the V(IV) complex in the solution phase, (2) the matrix and its deuteration have little to no impact on the V(IV) electronic spin relaxation, (3) modeling of T_m for **2** and **3** in OTP and **2** in its closed-shell, Ti(IV) analogue (**2-Ti**), $(n\text{-}Bu_3NH)_2[Ti(C_6H_4O_2)_3]$ (**2-Ti)** is consistent with

domination by the methyl groups and, therefore (4) the methyl groups of the counterion primarily controls spin-spin relaxation times in these vanadate complexes.

Methods

Sample Preparation. Detailed synthetic procedures can be found in the EXPERIMENTAL SECTION. Briefly, samples were synthesized and prepared under an inert atmosphere. Syntheses of all complexes proceeds easily at room temperature by reacting one equivalent of vanadyl acetylacetonate ($VO(acac)_2$) (or $TiO(acac)_2$ in the case of **2-Ti**), three equivalents of catechol, and two equivalents of the respective tri-alkyl amine using THF as the solvent. Solid state dilutions were prepared using stock solutions of **2** and **2-Ti** and removing volatile materials under reduced pressure. For deuteration of the ammonium counterion ion, the samples were washed and dried under vacuum three times with MeOD. Deuteration was confirmed by ^{1}H NMR. All preparation of samples in EPR tubes was done under inert atmosphere and tubes were flame sealed under static vacuum at ~100 mTorr helium.

T_1 measurements and fitting. Values of T_1 were measured by 3-pulse inversion recovery, as detailed in the EXPERIMENTAL SECTION. The inversion recovery curves were fit with stretched exponentials. At lower temperatures there frequently is a contribution to the inversion recovery curves from a faster concentration-dependent spectral diffusion process. To distinguish this contribution from T_1, the long component of the two component fits was used to analyze the temperature dependence of T_1. An alternate approach to fitting the data is a stretched exponential, which can be modeled as a sum of multiple exponentials.[17] Both the time constant and the stretch parameter, β, report information about the spin system. Values of T_1 for the long component of the two-component fit and from the stretch exponential fit are in Table 6.3. These values of β are significantly less than 1 and are characteristic of relatively wide distributions, as is commonly observed for transition metal complexes.[14] T_1 obtained from the stretched exponential

fit is consistently shorter than the long component of the two-component fit, but values from both fitting methods exhibit similar temperature dependence (Table 6.3). The temperature dependence of T_1 was modeled as the sum of contributions from the direct process (or other processes with similar temperature dependence including cross relaxation), the Raman process, and a local mode with an energy of about 280 K.

T_m measurements and fitting. T_m was measured by two-pulse spin echo experiment at a magnetic field in the center of the spectra. Previous experiments had shown minimal dependence of T_m on position in the spectrum.[14] Careful attention was paid to the short repetition time (SRT). As discussed in detail in the Experimental Section, if the SRT is shorter than T_1, the shape of the echo decay may be distorted and the apparent decay time is less than the T_m that would be measured for longer SRT, which can result in erroneous values of T_m. Values of T_m were found by fitting the spin echo decays to a stretched exponential.

Results and Discussion

First, we aimed to determine whether the R_3NH^+ counterions were bound to the $[V(C_6H_4O_2)_3]^{2-}$ complexes in OTP, using complex **2** (*n*-Bu_3NH^+ counterion) as a test case. Then we measured T_1 for **2** in different lattices to understand how the environment impacted spin-lattice relaxation time. With knowledge of T_1 we were better able to select parameters to compare T_m in a doped solid state and glassy solution. Finally, through careful remeasurement and examination of the experimental and data fitting procedures, we detail the role of methyl groups of the counterions in phase memory relaxation.

R_3NH^+ Counterion Binding in Glassy OTP Solution. In toluene, acetonitrile and THF solution the tumbling correlation times increased in the order τ_{corr}(**1**) < τ_{corr}(**2**) < τ_{corr}(**3**) < τ_{corr}(**4**), which was attributed to the impact of the cations on molar mass.[14] We applied X-band (*ca.* 9.7 GHz) electron spin-echo envelope modulation (ESEEM) spectroscopy to understand the binding

of the tri-alkyl ammonium counterions to the $[V(C_6H_4O_2)_3]^{2-}$ unit in OTP. We predicted that site-selective deuteration of the counterion NH protons would produce spin-echo envelope modulation if the counterion were bound to the complex. To test this prediction, we synthesized a deuterated analogue of **2** where the ammonium proton was replaced by a deuteron (n-$Bu_3N^2H^+$), **2-*d*^{2}**. We then prepared two samples of **2-*d*^{2}**, one as a 1 mM solution of **2-*d*^{2}** in OTP and the second as a solid-state dilution of **2-*d*^{2}** in its closed-shell, Ti(IV) analogue, (n-Bu_3N-$^2H)_2[Ti(C_6H_4O_2)_3]$ (**2-Ti-*d*^{2}**) at a *ca.* 0.05 % dilution level, **2-*d*$^2_{0.05\%}$**. In the latter case, the counterions would presumably still be attached to the complex, as is observed in the crystal structures of both species. We then performed three-pulse ESEEM experiments with these two samples at the strongest peak in the X-band EPR spectra of the species to compare the echo modulation (**Fig. 6.2**).

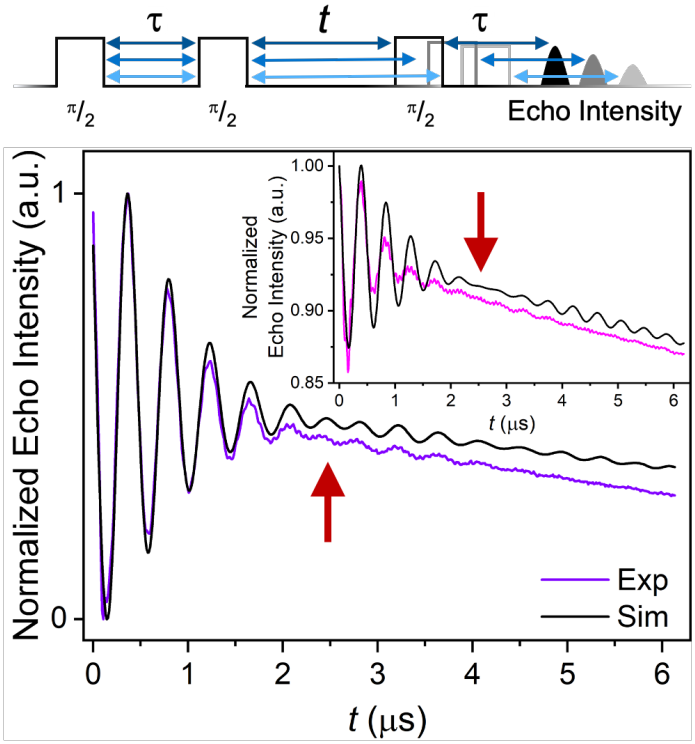

Figure 6.2. Three-pulse electron spin echo envelope modulation (ESEEM) for **2-*d*^{2}** in OTP (inset) and as a 0.05% solid state dilution in the diamagnetic titanium analogue (**2-Ti**). Experiments were performed at 3480 G with a frequency of 9.7010 GHz at 20 K. The initial τ value was 200 ns and increased incrementally by 12 ns. The τ value was held constant at 300 ns. Simulation of the deuterium modulation is shown in black for both samples. The phase reversal of the modulation occurs at the same time for both samples, at approximately 2.5 μs, indicating that the deuterium is at the same distance from the V(IV).

For both samples, we observed an oscillation in the intensity of the three-pulse stimulated echo consistent with ^{2}H ESEEM from the deuterated ammonium counterion. We can make three key observations. First, the period of this oscillation is *ca.* 0.5 μs, corresponding to a frequency of 2 MHz, which is the Larmor frequency of ^{2}H at the magnetic field of the experiment and indicates that ^{2}H is responsible for the modulation. Second, there is an apparent phase reversal in the modulation near a t value of 2.5 μs for both **2-*d*^{2}** and **2-*d*$^2_{0.05\%}$**. This phase reversal depends strongly on the distance between the deuteron and the V(IV).[18] Finally, we note that the modulation is much deeper for the solid-state preparation than the solution-phase one. The depth of the modulation is determined by the number of interacting nuclei and the distance between the nuclei and the paramagnetic center. This variation of modulation depth was observed over multiple preparation of the 1 mM **2-*d*^{2}** in OTP sample. The position of the time reversal was independent of the modulation depth which indicated that all the interacting deuterons were at about the same distance from the V(IV). Variation in the modulation depth could be the result of varying extents of dissociation of the cation. Alternatively, although extreme care was taken to remove water from the solvents and the glassware, there may be some back exchange of ND with adventitious exchangeable protons. The variability of modulation depth is more likely to be due to trace H_2O in the solvent than to variability in the extent of cation dissociation for samples that were handled similarly.

Simulations of the ESEEM were performed with EasySpin to analyze the modulation depth and phase reversal, as detailed in the EXPERIMENTAL SECTION. The depth of the modulation and phase reversal near 2.5 s for the data collected on **2-*d*$^2_{0.05\%}$** is closely reproduced by two deuterons equidistant (*ca.* 3.100(5) Å) from the unpaired electron (localized to the V ion). This observation is in excellent agreement with the crystal structure, wherein two counterions are bound to the $[V(C_6H_4O_2)_3]^{2-}$ complex and the hydrogen bonded protons are *ca.* 3.1 Å from the V

atom. The phase reversal occurs at the same time in the ESEEM for **2-*d*^{2}$_{0.05\%}$** and **2-*d*^{2}**, suggesting that the deuterated counterion is bound to the vanadate complex in OTP.

*Matrix Dependence of T_1 and T_m for $(Bu_3NH)_2[V(C_6H_4O_2)_3]$ (**2**).* The local chemical environment (predominantly defined as beyond the molecule itself, e.g. the glassy solvent cage or the Ti(IV) lattice) can be an important modifier on relaxation. We tested the spin-lattice relaxation time, T_1, for **2** to examine how sensitive the relaxation is to local environment for $[V(C_6H_4O_2)_3]^{2-}$, as prior studies demonstrated that changing counterion had minimal influence on T_1 times.[14] T_1 values, measured by inversion recovery experiments, were obtained for samples of **2** in three different matrices: **2** in OTP, **2** in d^{14}-OTP, **2**$_{0.05\%}$ and **2**$_{0.5\%}$. A plot of the spin lattice relaxation rate ($1/T_1$) versus temperature is shown in **Figure 6.3**. $1/T_1$ values for the four samples are within experimental error of each other over the entire temperature range above ca. 10 K. At T <10 K, spin concentration enhances cross relaxation and spectral diffusion contributions to $1/T_1$, so slight variations in local concentration (beyond what we can easily control in typical sample

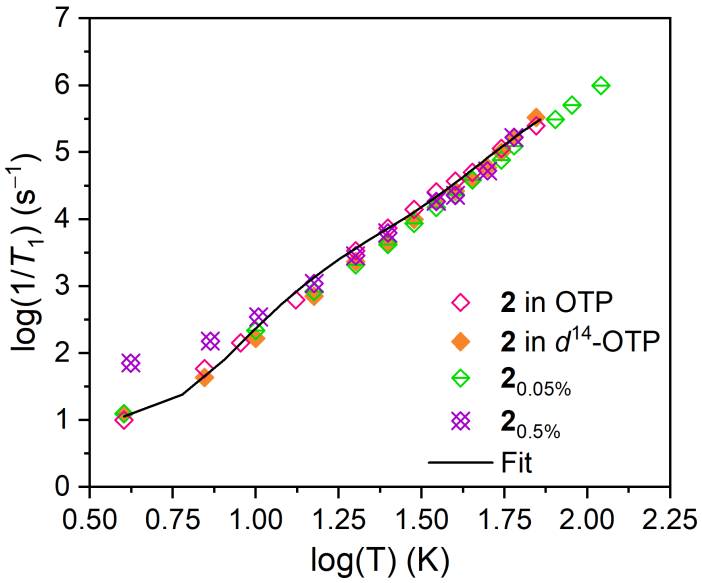

Figure 6.3. Rate of T_1 relaxation as a function of temperature for **2** in four different matrices: **2** in OTP, *2* in d^{14}-OTP, **2**$_{0.05\%}$, and **2**$_{0.5\%}$. Since the T_1 data are nearly the same for three matrices, only one representative fit for temperature dependent $1/T_1$ is shown. The details of modeling are described in the EXPERIMENTAL SECTION.

preparation) can result in significant changes in measured relaxation times. A fit of the temperature dependence of $1/T_1$ for **2** in the three matrices reveals contributions of direct, Raman, and local mode relaxation processes (see Experimental Section). It is particularly striking that there is so little difference between the glassy OTP and polycrystalline Ti lattices. The similarity in values of T_1 suggests that vibrational modes of the complexes are the dominant contributors to relaxation and are relatively insensitive to the surrounding lattice.

Next, we investigated the matrix dependence of T_m. T_m relaxation is often extremely sensitive to magnetic changes in the local environment, such as concentration of nearby spins and magnetic nuclei. For this reason, many relaxation times are collected in deuterated and protiated environments, where the lower-magnetic-moment deuterium atom engenders T_m values much longer than in protiated environments. If the spin echo dephasing is dominated by nuclear spin diffusion, deuteration of the lattice is expected to decrease T_m by the square of the ratio of the magnetic moments of H and D, which is about 6^2.[19] **Figure 6.4** shows temperature-dependent T_m times of **2** in four different matrices: **2** at a 1 mM concentration in OTP and d^{14}-OTP, and **2**

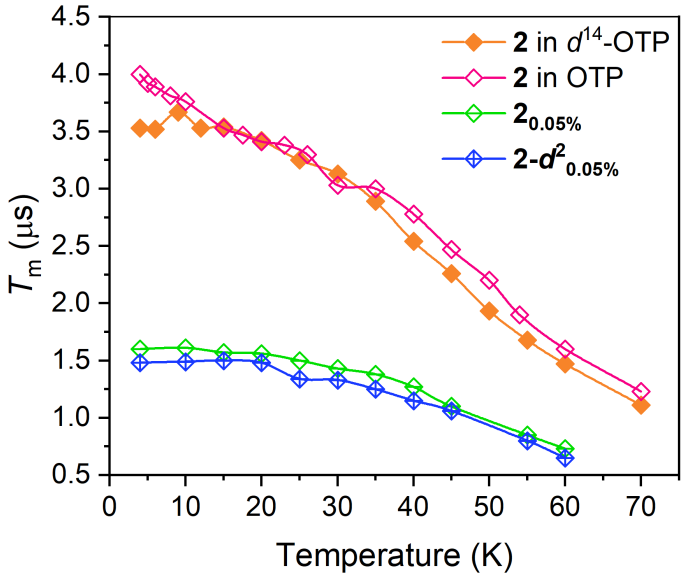

Figure 6.4. Variable temperature T_m data for **2** in d^{14}-OTP and OTP at a 1 mM concentration, $\mathbf{2}_{0.05\%}$, and $\mathbf{2}$-$d^2_{0.05\%}$ at X-band frequency (ca. 9.5 GHz). The lines connect the data points.

diluted in **2-Ti**: $\mathbf{2}_{0.05\%}$, and $\mathbf{2}$-$d^2_{0.05\%}$. T_m values were measured using a 2-pulse echo sequence for these samples (see SI for fitting description). At all temperatures, the T_m was about the same in glassy samples of **2** in OTP and d^{14}-OTP decay. The same is true for the two solid-state samples.

Comparison of the two data sets suggests that there is no significant dependence in T_m on matrix deuteration, indicating the solvent or matrix protons (or deuterons) play negligible roles in the spin echo dephasing. However, there is a large difference between the solid and solution-phase samples. We note that solid dilution preparations used here enforce two things. First, it forces both counterions to be hydrogen bound to the V(IV) complex, and forces compact conformations of the alkyl chains of the counterion which puts the CH_3 groups closer to the V(IV) than might occur in the OTP solution. Furthermore, in the solid phase, the CH_3 groups on the counterions of the diluent **2-Ti** enhances relaxation as neighboring counterions have CH_3 groups that are less than 10 Å from the V(IV) center based on distances taken from the crystal structure. The position of the CH_3 groups in the crystalline lattice are summarized in Table 6.9. Modeling of the echo decays show that these effects contribute to the substantially shorter T_m in the solid dilution than in the glassy solution.

Role of Shot Repetition Time in Previously Reported Low-Temperature Downturn of T_m. A practical aspect of any pulsed EPR measurement is the pulse sequence (or shot) repetition time (SRT), which is the timing separating the application of each 2-pulse echo sequence. In practice, if the shot repetition time is too short relative to the spin-relaxation time of the probed system, the system will not return to equilibrium between measurements. Hence, the echo intensity is suppressed, and the shape of the echo decay is distorted. In some cases, this phenomenon has been exploited to selectively record superimposed spectra.[20,21] The effect of SRT on echo amplitude is discussed in reference 22.[22] These distortions are greatest at short values of τ so the impact on values of T_m is greatest for samples with shorter T_m.

To demonstrate the impact of SRT, two-pulse echo experiments were performed on **1** in OTP at 4.2 K with three SRT values: 2, 10, and 100 ms (**Fig. 6.5**). At 4.2 K, the T_1 value of **1** is nearly 1 s, which is much longer than any of these SRT values. For each point in the echo decay curve (each value of τ) the echo intensity is averaged *n* times, where *n* is the parameter 'shots per point' in the Bruker Xepr software. The time between each of these *n* measurements in the shot repetition time (SRT). For these short SRT values the spins do not have time to relax between the pulse sequences so the echo intensity decreases as the SRT decreases. Since the extent of saturation and the ratio of SRT to the length of the 2-pulse experiment varies with τ the impact of the short SRT impacts the shape of the decay, as well as the overall intensity. There also is system overhead related to sending information to the Bruker Patternjet module that creates the pulses, which happens for each set of 16 averages in the example shown. The effective delay between pulse sequences is therefore longer for 1 shot per point than for larger numbers of shots per point. Furthermore, if there is a distribution of relaxation times, shorter values of SRT are

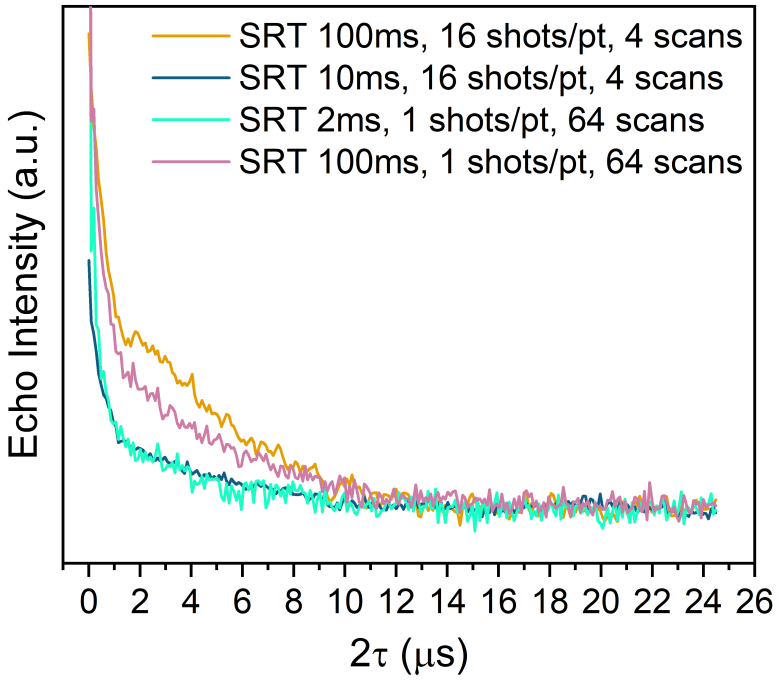

Figure 6.5. Shot repetition time (SRT) dependence of the echo decay curves at 4.2 K for **1** $(Et_3N)_2[V(C_6H_4O_2)_3]$. Data were measured at the highest amplitude point in the EDFS. Each measurement has a different SRT and/or number of scans. This plot highlights the changes in echo decay shape.

selective for spins with shorter relaxation times. If these factors were not impacting the echo decays, the decay curve should be independent of SRT and data acquired with 1 shot/pt and 64 scans should be identical to 16 shots/point and 4 scans. The strong dependence of the echo decay curves in **Fig. 6.5** on SRT and on shots/point demonstrates the large distortions that can occur when SRT is not sufficiently long. Analysis of the echo decays with stretched exponentials produced very different T_m values of 2.1, 1.0, and 0.06 μs for the SRTs of 100, 10, and 2 ms, respectively. Furthermore, the T_1 for vanadate is highly temperature-dependent in this range, like many other metal complexes. Hence, careful consideration of T_1 and SRT even between very closely spaced temperature points is essential for accurate determination of T_m.

We previously reported a low-temperature downturn in T_m for **1** that we had attributed to the CH_3 groups.[14] We now realize that the values of SRT used for the lower temperature measurements were not long enough and did not track with the large temperature dependence of T_1. With careful adjustment of SRTs, the downturn is eliminated in all four samples (see below).

Methyl Group Impact on Echo Decay Rate and Shape. Values of T_m were obtained by analysis of echo decay curves by fitting to a distribution of exponentials that is modeled with a stretched exponential function: $I(\tau) = I(0)\, e^{-\left(\frac{2\tau}{T_m}\right)^{\beta}}$ where β is the time between pulses, T_m is the phase memory relaxation time, and β the stretch factor. The magnitude of β depends on several mechanistic aspects of phase memory relaxation.[19,23] For example, values near 2 are characteristic of domination of T_m by nuclear spin diffusion. Rapid motions that modulate electron-nuclear interaction typically result in smaller values of β, as is documented for nitroxide radicals.[24] Practically, a larger stretch factor (β > 1) produces a sigmoidal shape for the echo decay, while a smaller β factor (β < 1) gives an appearance of a biexponential echo decay with a fast initial drop and then apparently slower decay at longer timescales. A β of 1 gives a curve that is a standard exponential decay.

We remeasured the variable-temperature 2-pulse echo decay curves for **1**-**4** from 4.2 to *ca.* 140 K, taking special care to ensure SRTs were much longer than the long T_1 components of the inversion recovery curves (Figs. 6.22, 6.24-26). We then fit the echo decay curves with stretched exponential functions to reexamine the temperature dependence of T_m and the stretch factor β (**Figure 6.6**). The T_m values are strongly dependent on counterion identity. At 5 K, **4** has

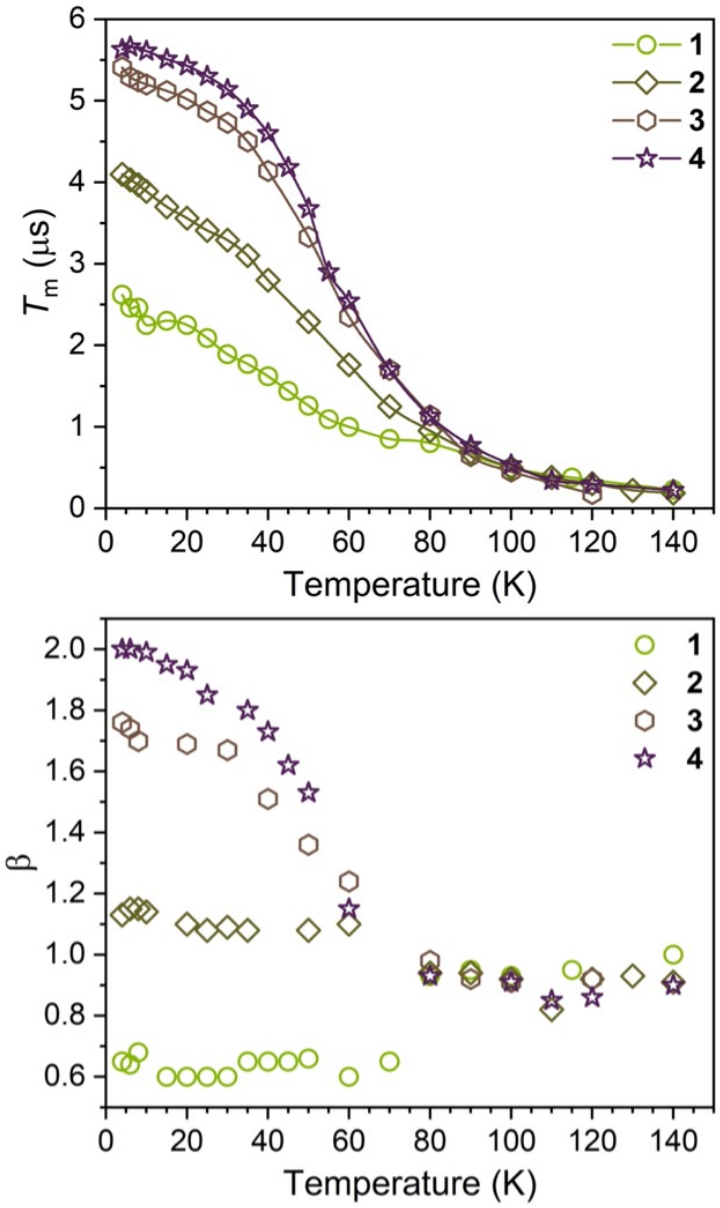

Figure 6.6. Variable temperature T_m data (top) and stretch parameters (β) (bottom) for 1 mM **1**–**4** in OTP at X-band frequency (ca. 9.5 GHz). The lines connect the data points.

the longest T_m of 5.63 μs, followed closely by **3** with a T_m of 5.41 μs. **2** and **1** follow with shorter T_m values of 4.10 and 2.62 μs, respectively. For **1**-**4**, T_m decreases from 4 K to 80 K, converging near *ca.* 1 μs at 80 K, which is the temperature at which T_1 begins to dominate T_m. Above 80 K, the T_m values and their temperature dependences are the same for **1**-**4**, which is consistent with the observation that T_1 is independent of cation. The stretch factor β also differs between **1**-**4**, having 5 K values of *ca*. 0.7, 1.1, 1.8 and 2.0 for **1**, **2**, **3**, and **4**, respectively. Between 5 and 80 K the shape of the echo decays for **1** do not fit well with a stretched exponential because of modulation with a period of 2τ~ 2 MHz that is attributed to the ethyl group, so there is greater uncertainty in the values of T_m and β compared to the other complexes. By 80 K T_m for **1** is short enough that the modulation is not detectable, and the decay curves fit well with β ~ 1. For **2**, β is about 1.1 between 5 and 80 K due to the more modest impact of the methyl groups on dephasing than for **1**. For **3** and **4**, β at 5 K approaches 2 as is characteristic of domination of dephasing by nuclear spin diffusion. With increasing temperature β for **3** and **4** decreases toward 1 at 80 K as the impact of T_1 on T_m increases. Similar to T_m, the temperature dependence of β above 80 K is about the same for **1**-**4**, and is approximately 1, as expected when T_1 dominates.

There are several key differences between the present results and our prior measurements.[14] First, the cation dependence of T_m at low temperature is even more pronounced, showing nearly a factor of 2 difference in T_m between the ethyl (**1**) and octyl cations (**4**). We underline the fact that the general trend is the same – higher T_m values are found where the counterion CH_3 is spaced further from the V(IV) ion. Furthermore, there is no longer a maximum in T_m for **1**-**4** near 20 K, as was previously observed. There are several factors that lead to these discrepancies. First, **2** exhibits much shorter T_m times relative to the prior measurements. Previously complexes **2**, **3**, and **4** were approximately equal, but now there is a large difference in these values at low temperature (< 40 K). In the case of **2**, multiple tests of newly prepared samples lead us to conclude that there must have been a mislabeling of the sample previously measured as

"$(Bu_3NH)_2[V(C_6H_4O_2)_3]$". A second origin of the stronger variation at low temperature is that we are now using sufficiently long SRT values. We stress this latter point as one of incredible importance for future studies of phase memory relaxation in complexes, where faulty pulse sequence parameters may lead to incorrect conclusions about the role of certain molecular features. In this case, we fortuitously find the overall trend reproduced. It may also be useful to note that all samples used in the current study were in EPR tubes that were back-filled with a helium pressure of about 100 mtorr. This low pressure of helium dramatically improves the speed of thermal equilibration of samples relative to ones that are under vacuum, because of the excellent insulating properties of a vacuum.

Finally, we sought to computationally model the echo decays as arising from spin diffusion of nearby protons and dynamic CH_3 groups of the R_3NH^+ counterions (**Fig. 6.7**). We applied a previously published model by some of us[24] that augmented the ambient bath spin diffusion model of Milov[25] by including the potent effect of CH_3 groups (see Experimental section). We applied this model to three systems. First, the solid-state dilution of **2** in **2-Ti**, wherein knowledge of the number and location of nearby magnetic nuclei (relative to the V atom) can be extracted from X-ray diffraction data. Second, a glassy solution of **2** in OTP. And finally, **3** in glassy OTP, to examine how well we could extend the model for **2** to the larger-counterion species. In the echo decay for **3** in OTP (**Fig. 6.7**) there is a rapidly decaying component at short values of τ, that is attributed to a small population of more rapidly relaxing spins as is commonly observed for many nitroxides[24] and is not included in the fitting of T_m to a stretch exponential or modeling of the echo decay.

We find that the model reasonably reproduces the data for all three samples with some adjustment of the location of the CH_3 groups in OTP solutions. Agreement is very good for the solid-state dilution, wherein exact distances between the V(IV) spin and nearby protons and CH_3 groups produce an echo decay that matches experiment. In the crystal structure of the doped solid **2-Ti** there are 25 CH_3 groups at distances of 6 to 9.5 Å from the V(IV) center, including those from neighboring complexes (**Table 6.9**). CH_3 groups at distances longer than 9.5 Å from the

V(IV) that have very little impact on T_m. The only adjustable parameter for calculation of the echo decays was the dephasing rate for the methyl groups, W_m = 5 MHz, which is similar to values used previously to model dephasing by alkyl methyl groups in glassy solvents.[24] For **2** in glassy OTP, inclusion of only CH_3 from the molecular unit in the crystal structure of **2-Ti** predicted 14 methyl groups at distances of 6.5 to 9 Å. The simulated decay curve using these distances predicted a faster relaxation than is observed. An improved agreement is obtained if the number of methyl groups is decreased to 8 at distances of 7.5 to 9 Å. This result is not a unique solution

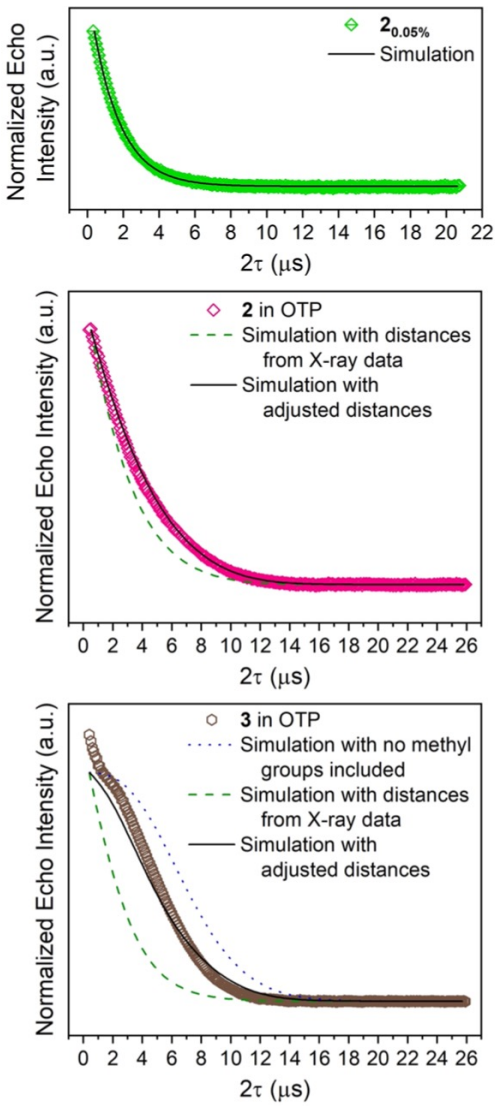

Figure 6.7. Echo decay curves and modeling simulations for **2** in OTP at a 1 mM concentration (top), $\mathbf{2}_{0.05\%}$ (middle), and **3** in OTP at a 1 mM concentration (bottom) at X-band frequency (ca. 9.5 GHz). Overlaid on the data are the models of the decay curves using the methyl group distances obtained from the crystal structure (or adjusted for the solution samples).

for the numbers of methyl groups and distances, but these values are representative of the adjustments required to match the data. There are two possible interpretations for these numbers. Either (1) one of the cations has dissociated, or (2) the alkyl chains take a more extended conformation in glassy OTP than in the crystal. For **3** in glassy solution, the crystal structure predicts 15 CH_3 groups at distances of 7.5 to 10 Å. Simulations based on those distances predict much faster echo decays than are observed experimentally (**Fig. 6.7**). Agreement with the experimental data could be obtained with five methyl groups at distances of 8.5 to 10 Å. The smaller number of CH_3 and longer distance could reflect extensive cation dissociation or extended conformations. It seems unlikely that the extent of dissociation of the cation is so much greater for the hexyl cation than for the butyl cation. It seems more likely that in both cases the alkyl chains adopt more extended conformations in OTP than in the crystals. Importantly, simulations of the echo decay for **3** without including the CH_3 groups produces an echo decay that is far slower than experiment.

A Nuanced Picture of Counterion Influence on Phase Memory Relaxation in $[V(C_6H_4O_2)_3]^{2-}$. Based on the foregoing observations, we revisit our previous conclusions of counterion impact on spin relaxation time and provide new insights into the effect. First, we now show that the impact of the CH_3 groups in the R_3NH^+ counterions on phase memory relaxation times is much more pronounced at low temperature than previously recognized, especially if the appropriate SRT is chosen for the 2-pulse-echo experiment. This outcome cements our prior conclusions while providing additional insight, which is that a low-temperature downturn in T_m may be attributable to a mismatch of SRT and the T_1 of the studied spin system, not any specific intrinsic molecular feature.

We now have greater insight into the mechanistic role of the CH_3 groups in phase memory relaxation. From the revised T_m data, we observe β at 5 K that is close to 2 for **4**, and decreases with decreasing counterion size, ultimately producing a β that is less than 1 for **1**. Recall that

longer β values stem from phase memory relaxation processes originating in spin diffusion while dynamic physical motion of magnetic nuclei results in β values below 1. We reason the following: as the alkyl chain of the counterion gets shorter, the impact of the CH_3 groups becomes amplified. As a result, from **4** to **1**, the dominant relaxation mechanism at low temperature transitions from being governed by nuclear spin diffusion to the rapid motions of the counterion.

From this mechanistic perspective, a new picture is painted of the impact of the molecule on phase memory relaxation, wherein the counterion's impact on phase memory relaxation overwhelms those of spin diffusion in the glassy solvent. In the doped solid the CH_3 groups from neighboring ions are closer than the intramolecular distances. The computations and matrix-dependence studies corroborate this point, as the effects of deuteration are negligible and the echo decay curves cannot be reproduced without considering molecular features. This outcome is consistent with relatively recent studies showing the heightened influence of magnetic nuclei *ca.* 6 Å from an unpaired electron.[26] The similarity of T_1 in OTP and the crystalline host demonstrate that for the vanadate ions the molecular environment also dominates T_1.

Conclusions

Based on the foregoing spectroscopic and modeling data, we conclude that the molecule itself, not just the solvent and chemical environment, is extraordinarily impactful for governing phase memory relaxation and spin lattice relaxation. In effect, the coordination shells of a metal complex define the environment that determines the relaxation mechanisms. This outcome seems intuitive, particularly in the sense of phase memory relaxation, which is enhanced by variations in dipolar interactions in the local environment. Indeed, magnetic effects driven by fluctuating dipolar fields would be anticipated to be greatest for magnetic nuclei closest to metal complex and in the coordination shell versus, e.g., solvent nuclei multiple nanometers away. The results thus underline the importance of molecular finetuning as an effective first step for

controlling relaxation. These results predict that if the CH_3 groups were removed from the first coordination sphere cations, the spin echo dephasing would be dramatically slowed at which point deuteration of the solvent would then be a useful strategy for further slowing dephasing. The observation that T_1 is the same in glassy OTP and in the polycrystalline Ti complex implies that low-energy vibrations of the complex and the electronic structure that is modulated by vibrations will need to be analyzed to determine how to control T_1.

Experimental

General Considerations. The complex (n-$Bu_3NH)_2[V(C_6H_4O_2)_3]$[14] (**2**) was reported to be air-sensitive.[27] Thus, all manipulations and syntheses of it were performed under a N_2 atmosphere with either a Vigor glovebox or Schlenk techniques. Glassware was either oven-dried at 150 °C for at least 4 h and/or flame-dried before bringing into the glovebox. Tetrahydrofuran (THF) and diethyl ether (Et_2O) were dried using a commercial solvent purification system from LC Technology Solutions and were stored over 4 Å molecular sieves prior to use. 4 Å molecular sieves were stored in a 150 °C oven and were activated at 280 °C under reduced pressure for at least 12 h prior to use. THF and Et_2O were subjected to a test with a standard purple solution of sodium benzophenone ketyl in THF to confirm low O_2 and H_2O content. Tri-*n*-butylamine (n-Bu_3N) and hexamethyldisiloxane (HMDSO) were purchased from commercial suppliers and dried by stirring over CaH_2 for at least 24 h then distilled over CaH_2. MeOD was purchased from Cambridge Isotope Labs and freeze-pump-thawed three times prior to use. (n-$Bu_3NH)_2[V(C_6H_4O_2)_3]$ (**2**),[14] d^2-catechol,[28,29] d^2-acetylacetone,[30] and $VO(d\text{-acac})_2$[31] were synthesized according to literature procedures. Catechol was purchased from Alfa Aesar and sublimed prior to use. $TiO(acac)_2$ was purchased from Alfa Aesar and used as received.

(n-$Bu_3ND)_2[V(C_6H_4O_2)_3]$ (**2-d^2**) This procedure is a modified synthesis of **2**. In a N_2-filled glovebox, a 20-mL scintillation vial was charged with 0.1369 g (0.512 mmol) $VO(d\text{-acac})_2$, 0.1722

g (1.536 mmol) d^2-catechol, ca. 3 mL MeOD, and a Teflon-coated magnetic stir bar. A solution of 238 μL (1.00 mmol) *n*-Bu_3N was added to the mixture with gentle shaking, resulting almost immediately in an intensely dark blue solution. The reaction mixture was allowed to stir overnight. All volatile materials (THF, H_2O, and acetylacetone) were removed under reduced pressure. The resulting dark blue residue was washed once with ca. 5 mL cold Et_2O (Note: the complex is slightly soluble in Et_2O) and once with ca. 5 mL hexanes and then was dried under reduced pressure to yield dark blue powder. The complex was further purified by slow evaporation of THF into a hexane solution at -35°C in the glovebox for 1 week to yield crystalline **2-*d*^{2}**. IR (ATR, cm^{-1}): 3050, 2999, 2959, 2933, 2873, 1568, 1466, 1378, 1254, 1097, 1012, 872, 800, 734, 630, 503, 414.

(*n*-$Bu_3NH)_2[Ti(C_6H_4O_2)_3]$ (**2-Ti**) In a N_2-filled glovebox, a 20-mL scintillation vial was charged with 0.5261 g (2.01 mmol) $TiO(acac)_2$, 0.6621 g (6.01 mmol) catechol, ca. 8 mL THF, and a Teflon-coated magnetic stir bar. A solution of 0.74412 g (4.01 mmol) *n*-Bu_3N was added to the mixture with gentle shaking, resulting almost immediately in an orange solution. The reaction mixture was allowed to stir overnight. All volatile materials (THF, H_2O, and acetylacetone) were removed under reduced pressure. The resulting dark orange residue was washed twice with ca. 5 mL cold Et_2O (Note: the complex is slightly soluble in Et_2O) and twice with ca. 5 mL hexanes and then was dried under reduced pressure to yield orange powder. The complex was further purified by slow evaporation of THF into a hexanes solution at -35°C in the glovebox for 1 week to yield 2.035 g (45.4% yield) of crystals suitable for SCXRD. The ^1H NMR can be seen in Figure 6.10 ^1H NMR ($CDCl_3$, 7.26 ppm): 11.01 (s, 2H), 6.43 (dd, *J* = 3.47, 5.67 Hz, 6H), 6.19 (dd, *J* = 3.47, 5.67 Hz, 6H), 3.27 (bs, 12H), 1.70 (bs, 12H), 1.31 (d, *J* = 7.49, 12H), 0.87 (bs, 18H) ppm. ^{13}C NMR: ($CDCl_3$, 77.16 ppm): 159.18, 117.35, 111.28, 52.02, 25.00, 20.14, 13.79 ppm. IR (ATR, cm^{-1}): 3051, 3005, 2958, 2931, 2870, 1570, 1471, 1378, 1335 1241, 1212, 1098, 1018, 1011, 897, 864, 797, 730, 632, 597, 503, 493, 405. UV-vis (THF); λ_{max} in cm^{-1} (ε_M, $M^{-1}cm^{-1}$): 36700 (19200), 26200 (9500). TOF-MS (m/z): positive ion mode: $\{H[n\text{-}Bu_3NH]_2[Ti(C_6H_4O_2)_3]\}^+$, 745.4624.

Combustion analyses calculated for $C_{42}H_{65}Br_3N_2O_6Ti$ (found): 67.72 (66.88) % C; 9.20 (8.77) % H; 3.76 (4.42) % N.

(*n*-$Bu_3ND)_2[Ti(C_6H_4O_2)_3]$ (**2-*d*^{2}-Ti**) In a N_2-filled glovebox, **2-Ti** was washed with MeOD and allowed to stir for 10 minutes. All volatile materials were removed under reduced pressure. This process was repeated two more times to give **2-*d*^{2}-Ti**.

(*n*-$Bu_3NH)_2[V_{0.483}Ti_{99.517}(C_6H_4O_2)_3]$ (**2$_{0.5\%}$**) In a N_2-filled glovebox, a 20-mL scintillation vial was charged with 0.4071g of **2-Ti** and 537 μL of a 10 mM solution of **2** in THF. All volatile materials (THF) were removed under reduced pressure.

(*n*-$Bu_3NH)_2[V_{0.064}Ti_{99.936}(C_6H_4O_2)_3]$ (**2$_{0.05\%}$**) In a N_2-filled glovebox, a 20-mL scintillation vial was charged with 0.4071g of **2-Ti** and 54.0 μL of a 10 mM solution of **2** in THF. All volatile materials (THF) were removed under reduced pressure.

(*n*-$Bu_3ND)_2[V_{0.504}Ti_{99.496}(C_6H_4O_2)_3]$ (**2-*d*$^2_{0.5\%}$**) In a N_2-filled glovebox, a 20-mL scintillation vial was charged with 0.4071g of **2-Ti** and 537 μL of a 10 mM solution of **2** in THF. All volatile materials (THF) were removed under reduced pressure. The powder was dissolved in MeOD then all volatile materials (MeOH and MeOD) were removed under reduced pressure three times to deuterate the N-H proton.

(*n*-$Bu_3ND)_2[V_{0.0635}Ti_{99.9365}C_6H_4O_2)_3]$ (**2-*d*$^2_{0.05\%}$**) In a N_2-filled glovebox, a 20-mL scintillation vial was charged with 0.4071g of **2-Ti** and 54 μL of a 10 mM solution of **2** in THF. All volatile materials (THF) were removed under reduced pressure. The powder was dissolved in MeOD then all volatile materials (MeOH or MeOD) were removed under reduced pressure three times to deuterate the N-H proton.

*X-ray Data Collection, Structure Solution and Refinement for **2-Ti**.* The diffraction data were collected at the X-Ray Diffraction facility of the Central Instrument Facility at Colorado State University. Data for **2-*Ti*** were collected on a Bruker D8 Quest ECO single-crystal X-ray diffractometer equipped with Mo Kα (λ = 0.71073 Å). Data were collected and integrated using

Bruker Apex 3 software. Absorption correction were applied using SADABS.[32] Space group assignments were determined by examination of systematic absences, E-statistics, and successive refinement of the structures. Crystal structures were solved using SHELXT and refined with the aid of successive difference Fourier maps by SHELXL operated in conjunction with OLEX2 software.[33–35] None of the crystals demonstrated decay by X-ray radiation over the course of the experiment. Hydrogen atoms were placed in ideal positions and refined using a riding model for all structures.

Electron Paramagnetic Resonance. All samples were prepared under an inert atmosphere and loaded into a 4 mm outer diameter (OD) quartz EPR tubes (Wilmad 707-SQ-250M) in a glove box, sealed with a septum, attached to a Schlenk line and cycled three times with He gas and flame sealed under static vacuum (~100 mTorr). Samples were stored at ambient temperature. Sample **2-*d*^{2}** was prepared by first loading 0.01 mL 10 mM THF solution into an EPR tube. Following removal of THF under reduced pressure, 0.116 g *o*-terphenyl (0.1 mL when molten) was loaded into the same tube. After sealing as described above, this sample was heated with a heat gun until a dark blue solution formed. While sample tubes prepared in this manner can be stored at room temperature for an extended period, the quality of the OTP glass deteriorates with time. Hence, prior to each measurement, the glassy OTP samples were remelted in a warm water bath (~ 60 ^{o}C) to ensure uniform glass formation and quickly inserted into a pre-cooled cryostat for liquid He measurements. The simulations for solid state (glassy solution or solid) EDFS spectra were done using Easyspin[36] with the function pepper and the esfit function was used to refine the simulations. Simulations of the CW spectra were performed with the Bruker Xepr routine AnisoSpin Fit because it has the option for anisotropic linewidths, which is not available in EasySpin. Uncertainties in the g and A values of the CW simulations were estimated by varying the fit parameters until there was discernable deviation of the simulation from the 'best-fit' simulation. These uncertainties were set as the deviation range in simulating the EDFS with EasySpin Esfit function

Pulsed EPR experiments and data collections were done at the University of Denver EPR Center on Bruker E580 spectrometer equipped with an ER4118X-MD5W1 dielectric resonator and an Oxford CF935 cryostat. The resonator assembly includes a calibrated cernox sensor to monitor temperature at the resonator. Temperature control was achieved with an Oxford ITC503 temperature controller for cryogenic temperatures. Temperatures of 70 K and below were achieved with a ColdEdge/Bruker Stinger closed-cycle helium system and an Oxford Mercury temperature controller. Temperatures of 80 K and above were achieved with a liquid nitrogen flow system and an Oxford ITC503 temperature controller. The X-band microwave frequency was about 9.710 GHz. Echo detected field-swept spectra (EDFS) were occasionally collected and checked throughout the series of variable temperature measurements to ensure that the sample was still glassy. In the past, it has been shown that when the glass is not good enough it leads to poor quality EDFS spectra (Fig. S22 in ref.1). For pulse experiments, the resonator was over-coupled to a Q of ca. 120 to 170 ns to minimize resonator ringdown from the microwave pulses. Data processing was done using Xepr, Matlab 2019a, and Origin Pro 2018b software packages.[37,38]

Since no significant orientation dependence was observed, T_1 data were collected using the inversion recovery sequence ($\pi - t - \pi/2 - \tau - \pi - \tau -$ echo) on the most intense resonance line in the center of the EDFS spectrum with a π/2 pulse length of 40 ns. The attenuation of the 1 kW TWT was selected to maximize the 2-pulse echo and typically was about15 dB. The constant τ was 200 ns. The initial value of t was 360 ns and was incremented in 256 steps with step sizes that decreased with increasing temperature to provide data that came to equilibrium at the end of the data acquisition window. Four-step phase cycle was used to get rid of unwanted echoes and ringdown. The inversion recovery data were fit with a bi-exponential function of the form:

$$Y(t) = C_0 + C_1 e^{(-t/T_1(long))} + C_2 e^{(-t/T_1(short))}$$

where C_2/C_1 is the ratio of contributions from relaxation processes with time constants of T_1(short) and T_1(long) or with a stretched exponential of the form $\mathrm{I}(\tau) = I(0) - Ae^{-\left(\frac{t}{Tm}\right)^{\beta}}$.[39,40,] T_1 changes by more than 4 orders of magnitude over the range of temperatures studied. To permit display of the experimental data for this wide range of temperatures in a single panel, semi-log plots are shown in Fig. 6.17 to 6.19. In this display an approximately exponential recovery appears sigmoidal. At each temperature the data points acquired with the shortest pulse timing t are most strongly impacted by spectral diffusion processes. In the least-squares fitting these points have a relatively small impact on the fit parameters, although discrepancies between experiment and fit function at the short values of t are highlighted in the semi-log display.

Many factors can contribute to uncertainty in values of T_1. The quality of fits is strongly dependent on the signal-to-noise (S/N) of the experimental data. When the S/N is low, the data may be fit with a single exponential as well as to a double exponential, or stretched exponential, even if the experimental decay really does have multiple components. However, the S/N was good for all the data sets used in our analysis. T_1 is strongly temperature dependent. Efficient thermal equilibration of the sample was facilitated by back-filling the deoxygenated samples with a partial pressure of Helium of about 100 mtorr. The cernox sensor built into the resonator assembly was used to monitor sample temperature. At most temperatures studied the inversion recovery data fit better to a stretch exponential than to a single exponential, indicating a distribution of relaxation times. When there is a distribution, the calculated relaxation time depends on the length of the data acquisition window. If the window does not extend to sufficiently long time, the long components of the distribution are under-sampled. There also is a possibility that components with short T_1 may be lost in the deadtime of the instrument or as the result of window selection, which causes under-sampling of those components. Because of the strong temperature dependence of T_1 under-sampling of short T_1 is of greater concern at higher temperature. These uncertainties impact the values calculated using either a stretch exponential

or the long component of the bi-exponential fit and make it difficult to calculate uncertainties in T_1. We typically estimate uncertainties of about 10%.

To gain insight into the processes that govern the spin-lattice relaxation, $1/T_1$ data were modeled using the following equation performed in Mathcad software:

$$\frac{1}{T_1} = A_{\mathrm{dir}}T + A_{\mathrm{Ram}}\left(\frac{T}{\theta_{\mathrm{D}}}\right)^9 J_8\left(\frac{\theta_{\mathrm{D}}}{T}\right) + A_{\mathrm{loc}}\left[\frac{e^{\Delta_{\mathrm{loc}}/T}}{\left(e^{\Delta_{\mathrm{loc}}/T}-1\right)^2}\right]$$

Here, $J_8\left(\frac{\theta_{\mathrm{D}}}{\mathrm{T}}\right)$ is the transport integral:

$$J_8\left(\frac{\theta_{\mathrm{D}}}{T}\right) = \int_0^{\theta_{\mathrm{D}}/T} x^8 \frac{\mathrm{e}^x}{(\mathrm{e}^x-1)^2}\,\mathrm{d}x$$

T_m data were collected on the most intense resonance line in the center of the EDFS spectra via a Hahn 2-pulse echo sequence ($\pi/2$ − τ − π − τ − echo) with a 2-step phase cycle where the $\pi/2$ was 40ns. The initial value of the inter-pulse delay τ was 200ns, which was incremented in 256 steps. The increments were selected to ensure equilibrium values at the end of the data acquisition window. In the Bruker software the pulse repetition time is denoted as the shot repetition time (SRT). If the SRT is shorter than the electron spin T_1 the echo decay curve may depend on the SRT because the spin populations have not fully returned to equilibrium after the prior echo sequence. One manifestation of this problem is that the amplitude of the recovery curve is decreased. Recovery is more complete for faster relaxing components in a distribution so short SRT also over-samples the faster relaxing spin and the calculated time constant decreases. If the shots/pt is 1 the software overhead imposes a delay between pulse sequences which allows more time for population equilibration than when a large number of shots/pt (e.g. up to 16) is used (Table 6.7). These distortions of the echo decay curves are most evident at the shorter pulse delays. If the inherent T_m is long, distortions for short pulse timings have less impact on the calculation of T_m than when T_m is shorter. The impact of SRT on the calculated value of T_m was most evident for **1** (Table 6.7).

The 2-pulse echo decay data were fit using the stretched exponential equation: $\mathrm{I}(\tau) = I(0) - Ae^{-\left(\frac{2\tau}{T_m}\right)^{\beta}}$ where β is a stretch parameter. The low temperature data for **4** and **3** fit better with stretched exponential equation than for **1** and **2** due to the dominant nuclear spin diffusion. It was observed that β approaches 1 as the temperature increases to roughly 70−80 K, indicating that a conventional single exponential fit could be used. Nevertheless, we used the stretched exponential fit throughout the whole temperature range for consistency. Contrary to the study published in 2018 (ref 1), the T_m at low temperatures for **2** in OTP can be fit with β = 1 indicating that the process that dominates T_m in **3** and **4** in OTP are different than for **2** in OTP. Additionally, it has been observed that the echo decay for **1** in OTP exhibits modulation with a 2 μs period, which is attributed to the ethyl groups of the cation.

The signal-to-noise was high for all the data reported, so that is not a major source of uncertainty in T_m. Although SRT > $5T_1$ was used to acquire the echo decays which is long enough to avoid the problems discussed above, a small rapidly decaying component was observed at short values of 2τ, which is attributed to a small population of more rapidly relaxing spins.[24] The fits to the data were obtained using the Bruker 'qualifier' option to exclude that segment of the decay. Values of T_m and β were weakly dependent on the starting time for the fitting, provided that the first point is later than the obvious end of the fast component. Echo modulation is a major source of uncertainty in fitting 2-pulse echo decay data. The length of the π/2 pulse was 40 ns, which is sufficiently selective that the proton ~ 14 MHz modulation was not conspicuous in the decays. Modulation was not observed in the echo decays for **2**, **3**, and **4**. The ~ 2 μs modulation on the echo decays for **1** introduces uncertainty in the T_m values, which becomes more problematic as T_m decreases and becomes comparable to the period of the modulation.

3P ESEEM data were collected on the most intense resonance line in the EDFS spectrum of **2-d²** in OTP and of **2-d²$_{0.05\%}$** via a three-pulse sequence ($\pi/2$ − τ − π/2 − t − π/2 - τ − echo) to characterize the ^{2}H modulation from the N-D. The simulation of 3P ESEEM data was performed

in EasySpin. The depth of the deuterium modulation depends on the number of interacting nuclei and the distance between the deuterium and the unpaired electron. Matching the simulation to the experimental data for **2-d$^2_{0.05\%}$** required two equivalent ^{2}H nuclei each at distance r = 3.10 (0.01) Å (**Fig. 6.2**). The simulation is very sensitive to distance and the "best" distance of 3.1 Å was selected to match the depth of the modulation at short t.

The depth of the modulation decreases with increasing t, goes through an apparent null at t ~ 2.5 μs, then increases before finally decreasing (**Fig. 6.2**). The observation of a null followed by increasing depth of modulation is called 'phase reversal'.[18] The time at which the phase reversal occurs depends on the pulse timing, the electron-nuclear distance and the isotropic hyperfine interaction (a_{iso}). A small isotropic interaction (a_{iso}) value of 0.016 (0.001) MHz was included to accurately simulate the timing of the phase reversal. Given a distance r = 3.1 Å between the electron and the nuclear spin, then the anisotropic hyperfine interaction T would be given by $T = (\frac{2.001*0.857*B_e*B_n}{r^3*h})/(1.0*10^6)$ which is 0.406 MHz. The three principal hyperfine values are therefore A_{xx} = Ayy = a_{iso}-T and A_{zz} = a_{iso}+2T which are 0.390 MHz and 0.829 MHz, respectively. To simulate the decrease in modulation depth with increasing t, a small quadruple coupling was included in the simulation as Q_{xx} = Q_{yy}= -0.0285(0.0005) MHz and Q_{zz}= 0.0570(0.0005) MHz. If the quadrupole coupling is omitted, the simulation still matches well with the modulation depth at short delays and with the timing of the phase reversal, but the simulation overestimates the modulation depth at longer delay times. The evidence that ESEEM originates from two equivalent nuclei and the fact that the distance calculated is in good agreement with the X-ray data indicates that both deuterons are in the local environment for the **2-d$^2_{0.05\%}$** sample in the diamagnetic Ti host and consistent with the proposed hydrogen bonding to the cation.

For **2-d^2** in OTP the depth of the deuterium modulation varied with sample preparation, but the time for the phase reversal was the same as in the Ti host. The consistent timing of the phase reversal indicates that all of the ^{2}H modulation arises from deuterium atoms at the same

distance from the vanadium. Decreased modulation depth could arise from partial dissociation of the cation or from back exchange of the ^2H with trace amounts of H_2O in the solvents.

Other Physical Measurements. ^1H NMR spectra were collected on a Bruker Avance NEO 400 MHz spectrometer. The spectra were referenced using residual protiated solvent signal as an internal standard ($CDCl_3$, 7.26 ppm). Infrared spectra were recorded on a Bruker TENSOR II FTIR spectrometer. Inductively Coupled Plasma Optical Emission Spectroscopy (ICP-OES) was carried out using a PerkinElmer Optima 7300 DV and the TOPM standards program in the Plant and Soil Science Laboratory at Colorado State University. All samples and reference standards were prepared by digesting in HNO_3 and diluting to 10% HNO_3 by volume with HPLC grade H_2O (filtered through 0.2 µm filter) and subsequent filtering of the digested sample through a glass fiber filter. Time of flight mass spectrometry (LTQ-MS) measurements were performed on acetonitrile solutions with an Agilent 6230 Time of Flight (TOF) LC-MS B-TOF at the Analytical Resources Core Center for Materials and Molecular Analysis (ARC-MMA) of the Colorado State University.

Modeling of T_m Data With Proton and Methyl Group Distances Obtained From Crystal Structures. Modeling was performed using the empirical model for the impact of methyl and non-methyl protons on spin echo dephasing that we reported in *Mol. Phys*. **95**, 1255 – 1263 (1998). A more recent analysis of spin echo dephasing using a deterministic quantum model did not include methyl groups.[26] Locations of methyl and non-methyl protons for **2-Ti** were assumed to be the same as in the crystal structure of **2-Ti•(THF)$_2$** and were 'binned' into shells with thickness of 0.5 Å. The shells in the calculation were centered at the midpoints of the bins (Table 6.9). It was assumed that the spin delocalization into the catecholate rings was large enough to shift these resonances and prevent participation in spin diffusion, which has been described as the 'black sphere'.[42,43] Protons (including methyl groups) closer than about 6 Å were also assumed

to be within the 'black sphere'. Calculations showed that the methyl groups were the dominant contributors to T_m. Although non-methyl protons with distances between 6 and 10 Å from the V were explicitly included in the simulations, the parameters for these nuclei had minimal impact on the modeling so the focus is on the methyl protons. Methyl groups more than 10 Å from the vanadium had minimal impact on the dephasing. The rate of averaging of environments for the methyl protons was adjusted to fit the decay curve for the sample **2-Ti** in the diamagnetic titanium analog. This rate at 5 – 10 K presumably is the quantum mechanical methyl tunneling frequency. It was assumed that this rate was the same in OTP as in the Ti host.

The distances to methyl and non-methyl protons for **2** in OTP were estimated from the structure of **2** previously published.[14] For **3** the distances were estimated from the structure of the pure vanadate complexes.[14] For **2-Ti** the only adjustable parameter was the methyl dephasing rate, which was adjusted to fit the decay curves. The resulting value of W_m was 5 MHz which is close to the values of about 10 MHz obtained for methyl groups on alkyl chains of solvents.[24] For both the butyl (**3**) and hexyl (**4**) complexes the echo decays were too fast when the distances from the X-ray structures were used in model the echo decays, and the methyl dephasing rate was assumed to be the same as in the Ti host. It seems plausible that in OTP the alkyl groups adopt more extended conformations than in the crystal. The positions and numbers of CH_3 groups shown in Table 6.9 for modeling the T_m data for the samples in OTP are not unique, but provide a sense of the extent to which the conformations have changed relative to the distances in the crystal structures.

Table 6.1. Crystallographic information for the structural refinement of **2-Ti•(THF)$_2$**.

Empirical formula	$C_{50}H_{84}N_2O_8Ti$
Formula weight	892.13 g/mol
Temperature	99.93 K
Crystal system	monoclinic
Space group	C2/c
a	12.8268(11) Å
b	21.9164(19) Å
c	17.7812(15) Å
α	90°
β	99.648(3)°
γ	90°
Volume	4927.9(7) Å^3
Z	4
ρ_{calc}	1.202 g/cm^3
μ	0.254 mm^{-1}
F(000)	1940.0
Crystal color	Dark orange red
Crystal size	0.403 × 0.202 × 0.184 mm^3
Radiation	MoKα (λ = 0.71073 Å)
2θ range for data collection	5.516 to 51.36°
Index ranges	−15 ≤ h ≤ 15, −26 ≤ k ≤ 26, −21 ≤ l ≤ 21
Reflections collected	34618
Independent reflections	4629 [R_{int} = 0.0553, R_{sigma} = 0.0324]
Data/restraints/parameters	4629/5/280
Goodness-of-fit on F^2	1.229
Final R indexes [I≥2σ (I)]	R_1 = 0.0657, wR_2 = 0.1446
Final R indexes [all data]	R_1 = 0.0756, wR_2 = 0.1510
Largest diff. peak/hole	0.50/−0.38 e·Å^{-3}

Table 6.2. Simulation parameters for the CW spectra of **2** in OTP, $\mathbf{2}_{0.5\%}$, and $\mathbf{2\text{-}d^2}_{0.5\%}$ at 60 K.[a,b]

Complex	**2** in OTP	$\mathbf{2}_{0.5\%}$	$\mathbf{2\text{-}d^2}_{0.5\%}$
g_x	1.944 (0.004)	1.932 (0.002)	1.944 (0.002)
g_y	1.932(0.004)	1.933 (0.002)	1.945(0.002)
g_z	1.994(0.002)	1.987(0.002)	1.996 (0.002)
A_x (MHz)	299 (3)	301 (3)	305 (5)
A_y (MHz)	369 (4)	366 (4)	360 (5)
A_z (MHz)	14 (8)	22(8)	25 (10)
A_x strain (MHz)	7	12	8
A_y strain (MHz)	6	8	12
A_z strain (MHz)	3	4	4
Lw_x (MHz)	20	21	25
Lw_y (MHz)	26	22	35
Lw_z (MHz)	10	10	15

[a] The simulation of the spectra was performed using the AnisoSpinFit software in the Bruker Xepr software. The values in parentheses are the uncertainties. The simulation program includes an option for anisotropic linewidths that gave improved agreement with experimental data. Peak to peak linewidths are defined as Lw_x, Lw_y, Lw_z along the three principal axes.
[b] The uncertainty in the parameters was estimated by varying the parameter within a small range and determining whether the simulation was still acceptable.

Table 6.3. Simulation parameters for the EDFS spectra of **2** in OTP, $\mathbf{2}_{0.5\%}$, and $\mathbf{2}\text{-}d^2_{0.5\%}$ at 4 K[a,b]

Complex	**2** in OTP	$\mathbf{2}_{0.5\%}$	$\mathbf{2}\text{-}d^2_{0.5\%}$
g_x	1.950	1.937	1.939
g_y	1.939	1.933	1.934
g_z	1.998	1.985	1.990
A_x (MHz)	300	295	295
A_y (MHz)	370	377	370
A_z (MHz)	24	23	10
A_x strain (MHz)	40	20	26
A_y strain (MHz)	0	10	10
A_z strain (MHz)	0	3	1
Lw	3.0	4.3	3.8

[a]The simulations were obtained with the Pepper function of EasySpin. The fitting parameters were constrained to be values obtained by fitting the CW spectra with AnisoSpinFit, but do not include anisotropic linewidths.

[b]The uncertainty in the fit parameters is similar to that for the CW spectra. The EDFS spectra are less well resolved than the CW simulations and are less sensitive to some parameters. For example, the A strain has an extremely small effect on EDFS and good spectral simulations can be produced without including the A strain in the fitting.

Table 6.4. T_1 values for **2** in d^{14}-OTP, $\mathbf{2}_{0.05\%}$, and $\mathbf{2}$-$d^2_{0.05\%}$ obtained by fitting the inversion recovery curves with a sum of exponentials or by fitting to a stretched exponential. For the two component fit the long component was assigned as T_1.

2 in d^{14}-OTP:		
T (K)	T_1 (ms)	T_1 (ms)[a]
4	82	41 (0.57)
10	6.4	3.6 (0.71)
20	0.43	0.30 (β = 0.83)
35	0.054	0.041 (β = 0.90)
50	0.018	0.011 (β = 0.91)

[a] Values obtained by fitting to a stretch exponential, with the stretch parameter β in parentheses.

$\mathbf{2}_{0.05\%}$:		
T (K)	T_1 (ms)	T_1 (ms)[a]
4	80	33 (0.55)
10	4.6	2.6 (0.68)
25	0.24	0.11 (0.77)
45	0.026	0.012 (0.81)
60	0.008	0.004 (0.83)

[a] Values obtained by fitting to a stretch exponential, with the stretch parameter β in parentheses.

$\mathbf{2}$-$d^2_{0.05\%}$:		
T (K)	T_1 (ms)	T_1 (ms)[a]
4	85	44 (0.55)
10	5.5	2.8 (0.75)
25	0.179	0.095 (0.80)
45	0.030	0.013 (0.79)
60	0.0084	0.0039 (β=0.81)

[a]Values obtained by fitting to a stretch exponential, with the stretch parameter β in parentheses

Table 6.5. Fit parameters for the temperature dependence of T_1 for **2** in OTP, **2** in d^{14}-OTP, and $\mathbf{2}_{0.05\%}$, using the long component of the two-component fit. See 'EPR Measurements' section for fitting equation. The standard error for each fit is reported in parentheses.

	$A_{dir}\,(s^{-1}K^{-1})$	$A_{Ram}\,(s^{-1})$	$\theta_D\,(K)$	$A_{loc}\,(s^{-1})$	$\Delta_{loc}\,(K)$
2 in OTP	2.8(0.2)	5.1(0.2)*10^5	65(3)	0.80(0.02)*10^7	260(20)
2 in d^{14}-OTP	3.5(0.2)	3.3(0.2)*10^5	66(3)	1.20(0.02)*10^7	280(20)
$\mathbf{2}_{0.05\%}$	3.8(0.2)	3.9(0.2)*10^5	68(3)	0.98(0.02)*10^7	300(20)

Table 6.6. 3P ESEEM fit parameters for $\mathbf{2\text{-}d^2}_{0.05\%}$.

	$\mathbf{2\text{-}d^2}_{0.05\%}$	
A (MHz)	*Axx* = *Ayy*	-0.390
	Azz	0.829
Q(MHz)	Q*xx* = Q*yy*	-0.0285
	Q*zz*	0.0570
r(Å)	3.1	

Table 6.7. Fit T_m values and stretch parameters for **1**-**4** OTP, **2-*d*^{2}** in OTP, **2$_{0.05\%}$**, and **2-*d*$^2_{0.5\%}$** from the stretched exponential fitting function: $I(2\tau) = I(0) - Ae^{-(\frac{2\tau}{T_m})^{\beta}}$.

1 in OTP:[a]

T (K)	T_m (μs)	β	T (K)	T_m (μs)	β
4	2.62	0.65	45	1.44	0.65
6	2.46	0.64	50	1.26	0.66
8	2.46	0.68	55	1.10	0.6
10	2.25	0.6	60	1.0	0.65
15	2.3	0.6	70	0.85	0.93
20	2.25	0.6	80	0.80	0.95
25	2.09	0.6	100	0.50	0.93
30	1.89	0.6	115	0.38	0.95
35	1.77	0.65	140	0.23	1
40	1.62	0.65			

[a] The shape of the echo decay is impacted by the echo modulation, so the apparent values of T_m may differ from the dephasing time that would be calculated if the modulation were modeled.

2 in OTP:

T (K)	T_m (μs)	β	T (K)	T_m (μs)	β
4	4.10	1.13	50	2.29	1.08
6	4.03	1.15	60	1.76	1.1
8	3.97	1.15	70	1.25	1.0
10	3.89	1.14	80	0.95	0.94
15	3.7	1.12	90	0.69	0.94
20	3.56	1.1	100	0.50	0.92
25	3.41	1.08	110	0.38	0.82
30	3.29	1.09	120	0.30	0.92
35	3.1	1.08	130	0.22	0.93
40	2.8	1.08	140	0.19	0.91

2 in d^{14}-OTP[a]:

T (K)	T_m (μs)	β	T (K)	T_m (μs)	β
4	3.53	0.95	35	2.89	0.84
6	3.52	0.94	40	2.54	0.83
9	3.67	0.93	45	2.26	0.84
12	3.53	0.91	50	1.93	0.82
15	3.54	0.92	55	1.68	0.81
20	3.42	0.90	60	1.47	0.80
25	3.25	0.88	70	1.11	0.76
30	3.13	0.85			

[a] The fit of the echo decays may be impacted by shallow ^{2}H modulation which cause greater uncertainty for the T_m and β values than for other samples.

3 in OTP:

T (K)	T_m (μs)	β	T (K)	T_m (μs)	β
4	5.41	1.76	40	4.14	1.51
6	5.29	1.74	50	3.33	1.36
8	5.24	1.70	60	2.35	1.24
10	5.2	1.68	70	1.7	1.12
15	5.12	1.67	80	1.14	0.98
20	5.02	1.69	90	0.64	0.92
25	4.87	1.66	100	0.45	0.91
30	4.73	1.67	120	0.18	0.92
35	4.5	1.67			

4 in OTP:

T (K)	T_m (μs)	β	T (K)	T_m (μs)	β
4	5.63	2.00	50	3.68	1.53
6	5.66	2.00	55	2.9	1.48
10	5.61	1.99	60	2.54	1.15
15	5.51	1.95	70	1.7	1.11
20	5.43	1.93	80	1.13	0.93
25	5.3	1.85	90	0.77	0.91
30	5.14	1.82	100	0.53	0.91
35	4.9	1.80	110	0.34	0.85
40	4.6	1.73	120	0.30	0.86
45	4.18	1.62	140	0.22	0.90

2$_{0.05\%}$:

T (K)	T_m (μs)	β
4	1.62	0.99
10	1.64	0.98
25	1.50	1.0
45	1.15	0.92
60	0.80	0.93

2-*d*^{2}$_{0.05\%}$:

T (K)	T_m (μs)	β
4	1.1	0.85
10	1.3	0.83
25	1.3	0.80
45	1.1	0.81
60	0.81	0.82

Table 6.8. T_m values showing the effect of SRT at 4.2 K for **1**. Data were fit using a stretched exponential fitting function: $I(2\tau) = I(0) - Ae^{-(\frac{2\tau}{T_m})^{\beta}}$.

SRT (ms)	100	10	10	2
Shots per point	16	16	1	1
Scans	4	4	64	64
Amplitude	9.6×10^5	5.2×10^5	1.85×10^6	1.85×10^6
T_m (μs)[a]	2.1	1.0	0.235	0.058
β[a]	0.54	0.47	0.30	0.28
T_m (μs)[b]	3.95	1.5	1.3	0.371
β[a]	0.85	0.54	0.46	0.43

[a] Calculated based on all data points.
[b] Calculated by omitting the early time points, prior to about 400 ns.

Table 6.9. Distances for protons on methyl groups taken from the crystal structure and distances used in modeling T_m data. Values denoted with and asterisk are assumed to be too close or too distant to include in the modeling.

All neighboring CH_3 for **2-Ti**, including intramolecular and intermolecular distances, based on the X-ray structure of **2-Ti•(THF)$_2$**.												
Distance range in Å	5 to 5.5	5.5 to 6	6 to 6.5	6.5 to 7	7 to 7.5	7.5 to 8	8 to 8.5	8.5 to 9	9 to 9.5	9.5 to 10	10 to 10.5	10.5 to 11
X-ray	2*	3*	1	6	3	3	2	3	7	1*	2*	1*
modeling			1	6	3	3	2	3	7			
Methyl groups within same molecular unit of **2** based on structure of **2-Ti•(THF)$_2$**.												
X-ray	2*	2*	0	6	2	0	0	0	6			
modeling						3	3	2				
Methyl groups within same molecular unit of $(Hex_3NH)^+$ on **3** based on its X-ray structure												
X-ray						2	2	9	1	1	3*	
modeling								1	3	1		

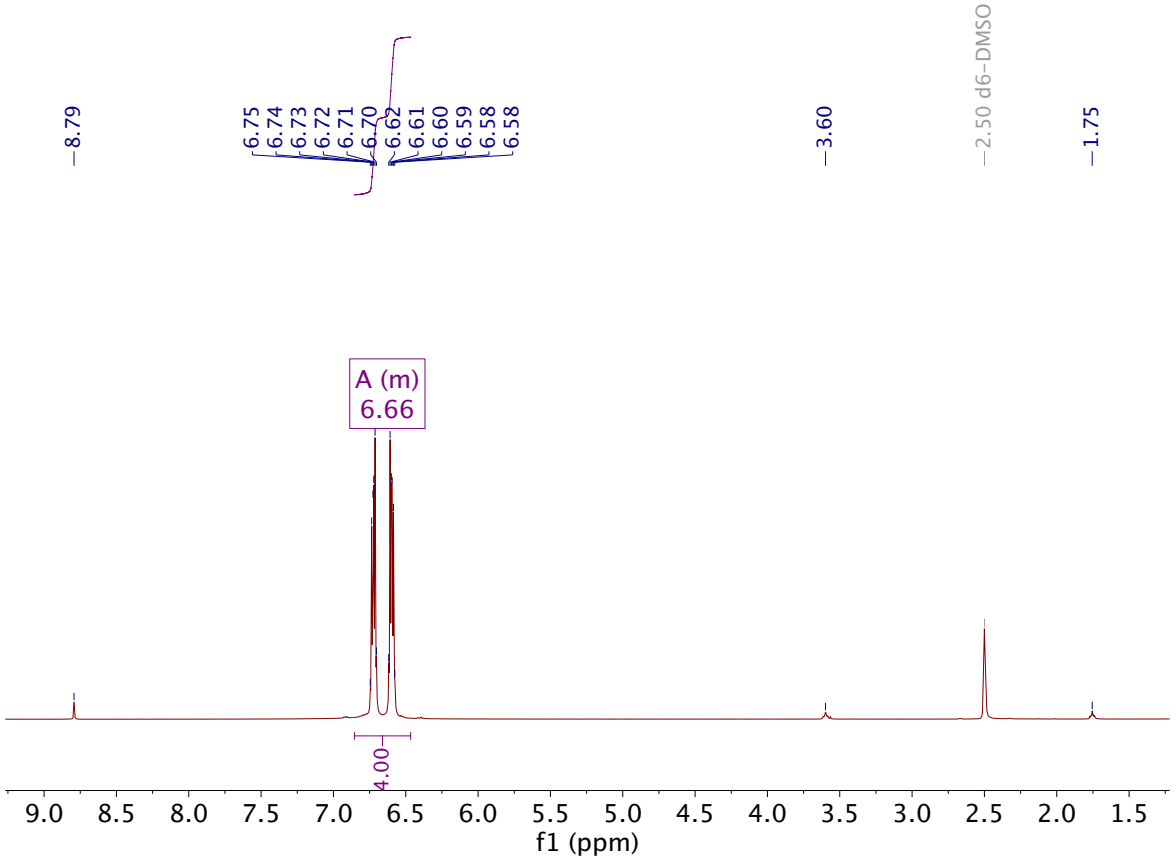

Figure 6.8. ^{1}H NMR of d^{2}-catechol in d^{6}-DMSO.

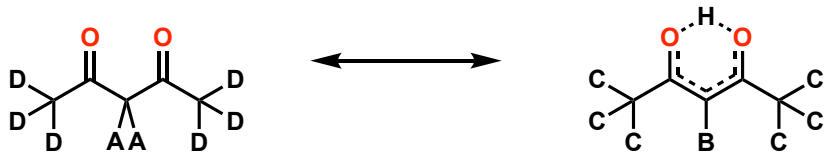

A = not visible due to deuteration

B = 5.04 ppm

C = 1.69 ppm

D = 1.75 ppm

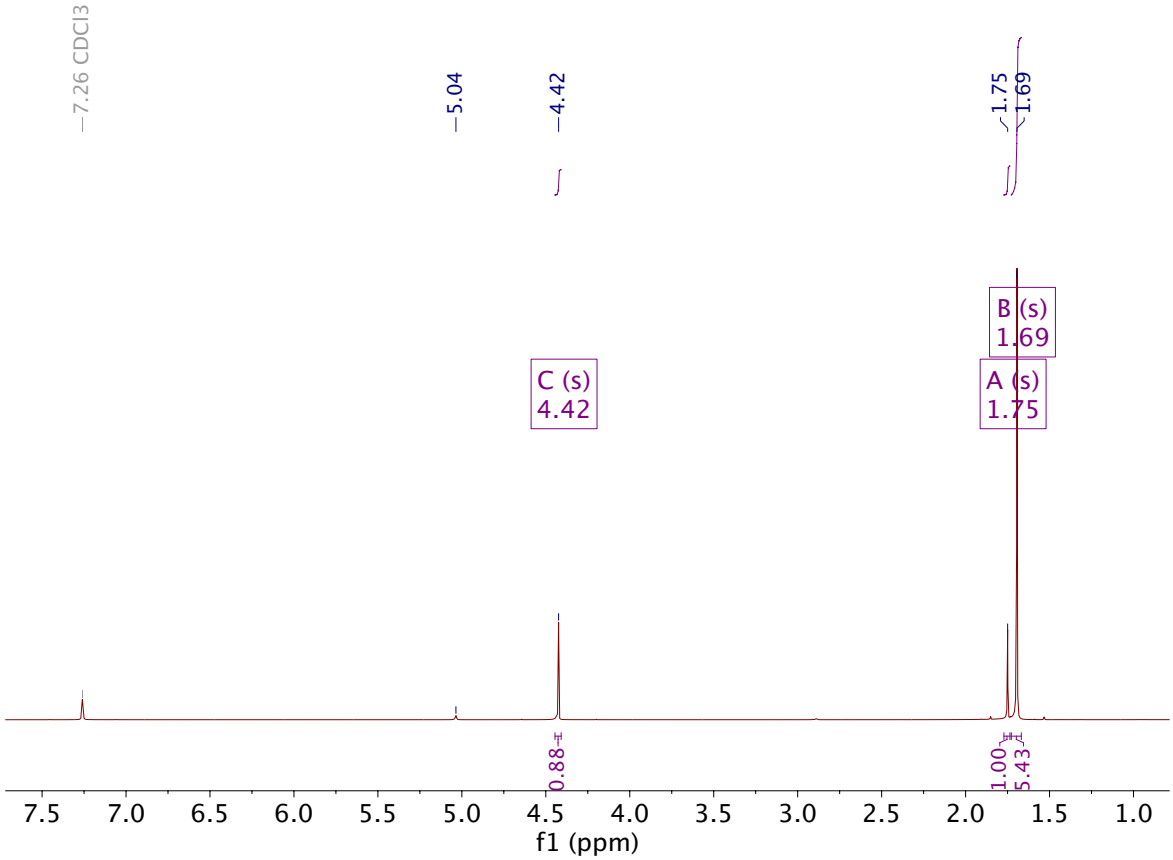

Figure 6.9. ^{1}H NMR of d^{2}-2,4-pentanedione in $CDCl_3$.

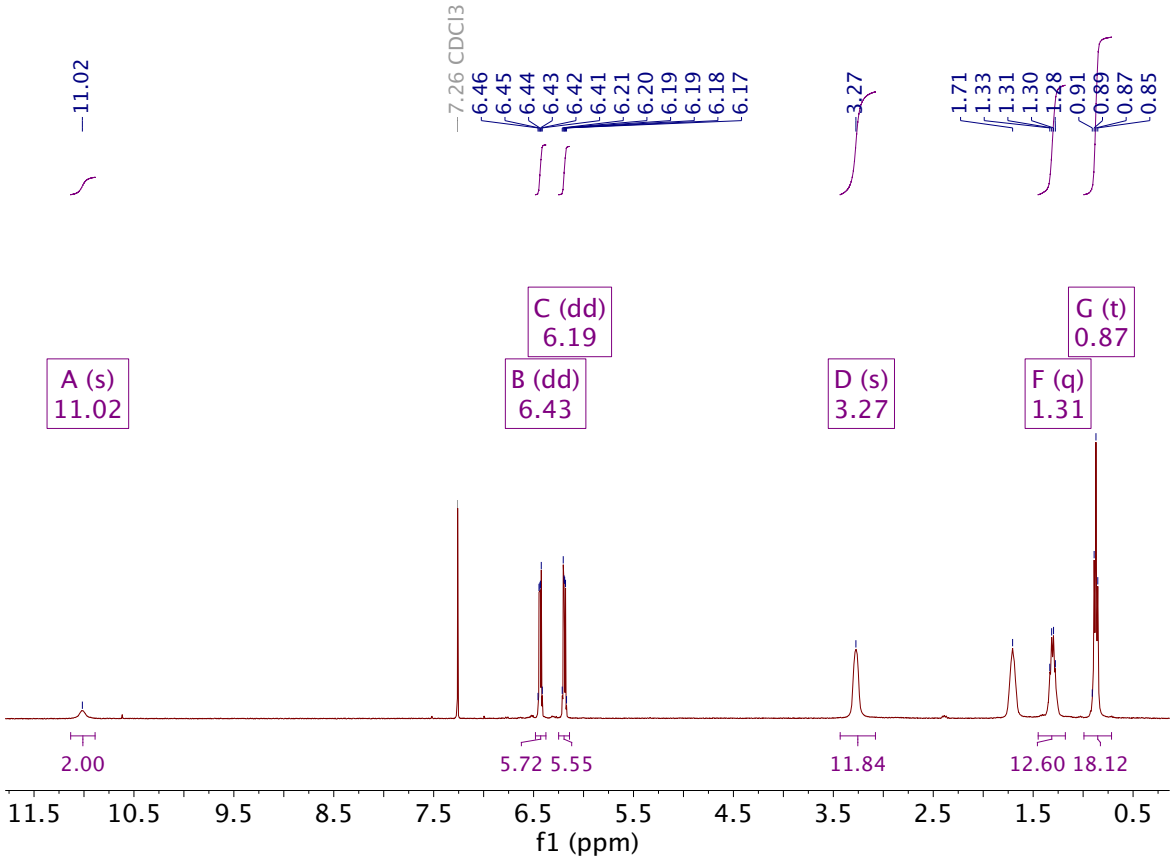

Figure 6.10. ^{1}H NMR of (*n*-Bu_3NH)[$Ti(C_6H_4O_2)_3$] (**2-Ti**) in $CDCl_3$.

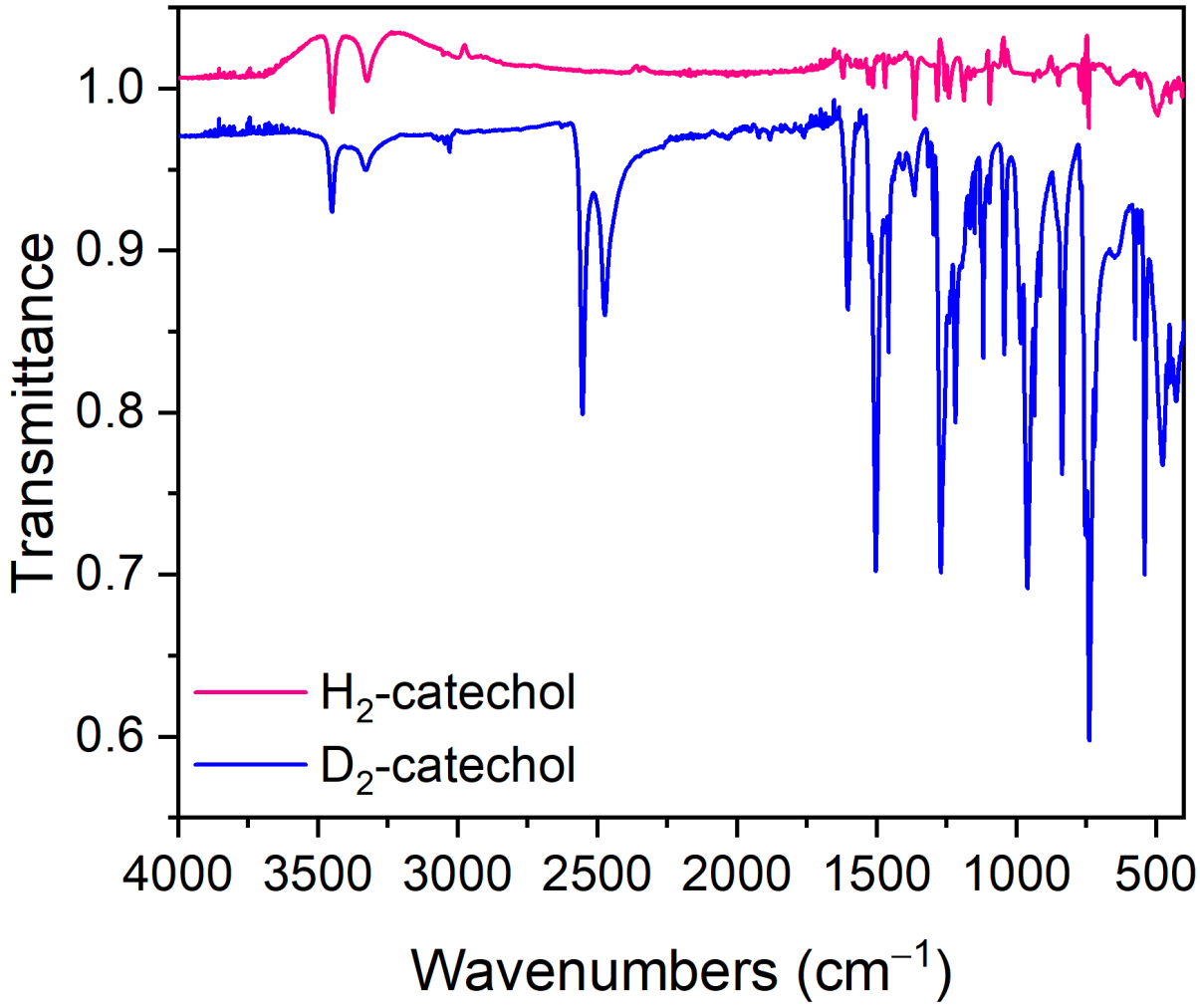

Figure 6.11. IR of catechol and d^2-catechol.

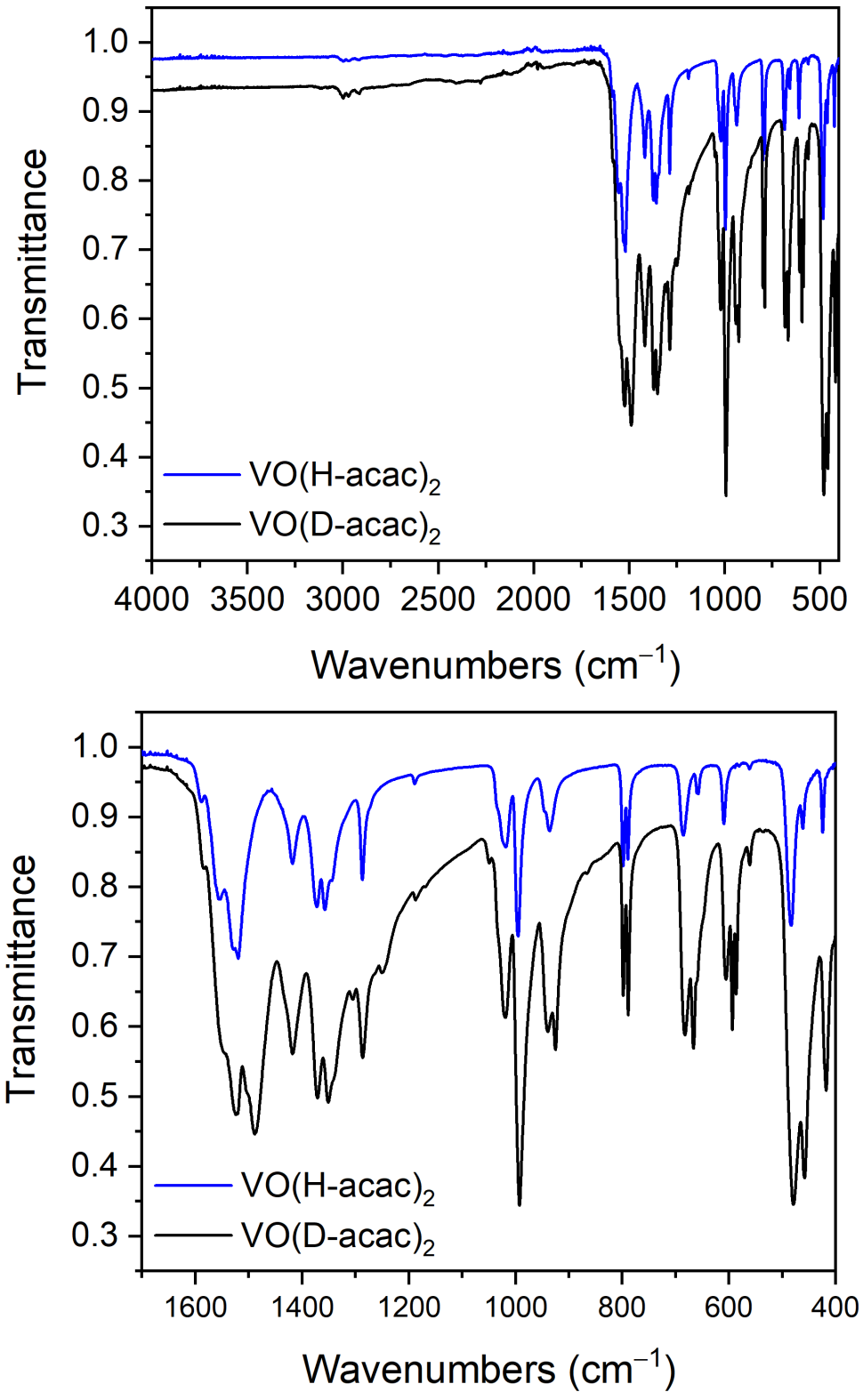

Figure 6.12. IR of VO(acetylacetonate-d^1) and VO(acetylacetonate).

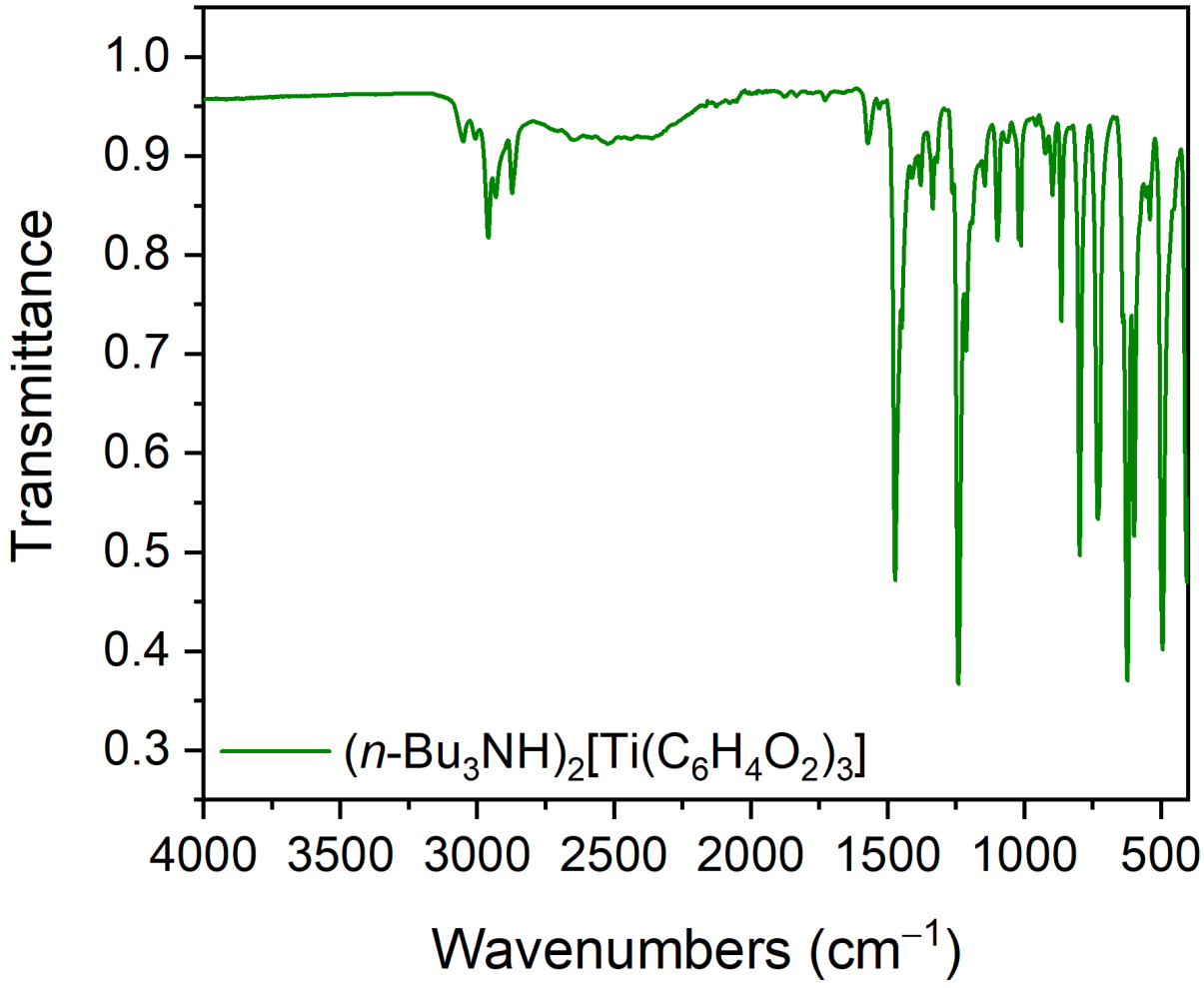

Figure 6.13. IR spectrum of (*n*-Bu_3NH)[$Ti(C_6H_4O_2)_3$] (**2-Ti**).

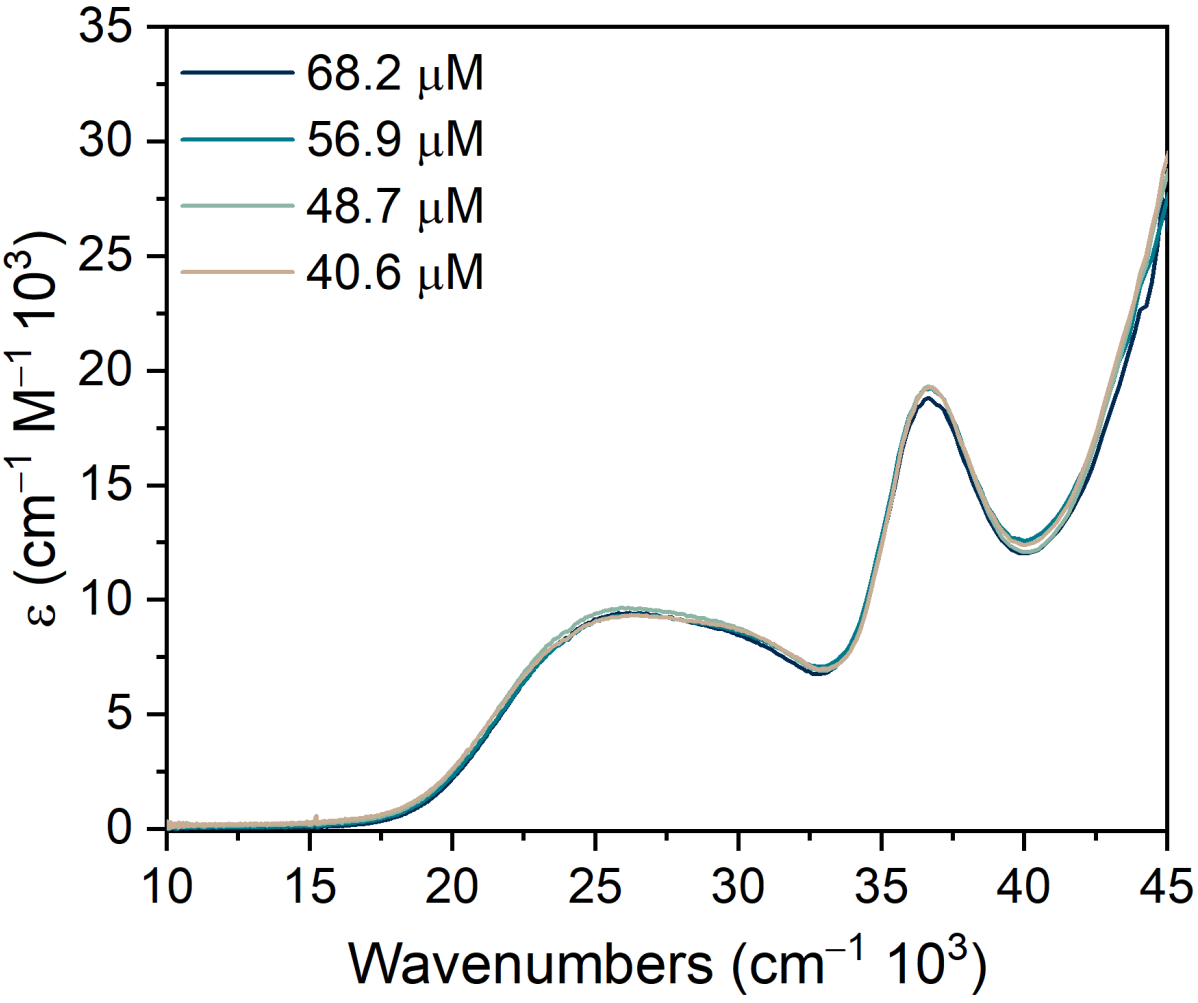

Figure 6.14. UV-Vis spectra of (*n*-Bu_3NH)[$Ti(C_6H_4O_2)_3$] (**2-Ti**).

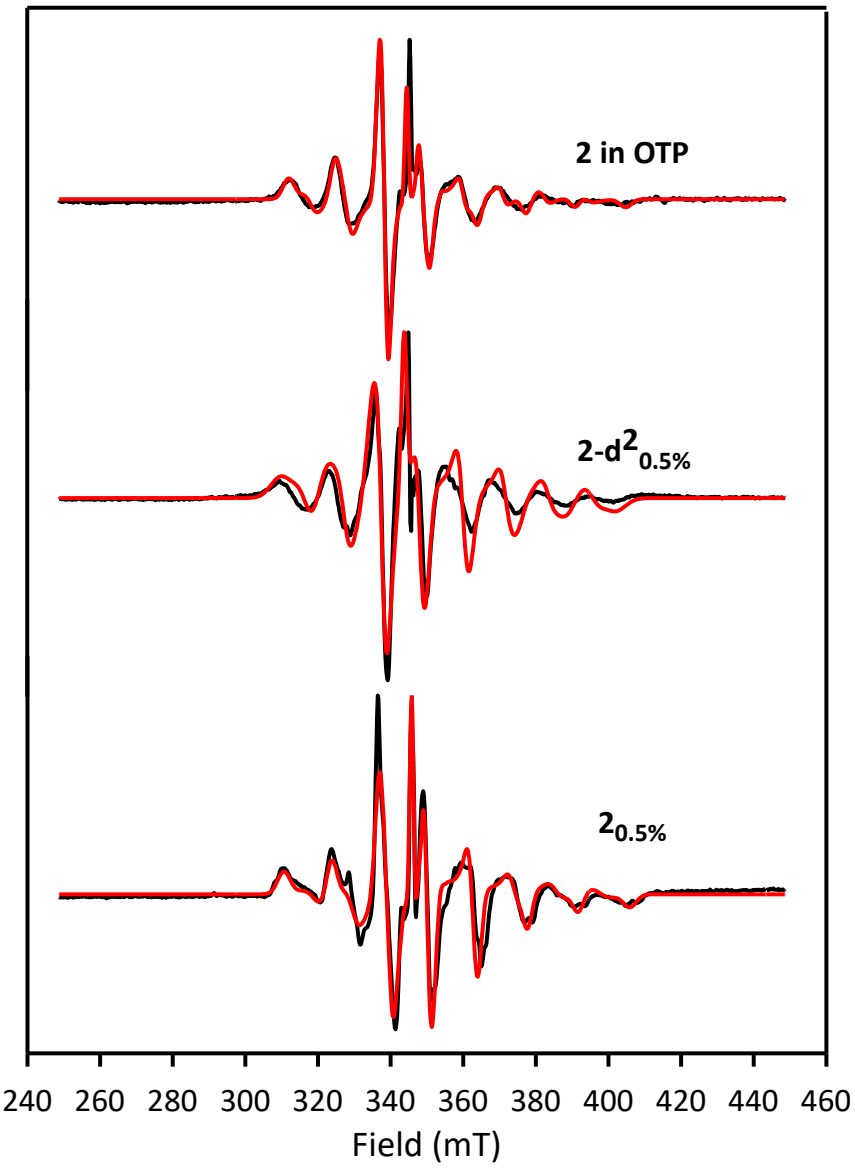

Figure 6.15. EPR spectra of **2** in OTP **(top), 2-*d*$^2_{0.5\%}$** (middle) **and 2$_{0.5\%}$** (bottom). Black line is the experiment and red line is the simulation. The parameters used for the simulation are listed in Table S2. Simulations were performed using AnisoSpinFit.

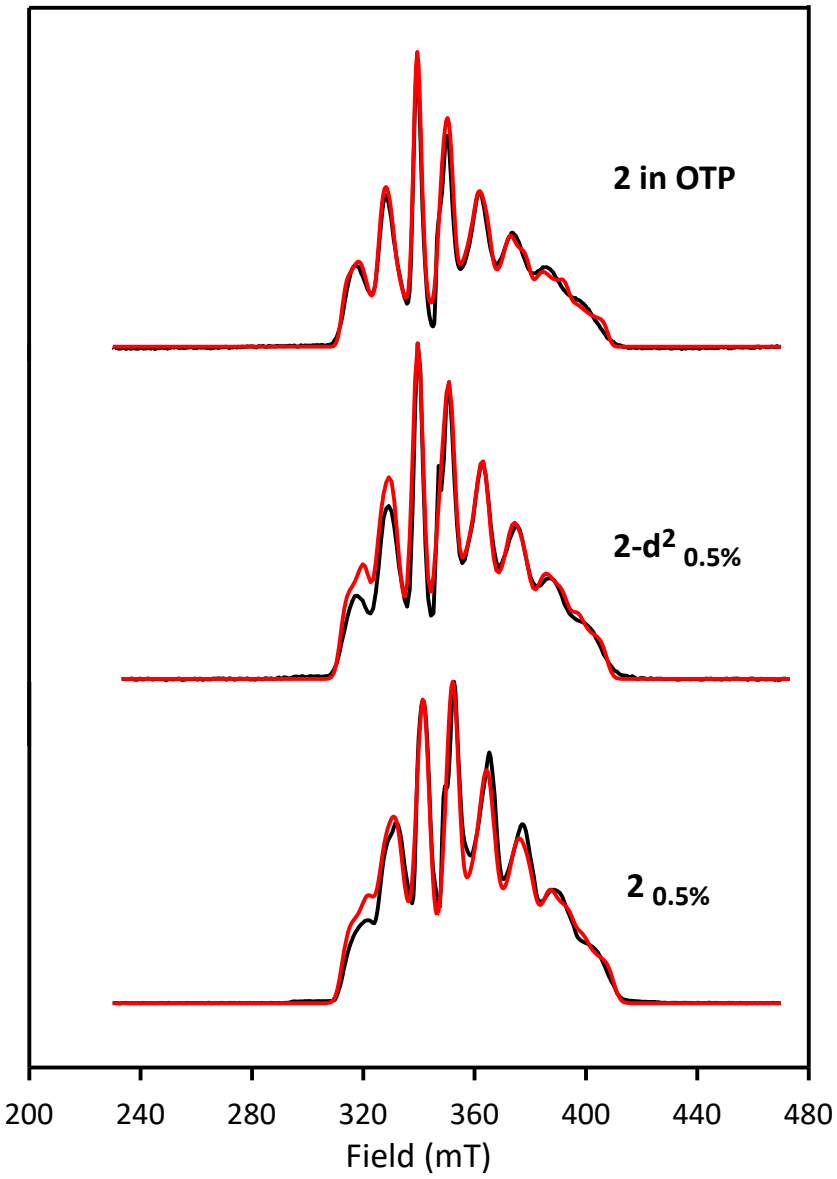

Figure 6.16. EDFS of **2** in OTP (top) and **2-*d*^{2}$_{0.5\%}$** (middle), and **2**$_{0.5\%}$ (bottom). Black line is the experiment and red line is the simulation. The parameters used to simulate the data are listed in Table 6.9. The simulation was performed in EasySpin using the Pepper function. Although the parameters cannot be exactly the same due to differences in the spectral lineshape, the simulation parameters were constrained to be similar to CW simulation.

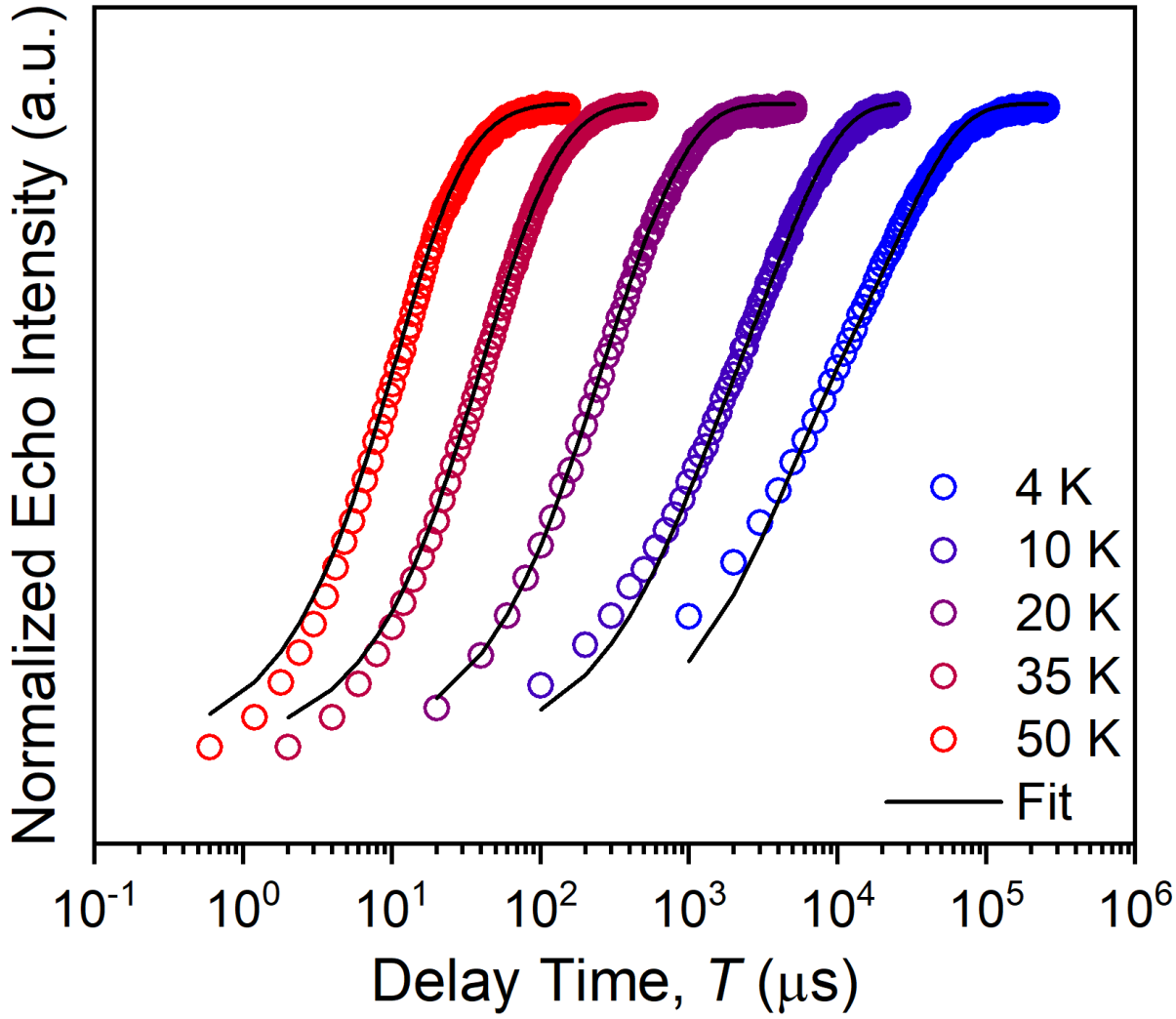

Figure 6.17. Variable temperature inversion recovery curves and fits for **2-*d*^{2}** in OTP.

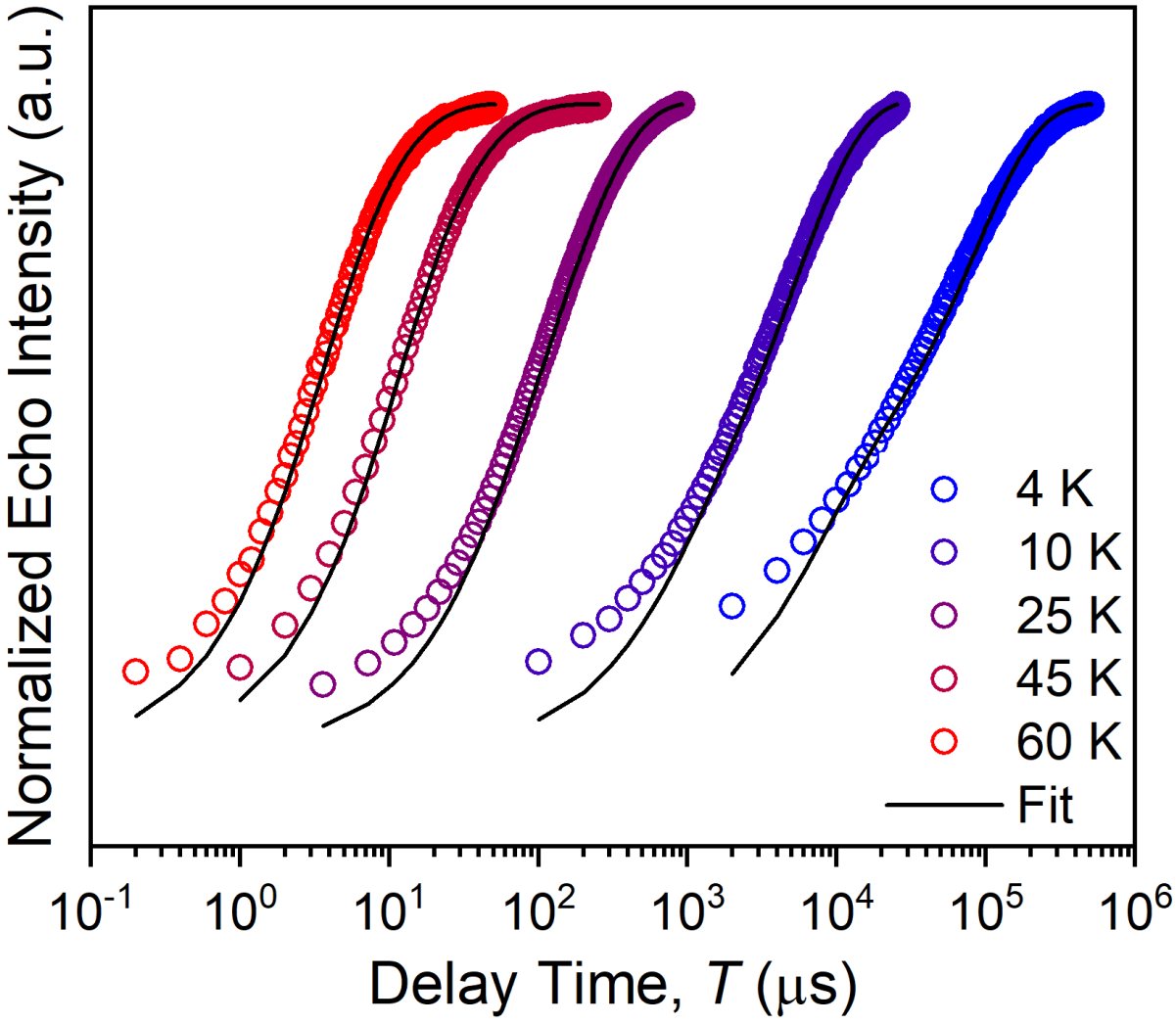

Figure 6.18. Variable temperature inversion recovery curves and fits for **2-$d^2_{0.05\%}$**.

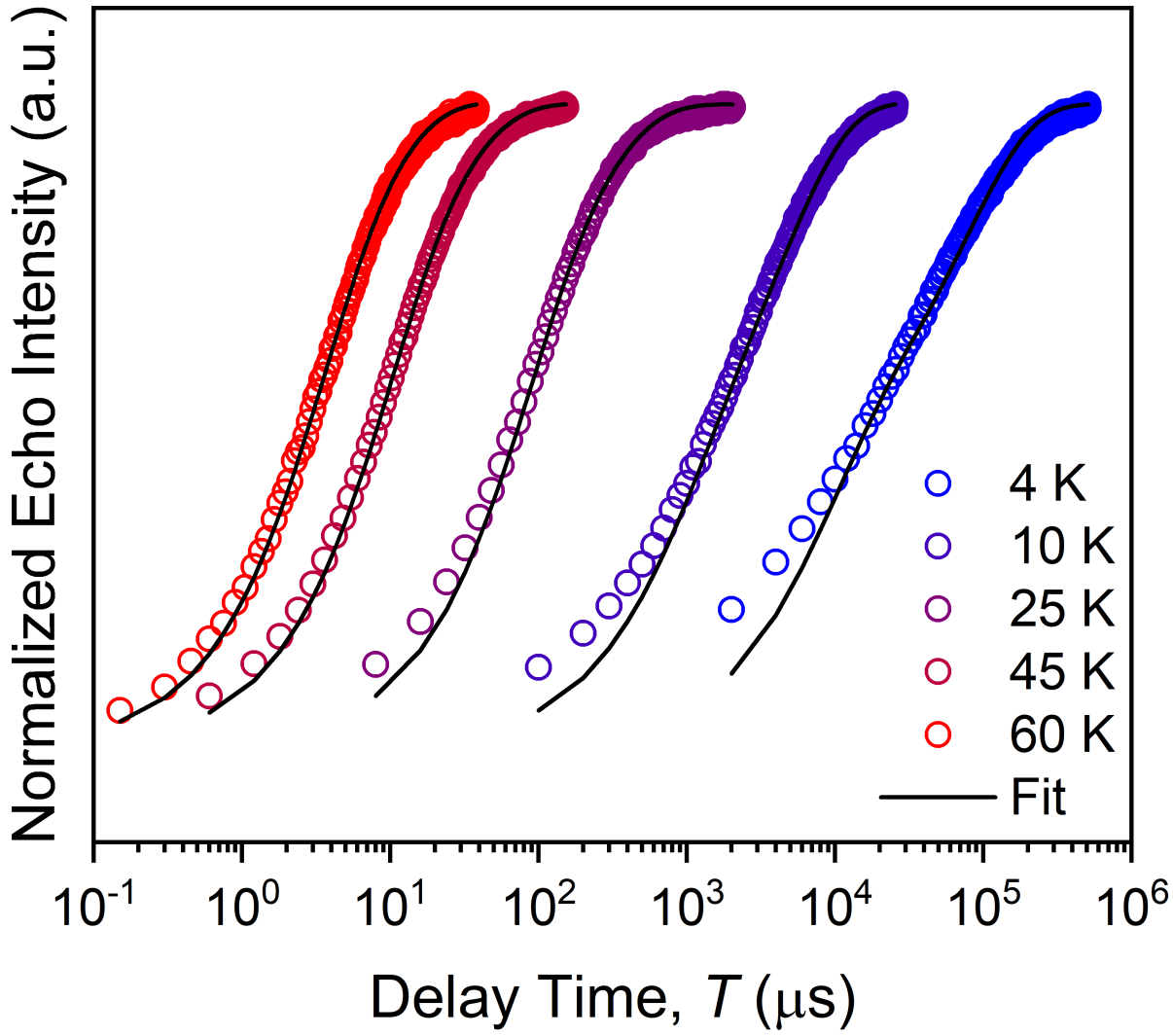

Figure 6.19. Variable temperature inversion recovery curves and fits for $\mathbf{2}_{0.05\%}$.

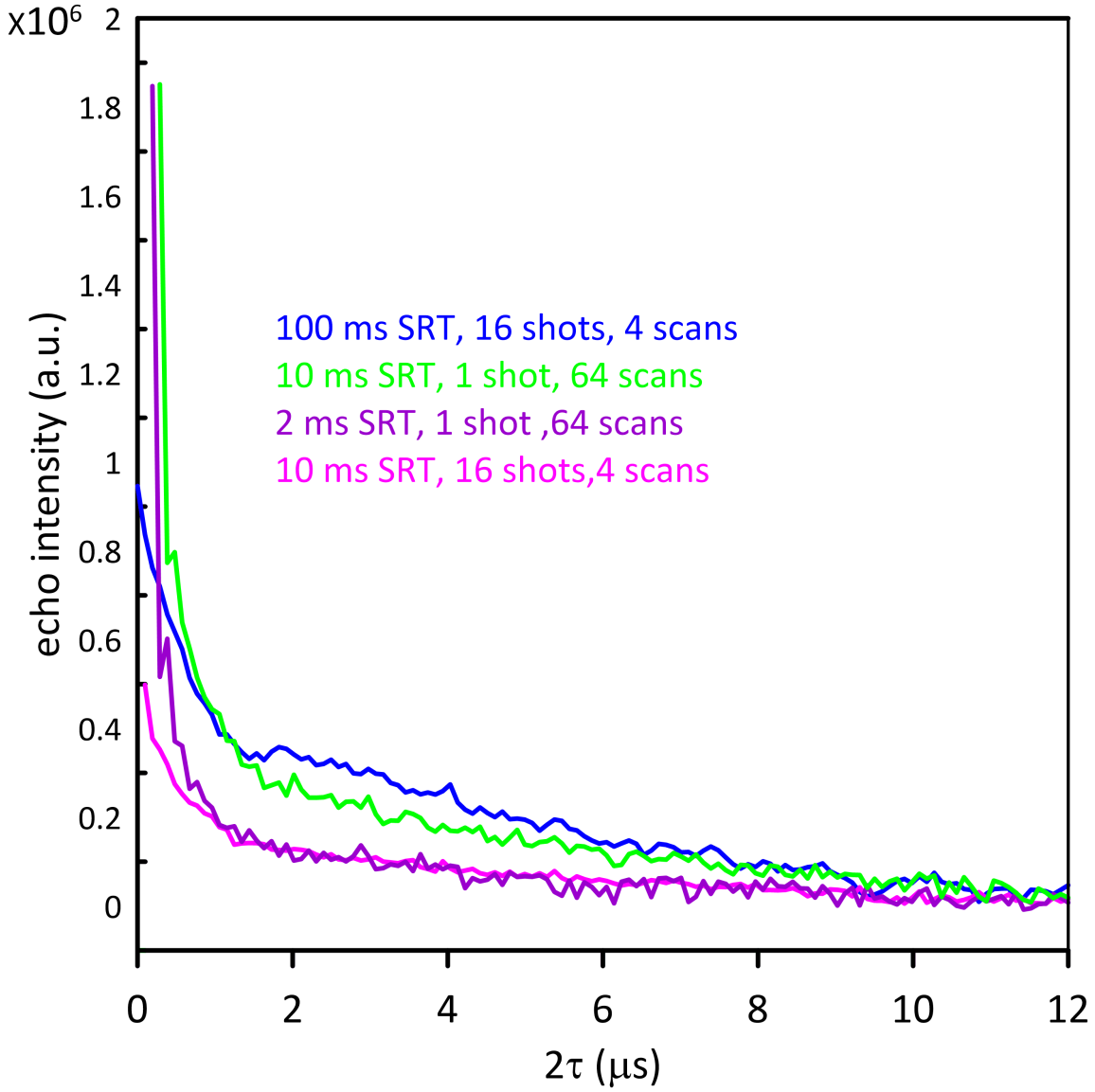

Figure 6.20. Alternate display of the SRT dependence of echo decay from Figure 6.5 showing relative intensities, without normalization, and a focus on values at shorter 2τ. Two-pulse echo decays for **1** in OTP at 4.2 K obtained with values of SRT ranging from 100 ms to 2 ms. The number of measurements averaged for each point is the product of shot/pt times number of scans, which was the same for the 4 traces shown. If SRT had been sufficiently long relative to T_1 the initial amplitude for the 4 traces should have been the same. To reflect differences in amplitudes the y axis (in arbitrary units) is the same for the 4 traces. The same data are shown in Figure 6.5, on a normalized y axis to highlight changes in the shapes of the echo decay.

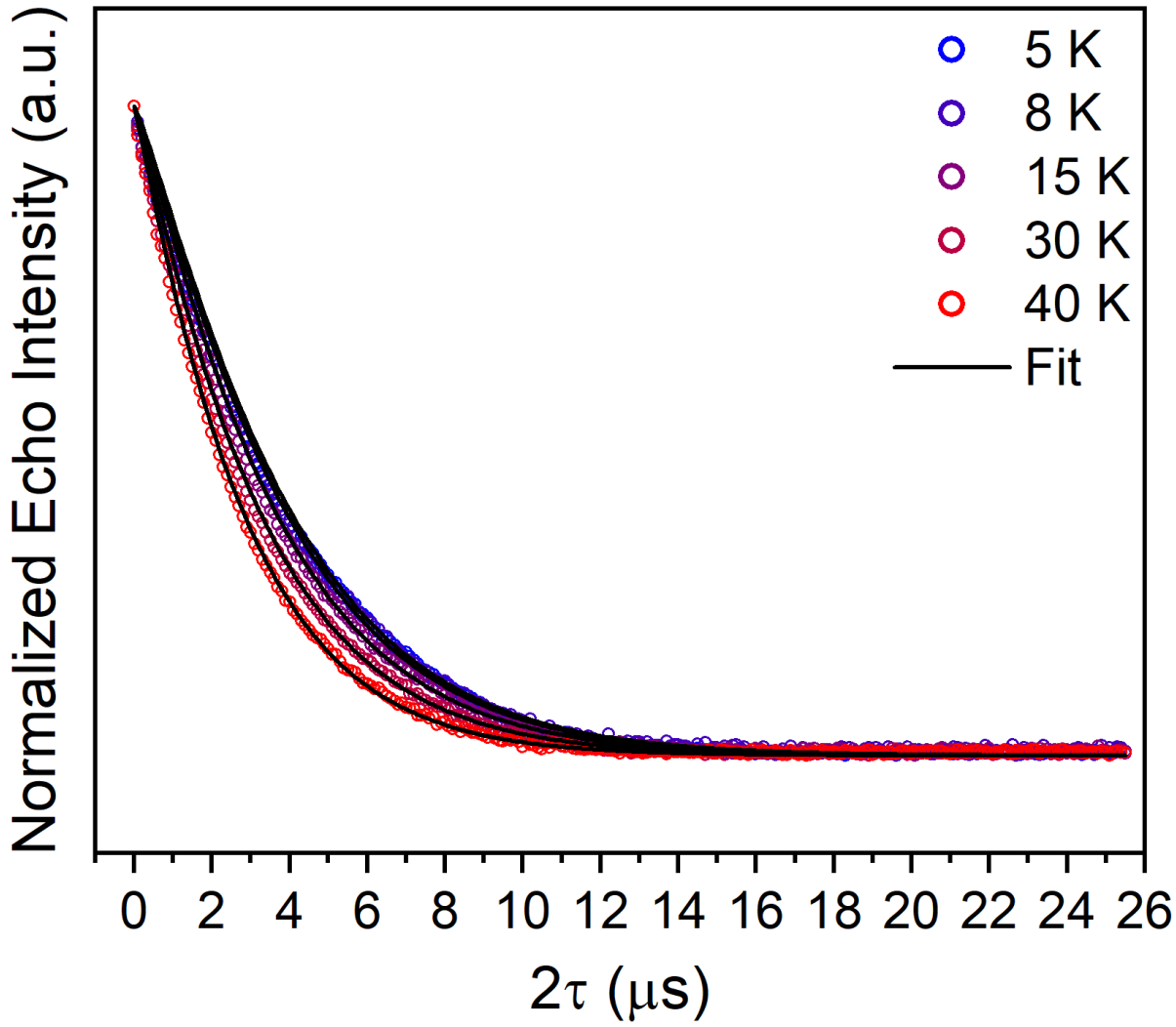

Figure 6.21. Selected variable-temperature 2-pulse echo decay curve and fits for **2** in OTP using the parameters listed in Table 6.6.

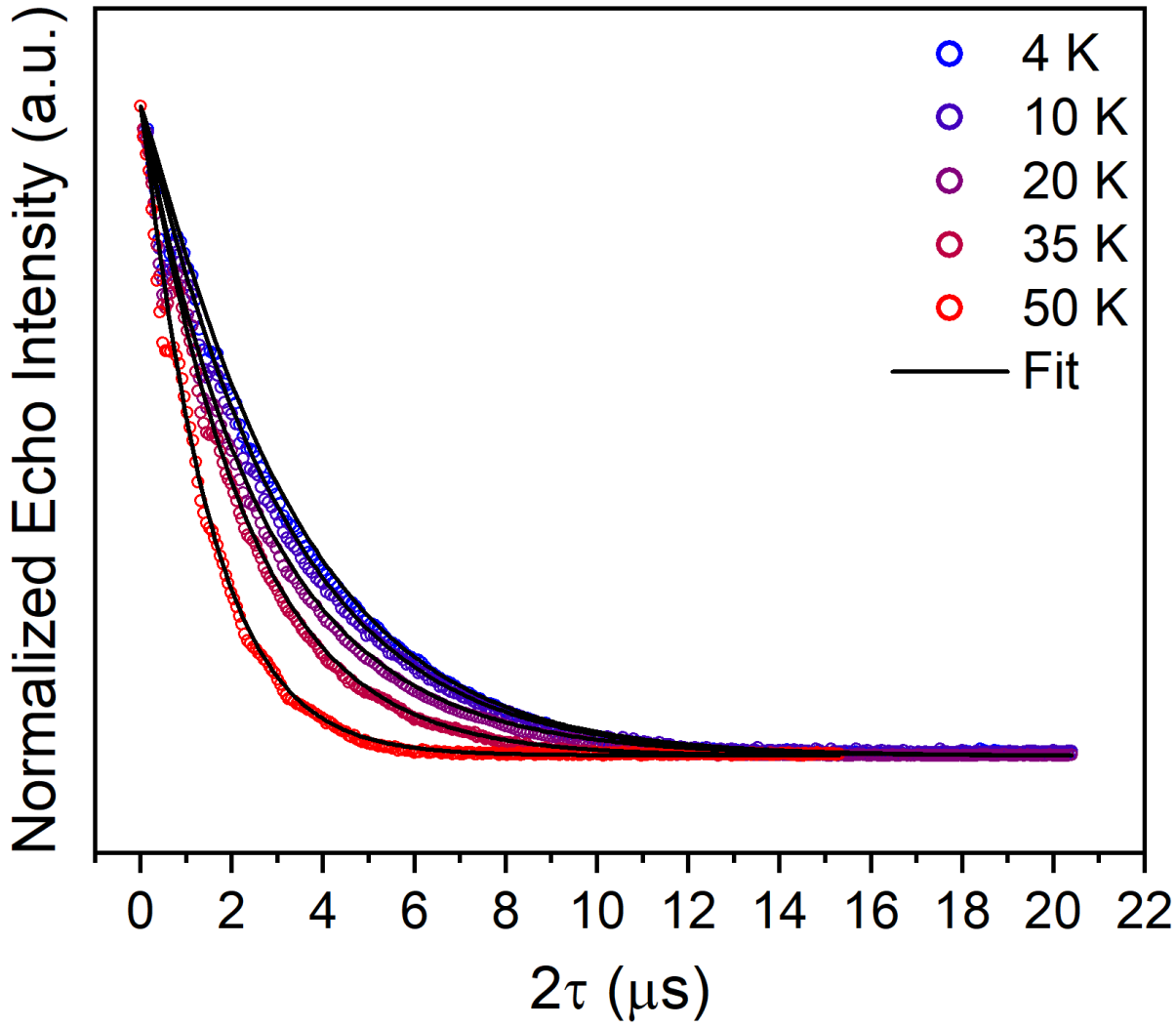

Fig. 6.22. Selected variable-temperature 2-pulse echo decay curves and fits for **2-*d*^{2}** in OTP using the parameters listed in Table 6.6**.**

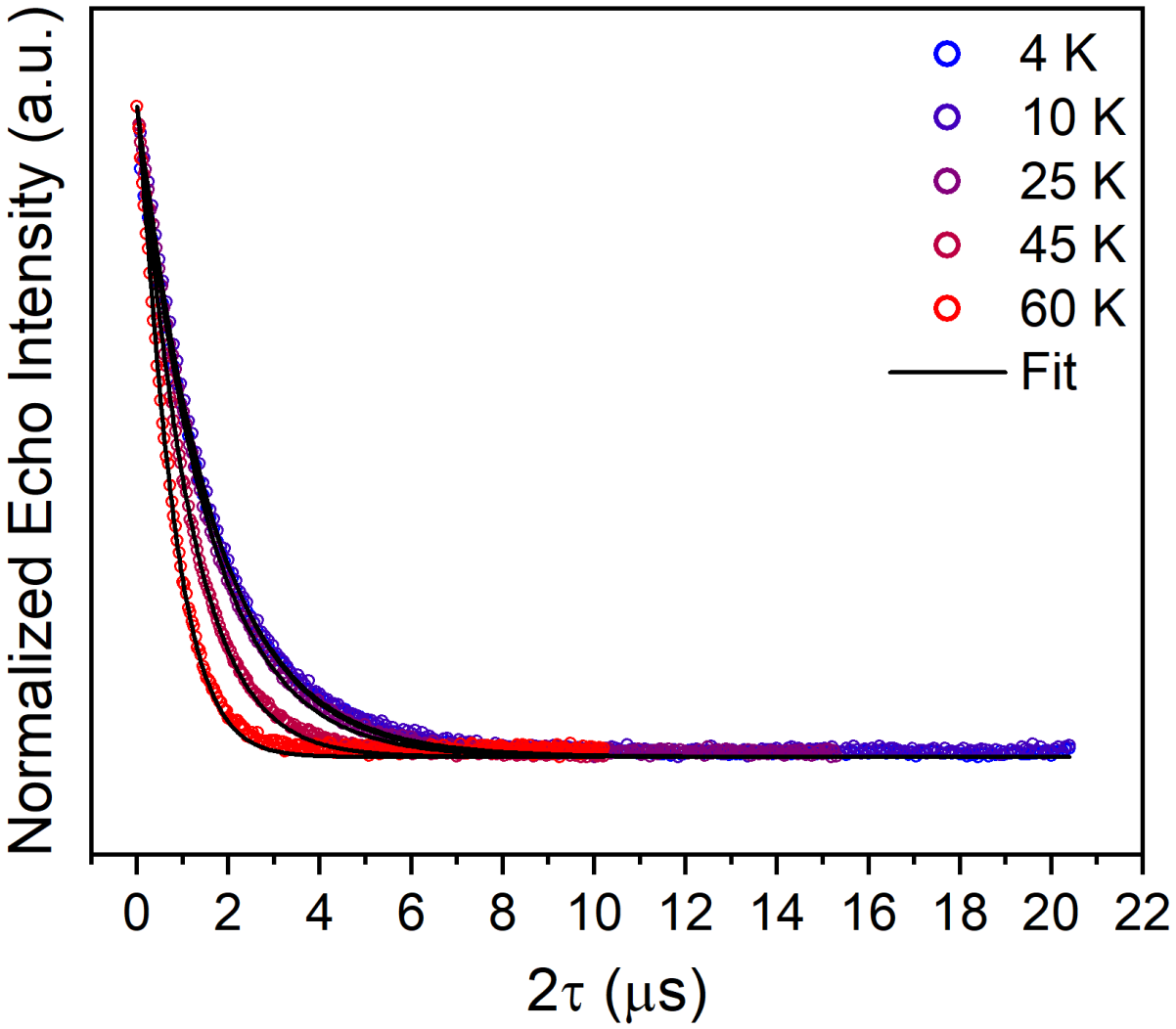

Fig. 6.23. Selected variable-temperature 2-pulse echo decay curves and fits for $\mathbf{2}_{0.05\%}$ using the parameters listed in Table 6.6.

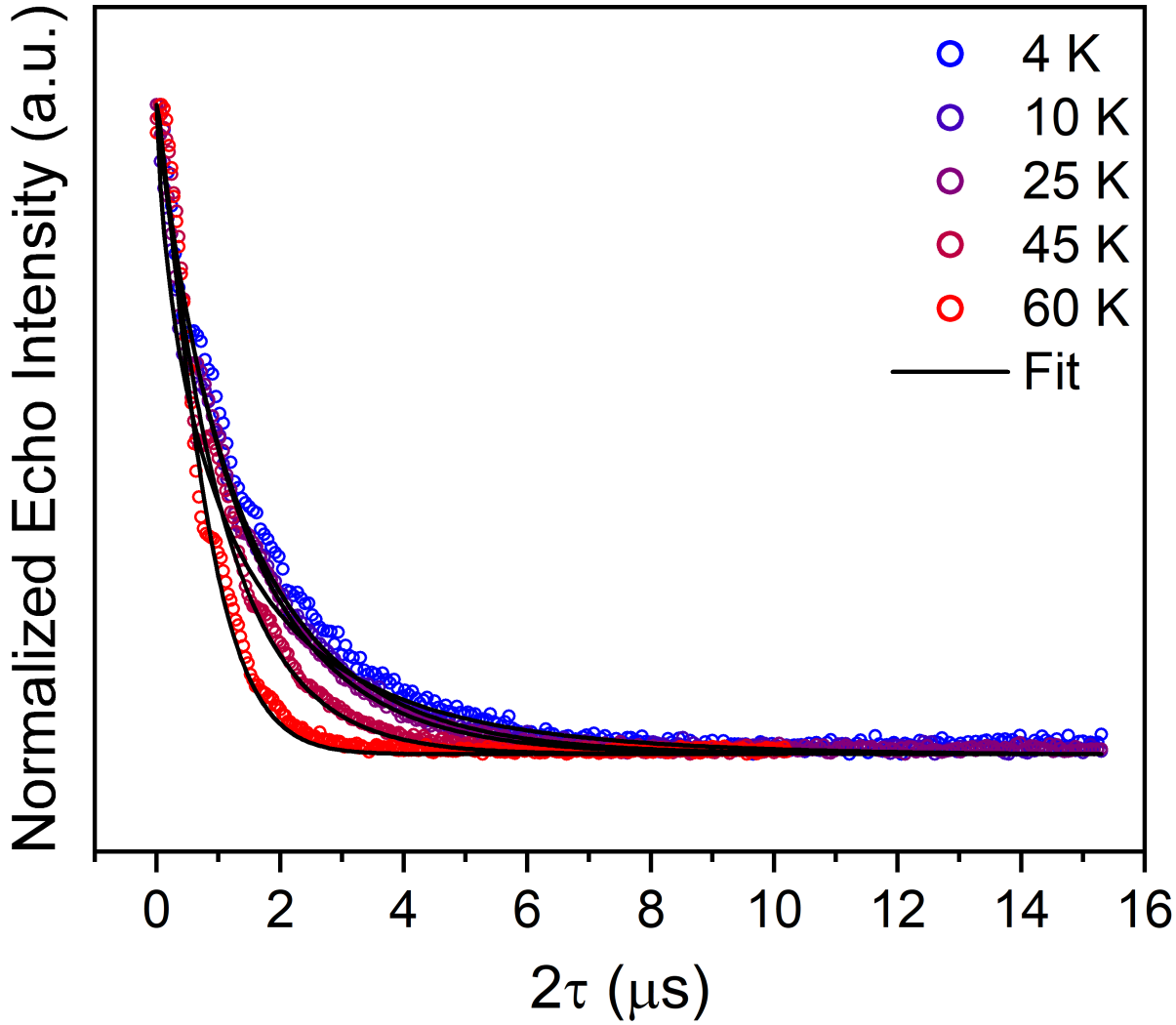

Fig. 6.24. Selected variable-temperature 2-pulse echo decay curves and fits for **2-$d^2_{0.05\%}$** using the parameters listed in Table 6.6

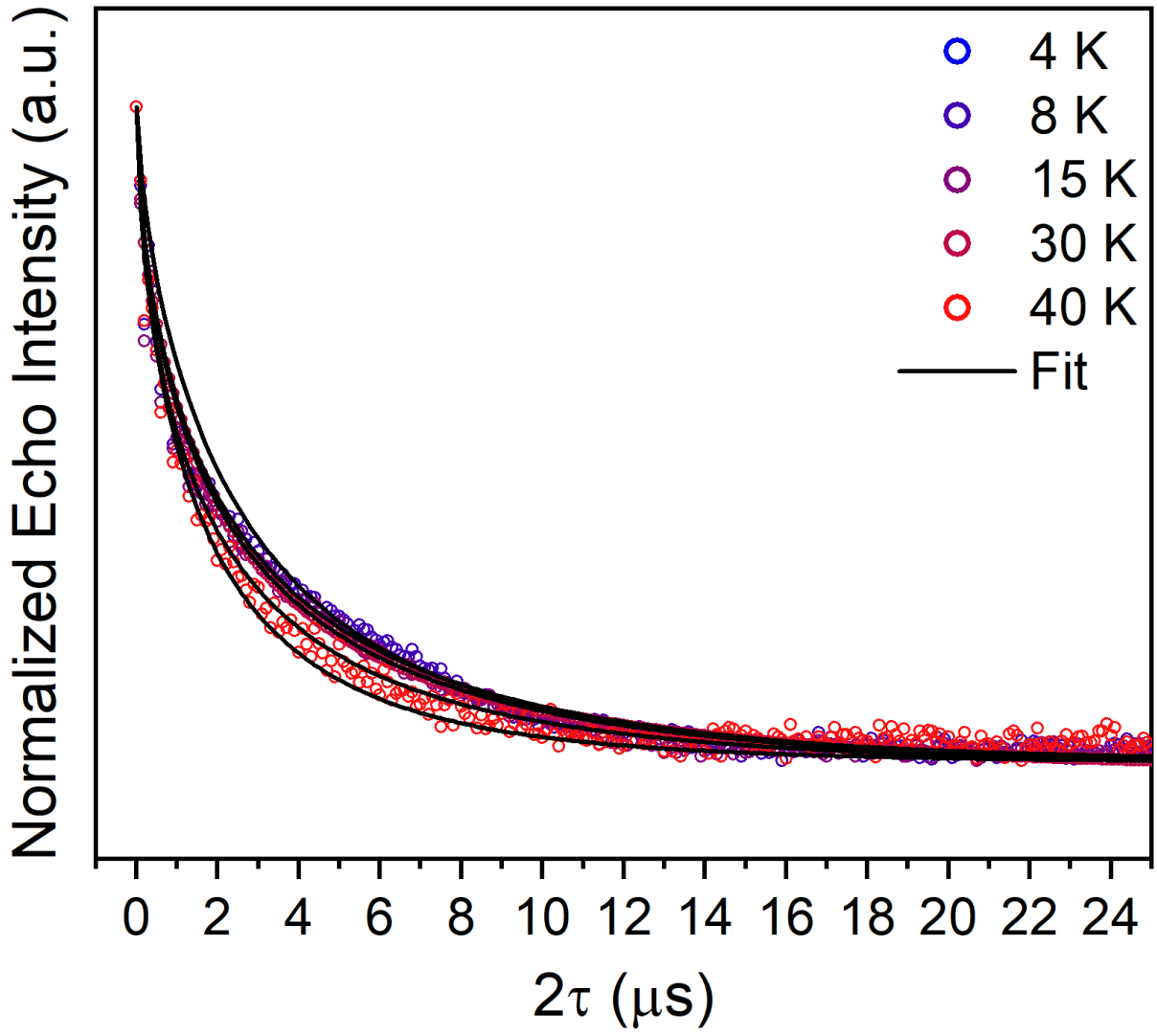

Fig. 6.25. Selected variable-temperature 2-pulse echo decay curves and fits for **1** in OTP using the parameters listed in Table 6.6**.**

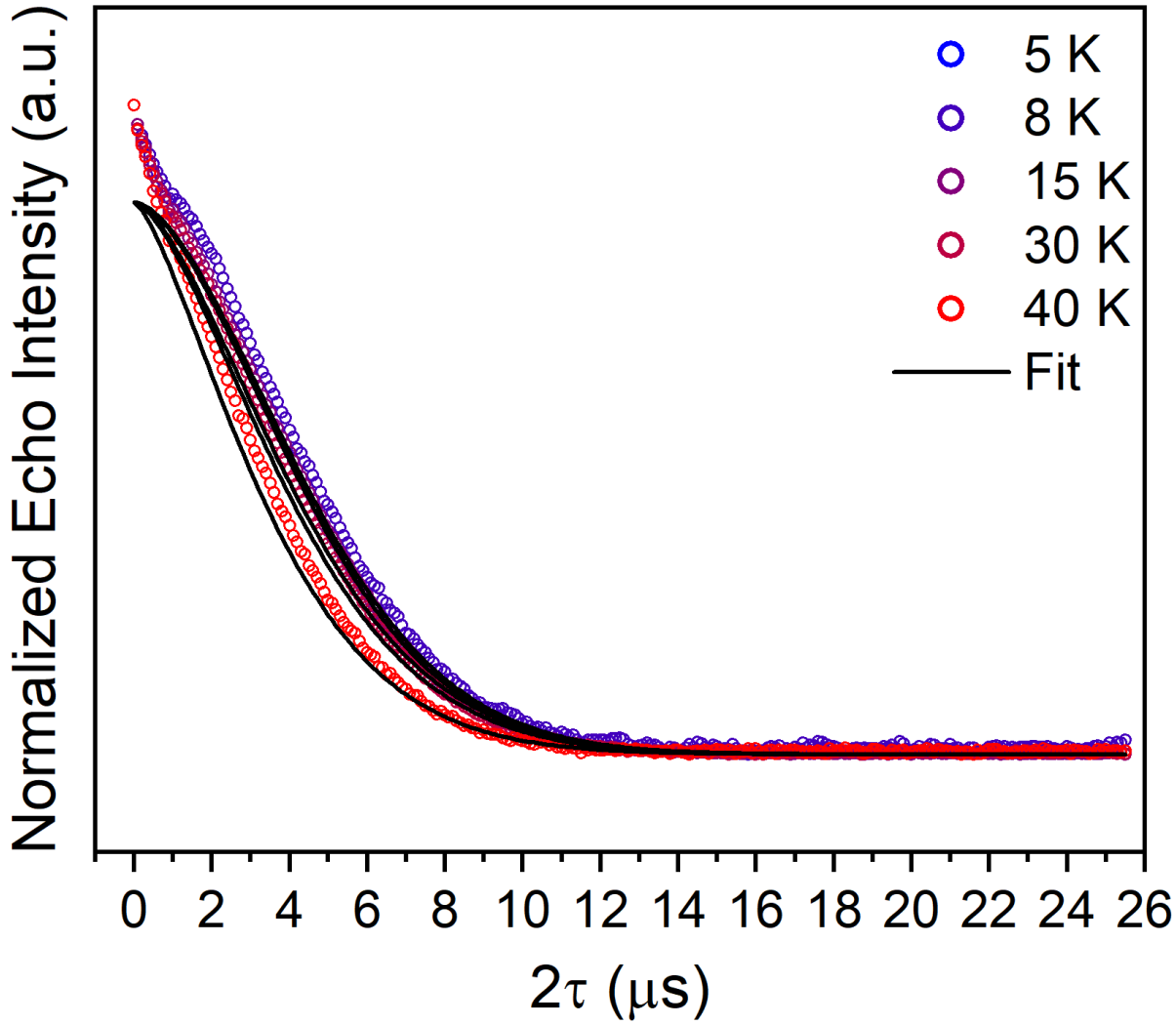

Fig. 6.26. Selected variable-temperature 2-pulse echo decay curves and fits for **3** in OTP using the parameters listed in Table 6.6**.**

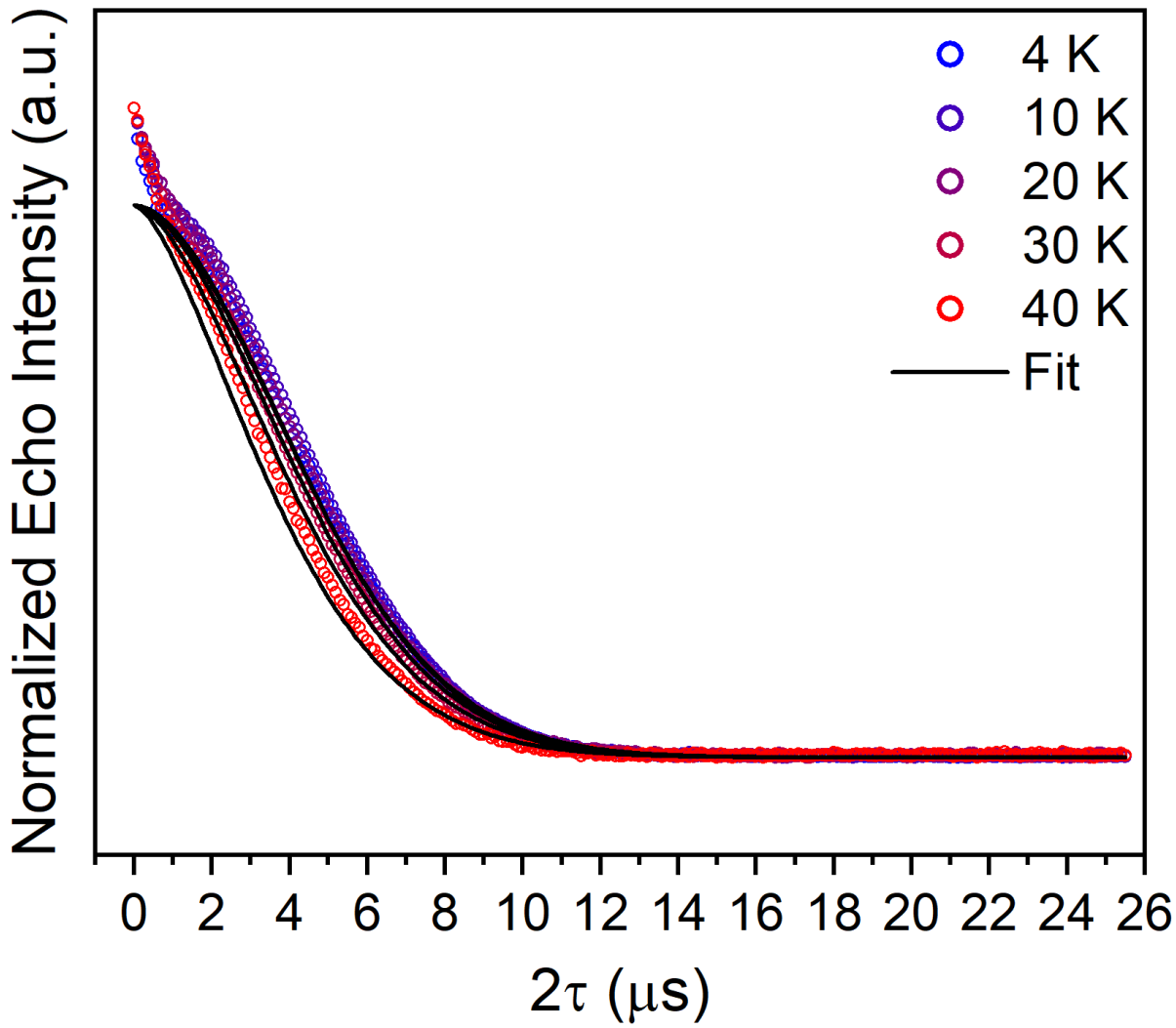

Fig. 6.27. Selected variable-temperature 2-pulse echo decay curves and fits for **4** in OTP using the parameters listed in Table S6**.**

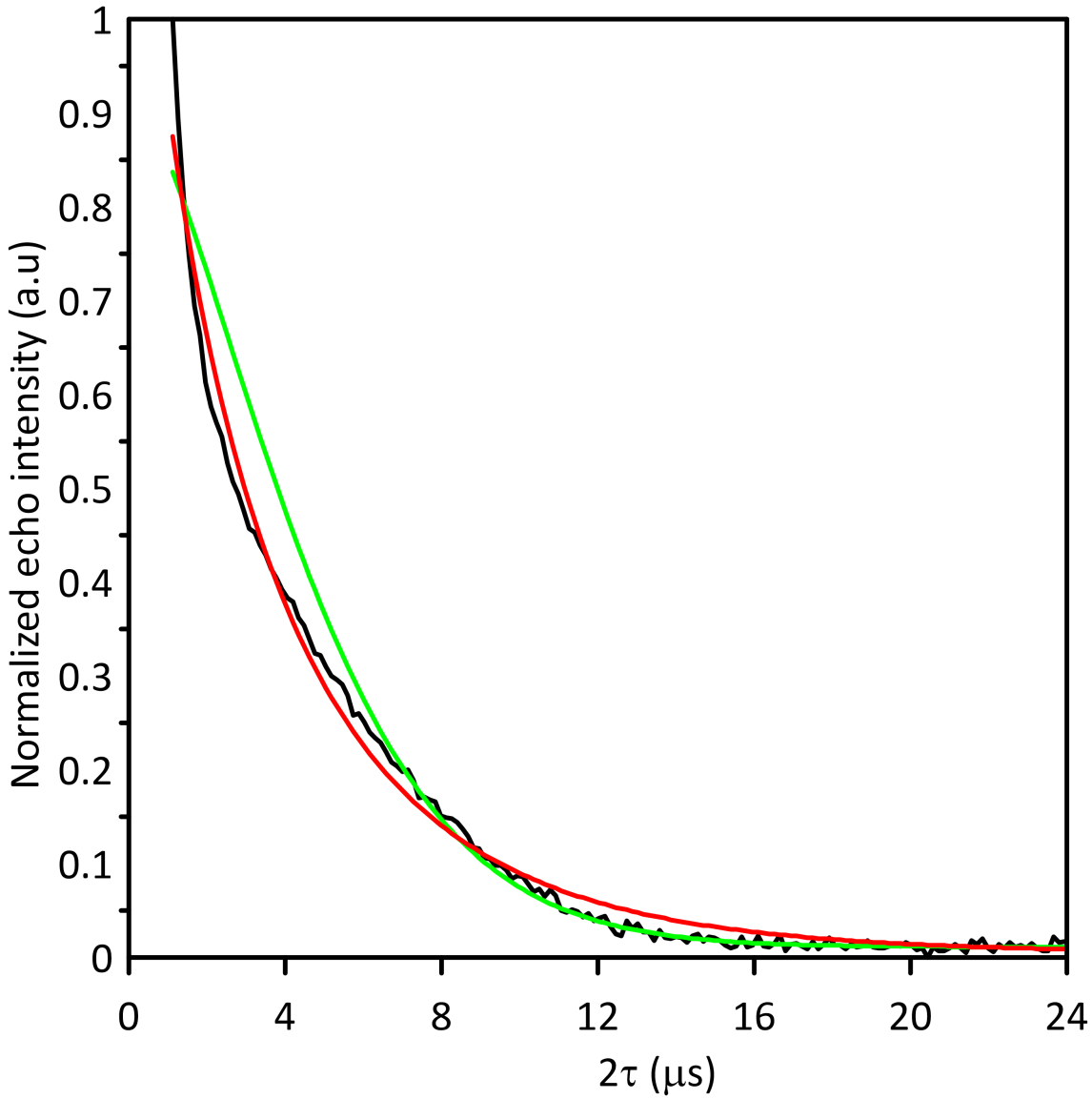

Fig. 6.27. Comparison of fits for two-pulse echo decays for **1** in OTP. When the two-pulse echo for **1** in OTP at 5 K (black) was fit with a stretched exponential (red) as shown in Figure 6.24, the deviation between the fit function and the experimental data is systematic and larger than for **2-4**. The deviation is attributed to echo modulation with a period of about 2 μs from protons of the ethyl group. An alternate fit to the data (green) obtained by selecting a few points at short τ and many points at longer τ has a systematic deviation that could arise from modulation.

References

1 G. Aromí, D. Aguilà, P. Gamez, F. Luis and O. Roubeau, *Chem. Soc. Rev.*, **2012**, *41*, 537–546.

2 M. N. Leuenberger, D. Loss, *Nature,* **2001**, *410* (6830), 789–793.

3 A. Gaita-Ariño, F. Luis, S. Hill and E. Coronado, *Nat. Chem.*, **2019**, *11*, 301–309.

4 E. Terreno, D. D. Castelli, A. Viale, S. Aime, *Chem. Rev.* **2010**, *110* (5), 3019–3042.

5 M. C. Heffern, L. M. Matosziuk and T. J. Meade, *Chem. Rev.*, **2014**, *114*, 4496–4539.

6 G. Tircs and Z. Baranyai , *The Chemistry of Contrast Agents in Medical Magnetic Resonance Imaging Stability and Toxicity of Contrast Agents*, John Wiley & Sons, 2013.

7 M. Atzori and R. Sessoli, *J. Am. Chem. Soc.*, **2019**, *141*, 11339–11352.

8 M. J. Graham, J. M. Zadrozny, M. S. Fataftah and D. E. Freedman, *Chem. Mater.*, **2017**, *29*, 1885–1897.

9 G. R. Eaton, S. S. Eaton, *J. Magn. Reson.* **1999**, *136* (1), 63–68.

10 Graham, M. J.; Yu, C.-J.; Krzyaniak, M. D.; Wasielewski, M. R.; Freedman, D. E. *J. Am. Chem. Soc.* **2017**, *139* (8), 3196–3201.

11 C. E. Jackson, C.-Y. Lin, S. H. Johnson, J. van Tol and J. Zadrozny, *Chem. Sci.*, **2019**, *10*, 8447-8454.

12 A.-M. Ariciu, D. H. Woen, D. N. Huh, L. E. Nodaraki, A. K. Kostopoulos, C. A. P. Goodwin, N. F. Chilton, E. J. L. McInnes, R. E. P. Winpenny, W. J. Evans, F. Tuna, *Nat. Commun.* **2019**, *10* (1), 3330.

13 M. J. Graham, J. M. Zadrozny, M. Shiddiq, J. S. Anderson, M. S. Fataftah, S. Hill, D. E. Freedman, *J. Am. Chem. Soc.* **2014**, *136* (21), 7623–7626.

14 C.-Y. Lin, T. Ngendahimana, G. R. Eaton, S. S. Eaton, J. M. Zadrozny, *Chem. Sci.* **2019,** *10*, 548-555.

15 K. Bader, D. Dengler, S. Lenz, B. Endeward, S.-D. Jiang, P. Neugebauer and J. van Slageren, *Nat. Commun.*, **2014**, *5*, 5304.

16 J. M. Zadrozny, J. Niklas, O. G. Poluektov and D. E. Freedman, *ACS Cent. Sci.*, **2015**, *1*, 488–492.

17 D. C. Johnston, *Phys. Rev. B* **2006**, *74* (18), 184430.

18 P. A. Narayana, L. Kevan, **1976**, *23* (3), 385–393.

19 K. M. Salikhov; Y. D. Tsvetkov. Time Domain Electron Spin Resonance, L. Kevan, Ch. 7; 1979.

20 T. Maly, G. T. Debelouchina, V. S. Bajaj, K.-N. Hu, C.-G. Joo, M. L. Mak–Jurkauskas, J. R. Sirigiri, P. C. A. van der Wel, J. Herzfeld, R. J. Temkin, R. G. Griffin, *J. Chem. Phys.* **2008**, *128* (5), 052211.

21 A. Cernescu, T. Maly, T. F. Prisner, *J. Magn. Reson.* **2008**, *192* (1), 78–84.

22 *Biological Magnetic Resonance*; Berliner, L., Ed.; Biological Magnetic Resonance; Springer US, 1978.

23 Schweiger, A.; Jeschke, G. *Principles of Pulse Electron Paramagnetic Resonance*; Oxford University Press, 2001.

24 A. Zecevic, G. R. Eaton, S. S. Eaton M. Lindgren, *Mol. Phys.* **1998**, *95* (6), 1255–1263.

25 A. D. Milov, K. M. Salikhov, Yu. D. Tsvetkov, *Fiz. Tverd. Tela* **1973**, *15* (4), 1187–1195.

26 E. R. Canarie, S. M. Jahn and S. Stoll, *J. Phys. Chem. Lett.*, **2020**, *11*, 3396–3400.

27 S. R. Cooper, Y. B. Koh and K. N. Raymond, *J. Am. Chem. Soc.*, **1982**, *104*, 5092–5102.

28 H. G. Kjaergaard, D. L. Howard, D. P. Schofield, T. W. Robinson, S. Ishiuchi, M. Fujii, *J. Phys. Chem. A* **2002**, *106* (2), 258–266.

29 D. Finkelstein-Shapiro, S. K. Davidowski, P. B. Lee, C. Guo, G. P. Holland, T. Rajh, K. A. Gray, J. L. Yarger, M. Calatayud, *J. Phys. Chem. C* **2016**, *120* (41), 23625–23630.

30 W. Egan, G. Gunnarsson, T. E. Bull, S. A. Forsen, *J. Am. Chem. Soc.* **1977**, *99* (14), 4568–4572.

31 Bryant, B. E.; Fernelius, W. C.; Busch, D. H.; Stoufer, R. C.; Stratton, W. Vanadium(IV) Oxy(Acetylacetonate). In Inorganic Syntheses; 1957; Vol. 5, pp 113–116.

32 Sheldrick, G. M. Program for Empirical Absorption Correction of Area Detector Data. SADABS 1996.

33 Sheldrick, G. M. *Acta Crystallogr. Sect. Found. Adv.* **2015**, *71*, 3–8.

34 Sheldrick, G. M. *Acta Crystallogr. Sect. C Struct.* Chem. 2015, 71 (1), 3–8.

35 Sheldrick, G. M. *Acta Crystallogr. A* **2008**, *64*, 112–122.

36 Stoll, S.; Schweiger, A. EasySpin, *J. Magn. Reson.* **2006**, *178*, 42–55.

37 *Matlab*; The MathWorks Inc.: Natick, MA, 2018.

38 *Origin*; OriginLab: Northampton, MA, 2018.

39 T. J. Pearson, D. W. Laorenza, M. D. Krzyaniak, M. R. Wasielewski, D. E. Freedman, *Dalton Trans.* **2018**, *47* (34), 11744–11748.

40 H. Chen, A. G. Maryasov, O. Y. Rogozhnikova, D. V. Trukhin, V. M. Tormyshev, M. K. Bowman, *Phys. Chem. Chem. Phys.* **2016**, *18* (36), 24954–24965.

41 Salikhov, K. M.; Tsvetkov, Y. D. Electron Spin-Echo Studies of Interactions in Solids. In *Time Domain Electron Spin Resonance*; Kevan, L., Schwartz, R. N., Eds.; John Wiley: New York, 1979; pp 232–277.

42 J. P. Wolfe, *Phys. Rev. Lett.*, **1973**, *31*, 907–910.

43 A. R. King, J. P. Wolfe, R. L. Ballard, *Phys. Rev. Lett.* **1972**, *28* (17), 1099–1102.

CHAPTER 7 – SUMMARY

Throughout this research, vanadium(IV) complexes were used as a platform to understand how very small interactions in the environment of an unpaired electron impact relaxation processes. Electronic spins are extremely sensitive to changes in the local environment which made metal-based complexes a suitable platform for investigating the role of ligand, counterion, and matrix. Modification of the ligand shell, counterions, orientation in a magnetic field, and matrix all change electronic spin relaxation processes, therefore contributing to the fields of quantum computing, medical imaging, information storage, and molecular magnetism. Through studying environmental modifications in vanadium(IV) complexes, five design principles were identified.

Since the initial report from our group detailing counterion impact on spin relaxation times and a report from Freedman et. al in 2015 detailing the importance of nuclear spins in the environment, our group has further explored the local environment of an unpaired electron on a metal complex. First, nuclear spins impacted phase memory time (T_m) through nuclear-nuclear spin diffusion contributing to the field of molecule-based qubits. Nuclear spin relaxation times were further investigated to gain a deeper understanding on the nuclear-nuclear interactions. The second design principle shows that nuclear-nuclear spin diffusion are strong contributors to electron spin relaxation. This work inspired us to change the nuclear spins on the ligand shell. These vanadium complexes also showed an orientation dependence varying as much as 20 % at very high magnetic field (4.4 T), directly influencing the field of surface-based technologies. Third, the orientation of a molecule in a magnetic field directly impacts spin relaxation and that orientation may not always have the highest echo intensity. Our initial counterion work was revisited to understand how the counterions in these complexes bind and impact spin relaxation. This work unveiled the importance, and fourth design principle, of meticulous experiment setup and sample preparation. Finally, fifth, counterion binding and methyl groups on counterions are

detrimental to long relaxation times. This project on counterion influence has led us to think about more diverse counterion structures which will be the next direction.

We envision the work described in this dissertation to lead to different counterion studies, more diverse ligand architectures, and a more detailed matrix study for paramagnetic metal complexes. All counterions studied contained methyl groups which are detrimental to long T_m times. Cyclic counterions obtained through amines like piperidine or quinuclidine may provide an avenue to study counterion influence without the presence of methyl groups. Counterions can also provide a way to test nuclear-spin-patterning. By changing the nuclear spins on the counterion as opposed to the ligand as described in Chapter 3, the nuclear spins are fully outside the spin diffusion barrier. To further study the nuclear spin interactions on a metal complex, fluorine could be used as the next halogen substituent on ligands. In Chapter 4 we were limited to proton NMR studies due to the fast relaxation of bromine isotopes. Fluorine NMR is well understood and can be used to understand halogen-hydrogen interactions through 2D NMR experiments. Finally, vanadium(IV) historically has long enough lifetimes to be studied through pulsed EPR. Other metals can be studied with the design principles detailed in this dissertation.